

MATERIALS PHYSICS AND MECHANICS

Vol. 53, No. 1, 2025

MATERIALS PHYSICS AND MECHANICS

Principal Editors:

Alexander Belyaev

Andrei Rudskoi

Institute for Problems in Mechanical Engineering of the Russian Academy of Science (RAS), Russia

Peter the Great St. Petersburg Polytechnic University, Russia

Founder and Honorary Editor: Ilya Ovid'ko (1961-2017)

Institute for Problems in Mechanical Engineering of the Russian Academy of Sciences (RAS), Russia

Associate Editor:

Anna Kolesnikova

Artem Semenov

Institute for Problems in Mechanical Engineering of the Russian Academy of Sciences (RAS), Russia

Peter the Great St. Petersburg Polytechnic University, Russia

Editorial Board:

E.C. Aifantis

Aristotle University of Thessaloniki, Greece

K.E. Aifantis

University of Florida, USA

U. Balachandran

Argonne National Laboratory, USA

A. Bellosi

Research Institute for Ceramics Technology, Italy

S.V. Bobylev

Institute for Problems in Mechanical Engineering (RAS), Russia

A.I. Borovkov

Peter the Great St.Petersburg Polytechnic University, Russia

G.-M. Chow

National University of Singapore, Singapore

Yu. Estrin

Monash University, Australia

A.B. Freidin

Institute for Problems in Mechanical Engineering (RAS), Russia

I.G. Goryacheva

Institute of Problems of Mechanics (RAS), Russia

D. Hui

University of New Orleans, USA

G. Kiriakidis

IESL/FORTH, Greece

D.M. Klimov

Institute of Problems of Mechanics (RAS), Russia

G.E. Kodzhaspirov

Peter the Great St. Petersburg Polytechnic University, Russia

S.A. Kukushkin

Institute for Problems in Mechanical Engineering (RAS), Russia

T.G. Langdon

University of Southampton, U.K.

V.P. Matveenko

Institute of Continuous Media Mechanics (RAS), Russia

A.I. Melker

Peter the Great St. Petersburg Polytechnic University, Russia

Yu.l. Meshcheryakov

Institute for Problems in Mechanical Engineering (RAS), Russia

R.R. Mulyukov

Institute for Metals Superplasticity Problems (RAS), Russia

Yu.V. Petrov

St. Petersburg State University, Russia

N.M. Pugno

Politecnico di Torino, Italy

B.B. Rath

Naval Research Laboratory, USA

A.E. Romanov

Ioffe Institute (RAS), Russia

A.M. Sastry

University of Michigan, Ann Arbor, USA

B.A. Schrefler

University of Padua, Italy

N.V. Skiba

Institute for Problems in Mechanical Engineering (RAS), Russia

A.G. Sheinerman

Institute for Problems in Mechanical Engineering (RAS), Russia

R.Z. Valiev

Ufa State Aviation Technical University, Russia

K. Zhou

Nanyang Technological University, Singapore

"Materials Physics and Mechanics" Editorial Office:

Phone: +7(812)552 77 78, ext. 224 E-mail: mpmjournal@spbstu.ru Web-site: http://www.mpm.spbstu.ru

International scientific journal "Materials Physics and Mechanics" is published by Peter the Great St. Petersburg Polytechnic University in collaboration with Institute for Problems for Mechanical Engineering in the Russian Academy of Sciences in both hard copy and electronic versions. The journal provides an international medium for the publication of reviews and original research papers written in English and focused on the following topics:

- Mechanics of composite and nanostructured materials.
- Physics of strength and plasticity of composite and nanostructured materials.
- Mechanics of deformation and fracture processes in conventional materials (solids).
- Physics of strength and plasticity of conventional materials (solids).
- Physics and mechanics of defects in composite, nanostructured, and conventional materials.
- Mechanics and physics of materials in coupled fields.

Owner organizations: Peter the Great St. Petersburg Polytechnic University; Institute of Problems of Mechanical Engineering RAS.

Materials Physics and Mechanics is indexed in Chemical Abstracts, Cambridge Scientific Abstracts, Web of Science Emerging Sources Citation Index (ESCI) and Elsevier Bibliographic Databases (in particular, SCOPUS).

© 2025, Peter the Great St. Petersburg Polytechnic University © 2025, Institute for Problems in Mechanical Engineering RAS



МЕХАНИКА И ФИЗИКА МАТЕРИАЛОВ

Materials Physics and Mechanics

Том 53, номер 1, 2025 год

Учредители:

Редакционная коллегия журнала

Главный редактор

д.т.н., академик РАН А.И. Рудской

Санкт-Петербургский политехнический университет Петра Великого

Главный научный редактор

д.ф.-м.н., чл.-корр. РАН А.К. Беляев

Институт проблем машиноведения Российской академии наук (РАН)

Основатель и почетный редактор

д.ф.-м.н. **И.А. Овидько (1961-2017)**

Институт проблем машиноведения Российской академии наук (РАН)

Ответственные редакторы

д.ф.-м.н. А.Л. Колесникова

Институт проблем машиноведения

Российской академии наук (РАН)

д.ф.-м.н. А.С. Семенов

Санкт-Петербургский политехнический университет

Петра Великого

Международная редакционная коллегия:

д.ф.-м.н. С.В. Бобылев

Институт проблем машиноведения РАН, Россия

к.т.н., проф. А.И. Боровков

Санкт-Петербургский политехнический ун-т Петра Великого, Россия

д.ф.-м.н., проф. Р.З. Валиев

Уфимский государственный технический университет, Россия

д.ф.-м.н., академик РАН И.Г. Горячева

Институт проблем механики РАН, Россия

д.ф.-м.н., академик РАН Д.М. Климов

Институт проблем механики РАН, Россия

д.т.н., проф. Г.Е. Коджаспиров

Санкт-Петербургский политехнический ун-т Петра Великого, Россия

д.ф.-м.н., проф. С.А. Кукушкин

Институт проблем машиноведения РАН, Россия

д.ф.-м.н., академик РАН В.П. Матвеенко

Институт механики сплошных сред РАН, Россия

д.ф.-м.н., проф. А.И. Мелькер

Санкт-Петербургский политехнический ун-т Петра Великого, Россия

д.ф.-м.н., проф. Ю.И. Мещеряков

Институт проблем машиноведения РАН, Россия

д.ф.-м.н., чл.-корр. РАН Р.Р. Мулюков

Институт проблем сверхпластичности металлов РАН, Россия

д.ф.-м.н., чл.-корр. РАН Ю.В. Петров

Санкт-Петербургский государственный университет, Россия д.ф.-м.н., проф. А.Е. Романов

Физико-технический институт им. А.Ф. Иоффе РАН, Россия

д.ф.-м.н. Н.В. Скиба

Институт проблем машиноведения РАН, Россия

д.ф.-м.н., проф. А.Б. Фрейдин

Институт проблем машиноведения РАН, Россия

д.ф.-м.н. А.Г. Шейнерман

Институт проблем машиноведения РАН. Россия

Prof., Dr. E.C. Aifantis

Aristotle University of Thessaloniki, Greece

Dr. K.E. Aifantis

University of Florida, USA

Dr. U. Balachandran

Argonne National Laboratory, USA

Dr. A. Bellosi

Research Institute for Ceramics Technology, Italy

Prof., Dr. G.-M. Chow

National University of Singapore, Singapore

Prof., Dr. Yu. Estrin

Monash University, Australia

Prof., Dr. D. Hui

University of New Orleans, USA

Prof., Dr. G. Kiriakidis

IESL/FORTH, Greece

Prof., Dr. T.G. Langdon

University of Southampton, UK

Prof., Dr. N.M. Pugno

Politecnico di Torino, Italy

Dr. B.B. Rath

Naval Research Laboratory, USA

Prof., Dr. A.M. Sastry

University of Michigan, Ann Arbor, USA Prof., Dr. B.A. Schrefler

University of Padua, Italy

Prof., Dr. K. Zhou

Nanyang Technological University, Singapore

Тел.: +7(812)552 77 78, доб. 224 E-mail: mpmjournal@spbstu.ru Web-site: http://www.mpm.spbstu.ru

Тематика журнала

Международный научный журнал "Materials Physics and Mechanics" издается Санкт-Петербургским политехническим университетом Петра Великого в сотрудничестве с Институтом проблем машиноведения Российской академии наук в печатном виде и электронной форме. Журнал публикует обзорные и оригинальные научные статьи на английском языке по следующим тематикам:

- Механика композиционных и наноструктурированных материалов.
- Физика прочности и пластичности композиционных и наноструктурированных материалов.
- Механика процессов деформации и разрушения в традиционных материалах (твердых телах).
- Физика прочности и пластичности традиционных материалов (твердых тел).
- Физика и механика дефектов в композиционных, наноструктурированных и традиционных материалах.
- Механика и физика материалов в связанных полях.

Редколлегия принимает статьи, которые нигде ранее не опубликованы и не направлены для опубликования в другие научные издания. Все представляемые в редакцию журнала "Механика и физика материалов" статьи рецензируются. Статьи могут отправляться авторам на доработку. Не принятые к опубликованию статьи авторам не возвращаются.

Журнал "Механика и физика материалов" ("Materials Physics and Mechanics") включен в систему цитирования Web of Science Emerging Sources Citation Index (ESCI), SCOPUS и РИНЦ.

Contents

Fractional strain analysis on reflection of plane waves at an impedance boundary of non-local swelling porous thermoelastic medium S. Sharma, D. Batra, R. Kumar	1-21
Study of different theories of thermoelasticity under the Rayleigh wave propagation along an isothermal boundary V. Gupta, M. Kumar, Sh. Goel	22-37
Multifractal properties of breaking bonds coordinates in heterogeneous materials revealed by the discrete element method V.L. Hilarov, E.E. Damaskinskaya	38-47
Influence of free surface on melting and crystallization in nickel and copper: molecular dynamics simulation G.M. Poletaev, Y.V. Bebikhov, A.S. Semenov, R.Y. Rakitin, D.V. Novoselova	48-56
Thermal cycling stability of the martensitic transformation in $Ti_{40.7}Hf_{9.5}Ni_{49.8-x}Cu_x$ (x = 1, 5 or 10 at. %) cast alloys N.N. Resnina, S.P. Belyaev, A.I. Bazlov, A.V. Sibirev, I.V. Ponikarova, M.E. Trofimova, A.M. Ivanov, R.M. Bikbaev	57-67
Creation of aluminum matrix composites reinforced with micro- and nanoparticles of titanium carbide with nickel coating and description of their hardening mechanisms E.G. Zemtsova, B.N. Semenov, N.F. Morozov, Yu.V. Sidorov, V.K. Kudymov, V.M. Smirno	68-77 v
EBSD on bainitic steel to assess parent austenite state after multi-pass hot rolling: Textural analysis versus reconstruction of prior grains A.A. Zisman, N.Yu. Zolotorevsky, D.A. Petrov, S.N. Petrov	78-88
Structural changes in a commercial Al-Cu alloy during hot equal channel angular pressing 8 O.S. Sitdikov	89-108
Effect of high pressure torsion and annealing on the microstructure and microhardness of Inconel 718 produced by selective laser melting K.S. Mukhtarova, R.V. Shakhov, Sh.Kh. Mukhtarov	09-116
Mechanical and durability properties of sustainable composites derived from recycled polyethylene terephthalate and enhanced with natural fibers: a comprehensive review A. Kumar, R. Bedi	17-142

Stydy of the influence of brombutyl and divinylstyrene caoutchoucs,	143-149
sevilen on the properties of seawater-resistant rubber	
E.N. Egorov, N.I. Kol'tsov	

Preparation and characterization of geopolymer/activated carbon composite 150–158 materials used as a bone substitute material

A. Moonphukhiao, B. Samran, S. Chaiwichian

Magnetism of the hybrid SiC/Si structure grown on silicon surface

V.V. Romanov, N.I. Rul', V.E. Gasumyants, I.D. Venevtsev, K.B. Taranets, A.V. Korolev,

S.A. Kukushkin, A.V. Osipov, N.T. Bagraev

Submitted: July 24, 2024 Revised: October 30, 2024 Accepted: November 29, 2024

Fractional strain analysis on reflection of plane waves at an impedance boundary of non-local swelling porous thermoelastic medium

S. Sharma ¹, D. Batra ^{2™}, R. Kumar ³ ¹

- ¹ Houston University, Houston, USA
- ² Kishan Lal Public College, Rewari, Haryana, India
- ³ Kurukshetra University, Kurukshetra, Haryana, India
- [™] divyabatra1982@gmail.com

ABSTRACT

The current work focuses on developing a model to examine wave analysis in non-local swelling porous thermoelastic medium under fractional order strain. After converting the governing equations into twodimensional and utilizing the dimensionless quantities for further simplification the Helmholtz decomposition theorem has been used to decompose the system into longitudinal and transverse components. The frequency dispersion relation is derived by assuming the plane wave solution in twodimensional case for the given problem. It is found that there exist two dilatational waves, a thermal wave and two transversal waves travelling at distinct velocities. The amplitude ratios for the reflected waves are obtained with the aid of impedance boundary restrictions. The obtained amplitude ratios are used to obtain the energy ratios of different reflected waves. Influence of fractional order parameter on distinct types of wave speeds is illustrated graphically and it is observed that increase in fractional order parameter diminishes the magnitude of all existing waves except longitudinal wave in solid. Also impacts of swelling pores and fractional order on the attained energy ratios are displayed graphically versus angle of incidence. It is verified that during reflection phenomena, the sum of energy ratio is equal to unity at each angle of incidence and there is no dissipation on the boundary surface. Swelling porosity decrease the impact of energy ratios of reflected longitudinal wave and thermal wave for all values of fractional order parameter. Some unique cases are also presented. The results find application in geophysics, civil engineering and structure related issues.

KEYWORDS

energy ratios • reflection coefficients • impedance border • fractional order strain • swelling porous

Citation: Sharma S, Batra D, Kumar R. Fractional strain analysis on reflection of plane waves at an impedance boundary of non-local swelling porous thermoelastic medium. *Materials Physics and Mechanics*. 2025;53(1): 1–21.

http://dx.doi.org/10.18149/MPM.5312025_1

Introduction

As wave phenomena have numerous applications in the field of geophysics, civil engineering, oil exploration, slurry, and agriculture scientists and researchers have long been very interested in studying wave phenomena in porous media. The model of wave circulation in fluid-saturated porous solids and the identification of the presence of lower and higher frequency ranges were initially presented by Biot [1,2]. Eringen [3] acknowledged the utility of mixture theory in the area of expanding porous elastic media. He used a combination of elastic solid, viscous liquid, and gas in his work and focused on



things like soil swelling, wood, paper, and fiber drying, among other things. Subsequently, other researchers have made contributions to the topic of porous elastic media swelling. The amplitude ratios resulting from plane wave reflection and transmission at the border of thermoelastic swelling porous media were determined by Kumar et al. [4].

Margin and Royston [5] being the first to propose the fractional order strain model that can both predict mechanical deformation of Hookean solid and Newtonian fluid by using zero-order and one-order derivative. More significantly fractional order parameter of fractional order strain model can be chosen freely within the range 0-1 according to the necessity of practical application. In recent year one can find that the concept of fractional order strain has been successfully used in thermomechanical analysis of elastic and dipolar material systems [6-10]. Moreover, global dependency and non-local property of the fractional derivative is one of the main reason for its increasing popularity. The concept of non-linearity using fractional differential operator in thermoelastic models opens up a new perspective on the study of thermoelastic deformation in solid mechanics. A significant contribution in the theory of thermoelasticity with non-locality can be found in [11-15]. Vlase et al. [16] determined the properties of eigen values for transverse and torsional vibrations in a mechanical system having two identical beams. Sharma et al. [17] examined basic theorems and plane wave in thermoelastic diffusion using multiphase lag model with temperature dependence. Relaxed Saint-Venant principle for thermoelastic micropolar diffusion is given by Marin et al. [18].

The reflection of plane waves in thermodiffusive elastic half-space with voids was investigated by [19]. Wave propagating in a micropolar thermoelastic medium with two temperatures and layers of half-spaces surrounded by an inviscid liquid was investigated by Sharma et al. [20]. In micropolar elastic materials, plane wave reflection and transmission were investigated by Sharma et al. [21,22]. The Rayleigh wave propagation in incompressible anisotropic half spaces with impedance boundary conditions was studied by Vinh and Hue [23]. Kumar and Sharma [24] developed uniqueness, reciprocity theorems, and variational principle in piezothermoelastic medium having fractional order derivative. Sharma and Khator [25,26] looked at a few issues related to the production of electricity from renewable sources. In a modified Green-Lindsay theory, Kumar et al. [27] investigated the effect of impedance factors on wave propagation in a micropolar thermoelastic medium. According to Singh and Kaur [28], when micropolar parameters grow, so does the influence of impedance parameters. Amin et al. [29] used fractional relaxation operators and studied the response of laser irradiation in viscoelastic thin film of metal. Kaushal et al. [30] studied the impact of stiffness and void when waves propagate through non-free surface and free surface.

Ezzat and Lewis [31] used fractional thermos viscoelasticity to study head induced mechanical response in human skin tissue. Amin et al. [32] constructed thermoviscoelastic metal film with fractional relaxation operators and studied the microscale response using laser pulse heat flux with non-Gaussian form. Ezzat and Muhiameed [33] studied the response of non-local size dependent piezoelectric materials in thermoviscoelastic theory. Ezzat [34,35] used state space approach to develop non-local thermo-viscoelastic model and studied the response of piezoelectric materials with fractional dual phase heat transfer. Yadav et al. [36] investigation on nonlocal porous thermo-micropolar diffusive medium revealed that both diffusion and porous properties

3

have no effect on transversal waves. When Kumar [37] examined the effect of fractional derivative on wave propagation using Eringen's non-local approach, he discovered that group speed decreased as elastic medium values increased.

Abouelregal et al. [38] studied the impact of non-local Moore Gibson Thompson on thermoelastic material under the model of memory dependent derivatives. Abouelregal et al. [39] used Eringen's non-local thermoelastic theory and studied changes in heat transfer in thermoelastic materials under initial stress. Alsaeed [40] used Atangana Baleanu fractional derivative and analysed magneto thermoelastic response in unbounded porous body in context of dual phase lag model. Abouelregal et al. [41] used fractional model for one dimensional non-local elasticity theory and studied the transfer of heat flow through nanomaterials. Non-local parameters enhances the amplitude ratios when longitudinal and thermal waves are incident in generalized thermoelastic medium with two temperature and impedance parameters [42]. Ezzat and Bary [43] used memory dependent derivative to investigate the problem of wave characteristics in thermoelectric viscoelastic solid. Yadav [44] investigated how the magneto-thermo-microstretch half space having an impedance boundary's diffusion parameter and fractional order parameter affected the reflection coefficients of plane waves. Elhagary [45] investigated the impact of fractional derivative on thermoelastic diffusive half-space using the integral transform technique. Alruwaili et al. [46] used new form of fractal form of Green-Naghdi theory and developed a mathematical model of thermoelectric MHD theory. Kumar et al. [47] studied the reflection of waves through swelling porous thermoelastic half space having boundary under dual phase lag model.

The purpose of this work is to examine wave analysis in nonlocal swelling porous thermoelastic medium and found that there exist three longitudinal waves namely *Ps*, *Pf*, *T* waves and two transverse waves *SVS*, and *SVF* waves. Impedance boundary restrictions are used to obtain the amplitude ratios and energy ratios of various reflected waves. Numerical calculations and graphical representation are also used to examine the effect of variation in fractional order strain and swelling porosity in energy ratios.

Methods

Basic Equations

In swelling porous thermoelastic medium basic equations in absence of body force is given as [3]:

$$\mu(1 + \tau^r D_1^r) u_{i,jj}^s + (\lambda + \mu)(1 + \tau^r D_1^r) u_{j,ji}^s - \sigma^f (1 + \tau^r D_1^r) u_{j,ji}^f + \xi^{ff} (\dot{u}_i^f - \dot{u}_i^s) + (\gamma^f - \alpha_0) \nabla T = \rho_0^s (1 - \xi_1^2 \nabla^2) \ddot{u}_i^s,$$
(1)

$$\mu_{v}(1+\tau^{r}D_{1}^{r})\dot{u}_{i,jj}^{f} + (\lambda_{v} + \mu_{v})(1+\tau^{r}D_{1}^{r})\dot{u}_{j,ji}^{f} - \sigma^{f}(1+\tau^{r}D_{1}^{r})u_{j,ji}^{s} - \sigma^{f}(1+\tau^{r}D_{1}^{r})u_{i,ji}^{f} - \xi^{ff}(\dot{u}_{i}^{f} - \dot{u}_{i}^{s}) - (\gamma^{f} + \alpha^{f})\nabla T = \rho_{0}^{f}(1-\xi_{2}^{2}\nabla^{2})\ddot{u}_{i}^{f},$$
(2)

$$(1 + \tau^r D_1^r) \nabla \cdot \dot{u}^f \left(\alpha^f + \frac{\zeta^f}{T_0} \right) + (1 + \tau^r D_1^r) \nabla \cdot \dot{u}^s \left(\alpha_0 + \frac{\zeta^f}{T_0} \right) + \alpha_1 \dot{T} - \frac{K^*}{T_0} \nabla^2 T = 0, \tag{3}$$

$$t_{ij}^{s} = \left(-\alpha_0 T - \sigma^f (1 + \tau^r D_1^r) u_{r,r}^f + \lambda (1 + \tau^r D_1^r) u_{r,r}^s\right) \delta_{ij} + \mu (1 + \tau^r D_1^r) (u_{i,j}^s + u_{j,i}^s), \tag{4}$$

$$t_{ij}^{f} = \left(-\alpha^{f}T - \sigma^{f}(1 + \tau^{r}D_{1}^{r})u_{r,r}^{s} - \sigma^{ff}(1 + \tau^{r}D_{1}^{r})\nabla \cdot u^{f} + \lambda_{v}(1 + \tau^{r}D_{1}^{r})\dot{u}_{r,r}^{f}\right)\delta_{ij} + \mu_{v}(u_{i,j}^{f} + u_{j,i}^{f}),$$
(5)

where s is a solid, f is a fluid, u_i^s , u_i^f are the displacement components of a solid and a liquid, respectively, ρ_0^s , ρ_0^f are the densities in a solid and a liquid respectively, λ , μ , λ_v , μ_v , σ^f , σ^{ff} , ξ^{ff} are the constitutive constants, α_1 , ζ^f , α^f , α_0 are the material constants, ξ_1 , ξ_2 are the non-local parameters, r is an order of fractional strain, T is a temperature and K^* is a thermal conductivity, t_{ij}^s , t_{ij}^f are the partial stress tensors.

Problem Statement and Simplification

We have considered an isotropic, homogeneous swelling porous thermoelastic half-space. The origin of the rectangular cartesian co-ordinate system (x_1,x_2,x_3) is taken at boundary $x_3=0$ with x_3 – axis is pointing normally into medium (Fig. 1). The x_2 – axis is an intersection of the plane's wavefront and the plane surface. We confine our study to plane strain problem parallel to x_1-x_3 plane. For two-dimensional problem, we take:

$$u^{k} = (u_{1}^{k}, 0, u_{3}^{k}); k = s, f.$$
(6)

Define dimensionless quantities as:

$$x'_{i} = \frac{\omega^{*}}{c_{1}} x_{i}, u_{i}^{k'} = \frac{\rho_{0}^{s} \omega^{*} c_{1}}{\alpha_{0} T_{0}} u_{i}^{k}, t_{ij}^{k'} = \frac{t_{ij}^{k}}{\alpha_{0} T_{0}}, T' = \frac{T}{T_{0}}, \xi'_{m} = \frac{\omega^{*}}{c_{1}} \xi_{m}, t' = \omega^{*} t, \omega' = \frac{\omega}{\omega^{*}},$$

$$\tau^{r'} = \omega^{*r} \tau^{r}, \xi'_{m} = \frac{\omega^{*}}{c_{1}} \xi_{m}, \tau^{r'} = \omega^{*r} \tau^{r}, z'_{l} = \frac{z_{l}}{\rho_{0}^{s} c_{1}}, z'_{5} = \frac{c_{1}}{K^{*}} z_{5}, \omega^{*} = \frac{\alpha_{1} T_{0} c_{1}^{2}}{K^{*}}, c_{1}^{2} = \frac{\lambda + 2\mu}{\rho_{0}^{s}},$$

$$(7)$$

where m = 1, 2; k = s, f; i, j = 1, 2, 3; l = 1, 2, 3, 4.

Using Helmholtz decomposition, displacement components $u_1^k(x_1,x_3,t)$, $u_3^k(x_1,x_3,t)$ are related to potentials ϕ and ψ as:

$$u_1^k = \frac{\partial \phi^k}{\partial x_1} - \frac{\partial \psi^k}{\partial x_3}, \ u_3^k = \frac{\partial \phi^k}{\partial x_3} + \frac{\partial \psi^k}{\partial x_1}. \tag{8}$$

Equations (1)–(3) with the help of Eqs. (6)–(8) becomes:

$$\left(P\nabla^2 - a_2 \frac{\partial}{\partial t} - (1 - \xi_1^2 \nabla^2) \frac{\partial^2}{\partial t^2}\right) \phi^s + \left(-a_1 P \nabla^2 + a_2 \frac{\partial}{\partial t}\right) \phi^f - a_3 T = 0,$$
(9)

$$\left(-\delta_1^2 P \nabla^2 + a_2 \frac{\partial}{\partial t} + (1 - \xi_1^2 \nabla^2) \frac{\partial^2}{\partial t^2}\right) \psi^s - a_2 \frac{\partial}{\partial t} \psi^f = 0, \tag{10}$$

$$\left(-h_1 P \nabla^2 + h_3 \frac{\partial}{\partial t}\right) \phi^s + \left(P \frac{\partial}{\partial t} \nabla^2 - h_2 P \nabla^2 - h_3 \frac{\partial}{\partial t} - h_5 (1 - \xi_2^2 \nabla^2) \frac{\partial^2}{\partial t^2}\right) \phi^f - h_4 T = 0, \tag{11}$$

$$\left(-h_3\frac{\partial}{\partial t}\right)\psi^s + \left(-\delta_2^2 P \nabla^2 \frac{\partial}{\partial t} + h_3 \frac{\partial}{\partial t} - h_5 (1 - \xi_2^2 \nabla^2) \frac{\partial^2}{\partial t^2}\right)\psi^f = 0, \tag{12}$$

$$(b_3 P \nabla^2 \frac{\partial}{\partial t}) \phi^s + (b_2 P \nabla^2 \frac{\partial}{\partial t}) \phi^f + \phi^f + (\frac{\partial}{\partial t} - \nabla^2) T = 0,$$
 (13)

where
$$\delta_1^2 = \frac{\mu}{\lambda + 2\mu}$$
, $a_1 = \frac{\sigma^f}{\lambda + 2\mu}$, $a_2 = \frac{\xi^{ff}}{\rho_0^8 \omega^*}$, $a_4 = \frac{\lambda}{\lambda + 2\mu}$, $a_3 = (1 - \tau_0)$, $\tau_0 = \frac{\gamma^f}{\alpha_0}$, $\beta_1 = \alpha_0 T_0 + \zeta^f$,

$$\delta_2^2 = \frac{\mu_v}{\lambda_v + 2\mu_v}, h_1 = \frac{\sigma^f}{\omega^*(\lambda_v + 2\mu_v)}, h_2 = \frac{\sigma^{ff}}{\omega^*(\lambda_v + 2\mu_v)}, h_3 = \frac{\xi^{ff}c_1^2}{\omega^{*2}(\lambda_v + 2\mu_v)}, \beta_2 = \alpha^f T_0 + \zeta^f,$$

$$h_4 = \frac{(1+\tau_1)\alpha^f \rho_0^s c_1^2}{\omega^* \alpha_0 (\lambda_v + 2\mu_v)}, h_5 = \frac{\rho_0^f c_1^2}{\omega^* (\lambda_v + 2\mu_v)}, \tau_1 = \frac{\gamma^f}{\alpha^f}, b_2 = \frac{\alpha_0 \beta_2}{\rho_0^s c_1^2 \alpha_1 T_0}, b_3 = \frac{\alpha_0 \beta_1}{\rho_0^s c_1^2 \alpha_1 T_0}, \nabla^2 = \left(\frac{\partial^2}{\partial x_1^2} + \frac{\partial^2}{\partial x_3^2}\right), P = 1 + \tau^r (-i\omega)^r.$$

Considering the motion to be time harmonic we assume:

$$(\phi^s, \phi^f, T, \psi^s, \psi^f) = (\bar{\phi}^s, \bar{\phi}^f, \bar{T}, \bar{\psi}^s, \bar{\psi}^f) e^{i\{k(x_1 \sin\theta - x_3 \cos\theta) - \omega t\}}, \tag{14}$$

where θ is the angle of inclination; k is a wave number.

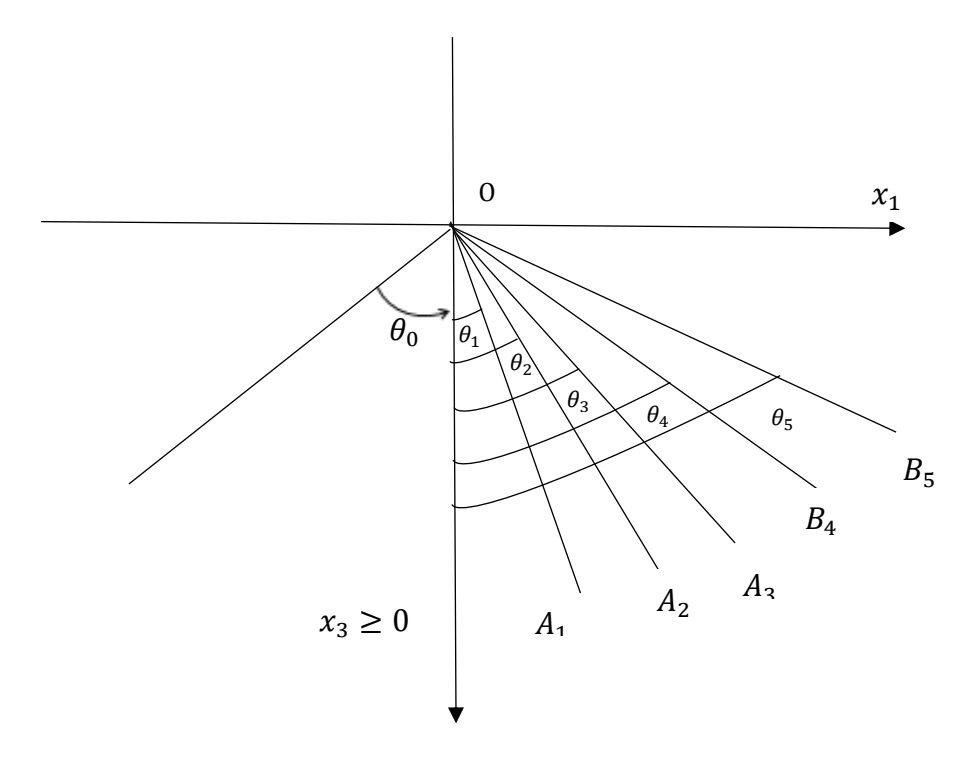


Fig. 1. Geometry of the problem depicting incident and reflected waves in swelling porous thermoelastic half-space

Making use of Eq. (14) in Eqs. (9)–(13), we obtain

$$Av^6 + Bv^4 + Cv^2 + D = 0, (15)$$

$$A_1 v^4 + B_1 v^2 + C_1 = 0, (16)$$

where $v_i(i=1,2,3)$ are the roots of Eq. (15) correspond to velocity of *Ps*-wave, *Pf*-wave and *T*-wave whereas $v_j(j=4,5)$ are the roots of Eq. (16) giving velocity of *SVS*-wave and *SVF*-

$$\begin{aligned} &\text{wave: } A = \tau_{12}\tau_{24} - \tau_{11}\tau_{21}, B = P_1\tau_{24} + d_1\tau_{12} + Pa_1\tau_{21} + d_3\tau_{11} + d_5\tau_{13}, \ D = P_1d_2 + Pa_1d_4, \\ &C = P_1d_1 + d_2\tau_{12} + Pa_1d_3 + d_4\tau_{11} + d_6\tau_{13}, A_1 = \tau_{44}\tau_{43} - \tau_{11}\tau_{21}, B_1 = \tau_{41}\tau_{43} + \tau_{44}\tau_{42}, \\ &C_1 = \tau_{41}\tau_{42}, P_1 = -P + \xi_1^2\omega^2, \ \tau_{11} = \frac{ia_2}{\omega}, \tau_{13} = \frac{-a_2}{\omega^2}, \tau_{12} = 1 + \tau_{11}, \ \tau_{21} = \frac{ih_3}{\omega}, \tau_{23} = \frac{-h_4}{\omega^2}, \\ &\tau_{22} = P(i\omega + h_2) + h_5\xi_2^2\omega^2, \ \tau_{24} = h_5 + \tau_{21}, \tau_{31} = -b_3\omega^2P, \ \tau_{32} = -b_2\omega^2P, \\ &d_1 = \tau_{22} - \tau_{32}\tau_{23}, \ d_2 = (\tau_{22} + \tau_{24})i\omega, d_3 = Ph_1 - \tau_{21}i\omega - \tau_{31}\tau_{23}, d_4 = Ph_1i\omega, \tau_{43} = h_5 - \tau_{21}, \\ &d_5 = -(\tau_{21}\tau_{32} + \tau_{31}\tau_{24}), \ d_6 = Ph_1\tau_{32} - \tau_{31}\tau_{22}, \tau_{41} = \delta_1^2P - 1, \ \tau_{44} = -(\xi_1^2 + \tau_{11}), \\ &\tau_{42} = -P\delta_2^2i\omega + h_5\xi_2^2\omega^2. \end{aligned}$$

Making use of Eqs. (6)–(8) in Eqs. (4)–(5) we obtain:

$$t_{33}^s = \left(1 + \tau^r D_1^r\right) \left(-a_1 \left(\frac{\partial^2 \phi^f}{\partial x_1^2} + \frac{\partial^2 \phi^f}{\partial x_3^2} \right) + a_4 \left(\frac{\partial^2 \phi^s}{\partial x_1^2} + \frac{\partial^2 \phi^s}{\partial x_3^2} \right) + 2\delta_1^2 \left(\frac{\partial^2 \phi^s}{\partial x_3^2} + \frac{\partial^2 \psi^s}{\partial x_3 \partial x_1} \right) \right), \tag{17}$$

$$t_{31}^s = \delta_1^2 (1 + \tau^r D_1^r) \left(2 \frac{\partial^2 \phi^s}{\partial x_3 \partial x_1} + \frac{\partial^2 \psi^s}{\partial x_1^2} - \frac{\partial^2 \psi^s}{\partial x_3^2} \right), \tag{18}$$

$$t_{33}^{f} = \left(1 + \tau^{r} D_{1}^{r}\right) \left(-a_{1} \left(\frac{\partial^{2} \phi^{s}}{\partial x_{1}^{2}} + \frac{\partial^{2} \phi^{s}}{\partial x_{3}^{2}}\right) - e_{1} \left(\frac{\partial^{2} \phi^{f}}{\partial x_{1}^{2}} + \frac{\partial^{2} \phi^{f}}{\partial x_{3}^{2}}\right) + e_{2} \left(\frac{\partial^{2} \dot{\phi}^{f}}{\partial x_{1}^{2}} + \frac{\partial^{2} \dot{\phi}^{f}}{\partial x_{3}^{2}}\right) +$$

$$(19)$$

$$+2e_3\omega^*\left(\frac{\partial^2\dot{\phi}^f}{\partial x_3^2}+\frac{\partial^2\dot{\psi}^f}{\partial x_3\partial x_1}\right)\right)-\tau_2T,$$

$$t_{31}^f = e_3 \omega^* (1 + \tau^r D_1^r) \left(2 \frac{\partial^2 \dot{\phi}^f}{\partial x_3 \partial x_1} + \frac{\partial^2 \dot{\psi}^f}{\partial x_1^2} - \frac{\partial^2 \dot{\psi}^f}{\partial x_3^2} \right), \tag{20}$$

where
$$\tau_2 = \frac{\alpha^f}{\alpha_0}$$
, $e_1 = \frac{\sigma^{ff}}{\lambda + 2\mu}$, $e_2 = \frac{\lambda_v \omega^*}{\lambda + 2\mu}$, $e_3 = \frac{\mu_v}{\lambda + 2\mu}$

Boundary conditions

Relevant boundary conditions at surface $x_3 = 0$ are:

(i)
$$t_{33}^s + \omega z_1 u_3^s = 0$$
, (ii) $t_{31}^s + \omega z_2 u_1^s = 0$, (iii) $t_{33}^f + \omega z_3 u_3^f = 0$, (iv) $t_{31}^f + \omega z_4 u_1^f = 0$, (v) $K^* \frac{\partial T}{\partial x_3} + \omega z_5 T = 0$, (21)

where z_1, z_2, z_3, z_4 are impedance parameters having dimension $\frac{Ns}{m^3}$; z_5 is impedance parameter having dimension $\frac{N}{mK}$.

We assume the values of ϕ^s , ϕ^f , T, ψ^s , ψ^f as:

$$\phi^{s} = \sum A_{0i}e^{i\{k(x_{1}sin\theta_{0} - x_{3}cos\theta_{0}) - \omega t\}} + A_{i}e^{i\{k(x_{1}sin\theta_{i} + x_{3}cos\theta_{i}) - \omega t\}}, \tag{22}$$

$$\phi^f = \sum \alpha_i (A_{0i}e^{i\{k(x_1sin\theta_0 - x_3cos\theta_0) - \omega t\}} + A_i e^{i\{k(x_1sin\theta_i + x_3cos\theta_i) - \omega t\}}), \tag{23}$$

$$T = \sum \beta_i (A_{0i} e^{i\{k(x_1 \sin \theta_0 - x_3 \cos \theta_0) - \omega t\}} + A_i e^{i\{k(x_1 \sin \theta_i + x_3 \cos \theta_i) - \omega t\}}), \tag{24}$$

$$\psi^{s} = \sum B_{0j} e^{i\{k(x_1 \sin\theta_0 - x_3 \cos\theta_0) - \omega t\}} + B_j e^{i\{k(x_1 \sin\theta_j + x_3 \cos\theta_j) - \omega t\}}, \tag{25}$$

$$\psi^f = \sum \gamma_j (B_{0j} e^{i\{k(x_1 \sin\theta_0 - x_3 \cos\theta_0) - \omega t\}} + B_j e^{i\{k(x_1 \sin\theta_j + x_3 \cos\theta_j) - \omega t\}}), \tag{26}$$

where
$$\alpha_i = \frac{-\tau_{23}V^2(P_1 + \tau_{12}V^2) + \tau_{13}V^2(h_1P - \tau_{21}V^2)}{(a_1P - \tau_{11}V^2)\tau_{23}V^2 - \tau_{13}V^2(\tau_{22} + \tau_{24}V^2)}$$
, $\beta_i = \frac{(\tau_{22} + \tau_{24}V^2)(P_1 + \tau_{12}V^2) - (a_1P - \tau_{11}V^2)(h_1P - \tau_{21}V^2)}{(a_1P - \tau_{11}V^2)\tau_{23}V^2 - \tau_{13}V^2(\tau_{22} + \tau_{24}V^2)}$, $\gamma_j = \frac{\tau_{41} + \tau_{44}V^2}{-\tau_{11}V^2}$, $(i=1,2,3;j=3,4)$.

Here $A_{0i}(i=1,2,3)$ denote amplitude of incident Ps-wave, Pf-wave and T-wave $A_i(i=1,2,3)$ correspond to reflected Ps-wave, Pf-wave and T-wave; $B_{0j}(j=3,4)$ correspond to amplitude of incident SVS-wave and SVF-wave and $B_j(j=3,4)$ associate to reflected SVS-wave and SVF-wave.

Snell's Law is represented as $\frac{\sin\theta_0}{v_0} = \frac{\sin\theta_i}{v_i}$ (i=1, 2, 3, 4, 5), where $k_1v_1 = k_2v_2 = k_3v_3 = k_4v_4 = k_5v_5 = \omega$. Using Eqs. (8), (17)–(20) in boundary conditions (21) we obtain the following relation coefficients (or amplitude ratios):

$$\sum a_{pj}Z_j = g_p$$
, $(p, j = 1, 2, 3, 4, 5)$, where

$$\begin{split} a_{1i} &= \left[P\left(\alpha_i a_1 - a_4 - 2\delta_1^2 \left(1 - \left(\frac{v_i}{v_1} \right)^2 \sin^2 \theta_0 \right) \right) - \frac{\beta_i}{k_i^2} \right] \left(\frac{v_1}{v_i} \right)^2 + \frac{v_1^2}{v_i} z_1 \sqrt{1 - \left(\frac{v_i}{v_1} \right)^2 \sin^2 \theta_0}, \\ g_1 &= P\left(\alpha_1 a_1 - a_4 - 2\delta_1^2 \cos^2 \theta_0 \right) - \frac{\beta_1}{k_1^2} + v_1 z_1 i cos \theta_0, \\ a_{1j} &= P\left(-2\delta_1^2 \sin \theta_0 \sqrt{1 - \left(\frac{v_j}{v_1} \right)^2 \sin^2 \theta_0} \right) \left(\frac{v_1}{v_j} \right) + i z_1 v_1 \sin \theta_0, \\ a_{2i} &= P\left(-2\delta_1^2 \sin \theta_0 \sqrt{1 - \left(\frac{v_j}{v_1} \right)^2 \sin^2 \theta_0} \right) \left(\frac{v_1}{v_i} \right) + i z_2 v_1 \sin \theta_0, \\ a_{2j} &= P\delta_1^2 \left(- \left(\frac{v_j}{v_1} \right)^2 \sin^2 \theta_0 + \left(1 - \left(\frac{v_j}{v_1} \right)^2 \sin^2 \theta_0 \right) \right) \left(\frac{v_1}{v_j} \right)^2 - \frac{v_1^2}{v_j} i z_2 \sqrt{1 - \left(\frac{v_j}{v_1} \right)^2 \sin^2 \theta_0}, \\ g_2 &= P\left(-2\delta_1^2 \sin \theta_0 \cos \theta_0 \right) - i z_2 v_1 \sin \theta_0, \\ a_{3i} &= \left[P\left(a_1 + e_1 \alpha_i + i k_i v_i \alpha_i \left(e_2 + 2 e_3 \omega^* \left(1 - \left(\frac{v_i}{v_1} \right)^2 \sin^2 \theta_0 \right) \right) \right) - \frac{\tau_2 \beta_i}{k_i^2} \right] \left(\frac{v_1}{v_i} \right)^2 + \\ + i \alpha_i z_3 \frac{v_1^2}{v_i} \sqrt{1 - \left(\frac{v_i}{v_1} \right)^2 \sin^2 \theta_0}, \\ g_3 &= - P(a_1 + e_1 \alpha_1 + i k_1 v_1 \alpha_1 (e_2 + 2 e_3 \omega^* \cos^2 \theta_0)) + \frac{\tau_2 \beta_i}{k_1^2} + v_1 z_3 \alpha_1 i \cos \theta_0, \\ a_{3j} &= i k_j \gamma_j 2 P e_3 \omega^* v_1 \sin \theta_0 \sqrt{1 - \left(\frac{v_j}{v_1} \right)^2 \sin^2 \theta_0} + i z_3 \gamma_j v_1 \sin \theta_0, \end{split}$$

$$\begin{split} a_{4i} &= i k_i \alpha_i 2 P e_3 \omega^* v_1 sin\theta_0 \sqrt{1 - \left(\frac{v_i}{v_1}\right)^2 sin^2\theta_0} + i \frac{v_1^2}{v_i} z_4 \alpha_i sin\theta_0, \\ g_4 &= i k_1 \alpha_1 2 P e_3 \omega^* v_1 sin\theta_0 cos\theta_0 - i v_1 z_4 \alpha_1 sin\theta_0, \\ a_{4j} &= \left[P e_3 \omega^* \left(i k_j \gamma_j v_j sin^2\theta_0 + \left(1 - \left(\frac{v_j}{v_1}\right)^2 sin^2\theta_0\right) \left(-i k_j \gamma_j \frac{v_1^2}{v_j}\right) \right) \right] - i z_4 \gamma_j \frac{v_1^2}{v_j} \sqrt{1 - \left(\frac{v_j}{v_1}\right)^2 sin^2\theta_0}, \\ a_{5i} &= i K^* \frac{\beta_i}{k_i} \left(\frac{v_1}{v_i}\right)^2 \sqrt{1 - \left(\frac{v_i}{v_1}\right)^2 sin^2\theta_0} + z_5 \frac{\beta_i}{k_i} \frac{v_1^2}{v_i}, g_5 = i K^* \frac{\beta_1}{k_1} cos\theta_0 - z_5 \frac{\beta_1}{k_1} v_1, a_{54} = a_{55} = 0, \\ \text{where } Z_i &= \frac{A_i}{A_{01}} \left(I = 1, 2, 3\right) \text{ and } Z_j &= \frac{B_j}{A_{01}} \left(j = 4, 5\right) \text{ are the amplitude ratios of reflected } \textit{Ps}, \\ \textit{Pf}, \textit{T} \text{ and } \textit{SVS}, \textit{SVF} \text{ waves respectively for an incident } \textit{Ps} \text{ wave.} \end{split}$$

Similarly, amplitude ratios of reflected waves can be calculated for the incident Pf or T or SVS or SVF waves.

Energy ratios of reflected waves

In this section the partition of energy among different reflected waves is calculated. Following Achenbach [48], the rate at which the energy is transmitted per unit surface area per unit time is expressed as:

$$P^{e} = \frac{1}{2} \sum_{k=s,f} \Re((t_{33}^{k}) \dot{\bar{u}}_{3}^{k})) + \frac{1}{2} \sum_{k=s,f} \Re((t_{31}^{k}) (\dot{\bar{u}}_{1}^{k})). \tag{28}$$

The average reflected wave energy at $x_3 = 0$ is given by:

$$|E_{i}| = -\left(\frac{A_{i}}{A_{01}}\right)^{2} \frac{\left(\frac{v_{1}}{v_{1}}\right)^{2} \sqrt{1 - \left(\frac{v_{i}}{v_{1}}\right)^{2} \sin^{2}\theta_{0}} \left[P(\alpha_{i}a_{1} - a_{4} - 2\delta_{1}^{2}) - \frac{\beta_{i}}{k_{i}^{2}} + r_{i}\right]}{\cos\theta_{0} \left[P(\alpha_{1}a_{1} - a_{4} - 2\delta_{1}^{2}) - \frac{\beta_{1}}{k_{i}^{2}} + r_{1}\right]},$$
(29)

The average reflected wave energy at
$$x_3 = 0$$
 is given by:
$$|E_i| = -\left(\frac{A_i}{A_{01}}\right)^2 \frac{\left(\frac{v_1}{v_i}\right)^2 \sqrt{1 - \left(\frac{v_i}{v_1}\right)^2 \sin^2\theta_0} \left[P(\alpha_i a_1 - a_4 - 2\delta_1^2) - \frac{\beta_i}{k_i^2} + r_i\right]}{\cos\theta_0 \left[P(\alpha_1 a_1 - a_4 - 2\delta_1^2) - \frac{\beta_1}{k_1^2} + r_1\right]},$$

$$|E_j| = -\left(\frac{B_j}{A_{01}}\right)^2 \frac{\left(\frac{v_1}{v_j}\right)^2 \sqrt{1 - \left(\frac{v_j}{v_1}\right)^2 \sin^2\theta_0} \left(P(-\delta_1^2 + i\omega e_3\omega^* \gamma_j^2)\right)}{\cos\theta_0 \left[P(\alpha_1 a_1 - a_4 - 2\delta_1^2) - \frac{\beta_1}{k_1^2} + r_1\right]},$$
(30)

where,
$$r_i = \alpha_i P(a_1 + e_1 \alpha_i + i k_i \alpha_i v_i e_2 + 2i e_3 \omega^* k_i \alpha_i) - \frac{\tau_2 \beta_i}{k_i^2}$$
, ($l = 1, 2, 3; j = 4, 5$).

Numerical results and Discussion

In order to demonstrate the impact of impedance parameter at various values of fractional order differential parameters on energy ratios of reflected Ps, Pf, T, SVS and SVF waves the following data is taken [47] (Table 1).

Table 1. Various values of fractional order differential parameters on energy ratios of reflected Ps, Pf, T, SVS and SVF waves

Symbol	Value	Symbol	Value	
λ, N/m ²	6.0·10 ⁹	α^f , N/m ² K	0.152· 10 ⁶	
μ, N/m ²	9.0· 10 ⁹	α_0 , N/m ² K	0.015· 10 ⁶	
λ_v , Ns/m ²	1.002· 10 ⁻³	K*, N/sK	0.498· 10 ²	
μ_v , Ns/m ²	8.88 • 10-4	T, K	298	
σ^f , N/m ²	8.9· 10 ⁶	ρ_0^s , Ns ² /m ⁴	2.65· 10 ³	
σ^{ff} , N/m ²	8.91·10 ⁵	ρ_0^f , Ns ² /m ⁴	9.90· 10²	
ξ^{ff} , Ns/m ⁴	4.950· 10 ⁶	τ, sec	0.002	
α_1 , N/m ² K ²	$0.03831 \cdot 10^2$	ζ^f , N/m ²	2.15· 10 ⁶	

Equations (29), (30) are solved numerically using the above numerical data and for the non-local parameters $\xi_1^2 = 11$, and $\xi_2^2 = 4.25$, as well as the impedance parameters $z_1 = 0.01$, $z_2 = 0.02$, $z_3 = 0.03$, $z_4 = 0.04$, $z_5 = 0.05$.

Impact of fractional order strain on phase velocity

The impact of fractional order strain on dilatational and transversal waves are shown with the help of Figs. 2–6.

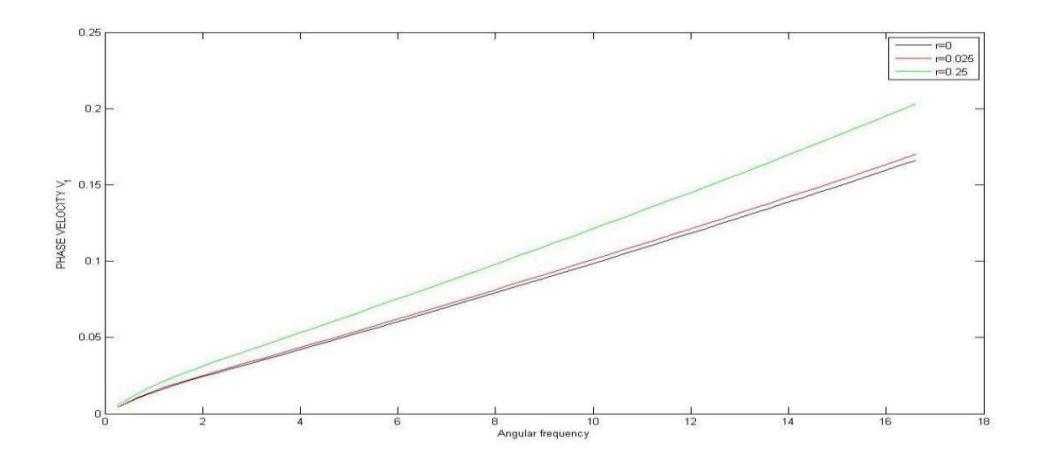


Fig. 2. Variation of longitudinal phase velocity V_1 w.r.t angular frequency

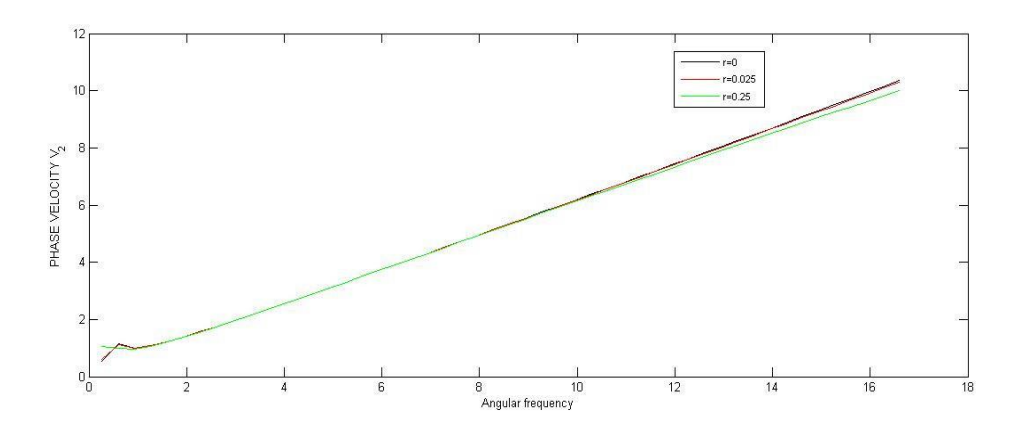


Fig. 3. Variation of longitudinal phase velocity V_2 w.r.t. angular frequency

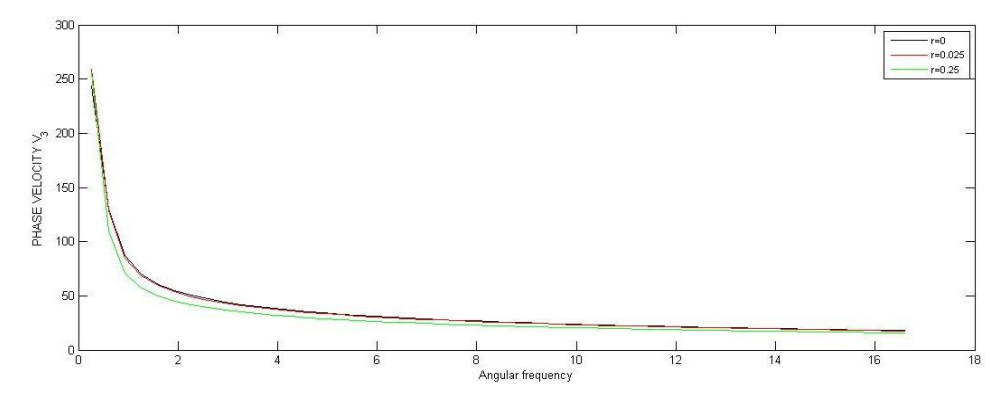


Fig. 4. Variation of longitudinal phase velocity V_3 w.r.t. angular frequency

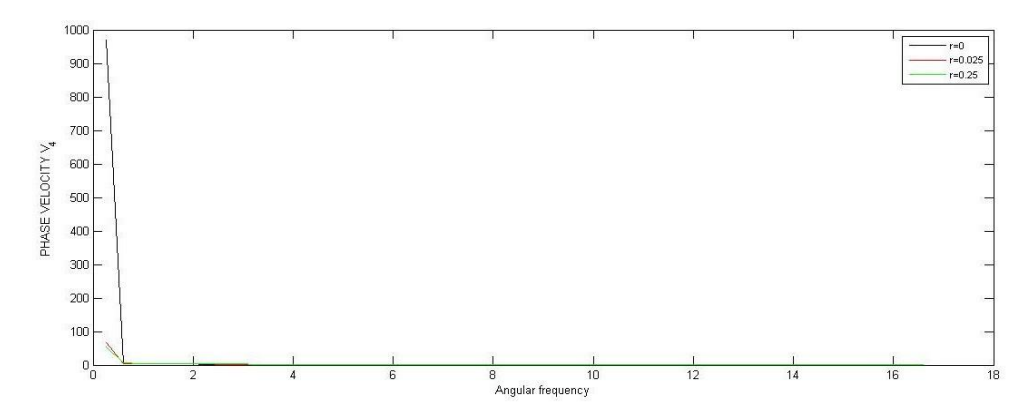


Fig. 5. Variation of transversal phase velocity V_4 w.r.t. angular frequency

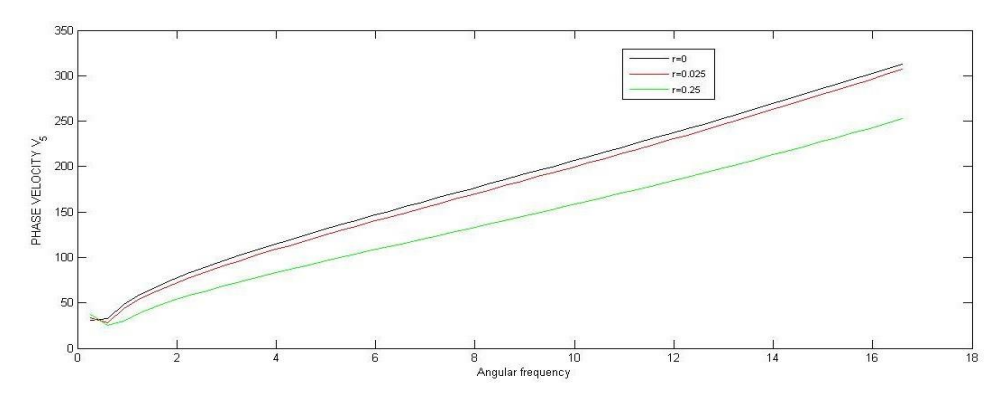


Fig. 6. Variation of transversal phase velocity V₅ w.r.t. angular frequency

Figures 2–4 shows the variation in longitudinal phase velocity w.r.t. angular frequency due to variation in fractional order strain. Figure 2 depicts that phase velocity V_1 increases with angular frequency. As values of fractional order strain is raised phase velocity V_1 also increase. From Fig. 3, it is prominent that phase velocity V_2 initially oscillates and then increase with higher values of frequency. When r = 0.25 velocity V_2 is greater than the velocity attained for r = 0 and 0.025 but for higher values of frequency opposite trend is noticed in their behavior. Impact of fractional order strain on variation of phase velocity V_3 is presented in Fig. 4. It is observed that tendency of phase velocity V_3 decrease with angular frequency and became dispersion less. Velocity V_3 decrease with higher values of fractional order strain. It is also observed that values of phase velocities for r = 0 and r = 0.025 are close to each other in entire region.

Figures 5 and 6 shows the variance in transversal velocity V_4 and V_5 w.r.t. angular frequency due to change in fractional order stain. From Fig. 5 it is noticed that values of velocity V_4 decrease with angular frequency. Initially V_4 for r=0 much higher than the values acquired for r=0.25 and 0.025 but its values seems to converge for for higher values of frequency. It is also detected that initially phase velocity decrease with higher values of fractional order strain but later they adverse behavior is depicted in their manner with respect to fractional order strain.

Variation of velocity V_5 with change in fractional order strain is demonstrated with the help of Fig. 6. It is observed that contrary to V_4 transverse velocity V_5 increase with frequency but decrease with higher values of r. It is also noticed that though trend of

velocity V_5 for for higher values of r remain same but its values are close to each other for r = 0 and 0.025.

Energy ratios

The energy ratios for the reflected *Ps*-wave, *Pf*-wave, *T*-wave, *SVS*-wave, and *SVF*-wave are obtained and graphically presented in Figs. 7–11.

The energy ratios |Ep| (p = 1, ..., 5) of these waves are plotted with respect to angle of incidence for three different values of the fractional strain parameter: r = 0, 0.025, and 0.25.

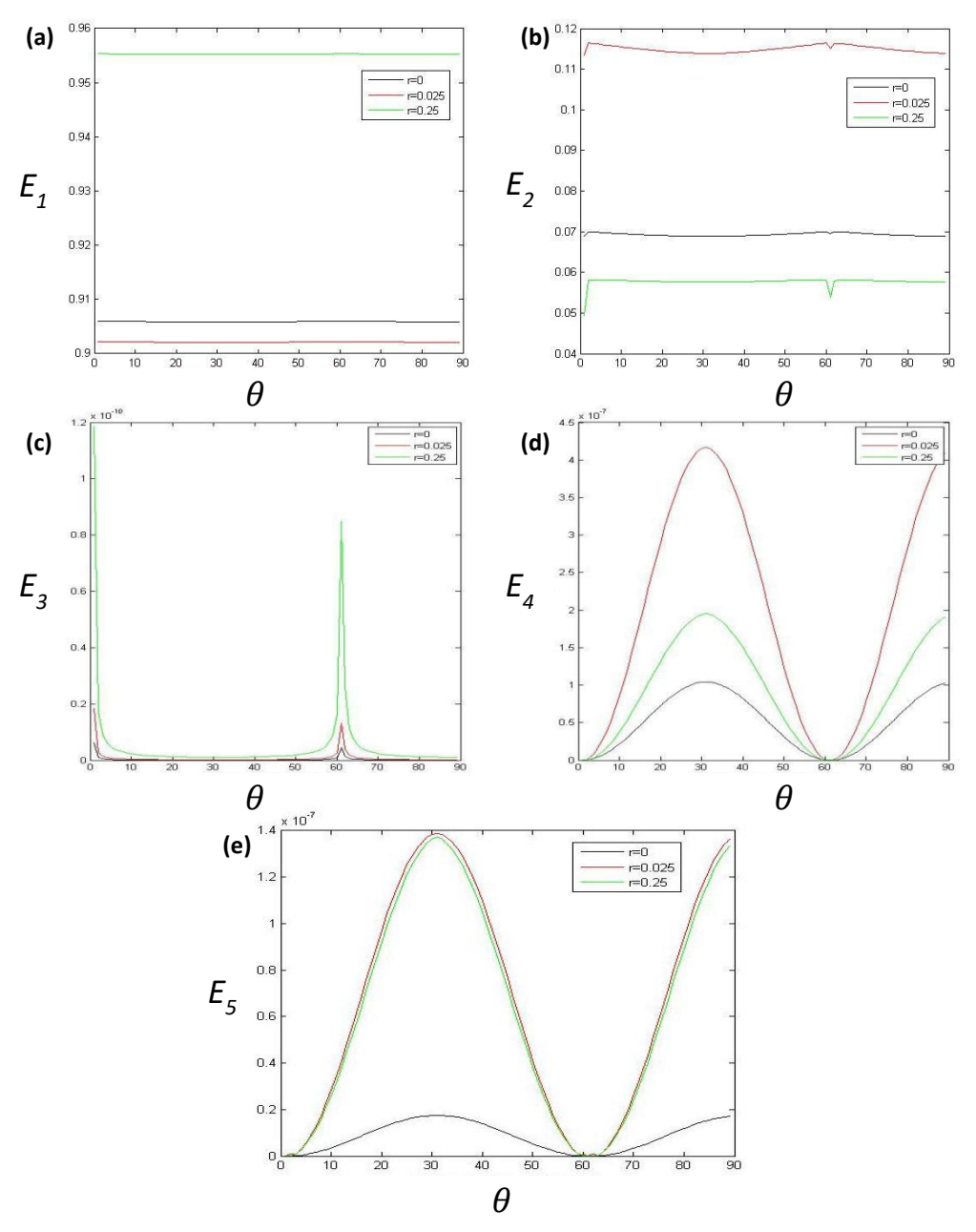


Fig. 7. Variation in energy ratios of reflected waves E for incidence of Ps wave in comparison of angle of incidence θ at distinct values of Ps: (a) E_1 , (b) E_2 , (c) E_3 , (d) E_4 , (e) E_5

The energy ratios of reflected waves when the Ps wave is incident are shown in Fig. 7. $|E_1|$ is found to change little with incidence angle. Also, the values of $|E_1|$ at r=0 is greater than the values attained at r=0.025 but less than the values acquired at r=0.25. The energy ratio $|E_2|$ first rises with the angle of incidence before fluctuating somewhat in its values. As similar to Fig. 2, the values of $|E_2|$ obtained at r=0 remain between the values obtained for r=0.025 and r=0.25. Higher values of r=0.025 result in higher values of r=0.025 for reflected r=0.025 and r=0.025 for r=0, r=0.025, and r=0.025, there is a rise in the values of r=0.025 and subsequently there is a fall with angle of incidence. Energy ratio values r=0.025 and r=0.025 and maximum value at r=0.025 are close to each other for r=0.025, and r=0.025. In comparison to other values of r=0.025 are close to each other for r=0.025, and r=0.025. In comparison to other values of r=0.025 and r=0.025. In comparison to other values of r=0.025 and r=0.025. In comparison to other values of r=0.025 and r=0.025 and r=0.025.

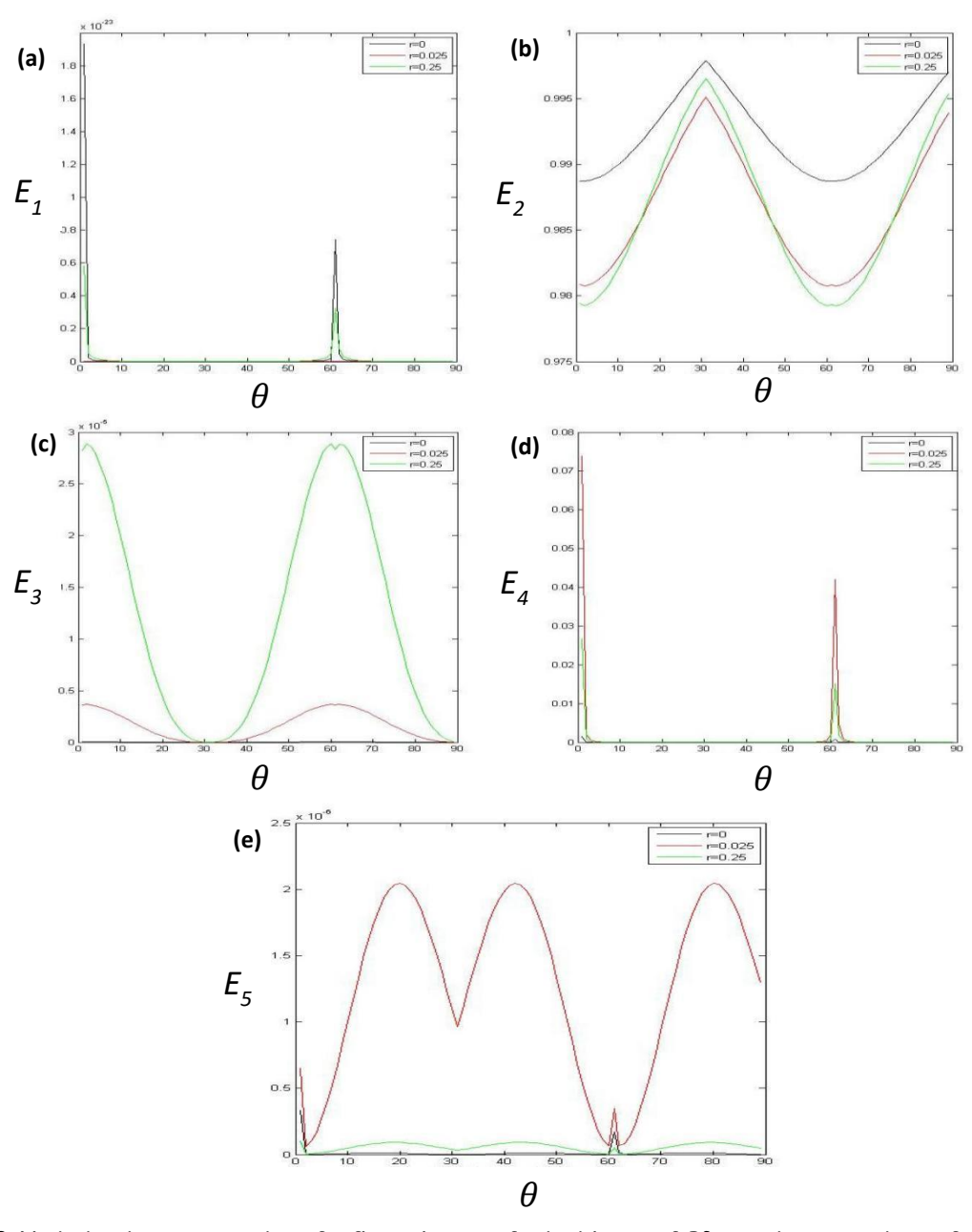


Fig. 8. Variation in energy ratios of reflected waves for incidence of Pf wave in comparison of angle of incidence at distinct values of Pf: (a) E_1 , (b) E_2 , (c) E_3 , (d) E_4 , (e) E_5

The fluctuation in energy ratios caused by Pf wave incidence is depicted in Fig. 8. The energy ratio, $|E_1|$, decreases in $1^{\circ} \leq \theta \leq 50^{\circ}$, then rises to reach its maximum value at $\theta = 62^{\circ}$ before beginning to decline at higher values of θ . Additionally, it is noted that when fractional strain increases in order, $|E_1|$ values drop. The values of the energy ratio $|E_2|$ remain roughly close to one, as seen in Fig. 8(b). It slowly increases at first, then decreases, and then starts to increase again. The values of $|E_2|$ drop as fractional order strain increases, while the values of $|E_3|$ grow as fractional order strain increases. The values found for $|E_4|$ and $|E_5|$ at r=0 continue to be the least and maximum at r=0.025. Also, $|E_4|$ acquires a sudden rise in values at $\theta=62^{\circ}$ for all values of r. $|E_5|$ also increase at $\theta=62^{\circ}$ for r=0 and 0.25 but when r=0.025 it becomes least for the same value of θ .

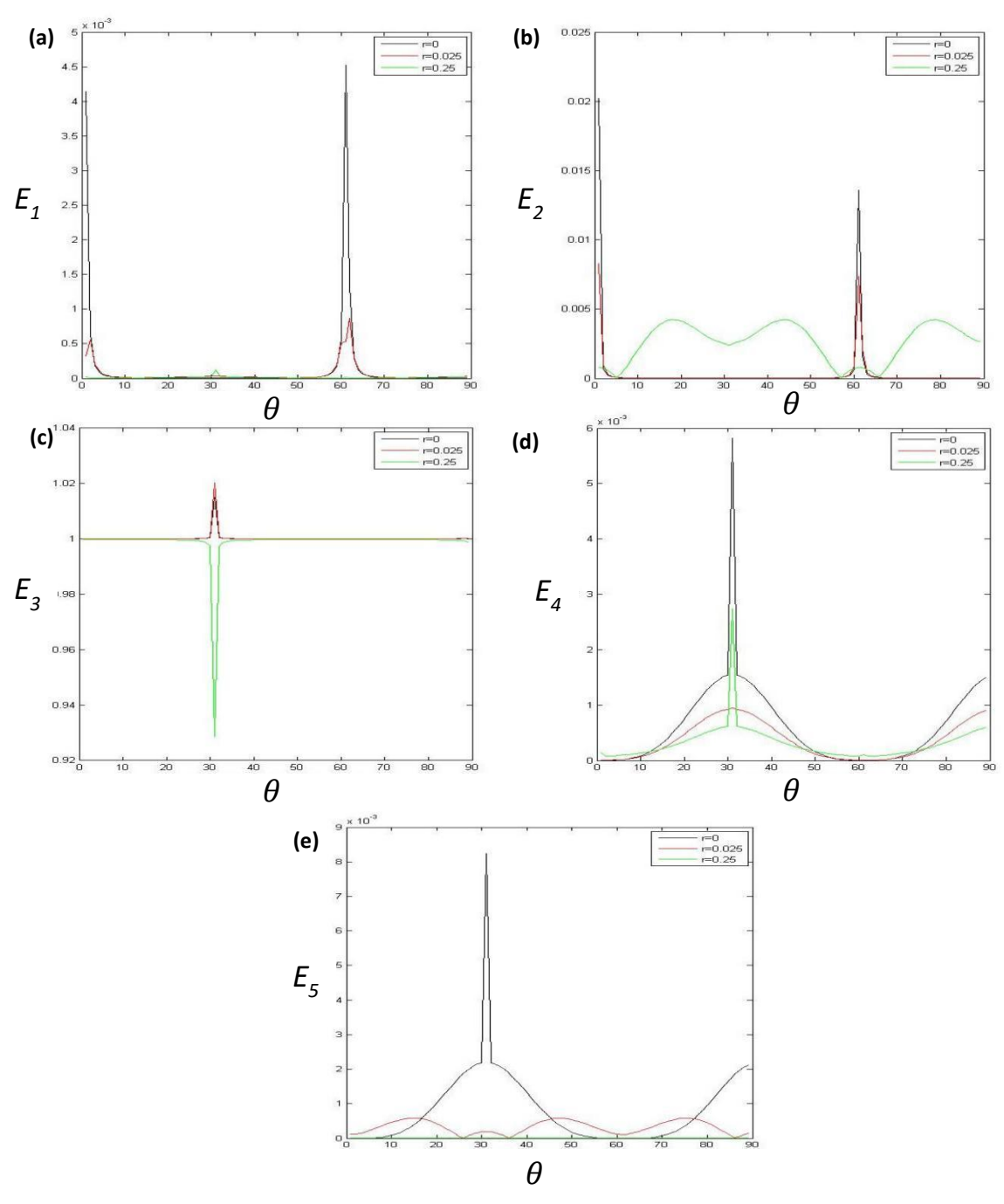


Fig. 9. Variation in energy ratios of reflected waves for incidence of T wave in comparison of angle of incidence at distinct values of r: (a) E_1 , (b) E_2 , (c) E_3 , (d) E_4 , (e) E_5

The energy ratios of reflected waves as a result of T wave incidence are shown in Fig. 9. It is observed that as the values of fractions order strain grow, $|E_1|$, $|E_3|$ and $|E_4|$ decrease. In the case of r=0, the energy ratio $|E_2|$ decreases initially and then increases, while for r=0.025, it oscillates across the whole range and reaches values that are greater than those obtained for r=0 and 0.25, with the exception of $\theta=62^\circ$. $|E_3|$ attains highest value at $\theta=62^\circ$ when r=0 and 0.25 but least value for r=0.025. $|E_4|$ attains a peak in its values when $\theta=30^\circ$ for all values of fractional order strain. The values of $|E_5|$ exhibit oscillatory behavior, acquiring the lowest values at r=0.25 when compared to other values of r.

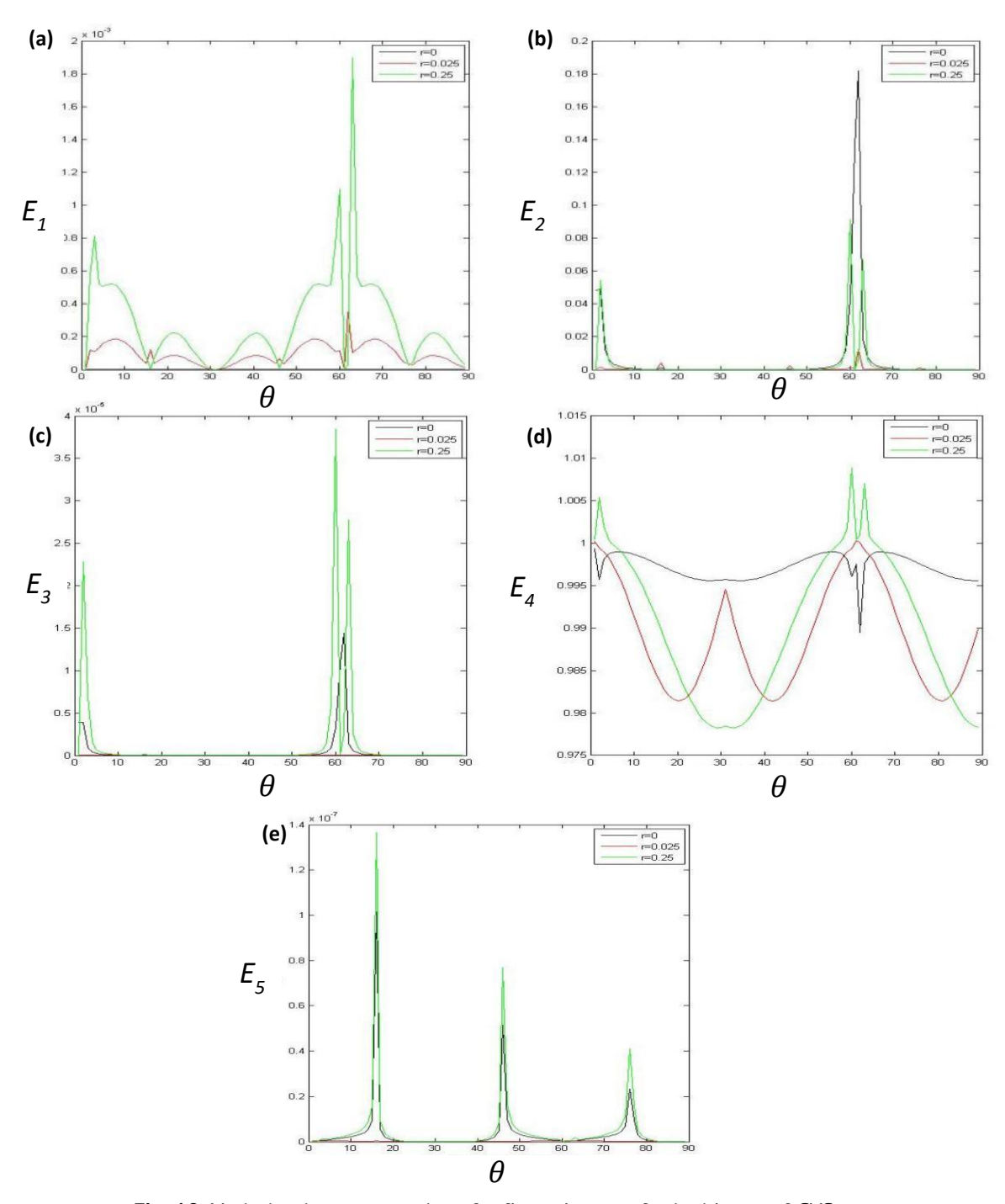


Fig. 10. Variation in energy ratios of reflected waves for incidence of *SVS* wave in comparison of angle of incidence at distinct values of r: (a) E_1 , (b) E_2 , (c) E_3 , (d) E_4 , (e) E_5

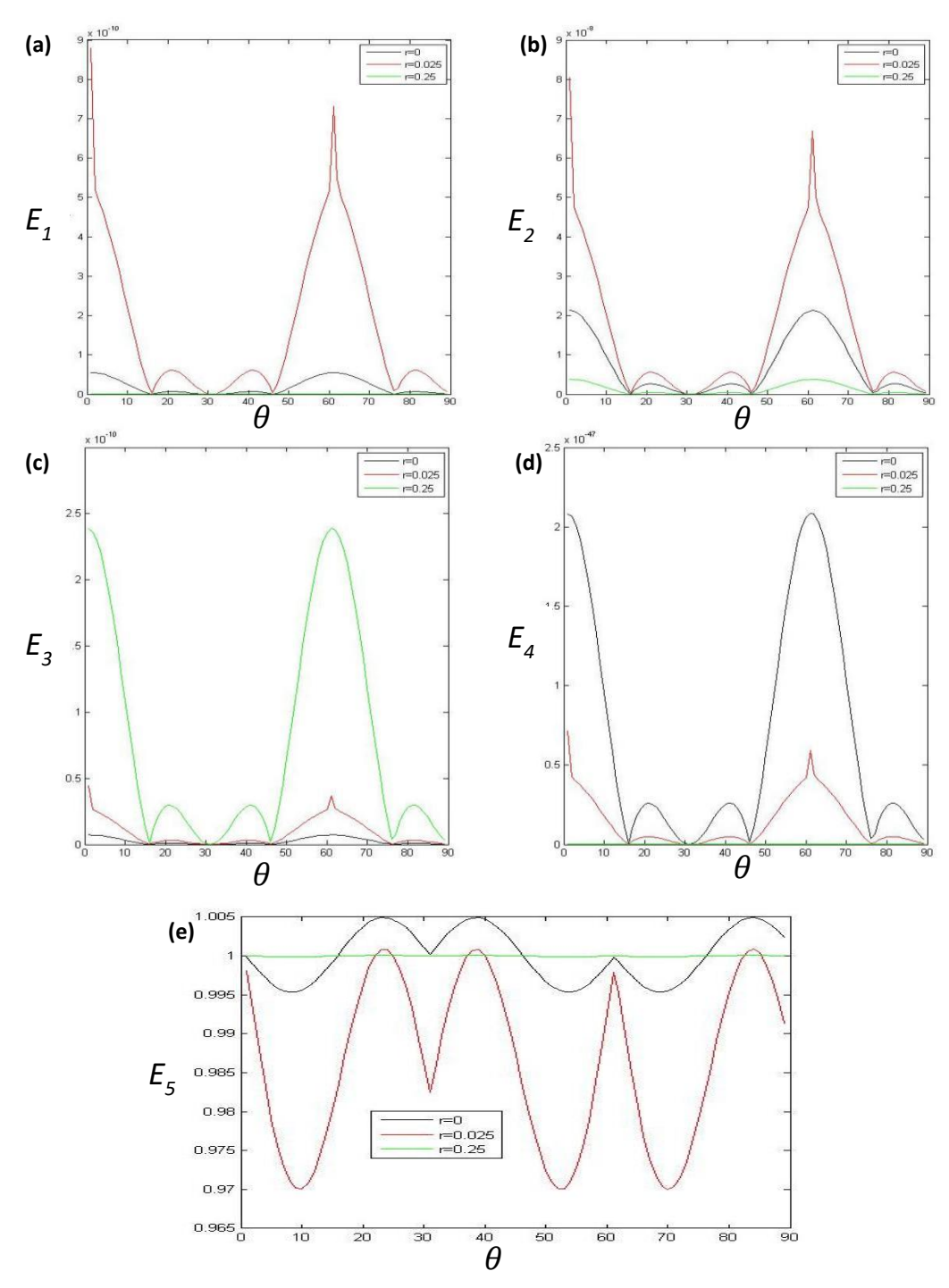


Fig. 11. Variation in energy ratios of reflected waves for incidence of *SVF* wave in comparison of angle of incidence at distinct values of r: (a) E_1 , (b) E_2 , (c) E_3 , (d) E_4 , (e) E_5

The energy ratio changes of reflected waves when *SVS* wave is incident is shown in Fig. 10. It is seen that $|E_1|$ exhibits oscillatory behavior, and its values increase with r. $|E_2|$ oscillates with angle of incidence and attains maximum values at $\theta = 62^\circ$ for all values of r. Also values of $|E_2|$ are maximum at r = 0. The values of $|E_3|$ and $|E_5|$ at r = 0 is higher than those obtained at r = 0.025, but they are still lower than the values obtained at r = 0.25. At $\theta = 62^\circ$, $|E_4|$ attains smallest value for r = 0, but highest values for r = 0.025 and 0.25.

The energy ratios when the *SVF* wave is incident are exhibited in Fig. 11. It is detected that reflected wave energy ratios exhibit oscillatory behaviour. At r = 0.25, the energy ratios $|E_1|$ and $|E_2|$ reach their minimum value and for r = 0.025 it acquires maximum value. While $|E_4|$ decreases as fractional strain values rise, $|E_3|$ values rise with greater values of r. For r = 0.025, the values of $|E_5|$ stay at their lowest at r = 0.25. $|E_2|$ and $|E_4|$ continue to be larger at r = 0 and smaller at r = 0.025.

Impact of swelling porosity on energy ratios

In order to depict the influence of swelling porosity on energy ratios, after substituting $\sigma^f = \xi^{ff} = \gamma^f = \mu_v = \lambda_v = \sigma^{ff} = \alpha^f = \rho_0^f = \zeta^f = 0$ in basic Eqs. (1)–(3), we get corresponding results for without swelling porous (WSP) elastic materials. In Figs. 12–14 energy ratios for swelling porous (SP) and WSP materials are obtained when Ps wave is incident. Here solid black line represents the graphs for swelling porous materials (SP) and the graphs in red line shows the results acquired for without swelling porous materials (WSP).

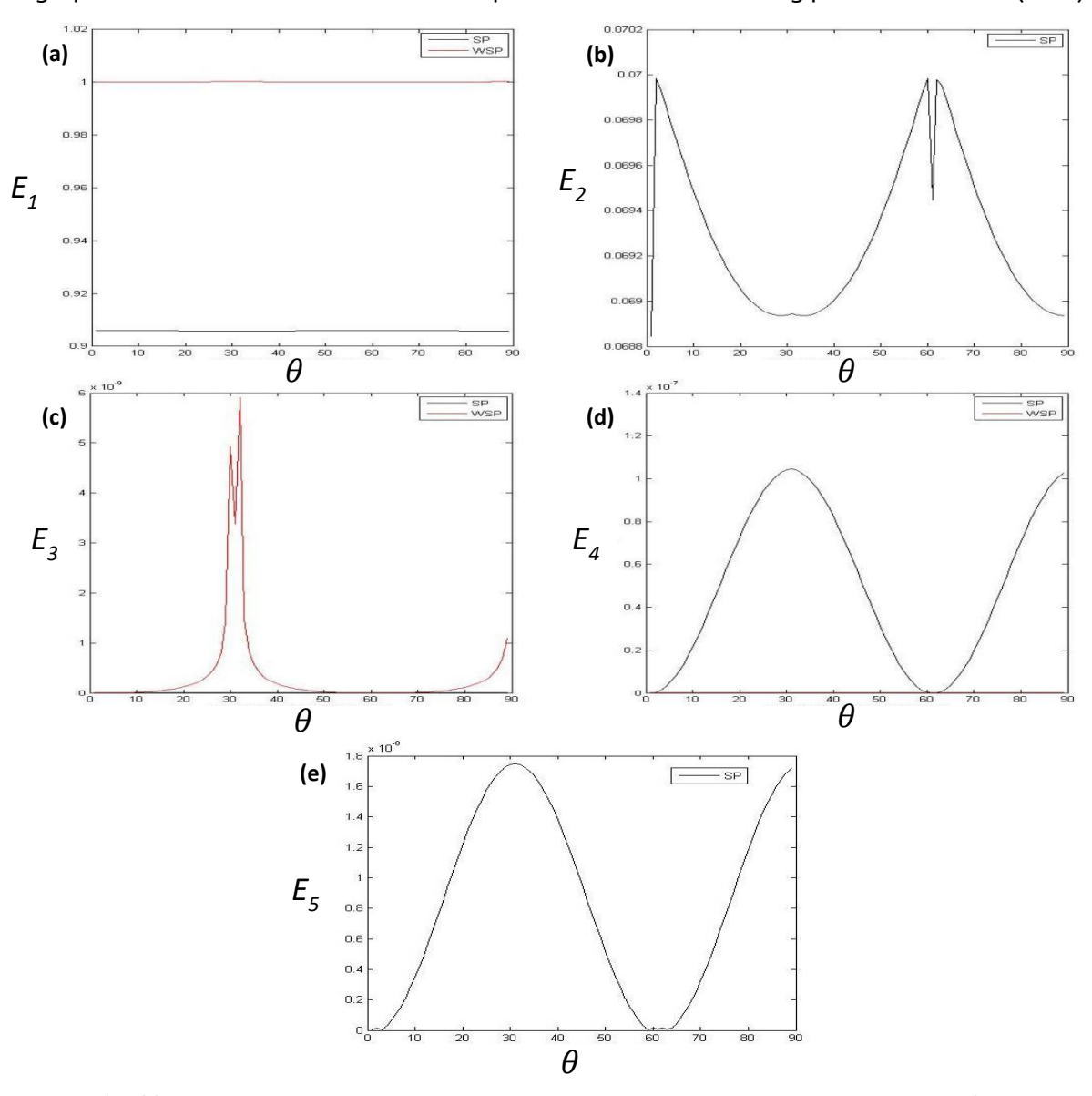


Fig. 12. Impact of swelling porosity on energy ratios when fractional order strain r = 0: (a) E_1 , (b) E_2 , (c) E_3 , (d) E_4 , (e) E_5

Figure 12 shows the energy ratios for SP and WSP w.r.t. angle of incidence when value of r = 0. Figure 12(a) demonstrates that energy ratio $|E_1|$ in both SP and WSP medium are close to one with less variation in values when Ps wave is incident, but its values in SP medium are less than those obtain for WSP medium for entire range. Energy ratio $|E_3|$ is of oscillatory behavior in both SP and WSP medium as shown in Fig. 12(c). Here also values of WSP medium dominates the values acquired for SP medium. Figure 12(d) depicts that $|E_4|$ keeps oscillating with angle of incidence for both the medium. In contrary to $|E_1|$ and $|E_3|$, here values in SP medium are higher than those obtain for WSP medium. Figure 13 demonstrate the comparison between the energy ratios attained for SP and WSP medium when value of r = 0.025. Here again values of WSP for $|E_1|$ and $|E_3|$ are greater than the results obtained for SP materials as observed in the case for r = 0. Value of $|E_1|$ is approximately one for both SP and WSP medium whereas $|E_3|$ is of oscillatory

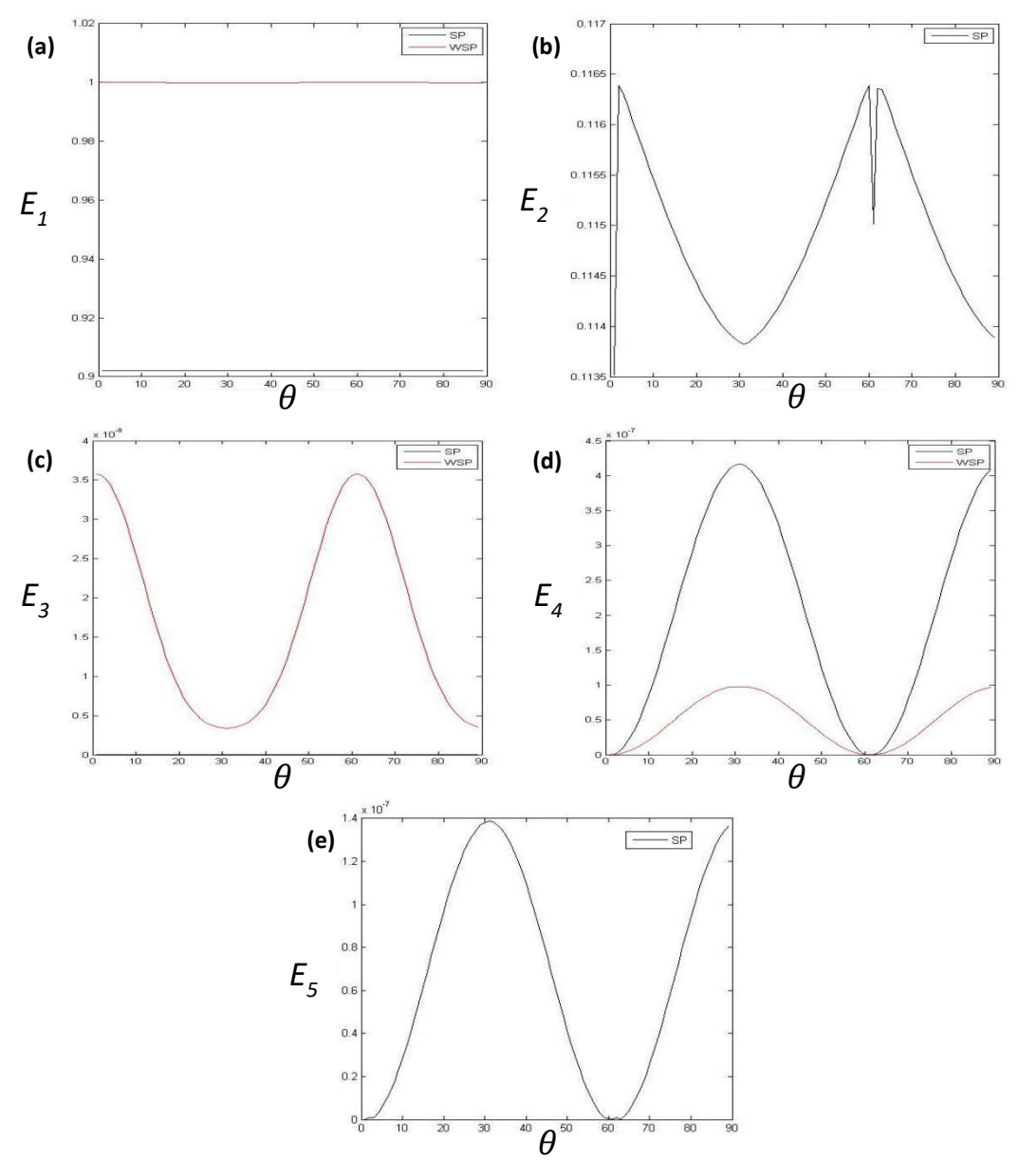


Fig. 13. Impact of swelling porosity on energy ratios when fractional order strain r = 0.025: (a) E_1 , (b) E_2 , (c) E_3 , (d) E_4 , (e) E_5

behavior. Figure 12(d) represents that energy ratio $|E_4|$ oscillates and obtains least value at $\theta = 62^\circ$. Here, values in SP medium are higher than those obtained for WSP medium. It clearly shows the impact of swelling porosity of the materials.

When value of r is raised to 0.25 energy ratios obtained in SP and WSP medium are represented in Fig. 14. Figure 14(a,c) shows that here also WSP medium dominates the values obtained for SP medium as observed in case when r = 0 and r = 0.025. Figure 14(d) depicts that trend of $|E_4|$ for SP and WSP medium is same with small difference in their values. It is also noticed that the values of energy ratios $|E_4|$ obtained for WSP medium are higher than the SP medium which is contrary to the case when r = 0 and 0.025.

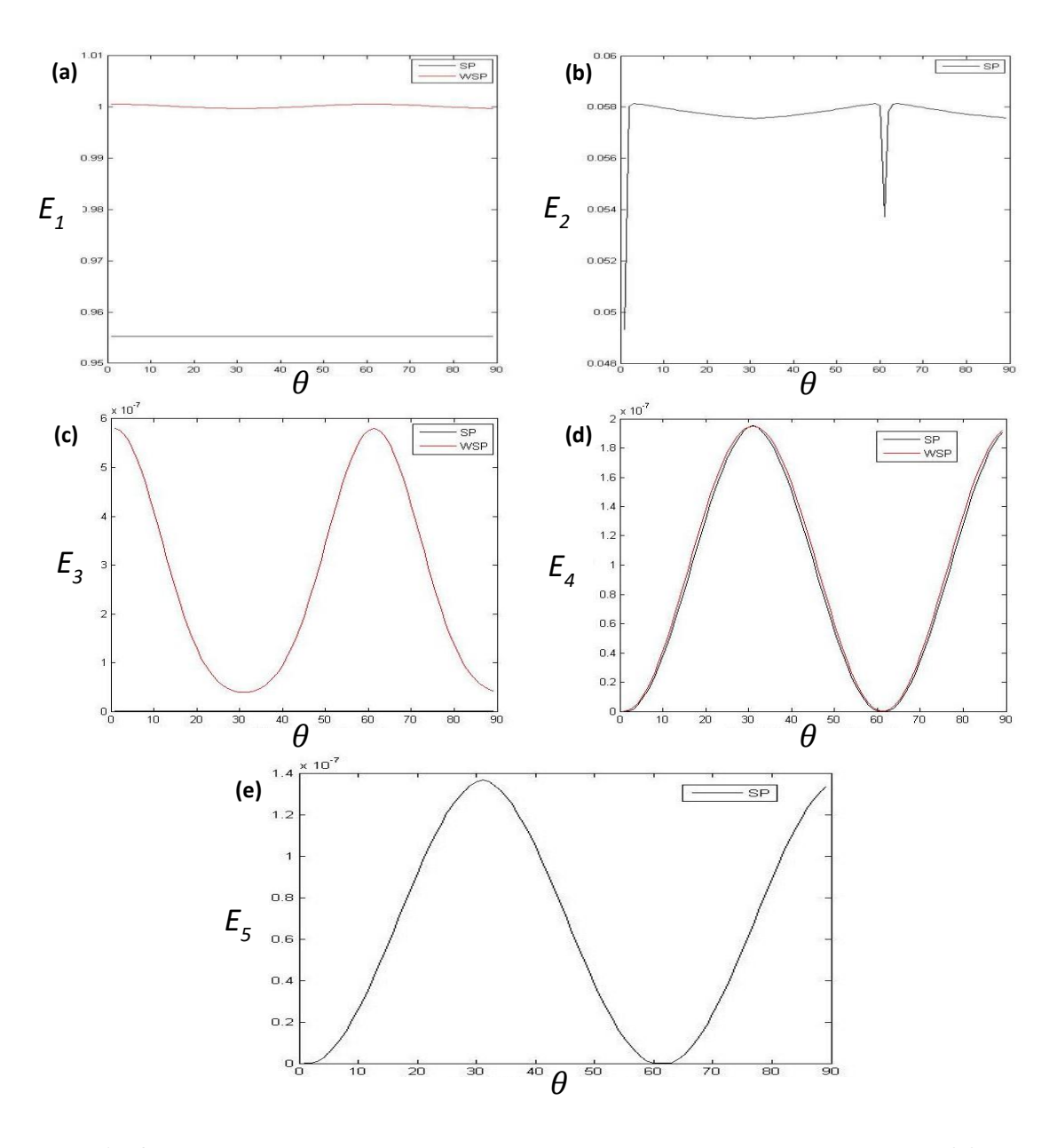


Fig. 14. Impact of swelling porosity on energy ratios when fractional order strain r = 0.25: (a) E_1 , (b) E_2 , (c) E_3 , (d) E_4 , (e) E_5

Conclusions

Plane wave propagation in nonlocal swelling porous thermoelastic under fractional order strain is scrutinized. It has been observed that there exist five plane waves consisting of three set of coupled longitudinal waves and two set of coupled transverse waves propagating with distinct speeds. The reflection phenomena of these waves at the impedance boundary have been examined. The expressions giving reflection coefficients and energy ratios at the stipulated boundary have been presented. The impact of fractional order strain and swelling porosity on energy ratios are obtained numerically and illustrated graphically. From the analysis of the illustrations, we derive the following conclusion: the energy ratios depend on the angle of incidence as well as the properties of the medium. The nature of dependence is distinct for distinct reflected waves. Theoretical as well as numerical results show that the energy ratios of various reflected waves are affected by fractional order strain and swelling porous parameters. Effect of nonlocal parameters is quite pertinent on the energy ratios. Phase velocity decrease with higher values of fractional order strain but *Ps* and *SVS* behaves in opposite manner. Phase velocity of thermal wave T and SVS wave decrease whereas velocity of Ps, Pf and SVF wave increase with angular frequency. All existing waves in stipulated medium are dominated by fractional order parameter. Energy ratios of reflected *T, SVS* and *SVF* wave are smallest for lower values of fractional order parameter when Ps and Pf wave is incident. Fractional order strain parameters decrease the energy ratios when T wave is encountered. Energy ratio of reflected Ps wave increase with fractional order strain in case of incident SVS wave, whereas energy ratio of reflected T wave decrease when SVF wave is incident. When longitudinal waves are incident $\theta = 62^{\circ}$ behaves like a critical angle. Swelling porosity decrease the magnitude of energy ratios of Ps and T wave for all values of fractional order parameter except for SVS wave. In WSP medium energy ratio of reflected Ps and T wave dominates the values obtained for SP medium on contrary to that energy ratios of reflected SVS wave are higher in SP medium. Increase in fractional order results in dominance of WSP over SP medium. The numerical result depict that the sum of modules values of energy ratio is approximately unity at each angle of incidence. This shows that there is no dissipation of energy during reflection phenomena and hence prove the law of conservation of energy.

Application

The results proffered in this work will prove to be helpful for researchers working with material science and physicists as well as those working on the expansion of a swelling porous thermoelasticity theories. The nonlocal and fractional order strain theory of thermoelasticity has dignified applications or usages in fracture mechanics, nuclear reactors and nano-mechanics. Moreover, the nonlocal swelling porous thermoelastic under fractional order strain is more realistic than the swelling porous thermoelasticity. Wave propagation is a powerful technique to detect minerals and fluid inside the earth. The problem explored in a stipulated model engages in a significant role in various engineering fields for example civil engineering, petroleum engineering and nuclear waste management.

CRediT authorship contribution statement

Saurav Sharma SC: writing-review and editing, conceptualization, investigation, supervision, data curation; **Divya Batra** SC: writing-review and editing, writing-original draft, Investigation, data curation; **Rajneesh Kumar** SC: writing-original draft, conceptualization, supervision, data curation.

Conflict of interest

The authors declare that they have no conflict of interest.

References

- 1. Biot MA. Theory of propagation of elastic waves in a fluid-saturated porous solid. I. Low-frequency range. *Journal of the Acoustical Society of America*. 1956;28(2): 168–178.
- 2. Biot MA. Theory of propagation of elastic waves in a fluid-saturated porous solid. II. Higher frequency range. *Journal of the Acoustical Society of America*. 1956;28(2): 17–191.
- 3. Eringen AC. A continuum theory of swelling porous elastic soils. *International Journal of Engineering Science*. 1994:32(8): 1337–1349.
- 4. Kumar R, Taneja D, Kumar K. Reflection and Transmission at the Boundary Surface of Thermoelastic Swelling Porous Media. *Journal of Applied Mechanical Engineering*. 2012:1(1): 1000104.
- 5. Magin R, Royston T. Fractional-order elastic models of cartilage: A multi-scale approach. *Communications in Nonlinear Science and Numerical Simulation*. 2010;15(3): 657–664.
- 6. Youssef HM. Theory of generalized thermoelasticity with fractional order strain. *Journal of Vibration and Control.* 2016:22(18): 3840–3857.
- 7. Chirilă A, Marin M. The theory of generalized thermoelasticity with fractional order strain for dipolar materials with double porosity. *Journal of Materials Science*. 2018;53(8): 3470–3482.
- 8. Youssef HM, Al-Lehaibi EA. State-space approach to three-dimensional generalized thermoelasticity with fractional order strain. *Mechanics of Advanced Materials and Structures*. 2019;26(10): 878–885.
- 9. Bassiouny E. Heating of thermoelastic half-space with fractional order strain and variable thermal conductivity. *Mechanics of Solids*. 2022;57(1): 163–177.
- 10. Al-Lehaibi EAN. Generalized Thermoelastic Infinite Annular Cylinder under the Hyperbolic Two-Temperature Fractional-Order Strain Theory. *Fractal and Fractional*. 2023;7(6): 476.
- 11. Sherief HH, Magdy AE. Solution of the generalized problem of thermoelasticity in the form of series of functions. *Journal of Thermal Stresses*. 1994;17(1): 75–95.
- 12. Ezzat MA, Othman MI, Smaan AA. State space approach to two-dimensional electromagneto-thermoelastic problem with two relaxation times. *International Journal of Engineering Science*. 2001:39(12): 1383–1404.
- 13. Ezzat MA. Fundamental solution in generalized magneto-thermoelasticity with two relaxation times for perfect conductor cylindrical region. *International Journal of Engineering Science*. 2004;42(13): 1503–1519.
- 14. Ezzat MA, El-Bary AA. State space approach of two-temperature magneto-thermoelasticity with thermal relaxation in a medium of perfect conductivity. *International Journal of Engineering Science.* 2009;47(4): 618–630. 15. El-Karamany AS, Ezzat MA. On the two-temperature Green–Naghdi thermoelasticity theories. *Journal of Thermal Stresses.* 2011;34(12): 1207–1226.
- 16. Vlase S, Marin M, Scutaru ML, Munteanu R. Coupled transverse and torsional vibrations in a mechanical system with two identical beams. *AIP Advances*. 2017;7(6): 065301.
- 17. Saurav S, Devi S, Kumar R, Marin M. Examining basic theorems and plane waves in the context of thermoelastic diffusion using a multi-phase-lag model with temperature dependence. To be published in *Mechanics of Advanced Materials and Structures*. [Preprint] 2024. Available from: doi.org/10.1080/15376494.2024.2370523.
- 18. Marin M, Abbas I, Kumar R. Relaxed Saint-Venant principle for thermoelastic micropolar diffusion. *Structural Engineering and Mechanics*. 2014;51(4): 651–662.
- 19. Sharma K. Reflection of plane waves in thermodiffusive elastic half-space with voids. *Multidiscipline Modeling in Materials and Structures*. 2012;8(3): 269–296.

20. Sharma K, Sharma S, Bhargava RR. Propagation of waves in micropolar thermoelastic solid with two temperatures bordered with layers or half spaces of inviscid liquid. *Materials Physics and Mechanics*. 2013;16(1):66–81.

- 21. Sharma K, Marin M. Effect of distinct conductive and thermodynamic temperatures on the reflection of plane waves in micropolar elastic half-space. *University Politehnica of Bucharest Scientific Bulletin-Series A-Applied Mathematics and Physics.* 2013;75(2): 121–132.
- 22. Sharma K, Marin M. Reflection and transmission of waves from imperfect boundary between two heat conducting micropolar thermoelastic solids. *Analele Stiintifice ale Universitatii Ovidius Constanta, Seria Matematica*. 2014;22(2): 151–176.
- 23. Vinh PC, Hue TTT. Rayleigh waves with impedance boundary conditions in incompressible anisotropic half-spaces. *International Journal of Engineering Science*. 2014; 85: 175–185.
- 24. Kumar R, Sharma P. Some theorems and wave propagation in a piezothermoelastic medium with two-temperature and fractional order derivative. *Materials Physics and Mechanics*. 2021;47(2): 196–218.
- 25. Sharma S, Khator S. Power generation planning with reserve dispatch and weather uncertainties including penetration of renewable sources. *International Journal of Smart Grid and Clean Energy.* 2021;10(4): 292–303.
- 26. Sharma S, Khator S. Micro-Grid Planning with Aggregator's Role in the Renewable Inclusive Prosumer Market. *Journal of Power and Energy Engineering*. 2022;10(4): 47–62.
- 27. Kumar R, Kaushal S, Kochar A. Response of impedance parameters on waves in the micropolar thermoelastic medium under modified Green-Lindsay theory. *ZAMM Journal of applied mathematics and mechanics: Zeitschrift für angewandte Mathematik und Mechanik.* 2022;102(9): 202200109.
- 28. Singh B, Kaur B. Rayleigh surface wave at an impedance boundary of an incompressible micropolar solid half-space. *Mechanics of Advanced Materials and Structures*. 2022;29(25): 3942–3949.
- 29. Amin MM, Hendy MH, Ezzat MA. Wave propagation due to laser irradiation in viscoelastic thin metal film with fractional relaxation operator. *Materials Physics and Mechanics*. 2022;48(1): 30–43.
- 30. Kaushal S, Kumar R, Kochar A. Wave propagation under the influence of voids and non-free surfaces in a micropolar elastic medium. *Materials Physics and Mechanics*. 2022;50(2): 226–238.
- 31. Ezzat MA, Lewis RW. Two-dimensional thermo-mechanical fractional responses to biological tissue with rheological properties. *International Journal of Numerical Methods for Heat & Fluid Flow.* 2022;32(6); 1944–1960.
- 32. Amin MM, Hendy MH, Ezzat MA. Wave propagation due to laser irradiation in viscoelastic thin metal film with fractional relaxation operator. *Materials Physics and Mechanics*. 2022;48(1): 30–43.
- 33. Ezzat MA, Al-Muhiameed ZIA. Thermo-mechanical response of size-dependent piezoelectric materials in thermo-viscoelasticity theory. *Steel and Composite Structures*. 2022;45(4): 535–546.
- 34. Ezzat MA, Ezzat SM, Alkharraz MY. State-space approach to nonlocal thermo-viscoelastic piezoelectric materials with fractional dual-phase lag heat transfer. *International Journal of Numerical Methods for Heat & Fluid Flow.* 2022;32(12): 3726–3750.
- 35. Ezzat MA, Ezzat SM, Alduraibi NS. On size-dependent thermo-viscoelasticity theory for piezoelectric materials. To be published in *Waves in Random and Complex Media*. [Preprint] 2022. Available from: doi.org/10.1080/17455030.2022.2043569.
- 36. Yadav AK, Carrera E, Schnack E, Marin M. Effects of memory response and impedance barrier on reflection of plane waves in a nonlocal micropolar porous thermo-diffusive medium. *Mechanics of Advanced Materials and Structures*. 2023;31(22): 5564–5580.
- 37. Senthilkumar V. Fractional derivative analysis of wave propagation studies using Eringen's nonlocal model with elastic medium support. *Journal of Vibration Engineering & Technologies*. 2023;11(8): 3677–3685.
- 38. Abouelregal AE, Marin M, Öchsner A. The influence of a non-local Moore–Gibson–Thompson heat transfer model on an underlying thermoelastic material under the model of memory-dependent derivatives. *Continuum Mechanics and Thermodynamics.* 2023;35(2): 545–562.
- 39. Abouelregal AE, Marin M, Askar SS, Foul A. A non-local fractional two-phase delay thermoelastic model for a solid half-space whose properties change with temperature and affected by hydrostatic pressure. *ZAMM Journal of applied mathematics and mechanics: Zeitschrift für angewandte Mathematik und Mechanik.* 2024;104(8): e202400102.
- 40. Alsaeed SS, Abouelregal AE, Elzayady ME. Magneto-thermoelastic responses in an unbounded porous body with a spherical cavity subjected to laser pulse heating via an Atangana-Baleanu fractional operator. *Case Studies in Thermal Engineering*. 2024;61: 104968.

- 41. Abouelregal AE, Civalek O, Akgöz B. A Size-Dependent Non-Fourier Heat Conduction Model for Magneto-Thermoelastic Vibration Response of Nanosystems. To be published in *Journal of Applied and Computational Mechanics*. [Preprint] 2024. Available from: doi.org/10.22055/jacm.2024.46746.4584.
- 42. Kaushal S, Kumar R, Bala I, Sharma G. Impact of non-local, two temperature and impedance parameters on propagation of waves in generalized thermoelastic medium under modified Green-Lindsay model. *Materials Physics and Mechanics.* 2024;52(1): 1–17.
- 43. Ezzat MA, El-Bary AA. Analysis of thermoelectric viscoelastic wave characteristics in the presence of a continuous line heat source with memory dependent derivatives. *Archive of Applied Mechanics*. 2023;93(2): 605–619.
- 44. Yadav AK. Reflection of plane waves from the impedance boundary of a magneto-thermo-microstretch solid with diffusion in a fractional order theory of thermoelasticity. *Waves in Random and Complex Media*. 2024;34(1): 404–433.
- 45. Elhagary MA. Thermoelastic diffusion in a half space due to fractional order theory. *Waves in Random and Complex Media*. 2024: 1–23.
- 46. Alruwaili AS, Hassaballa AA, Hendy MH, Ezzat MA. New insights on fractional thermoelectric MHD theory. *Archive of Applied Mechanics*. 2024;94: 1613–1630.
- 47. Kumar R, Batra D, Saurav S. Thermoelastic medium with swelling porous structure and impedance boundary under dual phase lag. *Engineering Solid Mechanics*. 2025;13: 81–92.
- 48. Achenbach JD. Wave Propagation in Elastic Solids. Amsterdam: Elsevier; 1973.

Submitted: August 21, 2024 Revised: October 2, 2024 Accepted: December 22, 2024

Study of different theories of thermoelasticity under the Rayleigh wave propagation along an isothermal boundary

V. Gupta ¹ , M. Kumar ² , Sh. Goel ≥ 2 .

ABSTRACT

The propagation of Rayleigh surface waves in an isotropic thermoelastic solid half-space is the focus of the current study, which takes into account the compact form of six distinct thermoelasticity theories. An isothermal boundary surface in the absence of tangential and normal stress is used to solve the problem. A dispersion equation with irrational terms is obtained after creating a mathematical model. This equation needs to be transformed into a rational polynomial equation in order to use the algebraic method to find exact complex roots. The roots are filters for in-homogenous wave propagation that decays with depth. Then these roots are used to compute the numerically characteristic properties of the Rayleigh wave, which include phase velocity, attenuation coefficient, and polarisation of particles. The results are presented graphically for particular cases of thermoelasticity by using the physical data of copper metal.

KEYWORDS

coupled model • G-N model • three phase lag model • L-S model • phase velocity • dual phase lag model G-L model • attenuation coefficient

Citation: Gupta V, Kumar M, Goel Sh. Study of different theories of thermoelasticity under the Rayleigh wave propagation along an isothermal boundary. *Materials Physics and Mechanics*. 2025;53(1): 22–37. http://dx.doi.org/10.18149/MPM.5312025 2

Introduction

Both natural and artificial materials are rated according to how they react to wave propagation parameters including wave polarization (particle oscillations) and travel time spans (or phase velocities). Among other things, specific heat, thermal expansion, and thermal conductivity all have an impact on these quantifiable values. The relationship between an elastic material temperature and the distribution of strain and stress, as well as the reciprocal impact of induced deformation on temperature distribution, are all examined by thermoelasticity theory. Applications for wave propagation phenomena are widely used in seismology, oil exploration, mineral and geophysical exploration. Thermoelasticity plane wave propagation has numerous applications in diverse engineering domains. When researching many facets of an earthquake, the surface waves are a great resource.

Biot [1] established the coupled theory of thermoelasticity using hyperbolic-parabolic field equations. Lord and Shulman (L-S) [2] and Green and Lindsay(G-L) [3] extended the coupled theory and called as generalised thermoelasticity. Green and Naghdi (G-N) [4] created a thermoelasticity theory lacking of energy dissipation. These theories [2-4] admit a finite heat-propagation speed, then the difference from coupled theory is created. Hetnarski and Ignaczak [5] and Ignaczak and Ostoja-Starzewski [6]



¹ Indira Gandhi National College, Haryana, India

² Baba Mastnath University, Haryana, India

[™] shruti1922goel@gmail.com

23 V. Gupta, M. Kumar, Sh. Goel

examined these illustrative generalised thermoelasticity theories. Tzou [7] worked on the two-phase- lag model. Roy-Choudhuri [8] studied the three-phase lag model. Numerous scholars have looked into wave propagation problems associated with coupled or generalised thermoelasticity [9-15].

The surface waves that travel along an elastic solid medium's free surface were examined by Rayleigh [16]. These Rayleigh waves are employed to observe the mechanical and structural characteristics of any material since they may travel over the surface, penetrate thick solid materials to a depth of one wavelength, and exhibit extremely sensitive behaviour to surface flaws. In thermoelasticity, the Rayleigh-type surface waves are thought to be useful in a variety of engineering domains and emerging technologies. There have been numerous reported uses of the Rayleigh wave in thermoelasticity theory up to this point. Some of them are as follows: Sinha and Sinha [17] examined the impact of modulating the Rayleigh wave velocity on altering the temperature environment. Sharma [18] investigated the characteristics of Rayleigh waves by employing the functional iteration approach to solve a difficult transcendental problem. Tomita and Shindo [19] analysed how Rayleigh waves propagate in a fully conducting elastic half-space in response to magnetic fields. Chadwick and Windle [20] examined the consequences of Rayleigh wave propagation along insulated and isothermal boundaries.

Dawn and Chakraborty [21] studied about the Green and Lindsay hypothesis in relation to the Rayleigh wave investigation in thermoelastic media. Chadwick and Windle [20] presented the work on the properties of the Rayleigh wave by considering two different boundary conditions. Ahmed [22] examined how temperature stress affected Rayleigh wave propagation in a granular media. Sharma et al. [23] analysed how thermal relaxation and rotation affected the Rayleigh surface waves in piezothermoelastic halfspace. Abd-alla [24] studied the surface wave in a generalised thermoelastic medium in the relaxation of the thermal time effect. Mahmoud [25] investigated the effect of magnetic field, rotation, relaxation times, gravity field, and initial stress on Rayleigh wave velocity in the space of a granular medium. Noguchi et al. [26] examined the use of Rayleigh waves by taking into account how long-period ground motion is affected by earthquakes. Bucur et al. [27] examined the ways in which thermal fields in a linear thermoelastic material with voids can dampen Rayleigh waves and harmonic waves. Zhao et al. [28] An analytical approach to the seismic response of composite-lined tunnels under Rayleigh waves in elastic ground. Xinxin et al. [29] studied seismic Rayleigh wave imaging for oil exploration using genetic-damped least squares joint inversion and multichannel surface wave analysis. Singh and Verma [30] examined many theories of thermoelasticity to study the Rayleigh wave's propagation in thermoelastic solid halfspace. Kumar et al. [31] examined the L-S theory under the influence of the initial stress, magnetic field, two temperatures, and diffusion in order to study the fundamental equation of thermoelasticity. Kumar and Gupta [32] examined Rayleigh waves in a massdiffusing, generalised thermoelastic media. Kumar et al. [33] examined the microrotation, tangential component of displacement, and normal boundary conditions for the shear, normal, and shear couple tractions at the surfaces, respectively.

Haque and Biswas [34] investigated the wave propagation using an algebraic differential equations Eigen value. Determine the attenuation coefficient and phase

velocity, then compare the graphs for void and non-void space. Saeed et al. [35] examined the propagation of Rayleigh waves in a temperature-dependent semi-conductor thermoelastic material. Singh and Kashyap [36] the propagation of micro polar thermoelastic material with time delay under memory-dependent derivatives has been investigated.

The current paper is structured as follows: in the "Basic equations" section, we address the compact version of the heat conduction equation of the six theories of thermoelasticity after first providing the basic equations employed in the study. The problem is formulated in the "Formulation of problem" section by utilising the displacement vector in the form of a potential function. Using potential functions, determine the longitudinal and transversal wave velocities in the "Solution of problem" section. In the "Boundary surface conditions" section, the secular dispersion equation is created using boundary conditions in order to discover complex filtered roots, which are used to determine the phase velocity, attenuation coefficient, and particle path, among other characteristics of the Rayleigh wave. In the "Path of particle" section, the phase velocity, attenuation coefficient, and path of six peculiar examples are presented graphically.

Basic equations

A compact form of the equations for thermoelasticity theories in the absence of external heat sources is as follows, in accordance with Kumar and Gupta [37].

The temperature-stress-strain relationship:
$$\sigma_{ij} = 2\mu e_{ij} + \lambda e_{kk}\delta_{ij} - \delta_{ij}\beta\left(1 + \tau_1\frac{\partial}{\partial t}\right)T$$
. (1)

Relation between strain and displacement:
$$e_{13} = e_{31} = (\partial u_1/\partial x_3 + \partial u_3/\partial x_1)/2$$
. (2)

The equations of motion:
$$(\lambda + \mu)u_{k,ki} + \mu u_{i,kk} - \beta \left(1 + \tau_1 \frac{\partial}{\partial t}\right)T_{,i} = \rho \ddot{u}_i.$$
 (3)

Modified Fourier's law:
$$K'\left(m^* + t_1 \frac{\partial}{\partial t} + t_3 \frac{\partial^2}{\partial t^2}\right) T_{,i} = -q_i.$$
 (4)

Energy equation:
$$\rho T_0 \dot{S} = -q_{i,i}$$
. (5)

Entropy-strain-temperature relation:

$$\rho C_E \left(m_1 \frac{\partial}{\partial t} + \tau_0 \frac{\partial^2}{\partial t^2} + t_2 \frac{\partial^3}{\partial t^3} + t_4 \frac{\partial^4}{\partial t^4} \right) T + T_0 \beta \left(m_1 \frac{\partial}{\partial t} + m_0 \tau_0 \frac{\partial^2}{\partial t^2} + t_2 \frac{\partial^3}{\partial t^3} + t_4 \frac{\partial^4}{\partial t^4} \right) e_{kk} = \rho T_0 \dot{S}. \quad (6)$$
The heat conduction equation:

$$K'\left(m^* + t_1 \frac{\partial}{\partial t} + t_3 \frac{\partial^2}{\partial t^2}\right) T_{,ii} = \rho C_E \left(m_1 \frac{\partial}{\partial t} + \tau_0 \frac{\partial^2}{\partial t^2} + t_2 \frac{\partial^3}{\partial t^3} + t_4 \frac{\partial^4}{\partial t^4}\right) T + T_0 \beta \left(m_1 \frac{\partial}{\partial t} + m_0 \tau_0 \frac{\partial^2}{\partial t^2} + t_2 \frac{\partial^3}{\partial t^3} + t_4 \frac{\partial^4}{\partial t^4}\right) e_{kk}.$$

$$(7)$$

In Eqs. (1)–(7), constants and parameters are used as following: λ , μ are the lame's constants, ρ is a mass density, C_E a the specific heat at the constant strain, e_{kk} are an dilatation, q_i are the heat flux components, u_i are the displacement components, σ_{ij} are the stress tensor components, S is an entropy per unit mass, K' is the thermal conductivity, T is an increment in temperature, $T = \theta - T_0$, where T_0 is a reference temperature and θ is an absolute temperature with condition satisfied as $|T/T_0| << 1$, $\beta = (3\lambda + 2\mu)\alpha_t$, α_t is the coefficient of thermal linear expansion, τ_0 , τ_1 , τ_q , τ_T , τ_v are relaxation times in thermal with condition $\tau_1 \geq \tau_0 \geq 0$, phase lags of heat flux, temperature gradient and thermal displacement gradient respectively, where m^* , m_0 , m_1 , t_1 , t_3 , t_2 , t_4 , τ_0 , τ_1 , are parameters.

25 V. Gupta, M. Kumar, Sh. Goel

Rayleigh surface wave propagation through an isotropic medium with thermoelasticity. The following values of the parameters in Eqs. (3) and (7) are used to study the various theories:

1. Coupled theory (C-T) condition of thermoelasticity is obtained when:

$$m^* = m_1 = 1, m_0 = t_1 = t_2 = t_3 = t_4 = \tau_0 = \tau_1 = 0,$$
 (8)

2. The thermoelasticity theory known as Lord-Shulman (L-S) is derived when:

$$m^* = m_0 = m_1 = 1, t_1 = t_2 = t_3 = t_4 = \tau_1 = 0,$$
 (9)

3. In thermoelasticity, the Green-Lindsay (G-L) theory is derived when:

$$m^* = m_1 = 1, \ m_0 = t_1 = t_2 = t_3 = t_4 = 0,$$
 (10)

4. The thermoelasticity theory known as Green-Nagdhi (Type-III) or G-N is derived from:

$$m^* > 0$$
, $m_0 = \tau_0 = t_1 = 1$, $m_1 = t_2 = t_3 = t_4 = \tau_1 = 0$, (11)

put in (7) results into equation:

$$K'\left(m^* + \frac{\partial}{\partial t}\right)T_{,ii} = \rho C_E \ddot{T} + \beta T_0 \ddot{e}_{kk}. \tag{12}$$

Here m^* is a constant having a dimension 1/sec, $\dot{T} = \vartheta$, and $m^*K' = K'^*$ is a constant characteristic of the theory. Equation (12) become:

$$K'^*T_{,ii} + K'\vartheta_{,ii} = \rho C_E \ddot{T} + \beta T_0 \ddot{e}_{kk}, \tag{13}$$

Subcase: when K' = 0 in Eq. (13), Green-Nagdhi (Type-II) theory is obtained.

5. The thermoelasticity two-phase-lag theory is derived when:

$$m^* = 1$$
, $m_0 = m_1 = 1$, $\tau_1 = t_3 = t_4 = 0$, $t_1 = \tau_T$, $t_2 = \frac{\tau_q^2}{2}$, $\tau_0 = \tau_q$, (14)

6. The thermoelasticity three-phase-lag theory is derived when:

$$m_0 = \tau_0 = 1$$
, $m_1 = \tau_1 = 0$, $t_2 = \tau_q$, $t_1 = 1 + m^* \tau_{\nu}$, $t_3 = \tau_T$, $t_4 = \frac{\tau_q^2}{2}$. (15)

Formulation of problem

To solve the problem related to two-dimensional space, consider the displacement vector $u=(u_1,0,u_3)$ in medium. The dimensionless quantities listed below are defined as:

$$T' = \frac{\beta T}{\rho c_1^2}, \ \{x_i', u_i'\} = \left\{\frac{\omega_1^* x_i}{C_1}, \frac{\omega_1^* u_i}{C_1}\right\}, \ \nabla^2 = \frac{\partial^2}{\partial x_i^2}, \ i = 1, 3,$$

$$\{\tau_1', \tau_0'\} = \{\tau_1, \tau_0\} \omega_1^*, \ t' = \omega_1^* t, \ \{\tau_q', \tau_T', \tau_v'\} = \{\tau_q, \tau_T, \tau_v\} \omega_1^*,$$

$$\sigma_{ij}' = \frac{\sigma_{ij}}{\beta T_0}, \omega_1^* = \frac{\rho C_E C_1^2}{K'}, \ \delta^2 = \frac{C_2^2}{C_2^2}, \ C_1^2 = \frac{\lambda + 2\mu}{\rho}, \ C_2^2 = \frac{\mu}{\rho}.$$

$$(16)$$

The displacement components in form of potential function ϕ_1 , ϕ_2 , ϕ_3 can be written as:

$$u_1 = \frac{\partial \phi_i}{\partial x_1} + \frac{\partial \phi_3}{\partial x_3}, \ u_3 = \frac{\partial \phi_i}{\partial x_3} - \frac{\partial \phi_3}{\partial x_1}, \ i = 1, \ 2.$$
 (17)

In Eqs. (3) and (7) with the help of (16), after suppressing the primes, apply the Eq. (17) we obtain:

$$\left(\nabla^2 - \frac{\partial^2}{\partial t^2}\right)\varphi - \left(1 + \tau_1 \frac{\partial}{\partial t}\right)T = 0,\tag{18}$$

$$\nabla^2 \varphi_3 - \frac{1}{\delta^2} \frac{\partial^2 \varphi_3}{\partial t^2} = 0, \tag{19}$$

$$\left(m^* + t_1 \frac{\partial}{\partial t} + t_3 \frac{\partial^2}{\partial t^2}\right) \nabla^2 T = \tag{20}$$

$$= \left(m_1 \frac{\partial}{\partial t} + \tau_0 \frac{\partial^2}{\partial t^2} + t_2 \frac{\partial^3}{\partial t^3} + t_4 \frac{\partial^4}{\partial t^4}\right) T + \frac{\beta^2 T_0}{\rho^2 C_E C_1^2} \left(m_1 \frac{\partial}{\partial t} + m_0 \tau_0 \frac{\partial^2}{\partial t^2} + t_2 \frac{\partial^3}{\partial t^3} + t_4 \frac{\partial^4}{\partial t^4}\right) \nabla^2 \varphi.$$

Solution of problem

We assume, for propagation of harmonic wave in consider plane as:

$$\{\phi, \phi_3, T\}(x_1, x_3, t) = \{\bar{\phi}, \bar{\phi}_3, \bar{T}\}e^{-i\omega t}.$$
 (21)

Substitute Eq. (21) in Eqs. (18) and (20) and then simplified, we get:

$$(Y_1 \nabla^4 + Y_2 \nabla^2 + Y_3) \bar{\varphi} = 0 \tag{22}$$

where
$$Y_1=R_2, Y_2=R_2\omega^2-R_3-R_1R_4, Y_3=-\omega^2R_3, R_1=1-i\omega\tau_1, R_2=(m^*-it_1\omega-t_3\omega^2),$$

$$R_3 = (-im_1\omega - \tau_0\omega^2 + it_2\omega^3 + t_4\omega^4), \ R_4 = \left(\frac{\beta^2 T_0}{\rho^2 C_F C_1^2}\right)(-im_1\omega - \tau_0 m_0\omega^2 + it_2\omega^3 + t_4\omega^4).$$

General solution $\bar{\phi}$ can be written as:

$$\bar{\phi} = \bar{\phi}_1 + \bar{\phi}_2,\tag{23}$$

where the potential $\bar{\varphi}_1$, $\bar{\varphi}_2$ are solutions of equation given by:

$$\left[\nabla^2 + \frac{\omega^2}{V_i^2}\right]\bar{\varphi}_i = 0, \quad i = 1, \quad 2$$
 (24)

where V_1 , V_2 , are the velocities of longitudinal waves (Pand SV wave), are the roots of equation:

$$R_3 V^4 - R_2 \omega^2 V^2 + R_1 \omega^4 = 0. (25)$$

Equation (19) can be solved for the transverse wave velocity $V_3 = \delta$ using Eq. (21). The result is provided by:

$$\left[\nabla^2 + \frac{\omega^2}{V_3^2}\right]\bar{\varphi}_3 = 0,\tag{26}$$

By using Eqs. (7), (21), (23) and (24) we obtain:

$$\{\varphi, T\} = \sum_{k=1}^{2} \{1, n_k\} \varphi_k,\tag{27}$$

$$\{\varphi,T\}=\sum_{k=1}^{2}\{1,n_{k}\}\varphi_{k},$$
 where $n_{k}=\frac{s_{1}s_{4}\omega^{2}}{s_{1}s_{2}\omega^{2}-s_{3}{V_{k}}^{2}}, \quad k=1,\ 2.$

The displacement potentials φ_1 , φ_2 , φ_3 for the propagation of harmonic wave with exponential decay in a plane is given as:

$$\varphi_k = A_k e^{i\omega \left(\frac{x_1 + q_k x_3}{c} - t\right)}, \quad k = 1, 2, 3,$$
(28)

where apparent phase velocity used as c, $q_1 = \sqrt{\frac{c^2}{{V_1}^2}-1}$, $q_2 = \sqrt{\frac{c^2}{{V_2}^2}-1}$, $q_3 = \sqrt{\frac{c^2}{\delta^2}-1}$.

Boundary surface conditions

For the isothermal and stress-free surface $x_3 = 0$:

(a) vanish normal and tangential stress component:

$$\sigma_{33} = 0, \tag{29}$$

$$\sigma_{31} = 0, \tag{30}$$

(b) isothermal boundary surface:

$$T = 0, (31)$$

Equation (28) is used in Eqs. (29)-(31) with the aid of Eqs. (1), (2), (17), and (27) to get the following system of three homogeneous equations:

$$\sum_{k=1}^{3} c_{ik} A_k = 0, (32)$$

where
$$c_{11}=-\omega^2\Pi_1+2\frac{\omega^2}{h}-\beta\frac{n_1}{\rho},\;c_{21}=2q_1,\;c_{31}=n_1,c_{12}=-\omega^2\Pi_2+2\frac{\omega^2}{h}-\beta\frac{n_2}{\rho},\;c_{22}=2q_2,\;c_{32}=n_2,\;c_{13}=2\frac{\omega^2q_3}{h},\;c_{23}=q_3^2-1,\;c_{33}=0.$$

The homogeneous system of equations has a non-trivial solution when the determinant of the coefficients of the equations in Eq. (32) disappears:

27 V. Gupta, M. Kumar, Sh. Goel

$$(2-h)[(2-\Pi_1 h) - \eta(2-\Pi_2 h)] = -4(q_1 - \eta q_2)q_3,$$
where $\eta = \frac{n_1}{n_2}$, $h = \frac{c^2}{\delta^2}$, $\Pi_i = \frac{\lambda + 2\mu}{\rho V_i^2}$, $i = 1, 2$. (33)

Since some of the terms in Eq. (32) are irrational, an algebraic approach cannot be used to solve it. This equation can be solved by eliminating radicals using two squares and manipulation, when applied to the given equation, yields an algebraic equation of degree seven that may be written as:

$$\begin{split} & \sum_{k=0}^{7} c_k \, h^k = 0, \\ & \text{where } c_0 = 1024 \eta (d - \eta \varepsilon_s), \ c_4 = -32a[a(d - 2\eta) + (a + b)g], \ c_1 = 256[d^2 - \eta (g + 4d)] - \\ & - 1024 \eta^2 \big(\varepsilon_p + 2\varepsilon_s \big), \ c_5 = 8a^2 (3g + 4ab - 8d), \ c_2 = 128[2\eta a(a + b) - (d - 2\eta)g] + \\ & + 1024 \eta^2 \big(2\varepsilon_p + \varepsilon_s \big), \ \ c_6 = -8a^3 (a + b), \ c_3 = 16[g^2 + 8a(a + b)(d - 2\eta) - 4\eta a^2] - 1024 \eta^2 \varepsilon_p, \\ & c_7 = a^4, \ a = (\Pi_1 - \eta \Pi_2), \ \ b = 1 - \eta, \ \ d = ab - (\varepsilon_1 + \eta^2 \varepsilon_2), \ \ \ g = a^2 + b^2 + 4d, \ \varepsilon_p = \varepsilon_1 \varepsilon_2, \\ & \varepsilon_s = \varepsilon_1 + \varepsilon_2, \quad \varepsilon_i = \left(\frac{\delta}{V_i}\right)^2, \ i = 1, \ 2. \end{split}$$

Seven complex roots are obtained from an algebraic Eq. (34) some of which are added after radicals are eliminated from Eq. (33). When the initial dispersion equation is not satisfied, these roots are recognised and distinguished in Eq. (33). The remaining roots that satisfy Eq. (33) are taken into consideration for the wave field decay as the increases of x_3 in the medium. These roots of the Rayleigh wave Eqs. (33) and (34) describing the existence and propagation in the isothermal plane boundary of a thermoelastic material are satisfied. The coefficient c_i depend upon ω therefore, the phase velocity V calculated from a root of Eq. (34) is also a function of ω . This implies the dispersive behaviour of Rayleigh wave on isothermal surface in thermoelastic medium. The complex value of cshows that waves are attenuated and positive imaginary part of vertical slowness (q_i/c) , i=1, 2, 3 indicates decay of wave with depth in region $x_3 \ge 0$.

Following [38], the phase velocity V and attenuation coefficient Q^{-1} can be calculated as:

$$V = \frac{\delta |h|}{Re(\sqrt{h})} = \frac{|c^2|}{Re(c)},\tag{35}$$

$$Q^{-1} = -\frac{Im(h)}{Re(h)} = \frac{Im(1/c^2)}{Re(1/c^2)}.$$
 (36)

Path of surface particles:

$$\varphi_i = A_1 \lambda_i e^{i(kx_1 - \omega t) + ikx_3 q_i}, \quad i = 1, 2, 3, \tag{37}$$

where $\lambda_i = A_i/A_1$, i = 1, 2, 3 are solution of Eq. (30) and $k = \omega/c$ is the complex number, $\lambda_1 = 1$, $\lambda_2 = -\eta$, $\lambda_3 = 2[(\eta q_2 - q_1)/(q_3^2 - 1)]$.

By using Eq. (37) in Eqs. (17) and (23), we get:

$$(u_1, u_3) = (|U_0|e^{i \arg U_0}, |W_0|e^{i \arg W_0})e^{i(kx_1 - \omega t)}, \tag{38}$$

$$(u_{1}, u_{3}) = (|U_{0}|e^{i \arg U_{0}}, |W_{0}|e^{i \arg W_{0}})e^{i(kx_{1}-\omega t)},$$

$$(U_{0}) = \begin{pmatrix} i[\hbar_{1}e^{ik_{R}x_{3}\delta_{1}} + \hbar_{2}e^{ik_{R}x_{3}\delta_{2}} + \hbar_{3}q_{3}e^{ik_{R}x_{3}\delta_{3}}] \\ [\hbar_{1}q_{1}e^{ik_{R}x_{3}\delta_{1}} + \hbar_{2}q_{2}e^{ik_{R}x_{3}\delta_{2}} - \hbar_{3}e^{ik_{R}x_{3}\delta_{3}}] \end{pmatrix} kA_{1}e^{i(kx_{1}-\omega t)},$$

$$(38)$$

where $\delta_i = [1 - i(c_I/c_R)]q_i$, i = 1, 2, 3, R is used for real part and I is used for imaginary part of complex quantity, K is wave number.

By using Eqs. (37) and (27), we get:

$$T = |T_0|e^{i \arg T_0}e^{i(kx_1 - \omega t)}, \tag{40}$$

$$T_0 = A_1 (n_1 \lambda_1 e^{ik_R x_3 \delta_1} + n_2 \lambda_2 e^{ik_R x_3 \delta_2}). \tag{41}$$

On the boundary surface $x_3 = 0$ Eq. (38) by considering the real part we get:

$$U = |U_0| \cos(\arg U_0 + \Phi) e^{-k_I x_1}$$

$$W = |W_0| \sin(\arg W_0 + \Phi) e^{-k_I x_1}$$
(42)

where $\Phi = K_R x - \omega t$ parameter varies in 0.2π to show the path traced. By using Eq. (28) in parametric form traces elliptical path.

Special Cases

Case 1: In order to derive the secular equation for the thermoelasticity coupled theory. Substitute $m^*=m_1=1$, $m_0=t_1=t_2=t_3=t_4=\tau_0=\tau_1=0$, into Eq. (25). For $\Pi_1=0$, $\eta=0$ Rayleigh wave propagation in an elastic medium is represented by Eq. (33) when reduced to equation $(2-h)^2=-4q_1q_3$. In line with Ewing et al. [39]. Case 2: In order to derive the secular equation for the thermoelasticity L-S theory with one relaxation of times. Substitute $m^*=m_0=m_1=1$, $t_1=t_2=t_3=t_4=\tau_1=0$, into Eq. (25). Case 3: In order to derive the secular equation for the thermoelasticity G-L theory with two relaxations of times. Substitute $m^*=m_1=1$, $m_0=t_1=t_2=t_3=t_4=0$, into Eq. (25). Case 4: In order to derive the secular equation for the thermoelasticity G-N (Type-III) theory. Substitute $m^*>0$, $m_0=\tau_0=t_1=1$, $m_1=t_2=t_3=t_4=\tau_1=0$, into Eq. (25). Case 5: In order to derive the secular equation for the thermoelasticity two-phase -lag theory. Put $m^*=1$, $m_0=m_1=1$, $\tau_1=t_3=t_4=0$, $t_1=\tau_T$, $t_2=\tau_q^2/2$, $\tau_0=\tau_q$, into Eq. (25). Case 6: In order to derive the secular equation for the thermoelasticity three-phase -lag theory. Put $m_0=\tau_0=1$, $m_1=\tau_1=0$, $t_2=\tau_q$, $t_1=1+m^*\tau_V$, $t_3=\tau_T$, $t_4=\tau_q^2/2$, into Eq. (25).

Numerical results and Discussion

Findings of phase velocity, attenuation coefficients

Phase velocity and attenuation coefficient for various theories of thermoelasticity are compared using MATLAB software, adopting frequencies ranging from 0.1 to 59.1 Hz. Now we find numerical results for copper material [38] the required data is given by: $K = 400 \text{ Wm}^{-1}$, $\lambda = 77.6 \text{ GPa}$, $\mu = 38.6 \text{ GPa}$, $\alpha_t = 1.78 \times 10^{-5} \text{K}^{-1}$, $C_E = 383 \text{ J Kg}^{-1}/\text{K}$, $\rho = 8920 \text{ kg/m}^3$, $T_0 = 318 \text{ K}$.

The relaxation time is given by: $\tau_0=0.1~\rm s$, $\tau_q=0.6~\rm s$, $\tau_1=0.2~\rm s$, $\tau_v=0.5~\rm s$, $\tau_T=0.4~\rm s$, $m^*=0.38710~\rm sec^{-1}$.

Tables 1 and 2 display the program's output for comparing various thermoelasticity theories with respect to frequency. The phase velocity and attenuation coefficient change with respect to frequency for various thermoelasticity theories are depicted in Fig. 1. The following thermoelasticity theories are represented in Fig. 1: coupled theory (C–T), Lord - Shulman theory (L-S), green - Lindsay theory (G-L), green - Naghdi theory (G-N), two-phase- lag theory (DPL), and three-phase-lag theory (TPL). Solid blue line, red dashed line, green dash line with asterisk, red dash line with circle, dark green only asterisk, and sky blue with plus sign, respectively. The phase velocity of the G-L theory increases smoothly in the range $0 \le \omega \le 5.1$, then starts decreasing with an increase in frequency and becomes stationary for $\omega \ge 55.1$. The phase velocity of the three-phase-lag theory increases smoothly in the range $0 \le \omega \le 7.1$, then starts decreasing with an increase in frequency and becomes stationary for $\omega \ge 55.1$.

Table 1. Phase velocity (V) value with respect to frequency in the context of various thermoelasticity theories

Frequency ω	C-T (V)	L-S (V)	G-L (V)	G-N (V)	DPL(V)	TPL (V)
0.1	0.4582	0.4581	0.457	0.4295	0.458	0.4295
1.1	0.4197	0.4216	0.4334	0.4257	0.4258	0.4249
2.1	0.4345	0.4374	0.4993	0.4793	0.4524	0.4955
3.1	0.4469	0.4506	0.4938	0.4776	0.4867	0.5028
4.1	0.4559	0.4603	0.4996	0.4816	0.4929	0.5098
5.1	0.4624	0.4675	0.5006	0.4848	0.4983	0.5154
6.1	0.4672	0.4729	0.4246	0.4873	0.5027	0.5205
7.1	0.471	0.4771	0.368	0.4894	0.5066	0.5252
8.1	0.474	0.4805	0.3244	0.4912	0.5101	0.4763
9.1	0.4764	0.4832	0.2899	0.4927	0.5133	0.4622
10.1	0.4784	0.4855	0.262	0.4941	0.5165	0.4427
11.1	0.48	0.4875	0.2389	0.4953	0.5195	0.4168
12.1	0.4814	0.4892	0.2195	0.4964	0.5225	0.3849
13.1	0.4826	0.4906	0.203	0.4975	0.5255	0.3495
14.1	0.4837	0.492	0.1887	0.4986	0.5285	0.3136
15.1	0.4846	0.4932	0.1764	0.4996	0.5314	0.2795
16.1	0.4854	0.4942	0.1655	0.5006	0.5343	0.2489
17.1	0.4861	0.4952	0.1559	0.5015	0.5372	0.2221
18.1	0.4868	0.4961	0.1474	0.5025	0.5401	0.1989
19.1	0.4874	0.4901	0.1397	0.7187	0.5429	0.179
20.1	0.4879	0.4978	0.1328	0.6973	0.5458	0.179
21.1	0.4884	0.4978	0.1265	0.6774	0.5485	0.1618
22.1	0.4888	0.4983	0.1208	0.6591	0.5513	0.1469
23.1						
24.1	0.4892	0.4999	0.1156	0.642 0.626	0.554 0.5567	0.1226
	0.4895	0.5006	0.1108			0.1127
25.1	0.4899	0.5012	0.1064	0.611 0.597	0.5594	0.1039
26.1	0.4902	0.5018	0.1024		0.562	0.0961
27.1	0.4905	0.5023	0.0986	0.5838	0.7117	0.0891
28.1	0.4907	0.5029	0.0951	0.5713	0.6566	0.0829
29.1	0.491	0.5034	0.0918	0.5595	0.6128	0.0773
30.1	0.4912	0.504	0.0888	0.5484	0.5768	0.0722
31.1	0.4914	0.5045	0.086	0.5378	0.5462	0.0676
32.1	0.4916	0.505	0.0833	0.5278	0.5192	0.0635
33.1	0.4918	0.5054	0.0808	0.5182	0.4951	0.0597
34.1	0.492	0.5059	0.0784	0.5091	0.4732	0.0563
35.1	0.4922	0.5064	0.0762	0.5004	0.4531	0.0531
36.1	0.4923	0.5069	0.0741	0.4921	0.4345	0.0502
37.1	0.4925	0.5073	0.0721	0.4841	0.4172	0.0475
38.1	0.4926	0.5078	0.0702	0.4765	0.4011	0.0451
39.1	1.1044	0.5082	0.0684	0.4692	0.386	0.0428
40.1	1.0913	0.5086	0.0667	0.4621	0.3719	0.0407
41.1	1.0788	0.5091	0.0651	0.4554	0.3586	0.0387
42.1	1.0666	0.5095	0.0635	0.4489	0.346	0.0369
43.1	1.0548	0.5099	0.062	0.4427	0.3342	0.0352
44.1	1.0434	0.5103	0.0606	0.4366	0.323	0.0336
45.1	1.0324	0.5107	0.0593	0.4308	0.3124	0.0321
46.1	1.0217	0.5112	0.058	0.4252	0.3024	0.0308
47.1	1.0113	0.5116	0.0568	0.4198	0.2929	0.0295
48.1	1.0012	0.512	0.0556	0.4146	0.2838	0.0283
49.1	0.9915	0.5124	0.0545	0.4095	0.2752	0.0271
50.1	0.9819	0.5128	0.0534	0.4046	0.267	0.026
51.1	0.9727	0.5132	0.0523	0.3998	0.2592	0.025
52.1	0.9637	0.5136	0.0513	0.3952	0.2518	0.0241
53.1	0.955	0.514	0.0504	0.3908	0.2447	0.0232
54.1	0.9465	0.5144	0.0494	0.3864	0.238	0.0232
55.1	0.9382	0.5148	0.0485	0.3822	0.2315	0.0225
56.1	0.9301	0.5152	0.0477	0.3781	0.2253	0.0213
57.1	0.9301	0.5156	0.0468	0.3742	0.2194	0.0208
58.1	0.9222	0.516	0.046	0.3703	0.2194	0.02
JU.1	0.9145	0.5164	0.046	0.3665	0.2137	0.0194

Table 2. The value of the attenuation coefficient with respect to frequency compared to various thermoelasticity theories

0.1 1.1 2.1 3.1 4.1 5.1	-0.1429 -0.0539 -0.0381	-0.1417 -0.0517	-0.1407 0.1649	-0.0156 0.0255	-0.1405	-0.0149
2.1 3.1 4.1		-0.0517	I 0 1649	1 0 0 2 5 5	0.0074	
3.1 4.1	-0.0381		_		-0.0231	0.0645
4.1		-0.039	0.0145	0.0212	0.0281	-0.0588
	-0.0395	-0.0433	5.0642	-0.0341	-0.0484	-0.0872
C 1	-0.0421	-0.0494	8.0095	-0.0483	-0.0881	-0.1053
	-0.0439	-0.055	11.1732	-0.0545	-0.1108	-0.114
6.1	-0.0449	-0.0597	17.5495	-0.0578	-0.1263	-0.115
7.1	-0.0453	-0.0636	13.8256	-0.0599	-0.1377	-0.1103
8.1	-0.0453	-0.0668	15.7837	-0.0612	-0.1464	0.2941
9.1	-0.045	-0.0695	10.5055	-0.0623	-0.1531	0.3214
10.1	-0.0446	-0.0717	9.6341	-0.0632	-0.1583	0.3488
11.1	-0.0441	-0.0736	9.0037	-0.064	-0.1623	0.3678
12.1	-0.0435	-0.0752	8.5273	-0.0648	-0.1653	0.3691
13.1	-0.0429	-0.0766	8.155	-0.0656	-0.1675	0.3502
14.1	-0.0423	-0.0779	7.8562	-0.0663	-0.1689	0.3187
15.1	-0.0418	-0.0791	7.6113	-0.0671	-0.1696	0.2848
16.1	-0.0412	-0.0802	7.407	-0.0678	-0.1698	0.2546
17.1	-0.0406	-0.0812	7.234	-0.0685	-0.1694	0.2298
18.1	-0.0401	-0.0822	7.0858	-0.0692	-0.1685	0.2099
19.1	-0.0396	-0.0832	6.9573	-2.4806	-0.1671	0.1937
20.1	-0.0391	-0.0841	6.8449	-2.47	-0.1654	0.1803
21.1	-0.0387	-0.085	6.7457	-2.4602	-0.1633	0.1691
22.1	-0.0382	-0.0858	6.6576	-2.451	-0.1609	0.1595
23.1	-0.0378	-0.0867	6.5788	-2.4423	-0.1582	0.1511
24.1	-0.0374	-0.0875	6.508	-2.4341	-0.1553	0.1311
25.1	-0.0374	-0.0883	6.4439	-2.4263	-0.1555	0.1438
26.1	-0.0371	-0.0892	6.3857	-2.4188	-72.149	0.1372
				-2.4116	-72.149	
27.1	-0.0364	-0.09	6.3326			0.126
28.1	-0.0361	-0.0908	6.2839	-2.4046	205.6	0.1211
29.1	-0.0357	-0.0916	6.2392	-2.3979	-207.43	0.1166
30.1	-0.0355	-0.0924	6.1979	-2.3914	-195.45	0.1125
31.1	-0.0352	-0.0932	6.1597	-2.3851	-292.40	0.1087
32.1	-0.0349	-0.094	6.1243	-2.3789	-259.12	0.1051
33.1	-0.0347	-0.0948	6.0913	-2.3729	-84.051	0.1018
34.1	-0.0344	-0.0956	6.0606	-2.3671	-55.813	0.0987
35.1	-0.0342	-0.0964	6.0318	-2.3614	-20.767	0.0958
36.1	-0.034	-0.0972	6.0048	-2.3558	-27.437	0.0931
37.1	-0.0338	-0.098	5.9795	-2.3503	-25.124	0.0905
38.1	-0.0336	-0.0988	5.9557	-2.3449	-23.459	0.0881
39.1	-0.7987	-0.0995	5.9333	-2.3396	-22.232	0.0858
40.1	-0.7979	-0.1003	5.9121	-2.3344	-21.312	0.0836
41.1	-0.7971	-0.1011	5.8921	-2.3293	-20.617	0.0815
42.1	-0.7963	-0.1019	5.8732	-2.3243	-20.091	0.0796
43.1	-0.7956	-0.1027	5.8552	-2.3194	-19.694	0.0777
14.1	-0.7949	-0.1035	5.8381	-2.3146	-19.400	0.0759
45.1	-0.7943	-0.1043	5.8219	-2.3098	-19.187	0.0742
46.1	-0.7937	-0.105	5.8064	-2.3051	-19.040	0.0726
47.1	-0.7931	-0.1058	5.7917	-2.3005	-18.94	0.071
48.1	-0.7926	-0.1066	5.7777	-2.2959	-18.901	0.0695
49.1	-0.7921	-0.1074	5.7642	-2.2914	-18.892	0.0681
50.1	-0.7916	-0.1081	5.7514	-2.287	-18.915	0.0667
51.1	-0.7911	-0.1089	5.7391	-2.2826	-18.967	0.0654
52.1	-0.7907	-0.1097	5.7274	-2.2784	-19.042	0.0642
53.1	-0.7903	-0.1104	5.7161	-2.2741	-19.138	0.0629
54.1	-0.7899	-0.1104	5.7052	-2.2699	-19.253	0.0618
55.1	-0.7895	-0.1112	5.6948	-2.2658	-19.383	0.0616
56.1	-0.7891	-0.112	5.6848	-2.2617	-19.528	0.0595
	-0.7888	-0.1127	5.6752	-2.2577	-19.528	0.0585
	1 -0.7 000	I -O.TTJJ	1 3.0/34	-4.4311	- I 7.003	L 0.0000
57.1 58.1	-0.7884	-0.1142	5.666	-2.2538	-19.853	0.0575

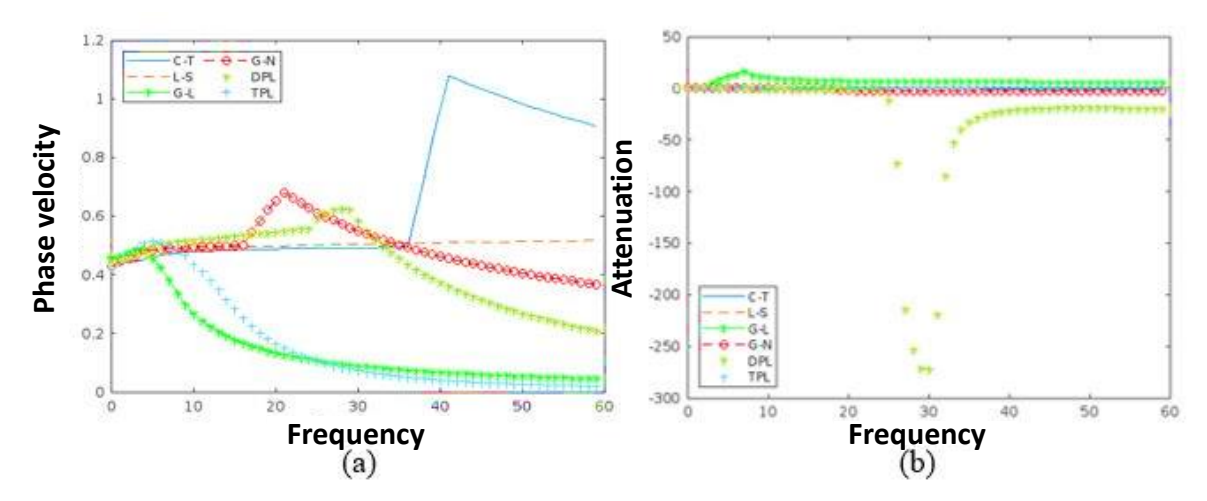


Fig. 1. Variation of phase velocities V (m/s) and attenuations (Q^{-1}) with frequency ω (Hz) for different theories of thermoelasticity

From Fig. 1(a), the two-phase-lag theory, which increases smoothly and attains maximum value at $\omega=27.1$, and after that phase, velocity starts deceasing and attains minimum value at $\omega=59.1$. For the G-N theory, the value of V increases smoothly in the range $0 \le \omega \le 15.1$ and attains a sharp edge at $\omega=19.1$. After this, it starts deceasing, constantly attaining the minimum value of phase velocity but higher than the two-phase-lag model velocity.

The L-S theory, depicts almost constant behaviour because there is very little change in phase velocity with an increase in values of frequency in the range $0 \le \omega \le 60$. The couple theory of thermoelasticity shows constant behaviour with very little difference in the value of phase velocity for frequency in the range $0 \le \omega \le 38.1$. After it, the constant increase in value V in the range $38.1 \le \omega \le 48.1$ then decreases. Overall, phase velocity near 0.4 is attained by all theories of thermoelasticity $\omega = 0.1$, with the maximum value V attained by coupled theory and the minimum value V attained by three-phase-lag theory $\omega = 30.1$. The values of V are very close to each other for the coupled L-S, G-N, and two-phase lag theories of thermoelasticity.

It depicts that in Fig. 1(b), the value of attenuation is near zero and attains negative values in the coupled and L-S theories. In the case of the three-phase lag theory, the value of attenuation attains a positive value near zero. In the case of the G-L theory, the value Q^{-1} increases in the range $0.1 \le \omega \le 8.1$ and then starts to decrease with an increase in the value of frequency. In the case of the G-N theory, the value of attenuation decreases as the value of frequency increases.

Two-phase-lag theory attains a minimum value of Q^{-1} at $\omega=31.1$. This is the lowest value attained in comparison to other theories. In this case, a large fluctuation is observed. The maximum value of attenuation is attained $\omega=8.1$ by the G-L theory of thermoelasticity. Two-phase theory attains a minimum value of attenuation coefficient with respect to other theories. The majority of values attained by all the theories are near to zero, either positive or negative, within the range $0.1 \le \omega \le 59.1$.

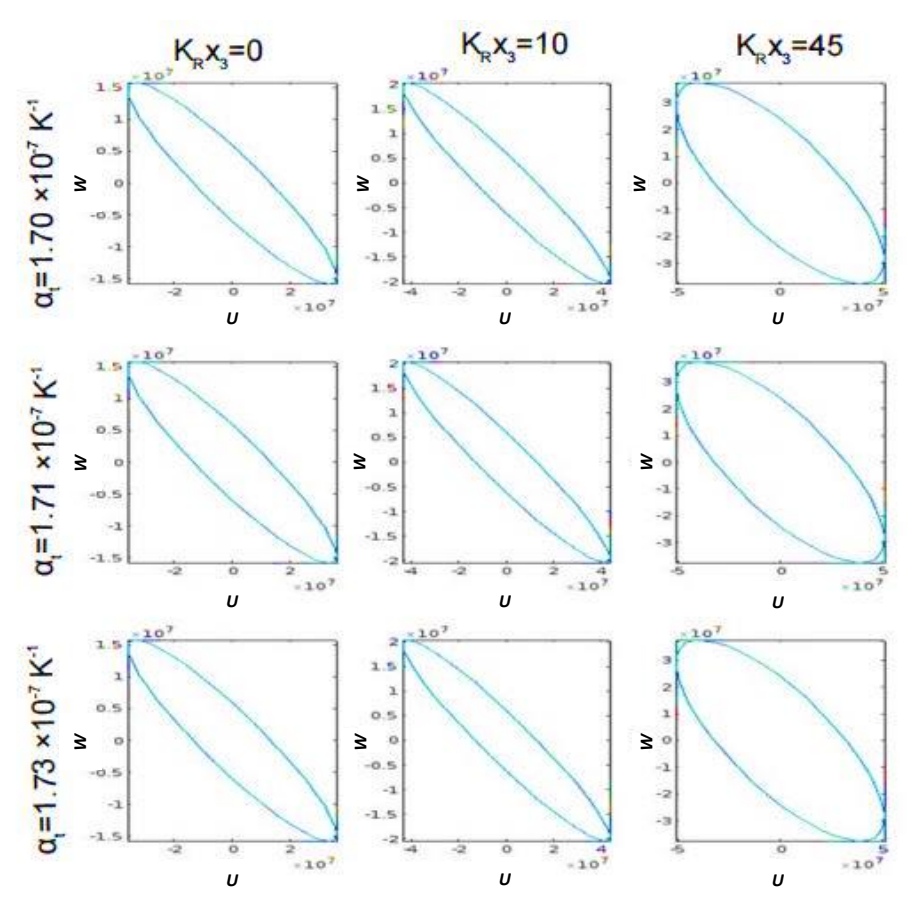


Fig. 2. Particle motion variation (U, W) with depth $K_R x_3 = 0$, 15, 45 for couple theory of thermoelasticity

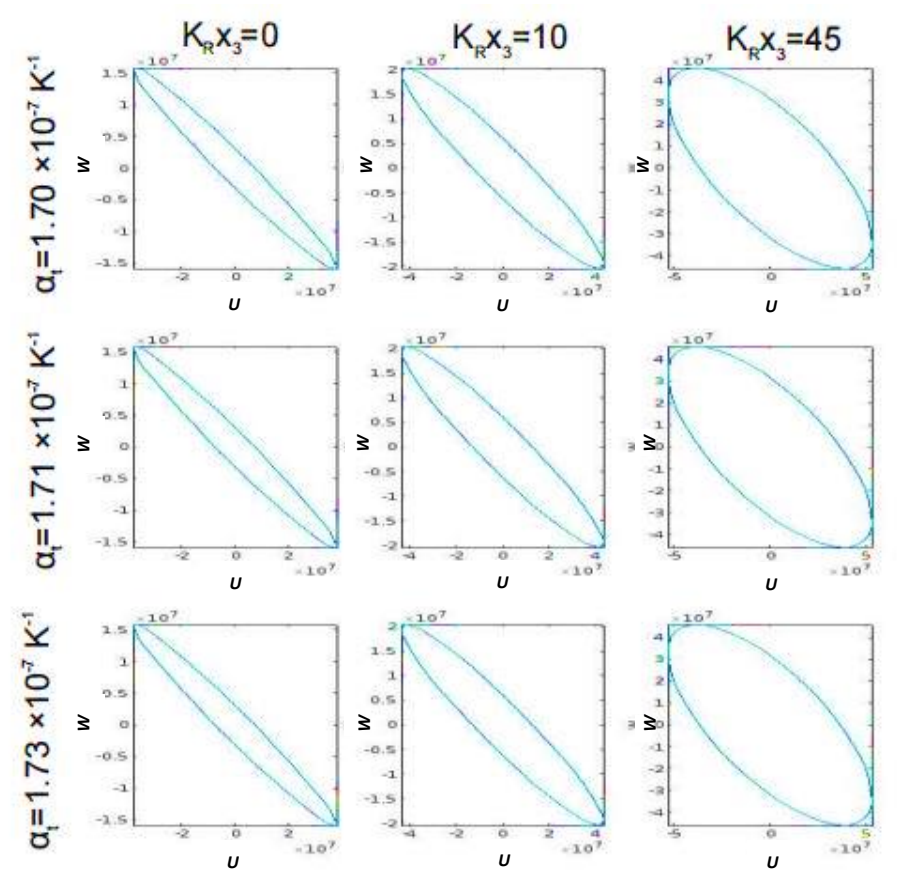


Fig. 3. Particle motion variation (U, W) with depth $K_R x_3 = 0$, 15, 45 for L-S theory of thermoelasticity

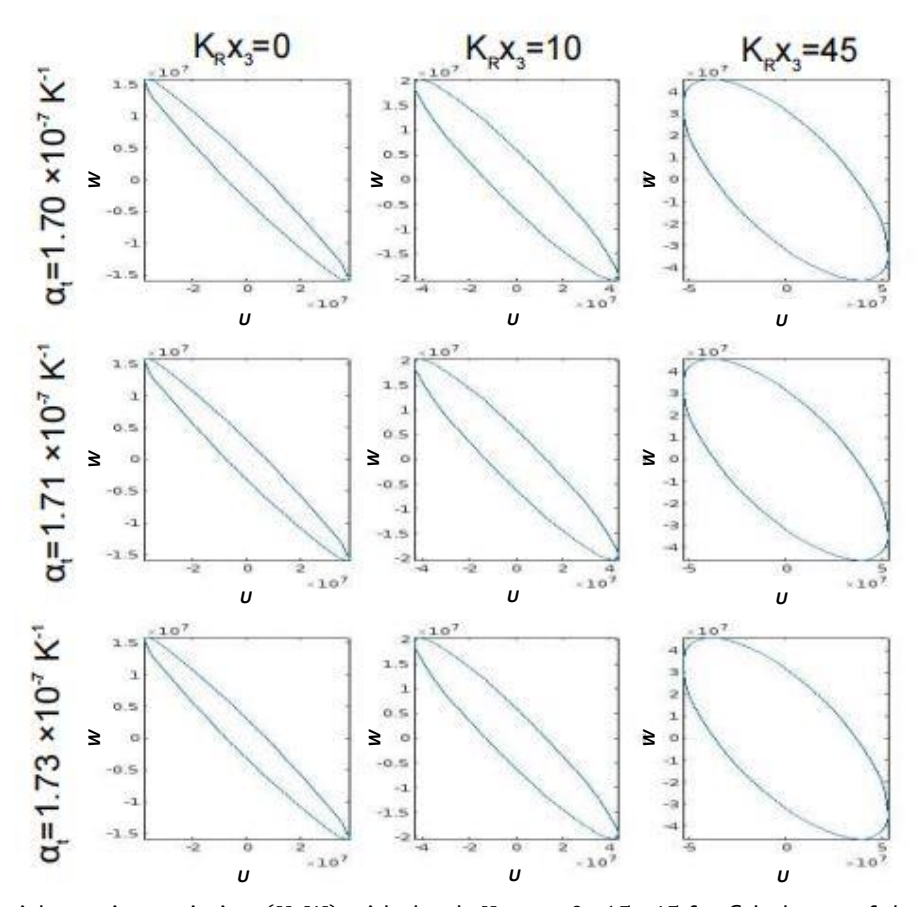


Fig. 4. Particle motion variation (U, W) with depth $K_R x_3 = 0$, 15, 45 for G-L theory of thermoelasticity

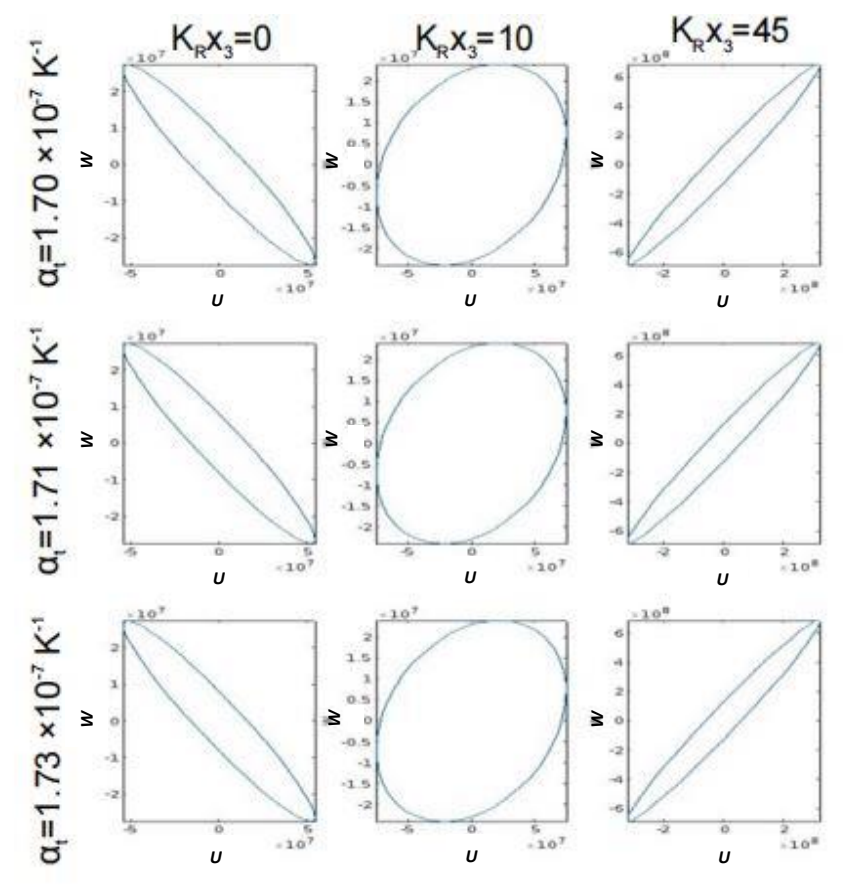


Fig. 5. Particle motion variation (U, W) with depth $K_R x_3 = 0$, 15, 45 for G-N theory of thermoelasticity

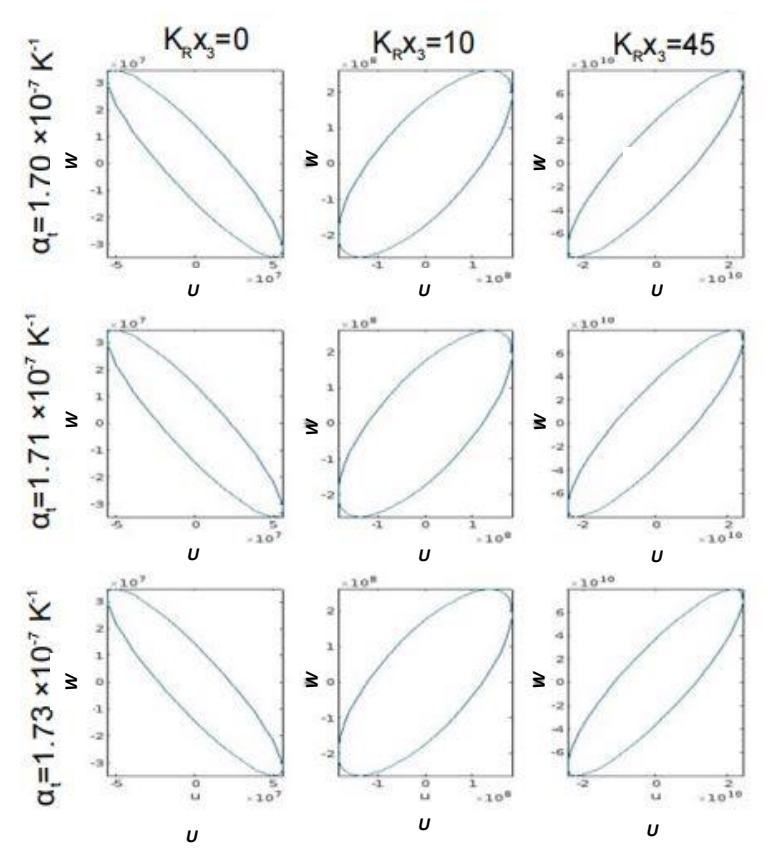


Fig. 6. Particle motion variation (U, W) with depth $K_R x_3 = 0$, 15, 45 for two-phase -lag theory of thermoelasticity

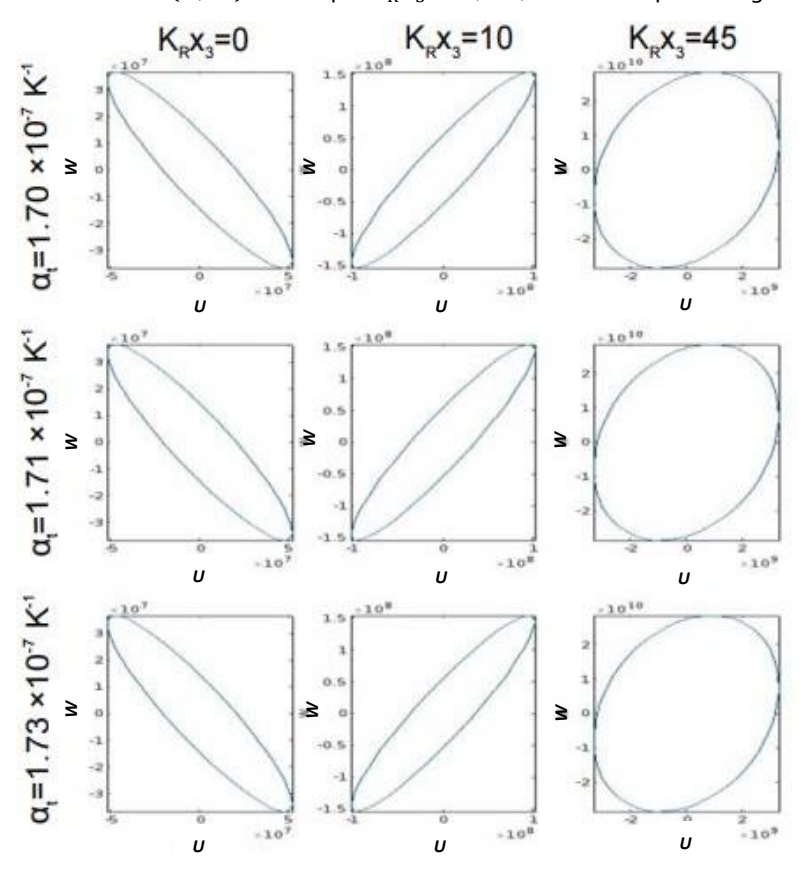


Fig. 7. Particle motion variation (U, W) with depth $K_R x_3 = 0$, 15, 45 for three phase lag theory of thermoelasticity

Path of particle

All the special cases discussed in the form of different theories of thermoelasticity are presented graphically by using the output of MATLAB software in Figs. 2-7. The polarisation of particle motion in two-dimensional space is represented by (U, W).

Physical data of copper material used with frequency $\omega=2\pi$ and parameter Φ varies in $0.2\,\pi$. Different depths vary as follows: $K_Rx_3=0$, 15, 45. The coefficient of thermal linear expansion varies as follows: $\alpha_t=(1.70\times 10^{-7},\ 1.71\times 10^{-7},\ 1.73\times 10^{-7})\ K^{-1}$. For one fixed value of depth, we present three figures for three different Coefficient of thermal linear expansion in such a way 9 figures obtained for three different depths in Figs. 2–7. Computed for coupled theory, L-S theory, G-L theory, G-N theory, two-phase-lag model, and three-phase-lag model of thermoelasticity.

In Fig. 2, it is observed that in the coupled theory of thermoelasticity, the motion of particles for the polarisation of the Rayleigh wave traces an elliptic path and tilt between the axes. Firstly, it shrinks and then expands into an elliptic shape with an increase in depth. In Fig. 3, it is depicted that in the case of the L-S theory of thermoelasticity, the motion of particles attains almost the same shape and size for two different values of depth and finally expands as they go deeper. As coupled theory is extended by L-S and G-L to generalise the theory of thermoelasticity, there is very little difference between these theories theoretically and numerically for the considered depth and coefficient of thermal linear expansion.

From Fig. 4, it is depicted that, using the G-L theory, the path of particle motion is tilted with an elliptic shape and becomes broad as we go deeper into the medium. In Fig. 5, elliptic path is covered by the particle during process of polarisation with tilt in opposite direction at depth $K_R x_3 = 0$ and $K_R x_3 = 45$.

In Fig. 6, the effect of the two-phase-lag theory at the depth $K_R x_3 = 0$ of the elliptic path is obtained between the axes. But as you go deeper, the shape obtained is opposite to the earlier and broad, then finally shrinks at the depth $K_R x_3 = 45$. In Fig. 7, it is observed that in the case of the three-phase-lag theory, the path of the particle is tilted between the axes. As they start going deep, the path of the particle remains the same but opposite in direction, and at the last motion, the particle is such that they obtain a broad elliptic shape.

Conclusion

The present work examines the coupled, L-S, G-L, G-N, two-phase-lag, and three-phase-lag theories of thermoelasticity under Rayleigh wave propagation in an isotropic homogenous medium using the compact form of the heat conduction equation. The dispersion equation for isothermal surfaces has irrational terms in it. We rationalise this equation to get a polynomial equation. Roots that meet both equations are filtered by examining the decay qualities of those roots in depth. The dispersive nature and inhomogeneous nature of Rayleigh waves are verified. Comparing different theories is important while researching the Rayleigh wave's distinctive characteristics.

The isothermal surface increases the speed of the Ryleigh wave. To compare various thermoelasticity theories, the phase velocity, attenuation coefficients, and particle motion path are computed numerically and graphically shown. It is observed that the phase velocity attains its maximum value in the case of coupled theory and its minimum value in the case of the three-phase lag theory. L-S theory shows constant behaviour as frequency increases. For couples, L-S, G-N, and two-phase-lag theories, the values of attenuation coefficient are very close, due to which curves are overlapping. The maximum value is attained by the G-L model, and the minimum value is attained by the two-phase-lag model. The effect of different theories is significant for the particle motion of the Rayleigh wave and shows an elliptic path for different depths and the coefficient of thermal linear expansion. In the G-L theory of thermoelasticity, amplitude increases as we go deeper into the medium. One of the surface waves that is highly useful for researching numerous aspects of an earthquake is the Rayleigh wave.

CRediT authorship contribution statement

Vandana Gupta ©SC: conceptualization, investigation, supervision, data curation; **Manoj Kumar** ©SC: investigation, supervision, data curation; **Shruti Goel** ©SC: writing – review & editing, writing – original draft.

Conflict of interest

The authors declare that they have no conflict of interest.

References

- 1. Biot MA. Thermoelasticity and irreversible thermodynamics. *Journal of Applied Physics*. 1956;27(3): 240–253.
- 2. Green AE, Lindsay KA. Thermoelasticity. *Journal of Elasticity*. 1972;2: 1–7.
- 3. Lord H, Shulman Y. A generalised dynamical theory of thermoelasticity. *Journal of Mechanical Physics and Solids*. 1967;15(5): 299–309.
- 4. Green AE, Naghdi PM. Thermoelasticity without energy dissipation. Journal of Elasticity. 1993;31: 189–208.
- 5. Hetnarski RB, Ignaczak J. Generalized thermoelasticity. *Journal of Thermal Stresses*. 1999;22(4-5): 451–476.
- 6. Ignaczak J, Ostoja-Starzewski M. Thermoelasticity with Finite Wave Speeds. Oxford University Press; 2009.
- 7. Tzou DY. A unified approach for heat conduction from micro to macro-scales. *Journal of Heat Transfer*. 1995;117(a): 8–16.
- 8. Choudhuri SKR. On thermoelastic three phase lag model. Journal of Thermal Stresses. 2007;30(3): 231–238.
- 9. Deresiewicz H. Effect of boundaries on waves in a thermo-elastic solid: Reflection of plane waves from plane boundary. *Journal of Mechanical Physics and Solids*. 1960;8(3): 164–172.
- 10. Sinha AN, Sinha SB. Reflection of thermoelastic waves at a solid half space with thermal relaxation. *Journal of Physics of the Earth*. 1974;22(2): 237–244.
- 11. Sinha SB, Elsibai KA. Reflection of thermoelastic waves at a solid half-space with two thermal relaxation times. *Journal of Thermal Stresses*. 1996;19(8): 763–777.
- 12. Sharma JN, Kumar V, Chand D. Reflection of generalized thermoelastic waves from the boundary of a half-space. *Journal of Thermal Stresses*. 2003;26(10): 925–942.
- 13. Singh MC, Chakraborty N. Reflection of a plane magneto-thermoelastic wave at the boundary of a solid half-space in presence of initial stress. *Applied Mathematics and Modelling*. 2015;39(5-6): 1409–1421.
- 14. Wei W, Zheng R, Liu G, Tao H. Reflection and refraction of P wave at the interface between thermoelastic and porous thermoelastic medium. *Transport in Porous Media*. 2016;113: 1–27.
- 15. Li Y, Li L, Wei P, Wang C. Reflection and refraction of thermoelastic waves at an interface of two couple-stress solids based on Lord-Shulman thermoelastic theory. *Applied Mathematics and Modelling*. 2018;55: 536–550.

16. Rayleigh L. On waves propagated along the plane surface of an elastic solid. *Proceeding of the Royal Society. London, Ser. A.* 1885;17: 4–11.

- 17. Sinha AN, Sinha SB. Velocity of Rayleigh waves with thermal relaxation in time. Acta Mechanica. 1975;23: 159-166.
- 18. Sharma MD. Phase velocity and attenuation of plane waves in dissipative elastic media: solving complex transcendental equation using functional iteration method. *International Journal of Engineering Science and Technology*. 2010;3(2): 130–136.
- 19. Tomita S, Shindo Y. Rayleigh waves in magneto-thermoelastic solids with thermal relaxation. *International Journal of Engineering Science and Technology.* 1979;17(2): 227–232.
- 20. Chadwick P, Windle DW. Propagation of Rayleigh waves along isothermal and insulated boundaries. *Proceeding of the Royal Society London.* 1964;280(1380): 47–71.
- 21. Dawn NC, Chakraborty SK. On Rayleigh wave in Green-Lindsay's model of generalized thermoelastic media. *Indian Journal of Pure and Applied. Mathematics.* 1988;20(3): 273–286.
- 22. Ahmed SM. Rayleigh waves in a thermoelastic granular medium under initial stress. *International Journal of Mathematical Science*. 2000;23: 627–637.
- 23. Sharma JN, Walia V, Gupta SK. Effect of rotation and thermal relaxation on Rayleigh waves in piezothermoelastic half space. *International Journal of Mechanical Science*. 2008;50(3): 433–444.
- 24. Abd-alla AN, Al-dawy AAS. Thermal relaxtion times effect on Rayleigh waves in generalised thermoelastic media. *Journal of Thermal Stress.* 2001;24(4): 367–382.
- 25. Mahmoud SR. Influence of rotation and generalized magneto-thermoelastic on Rayleigh waves in a granular medium under effect of initial stress and gravity field. *Meccanica*. 2012;47: 1561–1579.
- 26. Noguchi S, Maeda T, Furumura T. Ocean-influenced Rayleigh waves from outer-rise earthquakes and their effects on durations of long-period ground motion. *International Journal of Geophysical*. 2016;205(2): 1099–1107.
- 27. Bucur AV, Passarella F, Tibullo V. Rayleigh surface waves in the theory of thermoelastic materials with voids. *Meccanica*. 2014;49: 2069–2078.
- 28. Zhao W, Chen W, Yang D, Gao H, Xie P. Analytical solution for seismic response of tunnels with composite linings in elastic ground subjected to Rayleigh waves. *Soil Dynamics and Earthquake Engineering*. 2022;153: 107113.
- 29. Li X, Li Q, Shen H, Yang F, Zhang X. Research on oil exploration seismic Rayleigh wave imaging based on multi-channel analysis of surface waves and genetic-damped least squares joint inversion. *Journal of Applied Geophysics*. 2022;202: 104670.
- 30. Singh B, Verma S. On Propagation of Rayleigh Type Surface Wave in Five Different Theories of thermoelasticity. *International Journal of Applied Mechanics and Engineering*. 2019; 24(3): 661–673.
- 31. Sharma S, Kumari S, Singh M. Rayleigh wave propagation with the effect of initial stress, magnetic field and two temperatures in the dual phase lag thermoelasticity. *Journal of Advances in Mathematics*. 2020;9(9): 7535–7545.
- 32. Kumar R, Gupta V. Rayleigh waves in generalized thermoelastic medium with mass diffusion. *Canadian Journal of Physics*. 2015;93(10): 1039–1049.
- 33. Kumar R, Singh K, Singh D. Propagation of Rayleigh waves in a micropolar thermoelastic half-space with impedance boundary conditions. *Materials Physics and Mechanics*. 2018;35(1): 115–125.
- 34. Haque I, Biswas S. Rayleigh waves in nonlocal porous thermoelastic layer with Green-Lindsay model. *Steel and Composite Structures*. 2024;50(2): 123–133.
- 35. Saeed T, Khan MA, Alzahrani ARR, Jahangir A. Rayleigh wave through half space semiconductor solid with temperature dependent properties. *Physica Scripta*. 2024;99: 025208.
- 36. Singh K, Kashyap M. Memory effect on Rayleigh waves propagation in a micro polar thermoelastic half space. *Mechanics of Solids*. 2023;58: 1228–1238.
- 37. Kumar R, Gupta V. Uniqueness, reciprocity theorems and plane wave propagation in different theories of thermoelasticity. *Journal of Applied Mechanics and Engineering*. 2013;18(4): 1067–1086.
- 38. Sharma MD. Propagation and attenuation of Rayleigh waves in generalized thermoelastic media. *Journal of Seismology*. 2014;18: 61–79.
- 39. Ewing WM, Jardetzky WS, Press F. Elastic layers in Layered Media. New York: McGraw-Hill Company; 1957.

Accepted: February 18, 2025

Submitted: December 13, 2024 Revised: January 30, 2024

Multifractal properties of breaking bonds coordinates in heterogeneous materials revealed by the discrete element method

V.L. Hilarov [™] (10), E.E. Damaskinskaya (10)

loffe Institute, St. Petersburg, Russia

[™] vladimir.hilarov@mail.ioffe.ru

ABSTRACT

Using the discrete element method coordinates of elementary acoustic emission sources (breaking bonds) were calculated as a function of time for materials of different degrees of heterogeneity under mechanical loading. The time dependences of multifractal dimension spectra D(q) for these sources were calculated using the "sandbox" algorithm. The time behavior of spectra width w and box counting fractal dimension D_0 was studied. A narrowing of the multifractal dimension spectra was discovered (fractal self-organization of acoustic emission) before the destruction of materials and its subsequent expansion after the formation of a main crack. The influence of physical properties of the polycrystalline grain boundaries on the strength and ductility of materials has been revealed.

KEYWORDS

fracture of materials • discrete element method • multifractals • self-organization

Citation: Hilarov VL, Damaskinskaya EE. Multifractal properties of breaking bonds coordinates in heterogeneous materials revealed by the discrete element method. *Materials Physics and Mechanics*. 2025;53(1): 38–47.

http://dx.doi.org/10.18149/MPM.5312025_3

Introduction

The discrete element method (DEM) has recently been widely used to study the nature of solids fracture [1–11]. Its advantage over traditional continuum methods for calculating mechanical properties, such as finite element method (FEM) [12–14] is that it naturally takes into account discontinuities in materials. The material is specified by a set of particles of various shapes that simulate polycrystalline grains and bonds between these particles at the points of their contacts (BPM is a bonded particle model) [15]. We used spherical particles.

The advantage of the DEM method for calculating multifractal characteristics is that the coordinates of all broken bonds are known with great accuracy, which makes it possible to calculate spatial fractal characteristics directly based on these coordinates. In all laboratory acoustic emission (AE) experiments and field observations of seismic events, only a small part of the acoustic signals is recorded, and the coordinates of the signal sources are calculated from the spatial location of the sensors receiving these signals. When using the DEM method, such a procedure is not necessary.

Though there are many papers concerning DEM, we found none devoted to the analysis of the change in multifractal spectra in the fracture process of materials. Meanwhile, these investigations seem to be very important since multifractal self-organization can serve as a precursor of materials destruction in the fracture process [16–19]. Moreover, there are significant reasons to believe that fractal self-organization



is a common feature of disasters of various nature [17–23]. The presence of the same peculiarities in very different systems suggests that these peculiarities are not connected with the details of the system elements interaction but rather with the character of these elements collectivization. That is why the present study appears to be actual and noteworthy. Calculations using the discrete element method were carried out using the freely available MUSEN software package [24].

Computer simulation

Though the experimental scheme considered in this paper is similar to that described in [25], the quantities analyzed in the current study and discussed further are quite different from those in [25]. In that paper we analyzed stresses and acoustical signal distributions, while the present paper is devoted to the analysis of multifractal features of acoustic emission (AE) sources. Cylindrical samples with a diameter of 10 mm and a height of 20 mm were modeled. Cylinders were filled with spherical particles of the same or different sizes and packed until a porosity of 0.35–0.37 was reached. Particles and bonds between them (grains and grain boundaries) were assumed to be made of the materials listed in Table 1.

Though the parameters used are characteristic of granites, it should be noted that "microscopic" values of parameters for the particles and bonds result in different values for real material parameters. That is why calibration of the "microscopic" parameters is required to compare the values of the mechanical properties of the modeling materials with the real ones [15]. As this paper has not had the task to compare numerical values of the magnitudes for the modeled and real materials (for example, a strength thereof), such parameter calibration was not carried out.

Table 1. Material properties used in the simular	tion
---	------

#	Material	ρ , kg/m ³	E, GPa	ν	$\sigma_{\rm n}$, MPa	$\sigma_{\rm t}$, MPa	η, Pa·s
1	Quartz	2650	94	0.29	600	600	5E19
2	Orthoclase	2560	62	0.29	420	420	1E19
3	Oligoclase	2560	70	0.29	480	480	1E19
4	Glass	2500	50	0.22	50	50	1E40
5	Quartz-orthoclase bonds	2500	5.8	0.2	200	200	5E19
6	Quartz-oligoclase bonds	2500	5.8	0.2	300	300	5E19
7	Orthoclase-oligoclase bonds	2500	5.8	0.2	100	100	5E19

Here, ρ is the density of material, E is Young's modulus, v is Poisson's ratio, σ_n is normal strength, σ_t is shear strength, η is dynamic viscosity.

Four types of samples were used: two samples contained particles connected with orthoclase bonds. Diameters of these bonds in sample 1 were d=0.04 mm and in sample 2 d=0.1 mm. Grains (particles) in these samples had diameters and composition shown in Tables 2 (sample 2) and 3 (sample 1). For the sample 1 diameters were normally distributed with a mean value of 0.08 mm and a standard deviation of 0.025 mm. The diameter of fraction 4 for orthoclase was increased 10 times in order to increase the degree of heterogeneity. For the sample 2 diameters are normally distributed, with a mean value of 0.3 mm and a standard deviation of 0.1 mm obtained by a random number generator with a normal distribution. Sample 1 and sample 2 have 33670 and 48695 particles, respectively.

Sample 3 contained particles with diameters and composition shown in Table 3 (the number of particles is 33670). Particle diameters were the same as for sample 1. In this sample, bonds of the same material connected particles made from the same material, while glass bonds 4 from Table 1 connected particles from different materials. Bond diameters in this sample were $d \le 0.1$ mm.

Table 2. Particles diameters and composition for each fraction

	Par	ticles diame	The relative content of each fraction			
Quartz	0.36	0.188	0.52	0.28	0.42	0.0595745
Orthoclase	0.27	0.28	0.4	0.36	0.26	0.0702128
Oligoclase	0.16	0.168	0.288	0.24	0.4	0.0702128

Table 3. Particles diameters and composition for each fraction

	Par	ticles diame	The relative content of each fraction			
Quartz	0.09	0.047	0.132	0.079	0.106	0.0595745
Orthoclase	0.068	0.07	0.096	0.91	0.064	0.0702128
Oligoclase	0.041	0.042	0.077	0.063	0.098	0.0702128

Sample 4 had the same composition as sample 2. Bonds from the same material connected particles from the same material, while low-modulus bonds 5-7 (Table 1) with diameters $d \le 0.6$ mm connected particles from different materials.

For samples 2, 3 and 4, the bond diameters (*d*) were chosen by the MUSEN program bond generator to be equal to the smaller diameter of the pair of connected particles 1 and 2: $d = \min\{d_1, d_2\}$ [24].

Samples were placed in a virtual press. The lower plate was fixed, and the upper one moved down with a constant speed v = 0.02 m/s until the sample was destroyed. Thus, uniaxial compression was simulated. Since v = 0.02 m/s and the height of the sample is 0.02 m, the axial strain $\varepsilon = v \cdot t/h$ and time are numerically equal.

A large set of different mechanical parameters was recorded during the deformation of the samples. In the present work, these parameters were the lifetimes of broken bonds and their space coordinates. Each breaking of the bond is considered in this study to be an elementary acoustic emission event.

The following algorithm has been used in order to calculate the multifractal properties of the coordinates of acoustic emission (AE) centers. The entire time series of these coordinates (AE signals) was divided into successive samples of 4096 events. The time value was assigned to the time of the last sampling event. For each such sample, the multifractal dimension spectrum (MDS) was calculated using the "sandbox" algorithm [26–28]. According to this method, the generalized fractal dimension D_q is defined as: $D_q = \lim_{r \to 0} \frac{\ln c(M_i(r)/N)^{q-1}}{\ln (r/d)} \cdot \frac{1}{q-1}$, where d is the spatial size of the multifractal set, $M_i(r)$ is the number of AE signals emitted inside a sphere of radius r centered at the point of the i-th event, q is the scaling moment. Angle brackets indicate statistical averaging over randomly selected points. Due to the small size of the sets under study (N = 4096 events), all points of the set were taken into account in this work.

In practice, the scaling exponents $\tau(q)$ are first determined by linear regression of $lnS = ln < (M_i(r)/N)^{q-1} >$, constructed as a function of ln(r/d). After that, the multifractal dimension spectrum $D_q = \tau(q)/(q-1)$ for $q \ne 1$ has been estimated. A uniform sequence of 21 numbers in the range [-5-+5] was used as the set q. We did not calculate the information dimension D_1 in this work. Only parameters D_0 and $w = D_{-5} - D_5$ were used (the box counting fractal dimension and spectrum width).

No special choice for the points near the border of the sample was used. This led to boundary effects. However, it is well known that these effects violate the linear dependence of the statistical sum logarithm on the logarithm of scale on large scales. Therefore, nonlinearity on these scales was simply withdrawn from the regression.

The typical scaling dependence of $lnS = ln < (M_i(r)/N)^{q-1} >$, on ln(r) and the multifractal dimension spectrum $D_q = \tau(q)/(q-1)$ are shown in Fig. 1. Nonlinear regions on small and large scales were omitted during regression.

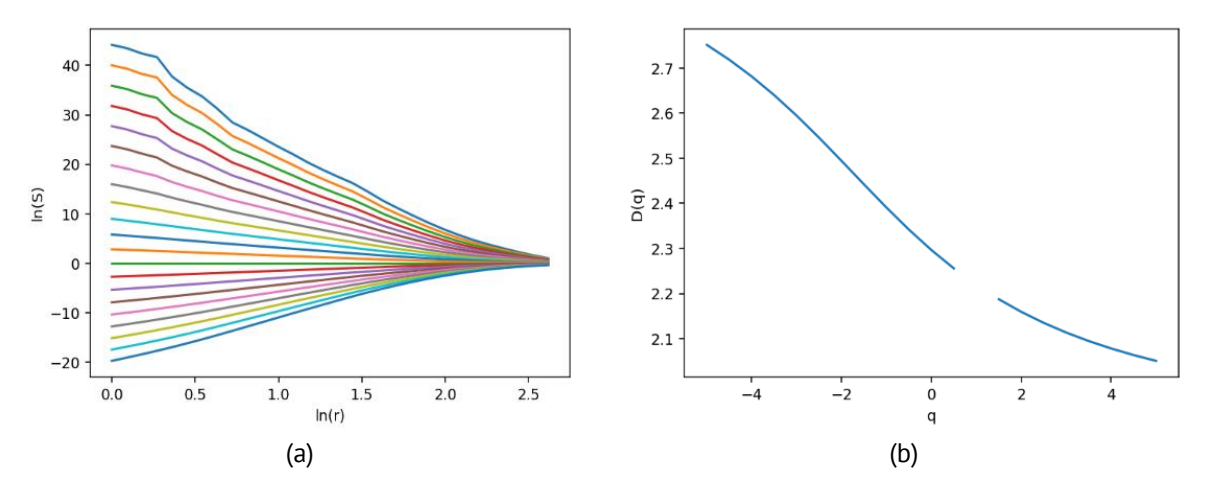


Fig. 1. Typical scaling dependence of $\ln S = \ln < (M_i(r)/N)^{q-1} > \text{on } \ln(r)$ and the multifractal spectrum D(q)

Main results

Figure 2 shows the loading diagram (the stress-strain curve), as well as the multifractal parameters D_0 (box counting fractal dimension) and w (the width of the multifractal dimension spectrum MDS) as functions of time for sample 1 with orthoclase bonds.

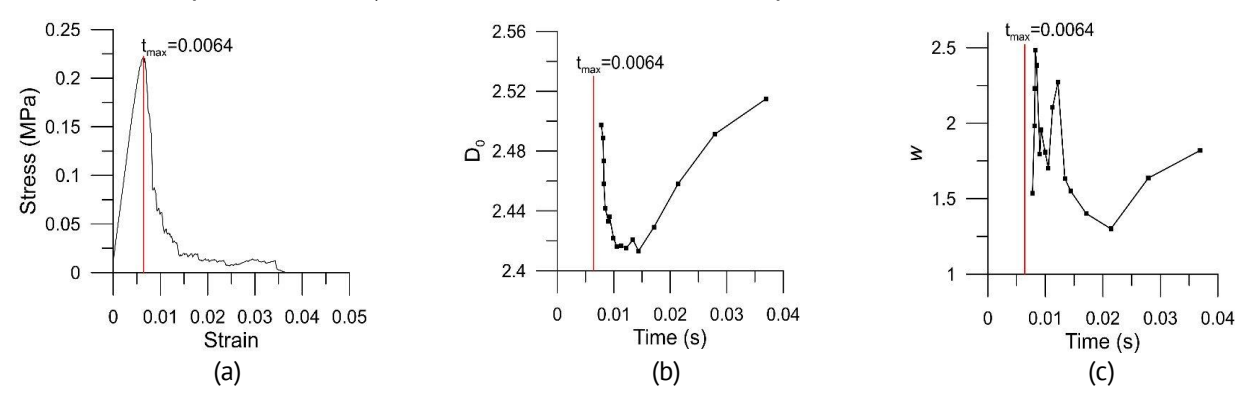


Fig. 2. Loading diagram (a) and time dependences of the fractal dimension (b) and the width of the multifractal dimension spectrum (c) of sample 1. Strain and time are numerically equal

Near time point $t \approx 0.01$ s, a source of destruction was formed [24], which subsequently evolved until the fracture of the entire sample occurred. Before its formation, both the fractal dimension D_0 and the spectral width w decreased. Vertical straight lines correspond to the maximum of the loading diagram at the time point $t=t_{max}$. There are not enough acoustic signals (bond breaking events) in order to calculate multifractal parameters in the pre-peak region.

Figure 3 shows similar dependences for an even more homogeneous sample 2, all bonds of which had the same thickness d=0.1 mm. Vertical straight lines correspond to the maximum load on the loading diagram and the moment of failure of the sample when this load decreases to zero. Acoustic emission characteristics are given starting from the time point of about $t \approx 0.014$ s, because up to this point, AE is practically absent. Before destruction, a decrease in the w is again observed. It slightly decreases before $t \sim t_{max}$ and sharply decreases just before the fracture time t_f (where the stress acting on the loading plane of the loading diagram approaches zero). It can be noted that immediately at the moment of destruction these parameters increase sharply. After this sample's destruction fragments hit the loading plates, so the breakdown continues. The multifractal spectrum parameters in this time range have no physical sense.

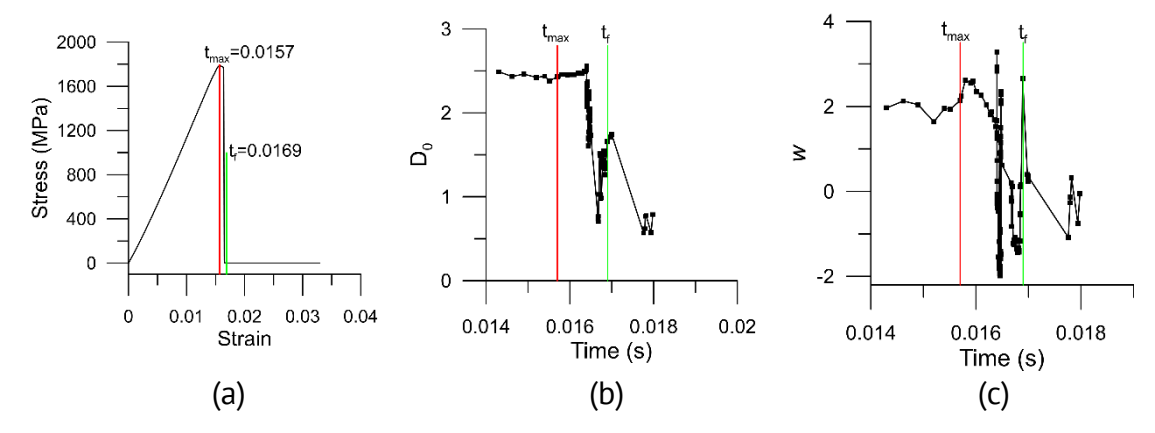


Fig. 3. Loading diagram (a) and time dependences of the fractal dimension (b) and the width of the multifractal dimension spectrum (c) of sample 2. Strain and time are numerically equal

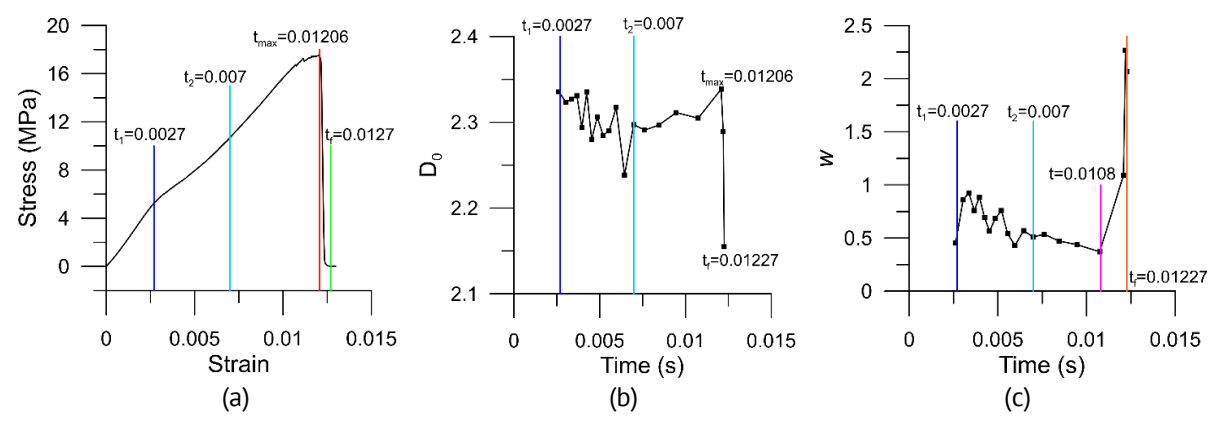


Fig. 4. Loading diagram (a) and time dependences of the fractal dimension (b) and the width of the multifractal dimension spectrum (c) of sample 3

Figure 4 depicts the multifractal characteristics of sample 3, containing low-strength glass bonds (#4 Table 1). One should notice that the loading diagram in this case becomes nonlinear. In the time interval $t \approx 0.0027 - 0.007$ s, the slope of this diagram changes. In this time range, an increase in the number of glass bond breaks is observed. Thus, the presence of glass bonds in the sample leads to its "quasi-plasticity" – the nonlinear character of the loading diagram caused by the glass bonds breakdown. Rather chaotic changes in multifractal characteristics D_0 and w occur during this time. When most of the glass bonds have broken, the slope of the loading diagram increases again while D_0 increases, and w decreases. During the sample destruction, there is a sharp downward jump in D_0 and an increase in w.

Figure 5 shows the multifractal parameters of sample 4, in which low-modulus bonds from Table 1 connected particles of different materials. The loading diagram has an almost horizontal section (shelf) for quite a long time (the loading speed was chosen in such a way that the deformation value and the time reference were numerically the same). During this time, the bonds between particles of the same materials are predominantly broken. The value of D_0 in this time range is quite high and does not change significantly. The spectrum width w also changes little and is very small in magnitude, i.e. the system is practically monofractal. During the destruction, there is a sharp decrease in D_0 and after it an increase in the spectrum width w.

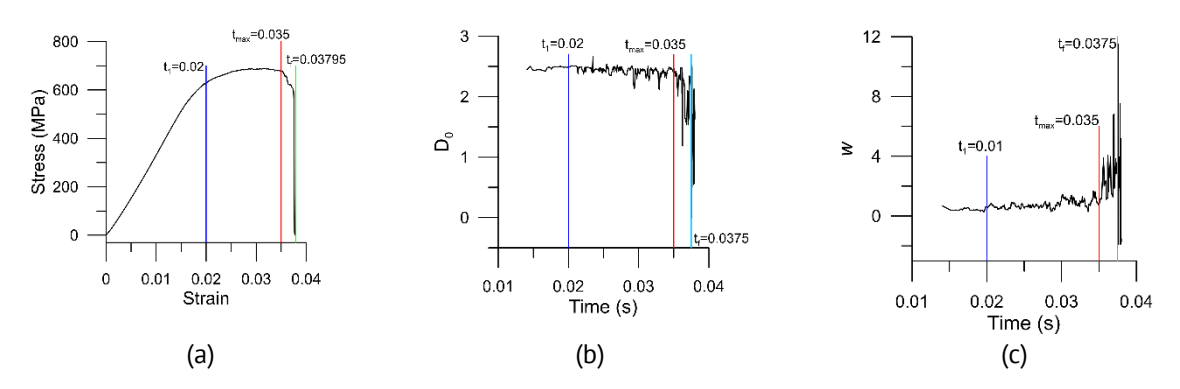


Fig. 5. Loading diagram (a) and time dependences of the fractal dimension (b) and the width of the multifractal dimension spectrum (c) of sample 4

Discussion

It is obvious that homogeneous samples 1 and 2 are destroyed in a brittle manner, as it follows from Figs. 2 and 3. Moreover, almost from the very beginning of deformation, a crack is formed in sample 1, which subsequently evolves [29]. Before its formation, the fractal dimension and spectral width w decrease. Sample 2 elastically deforms before crack formation, which is reflected in the linear dependence of stress on strain. Before the formation of the crack, a decrease in the spectrum width w is also observed. However, after the formation of the main crack, an increase in these parameters is seen in both samples. Similar dependencies were discovered in the surface profile transformation while deforming thin metal foils, for example [16,17]. After the formation of a main crack in these experiments, the widths of the multifractal singularity spectra increased, and it was hypothesized that this occurred because of stress relaxation caused by the formation of a main crack. Here we confirm this hypothesis, since the stress relaxation is directly

observed in the form of a sharp decrease in stress in the loading diagrams after the crack formation. The images of cracks discussed here are shown below.

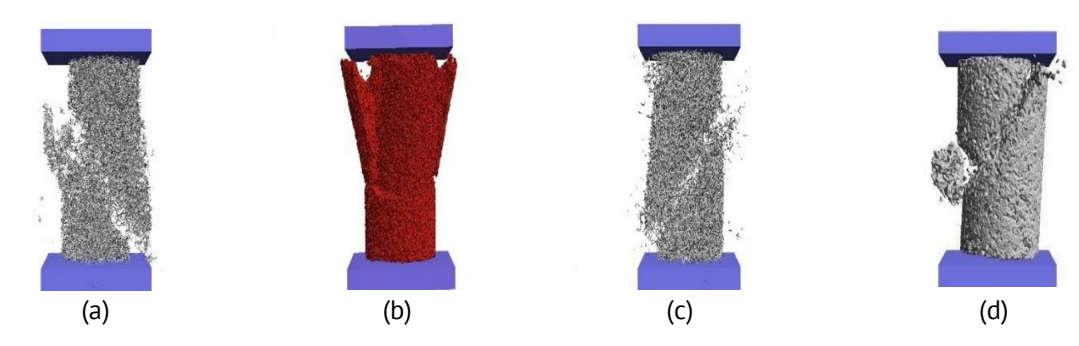


Fig. 6. Paterns of destruction for samples 1 (a), 2 (b), 3 (c) and 4 (d)

In heterogeneous sample 3 the loading diagram is nonlinear in the time range (t_1,t_2) . In this time range, mainly low-strength glass bonds are broken. The restoration of the elastic modulus at $t>t_2$ may be explained by the fact that in this time range, the rate of destruction of glass bonds significantly decreases while the rate of other bonds type breakage is not yet very high (Fig. 7(a)). Thus, the cause of stress relaxation in this case is the breakage of the glass bonds. The width of the multifractal dimension spectrum w decreases before the sample destruction, whereas the fractal dimension D_0 sharply decreases only during this destruction.

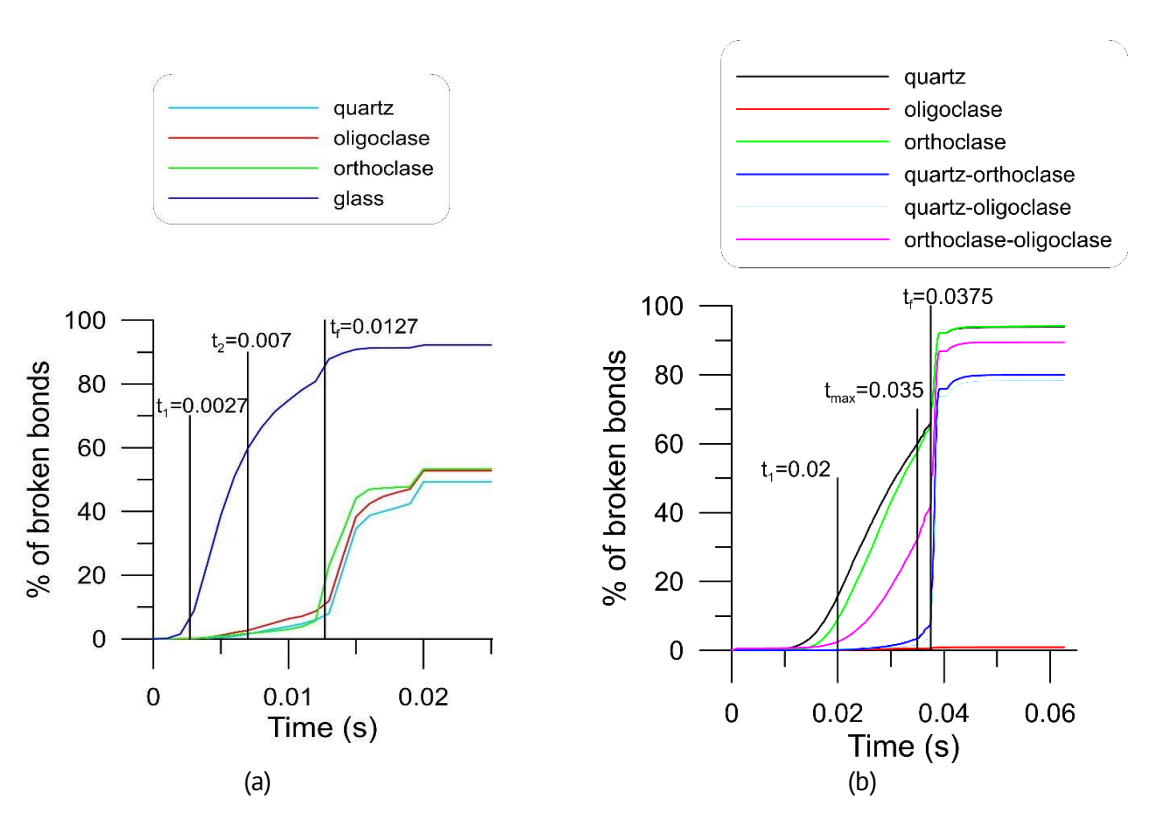


Fig. 7. Kinetics of different bonds types: (a) sample 3 with the "glass bonds", (b) sample 4 with low elastic modulus bonds

The nonlinearity of the loading diagram at $t>t_1$ for the sample 4 may be explained by the fact that in this time range the rate of rupture of high-strength bonds (1–3 from Table 1) reaches a maximum. The weaker bonds (5–7) remain mainly intact due to their deformation ability because of the low elastic modulus (Fig. 7(b)). Thus, in this case, the rupture of high-modulus strong bonds causes the stress relaxation. The fractal dimension D_0 experiences a sharp jump, and the spectrum width w sharply increases after the main crack formation $t>t_f$ due to the increased relaxation of mechanical stresses.

Similar loading diagrams and multifractal characteristics were observed in a laboratory research [30] on the fracture process in Westerly granite samples. Defect formation was monitored by recording acoustic emission (AE) signals. In these experiments, the monofractality of the AE centers was held until the moment of sample destruction, and the correlation fractal dimension D_2 decreased before this destruction [31]. Loading feedback took place in the laboratory experiments: the loading system reduced the external load if the acoustic activity exceeded a specified threshold. Thus, the loading system itself simulates stress relaxation. However, unlike a computer simulation, this feedback made it possible to significantly extend the time of the fracture process. Therefore, the time range of D_2 decrease in the laboratory experiment is significantly larger.

The nonlinearity of the loading diagram before the catastrophic stress decrease in heterogeneous samples can be explained in the computer simulations under consideration in two ways. The first one is the "quasi-plastic" deformation, the whose role of in sample 3 plays the breakage of low-strength glass bonds, and in sample 4 the breakage of high-modulus strong bonds. Secondly, in sample 3 this nonlinearity can be caused by intergranular fracture, since here the brittle bonds connecting grains of different materials are destroyed. While in sample 4 this nonlinearity is associated with intragranular fracture, since in this time range bonds connecting grains of the same materials are destroyed. In this case, the formation of a macro crack and the final destruction of the sample can be explained by intergranular destruction (the destruction of grain boundaries).

The mechanical strength of sample 4 is significantly higher than that of a similar sample with glass bonds of the same geometry (700 and 300 MPa), and the fracture strains are also significantly higher (0.037 and 0.015). Loading diagram for the glass bond sample is given in [25]. Since these samples have the same particle composition and differ only in the materials of intergranular bonds, it can be concluded that materials with the possibility of intergranular deformation have higher ductility compared to materials with rigid grain boundaries. The mechanical strength of materials is also determined by the strength of grain boundaries (intergranular bonds connecting particles of different materials, taking into account their diameter). The higher the strength of these boundaries, the higher the strength of the material as a whole.

The meaning of the decrease in the fractal dimension before the fracture occurs can be explained by the localization of the process with the crack formation at the late stage of the fracture process [31]. Breaking bonds start to form the crack, whose fractal dimension is close to that of the plane. The macro cracks are usually monofractal; that is why the width of the multifractal spectra decreases before crack formation.

Conclusion

Thus, the character of the fracture process changes in time while approaching destruction from the more complicated (stochastic, multifractal) to a more simple – monofractal one. A decrease in the width of the multifractal dimension spectra before the destruction of the material indicates the fractal self-organization of the process. We believe that this self-organization is a result of self-organized criticality like dynamics of the system. The obtained results could be used in detecting onset of failure of heterogeneous materials.

CRediT authorship contribution statement

Vladimir Hilarov Sc: conceptualization, methodology, software, writing - original draft, supervision, **Ekaterina Damaskinskaya Sc:** writing - review & editing, visualization, investigation.

Conflict of interest

The authors declare that they have no conflict of interest.

References

- 1. Hazzard JF, Young RP. Simulating Acoustic Emissions in Bonded-Particle Models of Rock. *Int J Rock Mech Min Sci.* 2000;37(5): 867–872.
- 2. Hofmann H, Babadagli T, Zimmermann G. A grain based modeling study of fracture branching during compression tests in granites. *Int J Rock Mech Min Sci.* 2015;77: 152–162.
- 3. Vora HB, Morgan JK. Microscale Characterization of Fracture Growth and Associated Energy in Granite and Sandstone Analogs: Insights Using the Discrete Element Method. *J Geophys Research: Solid Earth.* 2019;124(8): 7993–8012.
- 4. Cho N, Martin CD, Sego DC. A clumped particle model for rock. Int J Rock Mech Min Sci. 2007;44(7): 997 1010.
- 5. Hazzard JF, Young RP. Moment tensors and micromechanical models. *Tectonophysics*. 2002;356(1-3): 181-197.
- 6. Zhang XP, Wong LNY. Cracking Processes in Rock-Like Material Containing a Single Flaw Under Uniaxial Compression: A Numerical Study Based on Parallel Bonded-Particle Model Approach. *Rock Mech and Rock Engineering*. 2012;45: 711–737.
- 7. Lisjak A, Grasselli G. A review of discrete modeling techniques for fracturing processes in discontinuous rock masses. *J of Rock Mech. and Geotechnical Engineering*. 2014;6(4): 301–314.
- 8. Shunying Ji and Shaocheng D. Discrete element modeling of acoustic emission in rock fracture. *Theor & Appl Mech Lett.* 2013;3(2): 021009.
- 9. Lu JM, Li CF, Cao GC, Hu SM. Simulating Fractures with Bonded Discrete Element Method. *IEEE Transactions on Visualization and Computer Graphics*. 2022;28(12): 4810–4824
- 10. Munkholm L, Balling O, Serban R, Negrut D, Heck R, Green O. Modeling soil aggregate fracture using the discrete element method. *Soil and Tillage Research*. 2022;218: 105295
- 11. Tomac I, Gutierrez M. Micromechanics of hydraulic fracturing and damage in rock based on DEM modeling. *Granular Matter*. 2020;22: 56.
- 12. Segerlind L. Applied Finite Element Analysis. John Wiley & Sons Inc; 1984.
- 13. Erhunmun E., Ikponmwosa U. Review on Finite Element Method. *Journal of Applied Sciences and Environmental Management*. 2017;21(5): 999–1002.
- 14. Borovkov AI, Maslov LB, Zhmaylo MA, Tarasenko FD, Nezhinskaya LS. Finite element analysis for prediction of femoral component strength in hip joint endoprosthesis made from meta-biomaterial. *Materials Physics and Mechanics*. 2024;52(6): 38–60.
- 15. Potyondy DO, Cundall PA. A bonded-particle model for rock. *Int J Rock Mech Min Sci.* 2004;41(8): 1329–1364.

- 16. Korsukov VE, Ankudinov AV, Betekhtin VI, Butenko PN, Verbitskii VN, Hilarov VL, Hilarov IV, Knyazev SA, Korsukova MM, Obidov BA. Dynamics of the surface morphology of a tungsten foil under load. *Phys. Solid State.* 2020;62: 2249–2257.
- 17. Obidov BA, Korsukov VE, Hilarov VL, Ankudinov AV, Butenko PN, Knyazev SA, Korsukova MM. Multifractal properties of the molybdenum ribbon surface at mechanical loading. *Phys. Solid State.* 2022;64: 925–928.
- 18. Gibowicz SJ, Lasocki S. Seismicity induced by mining: Ten years later. Advances in Geophysics. 2001;44: 39–181.
- 19. Kasimova VA, Kopylova GN, Lyubushin AA. Variations in the Parameters of Background Seismic Noise during the Preparation Stages of Strong Earthquakes in the Kamchatka Region. *Izvestiya Physics of the Solid Earth*. 2018;53: 269–283.
- 20. Ivanov PCh, Amaral NLA., Goldberger AL, Havlin S, Rosenblum MG, Struzikk ZR, Stanley HE. Multifractality in human heartbeat dynamics. *Nature*. 1999;399: 461–465.
- 21. Jiang J-Q, Xie W-J, Zhou W-X, Sornette D. Multifractal analysis of financial markets: a review. *Rep Prog Phys.* 2019;82(12): 125901.
- 22. Hilarov VL. On the fractal self-organization of the financial time series. J Digit Sci. 2022;4(1): 71-77.
- 23. Zhukov S. Personality and Society in the Theory of Self-Organized Criticality. *Changing Societies & Personalities*. 2023;7(2): 10–33.
- 24. Dosta M, Skorych V. MUSEN: An open-source framework for GPU-accelerated DEM simulations. *SoftwareX*. 2020;12: 100618.
- 25. Hilarov VL, Damaskinskaya EE. Modeling of fracture and acoustic emission in polycrystalline solids with the discrete elements method. *Phys Sol. State.* 2022;64(6): 664–669.
- 26. Tél T, Fulop A, Vicsek T. Determination of fractal dimension for geometrical multifractals. *Physica A: Statistical Mechanics and its Applications*. 1989;159(2): 155–166.
- 27. Viscek T. Mass multifractals. *Physica A: Statistical Mechanics and its Applications*. 1990;168(1): 490–497.
- 28. Lopes R, Betrouni N. Fractal and multifractal analysis: A review. *Medical Image Analysis*. 2009;13(4): 634–649.
- 29. Hilarov VL, Damaskinskaya EE. Fractal features of fracture centers in heterogeneous materials revealed by discrete element method. *Materialwissenschaft und Werkstofftechnik*. 2023;54(12): 1554–1559.
- 30. Lockner DA, Byerlee JD, Kuksenko V, Ponomarev A, Sidorin A. Quasi-static fault growth and shear fracture energy in granite. *Nature*. 1991;350: 39–42.
- 31. Hilarov VL. Self-Similar crack generation effects in the fracture process in brittle materials. *Modeling Simul Mater Sci Eng.* 1998;6: 337 342.

Submitted: November 6, 2024

Revised: December 10, 2024

Accepted: February 24, 2025

Influence of free surface on melting and crystallization in nickel and copper: molecular dynamics simulation

G.M. Poletaev ¹ D, Y.V. Bebikhov ² A.S. Semenov ² R.Y. Rakitin ³ D, D.V. Novoselova ⁴ D

ABSTRACT

The influence of free surface on melting and crystallization processes in nickel and copper was studied using molecular dynamics simulation. It was shown that crystallographic orientation of the surface and, accordingly, the energy of atoms on the surface affect the melting onset temperature of the simulated metal cell. The melting onset temperatures from the surface are arranged in the following order of increase for the considered orientations: (110), (112), (100), (111). When studying the formation of crystalline nuclei during gradual cooling from the molten state, it was found that most of the nuclei are formed near the surface. The orientation of the crystal structure in the nuclei near the surface in most cases was such that the crystalline plane (111) was formed on the surface, which is the most energetically favorable.

KEYWORDS

molecular dynamics • melting • crystallization • surface

Citation: Poletaev GM, Bebikhov YV, Semenov AS, Rakitin RY, Novoselova DV. Influence of free surface on melting and crystallization in nickel and copper: molecular dynamics simulation. *Materials Physics and Mechanics*. 2025;53(1): 48–56.

http://dx.doi.org/10.18149/MPM.5312025 4

Introduction

The unique properties of metallic nanomaterials are largely due to the high volume fraction of surfaces and interfaces in them. One of these properties, important from the point of view of the operation and manufacturing technology of nanomaterials, is the dependence of the melting point on their effective size: grain size, film thickness, nanoparticle diameter. The so-called "size-dependent melting point depression phenomenon" has been most thoroughly studied for metallic nanoparticles. It is currently known that the melting point of round nanoparticles is inversely proportional to their diameter, which has been demonstrated both experimentally [1–5] and using molecular dynamics simulation [6–10], and also explained in theoretical works, in particular [11–16].

As for materials with a nanocrystalline structure, it was shown in [17–22] using molecular dynamics simulation that melting in them is not a homogeneous process; it usually begins from free surfaces and grain boundaries. A decrease in the average grain size in the aforementioned studies (in the range of sizes of about several nanometers) led to a decrease in the melting temperature of nanocrystalline Ag [18,19] and Al [20,21]. In [10,23], we also observed a decrease in the melting temperature for Ni nanoparticles



¹ Polzunov Altai State Technical University, Barnaul, Russia

² Polytechnic Institute of North-Eastern Federal University, Mirny, Russia

³ Altai State University, Barnaul, Russia

⁴ Kuzbass Institute of the Federal Penitentiary Service of Russia, Novokuznetsk, Russia

[™] qmpoletaev@mail.ru

with a nanocrystalline structure compared to single-crystal particles. The crystallographic parameters of the surface and interfaces should obviously affect the temperature at which melting begins to initiate on them; however, this issue remains open at present. It can be assumed that this is affected by the energy of defect formation or, more precisely, the difference in the potential energy of atoms in the material from the energy in an ideal crystal, since it is precisely by this value that one should expect a decrease in the heat of fusion, which, in turn, is proportional to the melting temperature. The most effective method for studying this issue at present is computer simulation, namely the molecular dynamics method.

This work is devoted to the study of the influence of the crystallographic orientation of the free surface on the melting onset temperature of the modeled metal using the molecular dynamics method. Nickel and copper are considered as metals, which, on the one hand, have a wide practical application, and, on the other hand, the various properties of which are well reproduced in molecular dynamics models. In addition, this work studies the influence of the free surface on the crystallization process during gradual cooling from the molten state. In [10,24], when studying the crystallization of nickel and copper nanoparticles, we noted that the surface affects the probability of formation of crystalline nuclei: crystalline nuclei more often appeared near the surface, and as the temperature decreased in [10], an increase in the probability of formation of nuclei near the surface was noted. Obviously, in this case, there is an effect of two competing factors. On the one hand, atoms near the surface are more mobile than in the volume, and structural rearrangements, including the formation of crystalline nuclei, occur comparatively faster. However, on the other hand, the atoms on the surface are in shallower potential wells, and they are less stable and leave these wells more easily due to thermal vibrations, which, on the contrary, reduces the probability of forming a stable crystalline nucleus. We previously observed the effect of the surface on the formation of crystalline nuclei in [10,24] using the example of round metal nanoparticles. In this work, in addition to melting, we focused on studying the influence of a flat surface on the crystallization process in nickel and copper.

Description of the model

To describe interatomic interactions in nickel in the molecular dynamics model, the EAM potential from [25] was used, and in copper – from [26]. These manybody EAM potentials were obtained based on comparison with experimental data and *ab initio* calculations for various properties of the metals under consideration. They reproduce well a wide range of their mechanical and structural-energetic properties [25–29], and have proven themselves well in various molecular dynamics studies, including the processes of melting, crystallization and self-diffusion in the melt [10,23,24,27,30].

The study was carried out using the software package for molecular dynamics calculations MDR [31]. The computational cells had the shape of a parallelepiped with the dimensions of approximately $28.2 \times 11.3 \times 18.3$ nm³ for nickel and $29.1 \times 11.7 \times 19.1$ nm³ for copper and contained about 380,000 atoms (Fig. 1). The boundary conditions along one axis were free (a free surface was modeled — the right and left edges of the computational cell in Fig. 1), and there were periodic conditions along the other two axes.

Four crystallographic surface orientations were considered: (100), (110), (111), and (112). Apart from the surface, the simulated fcc crystals of nickel and copper did not contain any defects. The NPT canonical ensemble in combination with the Nosé-Hoover thermostat was used in the model [30,32]. The time integration step in the molecular dynamics method was equal to 2 fs.

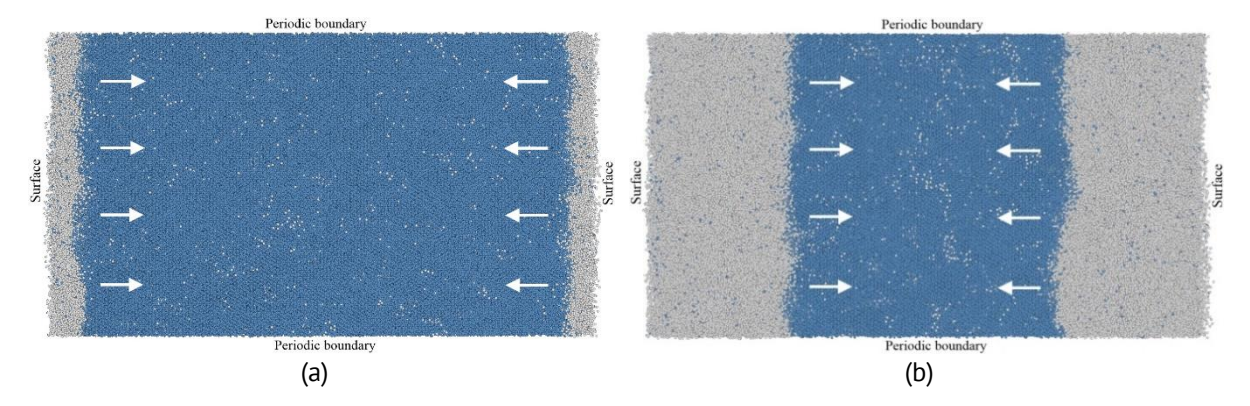


Fig. 1. Melting of the nickel computational cell from the (110) surface: (a) temperature 1770 K, time 30 ps; (b) temperature 1770 K, time 170 ps. Blue atoms represent the FCC crystal, while gray atoms represent the amorphous phase

Figure 1 shows an example of the movement of the melting front from the (110) surface in nickel using a crystalline phase visualizer based on the CNA (Common Neighbor Analysis) method [33], which clearly illustrates that melting starts from the surface. For different surface orientations, the destruction of the crystal structure on the surface and the beginning of the melting front movement occurred at different temperature values. To determine the melting temperature of the computational cell, the gradual heating method was used with the plotting of the average potential energy of the atom as a function of temperature, which is often used in similar problems [6–10,23,24,34]. In this case, the rate of temperature change is usually set from 10¹¹ to 10¹³ K/s. According to our previous works [10,23], the rate of 10¹² K/s turned out to be optimal for our research. In the model, the temperature was increased linearly by a corresponding increase in the moduli of the atomic velocities after a certain time step (5 ps in this case).

Results and Discussion

With a gradual increase in the temperature of the computational cell, upon reaching a certain value, the crystalline structure on the surface was destroyed (Fig. 1). Then the crystal-liquid front moved from the surface to the center of the computational cell at a speed of about several tens of meters per second, which, however, depended on the temperature and increased with its increase [35,36]. The influence of the orientation of the crystal-liquid front in the crystal on its speed and dependence on temperature was considered in [37–41], where it was noted, in particular, that the highest speed of the front movement is observed at the orientation (100) compared to the orientations (110) and (111).

Figure 2 shows the dependences of the average potential energy of an atom on temperature for the computational cells of nickel and copper with gradual heating. With

increasing temperature, the average energy of an atom for the same phase increases almost linearly due to an increase in atomic oscillation and thermal expansion. A sharp increase in the average energy of an atom on the graphs corresponds to a phase transition, i.e. melting. In this case, melting of the computational cell did not occur instantly, as was already mentioned above — the front propagated from the surface to the center of the cell with a finite velocity. Therefore, we determined the melting temperature based on the moment of the phase transition onset, which, in turn, was determined by the intersection of the approximation lines before and after the onset of melting. The speed of the front increased with increasing temperature, due to which the slope of the part on the graphs corresponding to the movement of the melting front is steeper at a higher temperature. Having reached a liquid state in the entire computational cell, the average energy of an atom again grew linearly with increasing temperature.

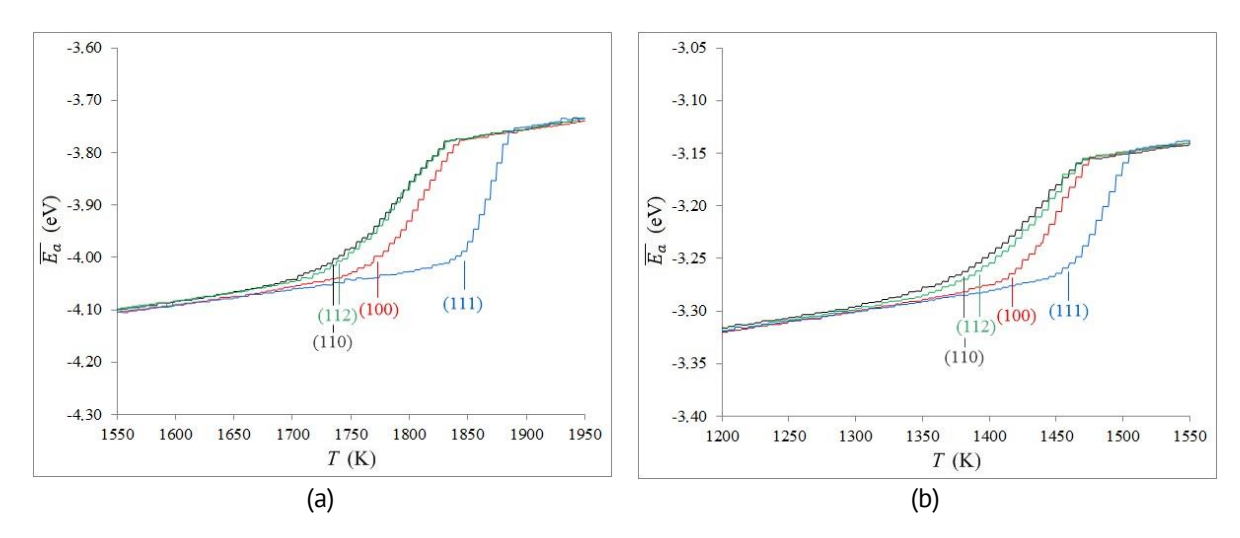


Fig. 2. Dependences of the average potential energy of an atom on temperature during heating for different surface orientations: (a) nickel; (b) copper

In Fig. 2, it is clearly seen that the orientation of the surface does influence the melting temperature of the computational cell. Moreover, this influence is quite strong in our case: the temperature at which melting began from the (111) surface was 6.5 % higher for nickel and 5.6 % higher for copper than the melting onset temperature from the (110) surface. It should be emphasized that the model is an idealized version, in which it is possible to single out one influencing factor and discard the others. The melting onset temperatures are arranged in the following order in ascending order: (110), (112), (100), (111). For nickel these are 1735, 1740, 1778, and 1847 K, respectively (Fig. 2(a)), for copper: 1381, 1393, 1417 and 1459 K (Fig. 2(b)).

Melting from the surface begins due to the comparatively easier destruction of the crystal structure on it, due to the fact that the atoms on the surface are in shallower potential wells compared to a pure crystal and it is easier for the atoms to leave them as a result of thermal vibrations. After the destruction of the structure on the surface, the formed front does not stand still (no static two-phase state was observed), it begins to move from the surface into the crystal volume. The atoms near the crystal-liquid front on the side of the crystal phase are also in comparatively shallower potential wells than in the crystal volume, due to the more disordered arrangement of the atoms on the side of

the melt. In addition, the melt has more intense self-diffusion and more free volume compared to the crystal, which is also the reason for the easier destruction of the crystal near the crystal-liquid front than inside the crystal volume, and the reason for the front movement.

To confirm all of the above, we constructed distributions of the average atomic energy depending on the distance from the surface for the crystalline state at a temperature of 300 K and at the moment of melting front movement (Fig. 3). In the second case, the crystalline structure was first destroyed from the surface and the front movement began, then the same temperature was set for all orientations (1770 K for nickel and 1380 K for copper) and the front movement was modeled to the same distance from the surface. This was done in order to then superimpose the energy distributions for different surface orientations under otherwise equal conditions. The distribution was constructed by calculating the average potential energy of an atom in layers 0.2 nm wide when moving with a step of 0.1 nm along the direction perpendicular to the surface.

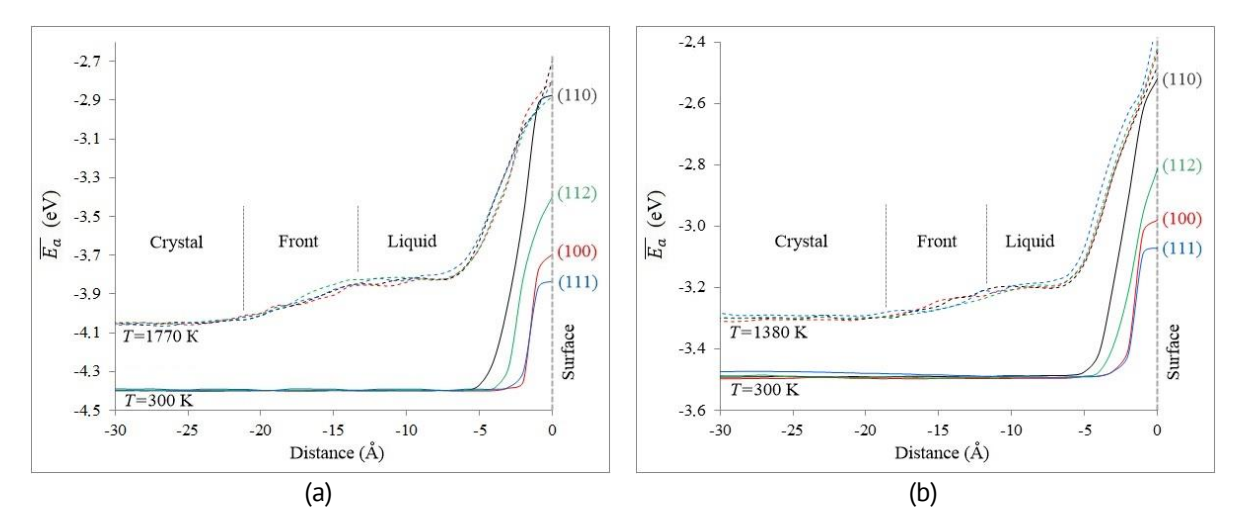


Fig. 3. Distributions of the average potential energy of an atom depending on the distance from the surface for the crystalline state at a temperature of 300 K and at the moment of movement of the melting front: (a) nickel; (b) copper

As can be seen, in the case of a crystalline state, the orientation of the surface significantly affects the average energy of an atom on the surface. Moreover, the average potential energy of an atom on the surface decreases in the same order among the considered orientations in which the melting onset temperature increases: (110), (112), (100), (111). The orientation of the surface affects the temperature at which the destruction of the crystalline structure begins, but further movement of the front, as was said above, depends on the temperature and the difference in energies in the crystalline and liquid phases. The front velocity, as noted in [37–41], depends on the orientation of the front relative to the crystal, but the distributions of the average atomic energy turned out to be identical for all considered orientations. In [41], it was suggested that the difference in the front velocity from the orientation in the crystal at the same temperature is due to different depths of the potential wells at the boundary of the forming crystal. Apparently, when calculating the average energy of all atoms in a layer (in our case the

layers were 0.2 nm thick), the orientation affects the range of values, but the average value itself is the same.

From the distributions shown in Fig. 3, one can estimate the width of the crystal-liquid front for the temperatures under consideration: approximately 0.8 nm for nickel at a temperature of 1770 K and 0.7 nm for copper at a temperature of 1380 K.

In addition to studying the influence of the surface on melting, this work also studied the influence of the surface on the process of initial formation of stable crystalline nuclei. As was already mentioned in the introduction, in this case there is an effect of two competing factors. On the one hand, self-diffusion on the surface and near it is higher than in the bulk of the material, i.e. all structural rearrangements near the surface should occur faster. However, on the other hand, the atoms on the surface are in shallower potential wells, due to which the position of such atoms is less stable than in the bulk, they more easily leave potential wells due to thermal vibrations, which, on the contrary, reduces the probability of formation of a stable crystalline nucleus.

In [10,24], when studying the crystallization of metal nanoparticles, we noted that crystallization most often begins from a free surface. In this paper, the formation of stable crystalline nuclei at the initial stage was studied using a rectangular computational cell with flat surfaces (Fig. 4). The computational cells for nickel and copper were the same as in the case of melting simulation, i.e., the boundary conditions along one axis were set as free, and along the other two, as periodic. First, the metal was melted by holding at a temperature above the melting point for a time sufficient to melt the entire volume of the computational cell. After this, gradual cooling was simulated. The forming crystalline nuclei were studied using a crystalline phase visualizer.

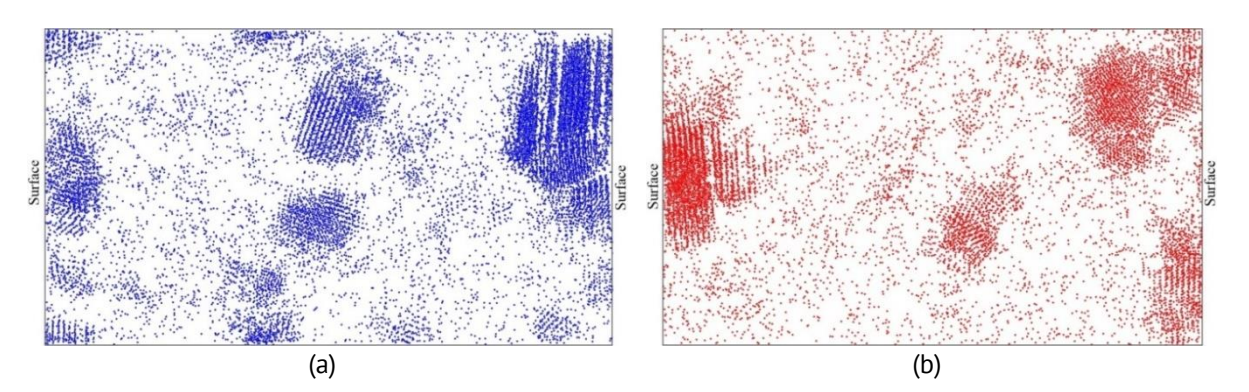


Fig. 4. Formation of crystalline nuclei during cooling of the melt at a rate of 10¹² K/s: (a) nickel; (b) copper

Figure 4 shows examples of crystal nuclei formed during cooling of the melt in nickel (Fig. 4(a)) and copper (Fig. 4(b)). As can be seen, a significant portion of the nuclei are indeed formed near the surface, but no clear dominance of the surface factor was observed: nuclei also arose far from the surface. It should be noted that the orientation in the nuclei near the surface was, as a rule, such that a crystal plane (111) was formed on the surface, which, as shown above, is the most energetically favorable.

For a more detailed study, distributions of the fraction of the crystalline structure in the computational cell were constructed. For nickel and copper, four different experiments were carried out, and the resulting distributions were superimposed on each other (Fig. 5). The distributions were constructed by calculating the fraction of atoms whose environment corresponded to the crystalline structure (mainly fcc, rarely hcp) in layers 0.2 nm wide when moving with a step of 0.1 nm along the direction perpendicular to the surface.

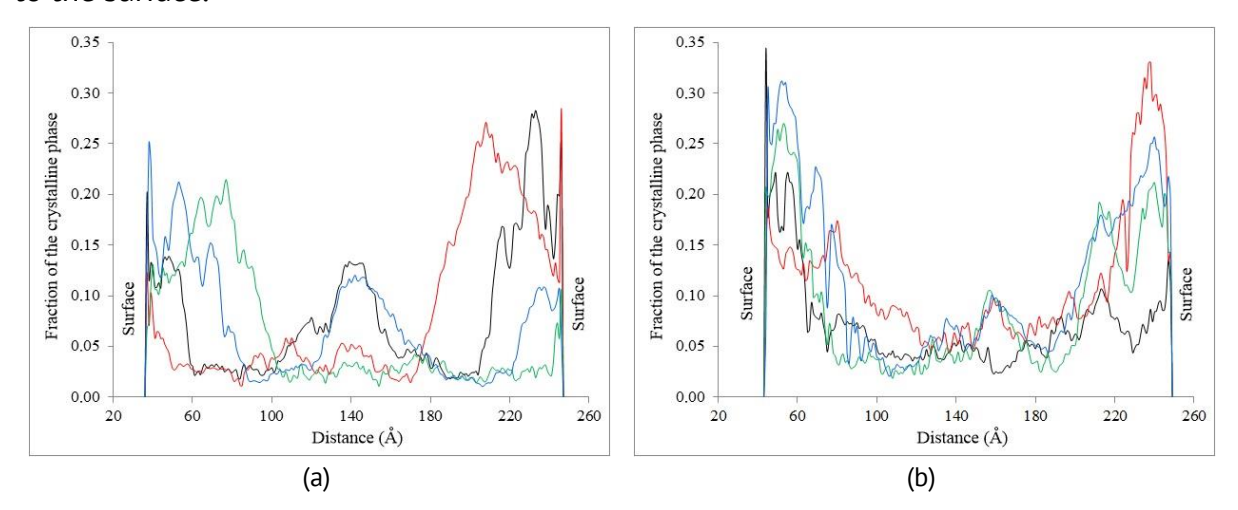


Fig. 5. Distribution of the fraction of the crystalline phase depending on the distance from the surface during the initial formation of stable crystalline nuclei: (a) nickel; (b) copper

As can be seen in Fig. 5, the fractions of the crystalline phase near the surface (on the left and right in the distributions) are indeed noticeably larger than in the volume of the computational cell. This was especially pronounced for copper (Fig. 5(b)). It can also be noted that the peaks of the distributions often do not coincide with the edge of the surface, but are located at some distance from it. This indicates that the centers of such nuclei are located at some distance from it, but, at the same time, their growth is due to the influence of the surface.

The two factors influencing the probability of crystalline nuclei formation and competing with each other, discussed above, more intense self-diffusion and relatively shallow potential wells, seem to make different contributions depending on the temperature. It can be assumed that at lower temperatures, for example, during the crystallization of metallic glasses, the so-called devitrification, an even more pronounced influence of the surface on the formation of the crystalline phase can be observed.

Conclusions

Using molecular dynamics simulation, the influence of the free surface on the processes of melting and crystallization in nickel and copper was studied. In the case of melting, the influence of the crystallographic orientation of the surface on the melting onset temperature of the simulated metal is considered. In the case of crystallization, the influence of the surface on the probability of the formation of stable crystalline nuclei during gradual cooling from the molten state was studied.

It is shown that with gradual heating, melting begins from the surface due to the comparatively easier destruction of the crystal structure on it, due to the fact that the atoms on the surface are in shallower potential wells compared to a pure crystal and it is easier for them to leave them as a result of thermal vibrations. In this case, the energy of surface atoms and the crystallographic orientation of the surface affect the melting onset

temperature: the lower the energy of surface atoms, the higher the melting onset temperature. For nickel and copper, the melting onset temperatures are arranged in the following order of increase for the orientations considered: (110), (112), (100), (111).

When studying the formation of crystalline nuclei during gradual cooling from the molten state, it was found that most of the nuclei were formed near the surface. The orientation in the nuclei near the surface was, as a rule, such that the crystalline plane (111) was formed on the surface, which is the most energetically favorable.

CRediT authorship contribution statement

Gennady M. Poletaev Scr: conceptualization, writing – review & editing, writing – original draft; Yuriy V. Bebikhov Scr: investigation, data curation; Alexander S. Semenov Scr: investigation, data curation; Roman Y. Rakitin Sc: investigation, data curation; Darya V. Novoselova Sc: investigation, data curation.

Conflict of interest

The authors declare that they have no conflict of interest.

References

- 1. Castro T, Reifenberger R, Choi E, Andres RP. Size-dependent melting temperature of individual nanometer-sized metallic clusters. *Physical Review B*. 1990;42: 8548–8556.
- 2. Dick K, Dhanasekaran T, Zhang Z, Meisel D. Size-denpendent melting of silica-encapsulated gold nanoparticles. *Journal of the American Chemical Society*. 2002;124: 2312–2317.
- 3. Hirasawa M, Orii T, Seto T. Size-dependent crystallization of Si nanoparticles. *Applied Physics Letters*. 2006;88: 093119.
- 4. Tang S, Zhu S, Lu H, Meng X. Shape evolution and thermal stability of Ag nanoparticles on spherical SiO₂ substrates. *Journal of Solid State Chemistry*. 2008;181: 587–592.
- 5. Kim HK, Huh SH, Park JW, Jeong JW, Lee GH. The cluster size dependence of thermal stabilities of both molybdenum and tungsten nanoclusters. *Chemical Physics Letters*. 2002;354: 165–172.
- 6. Qi Y, Cagin T, Johnson WL, Goddard III WA. Melting and crystallization in Ni nanoclusters: the mesoscale regime. *The Journal of Chemical Physics*. 2001;115: 385–394.
- 7. Shim JH, Lee BJ, Cho YW. Thermal stability of unsupported gold nanoparticle: a molecular dynamics study. *Surface Science*. 2002;512: 262–268.
- 8. Li X. Modeling the size- and shape- dependent cohesive energy of nanomaterials and its applications in heterogeneous systems. *Nanotechnology*. 2014;25: 185702.
- 9. Chepkasov IV, Gafner YY, Vysotin MA, Redel LV. A study of melting of various types of Pt-Pd nanoparticles. *Physics of the Solid State*. 2017;59: 2076–2081.
- 10. Poletaev GM, Gafner YY, Gafner SL. Molecular dynamics study of melting, crystallization and devitrification of nickel nanoparticles. *Letters on Materials*. 2023;13(4): 298–303.
- 11. Nanda KK, Sahu SN, Behera SN. Liquid- drop model for the size- dependent melting of low-dimensional systems. *Physical Review A.* 2002;66: 013208.
- 12. Qi WH, Wang MP, Zhou M, Shen XQ, Zhang XF. Modeling cohesive energy and melting temperature of nanocrystals. *Journal of Physics and Chemistry of Solids*. 2006;67(4): 851–855.
- 13. Luo W, Hu W, Xiao S. Size effect on the thermodynamic properties of silver nanoparticles. *The Journal of Physical Chemistry C*. 2008;112: 2359–2369.
- 14. Luo W, Deng L, Su K, Li K, Liao G, Xiao S. Gibbs free energy approach to calculate the thermodynamic properties of copper nanocrystals. *Physica B*. 2011;406: 859–863.
- 15. Li H, Han PD, Zhang XB, Li M. Size-dependent melting point of nanoparticles based on bond number calculation. *Materials Chemistry and Physics*. 2013;137: 1007–1011.

- 16. Zhu J, Fu Q, Xue Y, Cui Z. Accurate thermodynamic relations of the melting temperature of nanocrystals with different shapes and pure theoretical calculation. *Materials Chemistry and Physics*. 2017;192: 22–28.
- 17. Phillpot SR, Lutsko JF, Wolf D, Yip S. Molecular-dynamics study of lattice-defect-nucleated melting in silicon. *Physical Review B.* 1989;40: 2831.
- 18. Xiao S, Hu W, Yang J. Melting behaviors of nanocrystalline Ag. *The Journal of Physical Chemistry B*. 2005;109(43): 20339–20342.
- 19. Xiao S, Hu W, Yang J. Melting temperature: from nanocrystalline to amorphous phase. *Journal of Chemical Physics*. 2006;125(18): 184504.
- 20. Wejrzanowski T, Lewandowska M, Sikorski K, Kurzydlowski KJ. Effect of grain size on the melting point of confined thin aluminum films. *Journal of Applied Physics*. 2014;116(16): 164302.
- 21. Noori Z, Panjepour M, Ahmadian M. Study of the effect of grain size on melting temperature of Al nanocrystals by molecular dynamics simulation. *Journal of Materials Research*. 2015;30: 1648–1660.
- 22. Poletaev GM, Sitnikov AA, Yakovlev VI, Filimonov VY, Novoselova DV. Study of the melting nanocrystalline aluminum by the molecular dynamics method. *Materials Physics and Mechanics*. 2024;52(2): 106–113.
- 23. Poletaev GM, Bebikhov YV, Semenov AS. Molecular dynamics study of the formation of the nanocrystalline structure in nickel nanoparticles during rapid cooling from the melt. *Materials Chemistry and Physics*. 2023;309:128358.
- 24. Poletaev G, Gafner Y, Gafner S, Bebikhov Y, Semenov A. Molecular dynamics study of the devitrification of amorphous copper nanoparticles in vacuum and in a silver shell. *Metals*. 2023;13(10): 1664.
- 25. Purja Pun GP, Mishin Y. Development of an interatomic potential for the Ni-Al system. *Philosophical Magazine*. 2009;89: 3245–3267.
- 26. Williams PL, Mishin Y, Hamilton JC. An embedded-atom potential for the Cu-Ag system. *Modelling and Simulation in Materials Science and Engineering*. 2006;14: 817.
- 27. Levchenko EV, Ahmed T, Evteev AV. Composition dependence of diffusion and thermotransport in Ni-Al melts: a step towards molecular dynamics assisted databases. *Acta Materialia*. 2017;136: 74–89.
- 28. Muser MH, Sukhomlinov SV, Pastewka L. Interatomic potentials: achievements and challenges. *Advances in Physics: X.* 2023;8: 2093129.
- 29. Drewienkiewicz A, Zydek A, Trybula ME, Pstrus J. Atomic level insight into wetting and structure of Ag droplet on graphene coated copper substrate molecular dynamics versus experiment. *Nanomaterials*. 2021;11: 1465.
- 30. Poletaev GM, Bebikhov YV, Semenov AS, Starostenkov MD. Self-diffusion in melts of Ni-Al and Ti-Al systems: molecular dynamics study. *Letters on Materials*. 2021;11(4): 438–441.
- 31. Poletaev GM. *Molecular dynamics research (MDR)*. Certificate of state registration of a computer program No. 2015661912 dated 12 Nov 2015.
- 32. Poletaev GM, Starostenkov MD. Mutual diffusion at the interface in a two-dimensional Ni-Al system. *Technical Physics Letters*. 2003;29(6): 454–455.
- 33. Tsuzuki H, Branicio PS, Rino JP. Structural characterization of deformed crystals by analysis of common atomic neighborhood. *Computer Physics Communications*. 2007;177: 518–523.
- 34. Poletaev G., Rakitin R., Bebikhov Y., Semenov A. Molecular dynamics study of melting initiation at tilt grain boundaries depending on their misorientation angle in aluminum. *Physica Scripta*. 2025;100: 015988.
- 35. Chan W-L, Averback RS, Cahill DG, Ashkenazy Y. Solidification velocities in deeply undercooled silver. *Physical Review Letters*. 2009;102: 095701.
- 36. Zhang HY, Liu F, Yang Y, Sun DY. The molecular dynamics study of vacancy formation during solidification of pure metals. *Scientific Reports*. 2017;7: 10241.
- 37. Mendelev MI, Zhang F, Song H, Sun Y, Wang CZ, Ho KM. Molecular dynamics simulation of the solid-liquid interface migration in terbium. *The Journal of Chemical Physics*. 2018;148: 214705.
- 38. Zhang HY, Liu F, Yang Y, Sun DY. The molecular dynamics study of vacancy formation during solidification of pure metals. *Scientific Reports*. 2017;7: 10241.
- 39. Mendelev MI, Rahman MJ, Hoyt JJ, Asta M. Molecular-dynamics study of solid-liquid interface migration in fcc metals. *Modelling and Simulation in Materials Science and Engineering*. 2010;18: 074002.
- 40. Sun DY, Asta M, Hoyt JJ. Kinetic coefficient of Ni solid-liquid interfaces from molecular-dynamics simulations. *Physical Review B*. 2004;69: 024108.
- 41. Poletaev GM, Karakulova IV, Rakitin RY. Crystallization front motion velocity in nickel depending on orientation and supercooling temperature: molecular dynamics simulation. *Russian Physics Journal*. 2022;65(8): 1323–1327.

Accepted: January 22, 2025

Submitted: November 13, 2024

Revised: December 6, 2024

Thermal cycling stability of the martensitic transformation in $Ti_{40.7}Hf_{9.5}Ni_{49.8-x}Cu_x$ (x = 1, 5 or 10 at. %) cast alloys

I.V. Ponikarova ¹, M.E. Trofimova ¹, A.M. Ivanov ¹, R.M. Bikbaev ¹

ABSTRACT

The martensitic transformation and the defect density variation were studied during 500 thermal cycles of the $Ti_{40.7}Hf_{9.5}Ni_{49.8-x}Cu_x$ shape memory alloys with various copper concentration (x = 1, 5 or 10 at. %). It was found that regardless the Cu content, the transformation temperatures decreased on thermal cycling. An increase in the Cu concentration led to alloys hardening but it did not improve thermal cycling stability. The variation in the defect density on thermal cycling did not correlate with the yield limit for dislocation slip measured in samples before cycling. The variation in the defect density variation did not correlate with the variation in the transformation temperatures on thermal cycling. This showed that the variation in defect density was not the only reason for the variation in the transformation temperatures on thermal cycling of cast Ti-Hf-Ni-Cu alloys.

KEYWORDS

shape memory alloys • thermal cycling stability • martensitic transformation • alloy hardening

Funding. This work has been supported by the grant of the Russian Science Foundation, RSF 23-19-00280.

Acknowledgements. The research was carried out using the equipment of the resource centers of the St. Petersburg State University Scientific Park "X-ray Diffraction research methods".

Citation: Resnina NN, Belyaev SP, Bazlov AI, Sibirev AV, Ponikarova IV, Trofimova ME, Ivanov AM, Bikbaev RM. Thermal cycling stability of the martensitic transformation in Ti40.7Hf9.5Ni49.8-xCux (x = 1, 5 or 10 at. %) cast alloys. *Materials Physics and Mechanics*. 2025;53(1): 57–67. http://dx.doi.org/10.18149/MPM.5312025_5

Introduction

NiTi-based shape memory alloys are the smart materials which are widely used in various technological branches. One of the most frequent applications is the actuators of repeat action which are applicable for car, aircraft, space and other industries [1–3]. The repeat action actuators usually consist of the pre-deformed shape memory alloy element which is connected to the elastic counter-body. On heating through the temperature range of the reverse martensitic transformation, the shape memory effect occurs and the strain recovers in the shape memory element. This leads to the deformation of the counter-body and the recovery stress appears in the system. On cooling through the temperature range of the forward martensitic transformation, the counter-body deforms the shape memory element, its strain increases, while the recovery stress decreases. On next heating, the described procedure repeats so, the recoverable strain and stress variation take place on thermal cycling [2,3]. For the actuators, the thermal cycling stability is the key factor



¹ St. Petersburg State University, St. Petersburg, Russia

² National University of Science and Technology "MISIS", Moscow, Russia

[™] resnat@mail.ru

because the device must demonstrate the stable stress and strain variation in the same temperature range during the life-time period [4].

The NiTi-based shape memory alloys are the best candidates for the actuators because they demonstrate the best combination of the functional and operating properties such as high recovery strain and stress, high strength and corrosion resistance [5]. However, their thermal cycling stability is weak so, the recovery stress and strain as well as the temperatures of the strain and stress variation significantly change on thermal cycling [6-19]. Moreover, the plastic strain accumulates during thermal cycling that changes the geometrical sizes of the shape memory element and affects the recovery strain and stress [7,9,11,14]. The reason for the plastic strain accumulation is a high local stress appears on a growth of the martensite plate on cooling that leads to the local dislocation slip and increases the dislocation density [12,13,16-18]. One believes, that this is the reason for a weak thermal cycling stability of the martensitic transformation, that reveals as a decrease in the transformation temperatures of the forward and reverse transformations [12,13,16,18]. Thus, the alloy hardening, such as preliminary deformation, the precipitate hardening and a decrease in grain size is usually used to improve the thermal cycling stability of the martensitic transformation on thermal cycling of NiTi-based alloys [19–21].

The solid solution hardening is also used to improve the thermal cycling stability. Usually, the NiTi-based alloys are doped by third element, such, as Hf, Zr, Fe, Cu elements, which dissolve in the NiTi solid solution that increases the yield limit for dislocation slip. Last time, the quaternary Ti-Hf-Ni-Cu shape memory alloys were developed [22-27]. In [24,25], it was shown that the thermal cycling stability of the martensitic transformations in the cast Ti-Hf-Ni-Cu alloy with a 5 at. % of Hf and Cu atoms was better than in binary NiTi. In [27], it was found, that thin ribbons of Ti-Hf-Ni-Cu alloys with 9.5 at. % of Hf and various Cu content $(Ti_{40.7}Hf_{9.5}Ni_{44.8}Cu_5)$ and $Ti_{40.7}Hf_{9.5}Ni_{39.8}Cu_{10}$ demonstrated the prefect thermal cycling stability of the B2 ↔ B19' transformation. The temperatures of the martensitic transformation were constant during 50 thermal cycles that had never been found for binary NiTi alloy. One may assume that perfect stability is caused by the solid solution hardening induced by the presence of the Hf and Cu atoms, which act as substitutional defects. On the other hand, the perfect thermal cycling stability may be attributed to a small grain size because thin ribbons had an average grain size of 800 nm in [27]. The aim of the present paper was to study the variation in the martensitic transformation and defect density variation on thermal cycling of cast $Ti_{40.7}Hf_{9.5}Ni_{48.8}Cu_1$, $Ti_{40.7}Hf_{9.5}Ni_{44.8}Cu_5$ and $Ti_{40.7}Hf_{9.5}Ni_{39.8}Cu_{10}$ alloys. This allows one to clarify the influence of the Cu concentration in cast Ti_{40.7}Hf_{9.5}Ni_{49.8-x}Cu_x alloys on the alloy hardening and thermal cycling stability.

Materials and Methods

The $Ti_{40.7}Hf_{9.5}Ni_{49.8-x}Cu_x$ alloys (x = 1, 5 or 10 at. %) were produced in a vacuum arc furnace under an argon atmosphere purified by a Ti getter. The chemical composition of the alloy is correspond to the composition of the casting charge. High-purity single metals (99.9 wt. %) were used as raw materials. Each ingot with a mass of 20 g and a diameter

of 20 mm were turned over and remelted five times to obtain a homogeneous composition. For convenience, the alloys were labeled as Cu-1, Cu-5, Cu-10.

The structure was studied by X-ray diffraction (XRD) analysis at room temperature (Rigaku MiniFlex, $Cu_{K\alpha}$ radiation, θ -20 mode). The martensitic transformations were studied by differential scanning calorimetry (Mettler Toledo 822e) on cooling and heating in a temperature range from 200 to -100 °C with a rate of 10 °C/min. The resistivity (in the regime of the direct current) was measured by 4-probes technique on cooling and heating in the same temperature range using the self-made stand including two nanovoltmeters and one source of direct current. The samples for DSC study with a size of $3 \times 3 \times 1$ mm³ and samples for resistivity measurement with a size of $20 \times 1 \times 0.3$ mm³ were cut by electro-discharge machine from ingots.

The samples were subjected to 500 thermal cycles and the resistivity vs temperature curves were measured in the 1st, 10th, 20th, 30th, 40th, 50th, 75th, 100th, 200th, 300th, 400th and 500th cycles. Between these cycles, samples were thermal cycled by holding in the furnace at 200 °C for 40 s and holding in liquid nitrogen for 40 s.

To study whether the Cu content leads to alloy hardening, the samples were subjected to tension at a temperature of A_f + 50 °C (in the austenite state) before thermal cycling. Dog-bone samples with a size of gauge area of $7 \times 1 \times 0.8$ mm³ were cut by discharge machine from ingots, installed to the inter-grips which were fixed in the standard grips of the testing machine (Lloyd 30k Plus, Shimadzu 50kN-AG) equipped with a thermal chamber. The sample was heated to chosen temperature, hold for 40 min for homogenization of the temperature in the samples and grips and deformed by tension up to fracture. The stress was measured by standard cell, the strain was detected by video extensometer as the variation in distance between two white stripes drawn on the black sample surface.

Results and Discussion

Figure 1 shows the XRD patterns obtained at room temperature. The diffraction peaks of the B19' martensite phase can be observed, hence all alloys underwent the B2 \rightarrow B19' transformation on cooling to room temperature. Among the reflexes of main phase, weak reflexes of the Ti₂Ni-type precipitates were found.

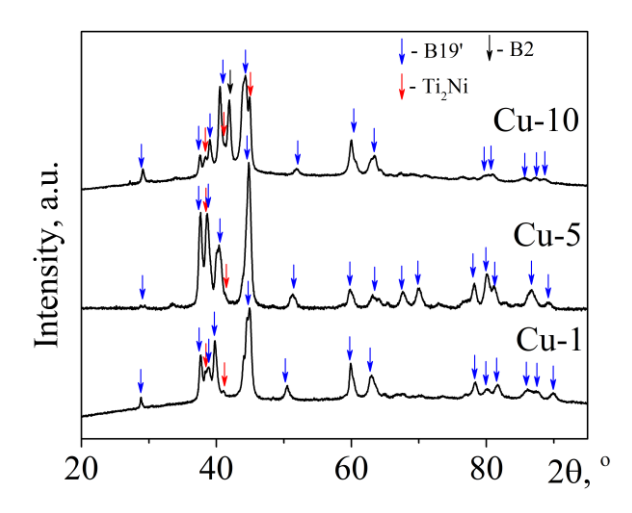


Fig. 1. XRD patterns of the Cu-1, Cu-5 and Cu-10 samples measured at room temperature

Figure 2 shows the calorimetric and resistivity curves found on the first cooling and heating of the $Ti_{40,7}Hf_{9,5}Ni_{49,8-x}Cu_x$ alloys. It is seen that in all samples, a peak of the heat release was found on cooling and a peak of heat absorption was observed on heating due to the B2 \leftrightarrow B19' transformation. In Cu-10 sample, the M_f temperature was less than room temperature that was why the austenite reflexes were observed on the XRD pattern (Fig. 1). The resistivity curves showed the anomalous behavior on cooling and heating: the resistivity increased on cooling due to the forward B2 \rightarrow B19' transformation; and it decreased on heating during the reverse B19' \rightarrow B2 transformation. It is seen that the temperatures of the anomalous on the ρ (T) curves were the same as the temperatures of the peak on the calorimetric curves. Thus, using the ρ (T) curves, one may determine the transformation temperatures as well as the absolute value of the resistivity which reflects the defect density.

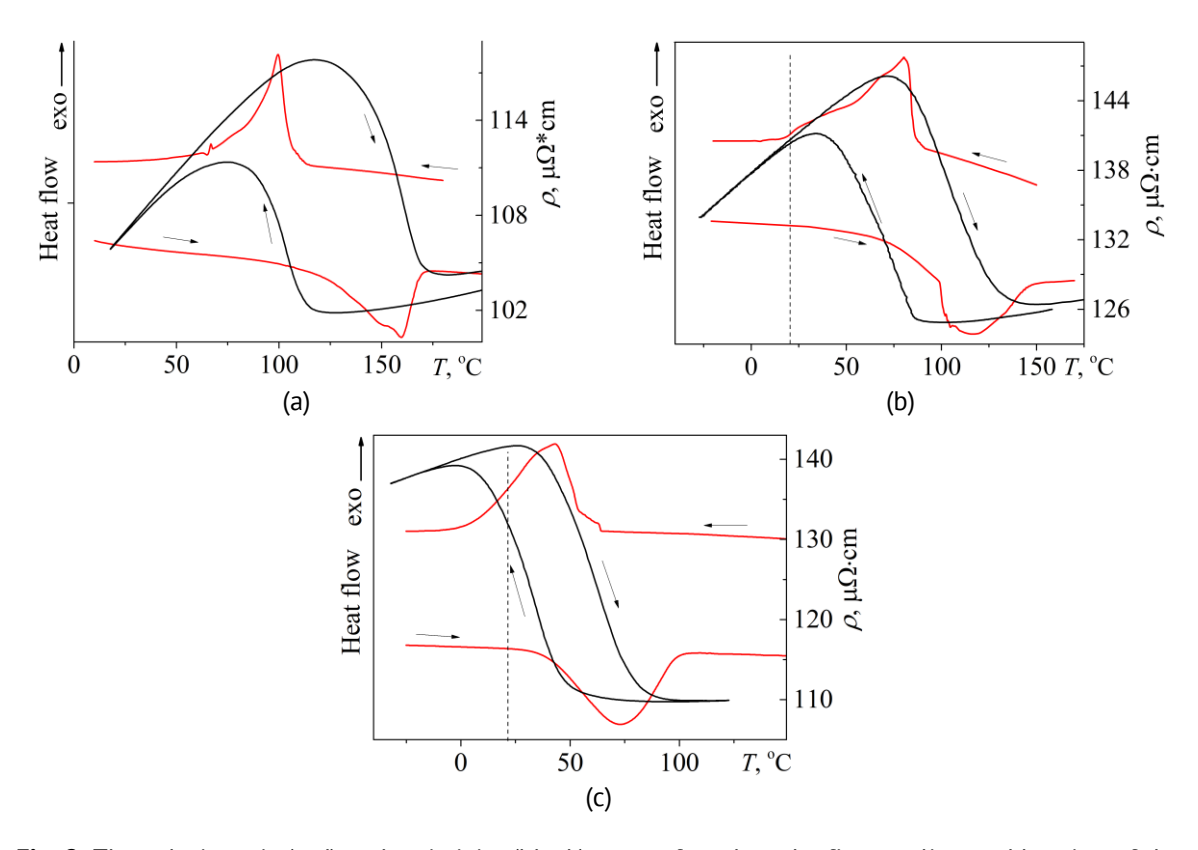


Fig. 2. The calorimetric (red) and resistivity (black) curves found on the first cooling and heating of the cast Cu-1 (a), Cu-5 (b) and Cu-10 (c) alloys. Dash line shows the room temperature

Figure 3 shows the ρ (T) curves found in the 1st, 10th, 100th and 500th thermal cycles in the samples with various Cu content. It is seen that the ρ (T) curves shifts on thermal cycling in different manner depending on Cu content. In Cu-1 alloy, an increase in thermal cycle number (N) from 1st to 100th shifted the ρ (T) curves to high resistivity value and low temperatures. Further increase in cycle number to 500th cycle shifted the ρ (T) curve to low resistivity (Fig. 3(a)). In Cu-5 and Cu-10 alloy, the ρ (T) curves shifted to high resistivity value and low temperatures during 500 thermal cycles. However, it is seen that in Cu-5 alloy, the ρ (T) curves measured in the 100th and 500th cycles were close to each other (Fig. 3(b)), hence the thermal cycling from the 100 to 500 cycles had a small effect

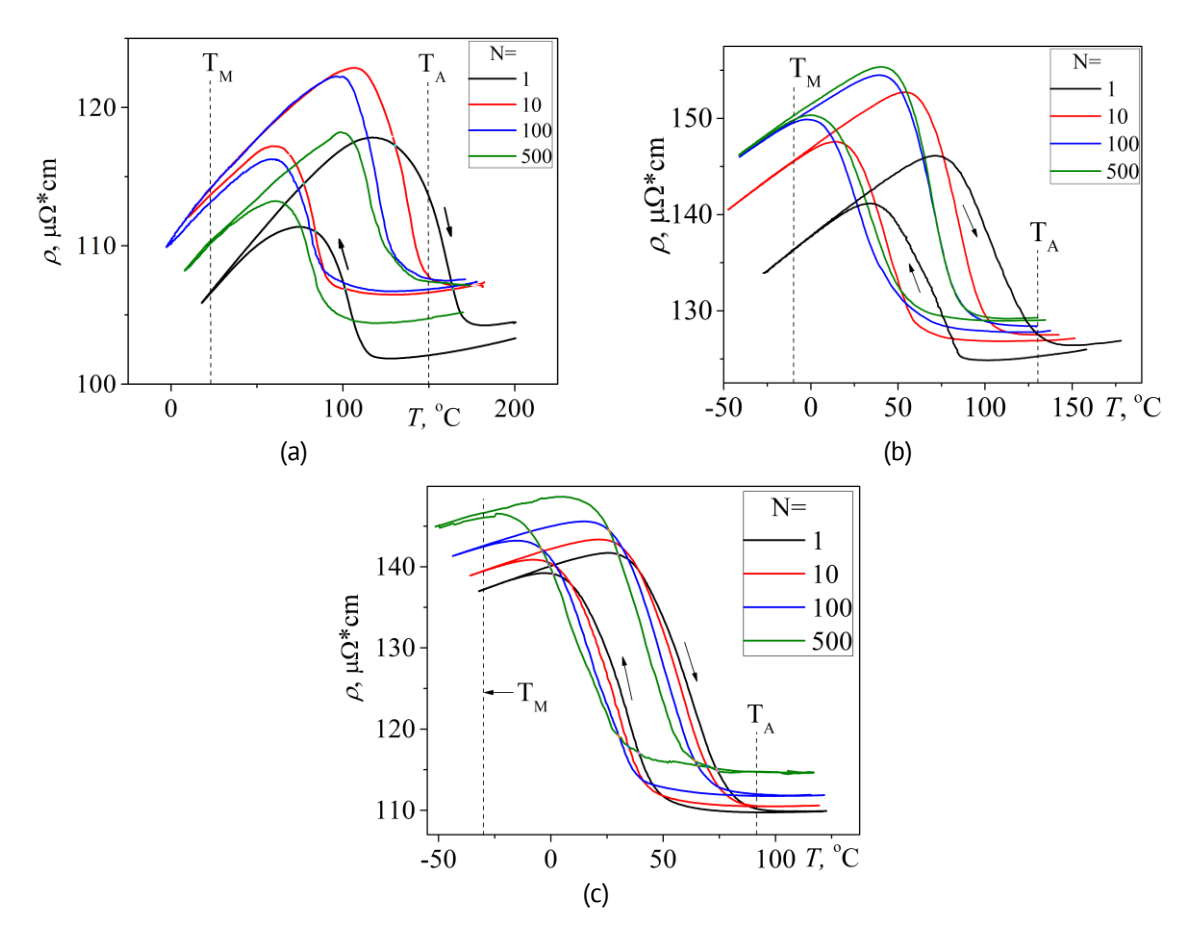


Fig. 3. The resistivity vs temperature curves measured for Cu-1 (a), Cu-5 (b) and Cu-10 (c) alloys in the 1^{st} , 10^{th} , 100^{th} and 500^{th} thermal cycle

on the defect density in this alloy. In Cu-10 alloy, thermal cycling from 100 to 500 cycles considerable shifted the ρ (T) curve to high resistivity and low temperatures (Fig. 3(c)).

Using the $\rho(T)$ curves, the transformation temperatures were determined as intersection of tangent lines and their dependences on the thermal cycle number are given in Fig. 4. First of all, contrary to the results found for ribbons in [27], the cast alloys with the same chemical composition did not demonstrate the stability of the martensitic transformation temperatures on thermal cycling. In Cu-1 and Cu-5 alloys (Fig. 4(a,b)), the transformation temperatures decreased during the first 100 – 200 cycles and then slightly increased (the exception was found in Cu-5 alloy, where the A_f temperature and the M_f temperature were constant at N > 200). For instance, in Cu-1 alloy, the M_s temperature was equal to 113 °C in the 1st cycle to 90 °C in the 100th cycle and 92 °C in the 500th cycle. At the same time, the A_s temperature was equal to 136 °C in the 1st cycle, 102 °C in the 200th cycle and 106 °C in the 500th cycle. In Cu-5 alloy, the M_s temperature was equal to 79 °C in the 1st cycle, 52 °C in the 100th cycle and 55 °C in the 500th cycle. The A_s temperature was equal to 71 °C in the 1st cycle, 48 °C in the 200th and 51 °C in the 500th cycles. In Cu-10 alloy, the transformation temperatures decreased during 500 cycles without saturation (Fig. 4(c)). So, during 500 cycles, the M_s temperature dropped from 48 to 35 °C, whereas the A_s temperature decreased from 37 to 20 °C. Thus, it is seen that the different temperatures changes on thermal cycling in different ways and it is hardly affected by the Cu concentration. So, Cu-10 alloy showed the minimum variation

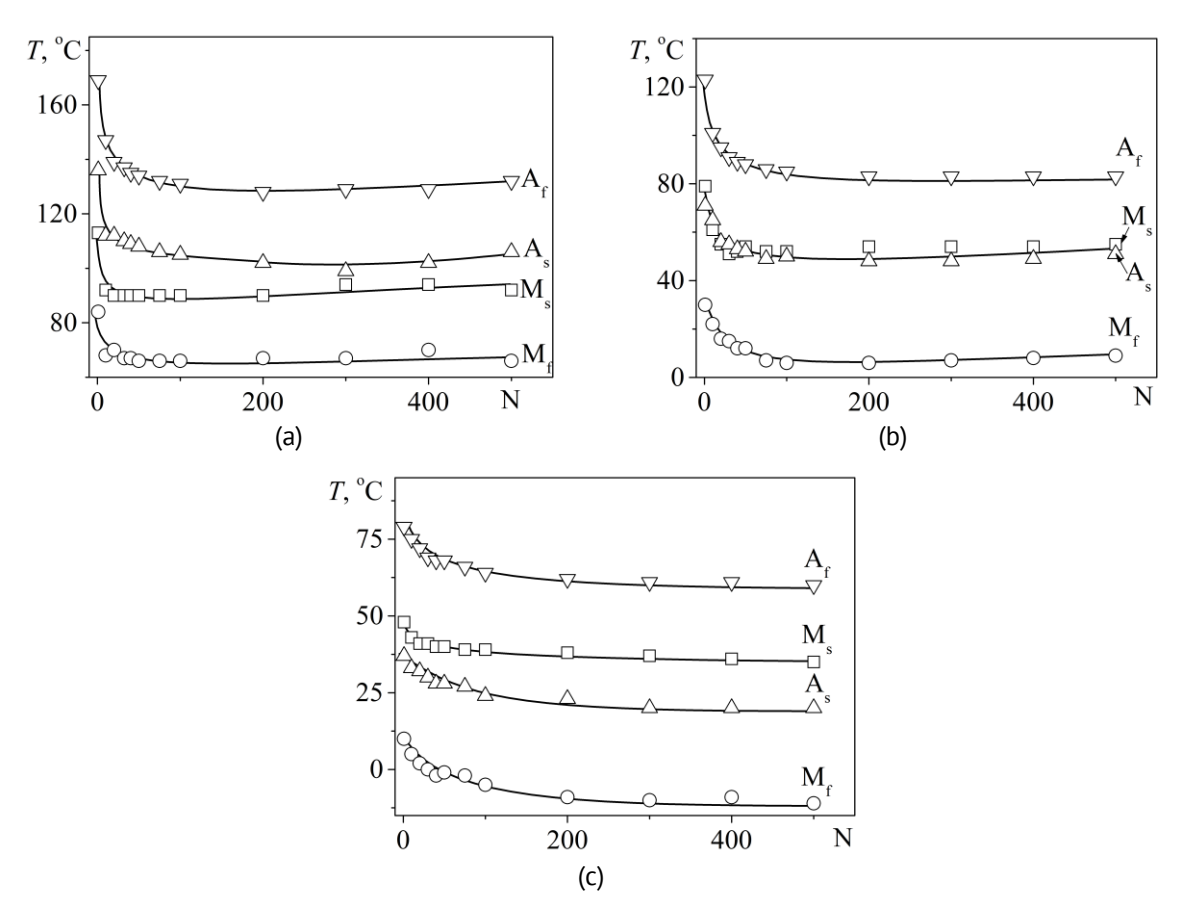


Fig. 4. The variation in transformation temperatures on thermal cycling of the Cu-1 (a), Cu-5 (b) and Cu-10 (c) alloys

in M_s temperature compared to the Cu-1 and Cu-5 samples, while the variation in the A_s temperature in Cu-10 and Cu-5 alloys were comparable and less than in Cu-1 alloy.

The resistivity values (ρ_A and ρ_M) were measured in a pure austenite state at the T_A temperature and pure martensite state at the T_M temperatures as shown by dash line in Fig. 3. As the absolute resistivity value depends on the defect density, hence the variation in the ρ_A and ρ_M values on thermal cycling shows the variation in defect density. The $\rho_A(N)$ and $\rho_M(N)$ curves for all samples are shown in Fig. 5. In Cu-1 sample, both the ρ_A and ρ_M values rapidly increase during first 10 cycles. The resistivity hardly changes from the 10^{th} to the 100^{th} cycle in the martensite state or from 10^{th} to 200^{th} cycle in the austenite state. At N > 100 (200) cycles, the resistivity decreases (Fig. 5(a)). The larger the Cu content in the alloy, the more cycles is taken for rapid increase in the resistivity. It occurs within 30 cycles in Cu-5 sample (Fig. 5(b)), and 80 cycles in Cu-10 sample (Fig. 5(c)).

To study the influence of the Cu content on the limit for dislocation slip, the samples were subjected to tension in the austenite state (at $T = A_f + 50$ °C) up to failure (Fig. 6) and the yield limit for dislocation slip was measured as $\sigma_{0.2}$ value. This value was equal to 480 MPa for Cu-1 alloy, 580 MPa for Cu-5 alloy and 730 MPa for Cu-10 alloy. According to SEM study which was not included in this paper, the volume fraction of precipitates did not change on a rise in the Cu concentration, hence an increase in $\sigma_{0.2}$ value on a rise in Cu content was caused by solid solution hardening.

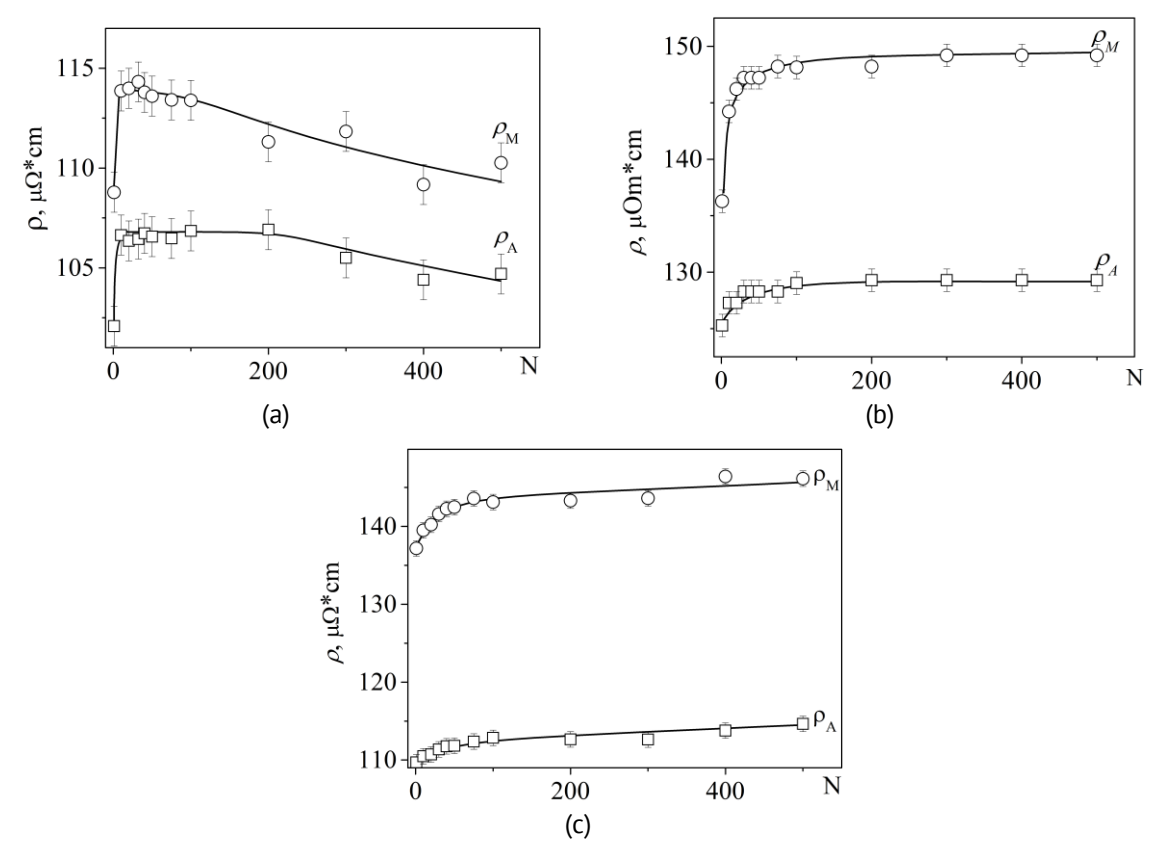


Fig. 5. The variation in the ρ_A and ρ_M values on thermal cycling of the Cu-1 (a), Cu-5 (b) and Cu-10 (c) alloys

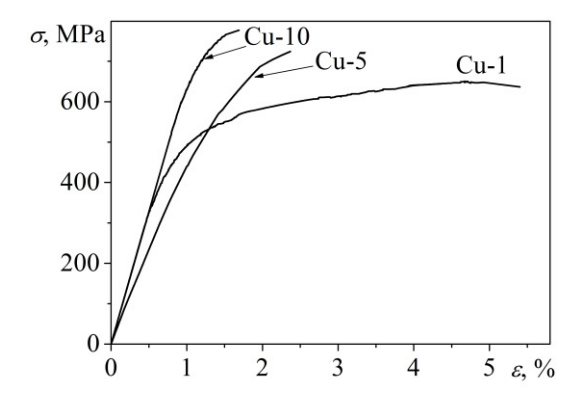


Fig. 6. Engineering stress vs strain curves of the Cu-1, Cu-5 and Cu-10 samples measured in the austenite state at $T = A_f + 50$ °C

The results of this study showed that the cast $Ti_{40.7}Hf_{9.5}Ni_{49.8-x}Cu_x$ alloys (x = 5 or 10 at. %) did not demonstrate the stability of the martensitic transformation contrary to the ribbons with the same composition which showed the perfect stability in [27]. One may assume that the main reason for different thermal cycling stability in cast and ribbon samples was the grain size which was 0.8 μ m in ribbons and 130–150 μ m in cast samples. The larger the grain size, the less the dislocation yield limit according to Hall-Petch law and the more intensive dislocation density variation on thermal cycling.

According to [18,28,29], an increase in dislocation density gives an additional term to the elastic energy which is included in the thermodynamic balance for the forward

martensitic transformation: $\Delta G^{A \to M} = E_d + E_{el}^{A \to M} + E_{el}^d$, where $\Delta G^{A \to M}$ is the increment in Gibbs energy during transformation, E_d is a dissipative energy which is responsible for hysteresis, $E_{el}^{A \to M}$ is an elastic energy stored during transformation, E_{el}^d is an elastic energy associated with the defect density [28]. If the defect density increases on thermal cycling, hence the E_{el}^d term increases and the larger increment in Gibbs energy must be provided to overcome the sum of dissipative and elastic energy and to start the martensitic transformation. This may be realized by overcooling that is why the start temperature of the martensitic transformation decreases on a rise in the defect density during thermal cycling.

One may assume that the dislocation density variation must depend on the yield limit for the dislocation slip ($\sigma_{0.2}$). It is obvious that in the alloys with a high $\sigma_{0.2}$ value, the variation in the defect density must be less than in the alloys with a low $\sigma_{0.2}$ value. Table 1 shows that an increase in the Cu concentration in the Ti_{40.7}Hf_{9.5}Ni_{49.8-x}Cu_x alloys increases the yield limit for dislocation slip from 480 MPa in Cu-1 alloy to 730 MPa in Cu-10 alloy. So, one may expect that the variation in the defect density and the variation in the transformation temperatures must be the smallest in the Cu-10 sample and the largest in the Cu-1 alloy.

Table 1. Yield limit for dislocation slip, increment in the transformation temperatures, increment in ρ_M and

$\rho_{\!\scriptscriptstyle A}$ values during 500 cycles	III 1140.7H19.5IN149.8-xCUx alloyS
	C., 1

	Cu-1	Cu-5	Cu-10
$\sigma_{0.2}$, MPa	480	580	730
$\Delta \rho_{\rm M}^{500}$, μ Ω ·cm	5.5	12.9	9
$\Delta \rho_{\rm A}^{500}$, μ Ω ·cm	4.6	4	4.9
∆M _s ⁵⁰⁰ , °C	-21	-24	-13
<i>∆M_f</i> ⁵⁰⁰ , °C	-18	-21	-21
△A _s ⁵⁰⁰ , °C	-30	-20	-17
<i>∆A_f</i> ⁵⁰⁰ , °C	-37	-40	-19

Table 1 shows that the variation in resistivity measured in the martensite state was larger than in the austenite state in all alloys. This may be due to the resistivity variation in the austenite state depends on the variation in density of dislocation and point detect, while the resistivity in the martensite is additionally affected by the martensite twin structure which also changes on thermal cycling [30].

The resistivity increment measured in the austenite state during 500 thermal cycles was comparable for all alloys. The minimum value was 4 $\mu\Omega$ ·cm in Cu-5 sample, while the maximum value of 4.9 $\mu\Omega$ ·cm was measured in Cu-10 alloy (Table 1). At the same time, the error in resistivity value was equal to 1.1 $\mu\Omega$ ·cm (measured as the error for indirect measurement taking into account the errors in the length, current and voltage measurements). This means that the variation in the defect density in the austenite state is the same for all alloys and it does not depend on the yield limit for dislocation slip.

In the martensite state, the maximum increment in the resistivity is found in Cu-5 sample which has the medium value of the yield limit for dislocation slip, while the minimum increment in the resistivity is observed in Cu-1 sample with the smallest yield limit for dislocation slip. Hence, there is no correlation between the alloy hardening and the variation in defect density measured in the martensite state. Thus, the results of the

study show that the variation in the defect density on thermal cycling does not depend on the yield limit for dislocation slip measured in the alloys before thermal cycling. One may assume that the $\sigma_{0.2}$ value also changes on thermal cycling that affects the variation in the defect density.

To find the relation between the defect density variation and the transformation temperature variation, the increments in the resistivity and temperatures were analysed. One may assume that if the most of the alloy is in the austenite state at the M_s and A_f temperatures, hence these temperatures must depend on the defect density in the austenite state. Contrary, the A_s and M_f temperatures at which most of the alloy is in the martensite state must be affected by the defect density in the martensite state. Table 1 shows that the variation in defect density in the austenite state is the same in all alloys however, the variations in the M_s and A_f temperatures in Cu-1 and Cu-5 alloys are approximately 1.8 times larger than in Cu-10 sample. In the martensite state, the minimum resistivity variation is found in Cu-1 alloy and the maximum value is observed in Cu5 alloy. At the same time, the M_f temperature is approximately the same in all alloys, while the variation in A_s temperature in Cu-5 and Cu-10 alloys is in 1.5 times less than in Cu-1 alloy. Thus, the results of the paper clearly show that the variation in the transformation temperatures on thermal cycling has no relation with the variation in the defect density.

The comparison of the transformation temperature increments and the yield limit for dislocation slip shows that there is no ratio between these parameters. So, as it was mentioned above, the increment of the M_f temperature was the same in Cu-1 and Cu-10 alloy, while the difference in yield limit for dislocation slip was 1.5 times. The A_f increment in Cu-1 and Cu-5 alloys was the same, whereas the yield limit for dislocation slip in Cu-5 alloy was 100 MPa higher than in Cu-1 alloy.

Thus, the results of the study show that the defect density variation and the transformation temperatures change independently on thermal cycling and their variation does not depend on the yield limit for dislocation slip measured in the sample before thermal cycling. First, this means that the defect density variation is not the only reason for the variation in the transformation temperatures on thermal cycling in the NiTi-based alloys. Other reasons must be found that affect the thermal cycling stability of the martensitic transformations in NiTi-based alloys. The other main result is that the yield limit for dislocation slip measured in the sample before thermal cycling does not reflect the stability of the transformation temperatures. Hence, the chosen of the NiTi-based alloy with a high dislocation yield limit for application does not guarantee the high thermal cycling stability of the functional properties.

Conclusions

Thermal cycling stability of the martensitic transformations was studied in cast $Ti_{40.7}Hf_{9.5}Ni_{49.8-x}Cu_x$ alloys with various Cu concentrations. The analysis of the variation in the transformation temperatures, defect density and the yield limit for dislocation slip was carried out. The obtained results may be summarized as follows:

1. The variation in transformation temperatures on thermal cycling are different for the $Ti_{40.7}Hf_{9.5}Ni_{49.8-x}Cu_x$ alloys with various Cu concentration. If Cu concentration in the

 $Ti_{40.7}Hf_{9.5}Ni_{49.8-x}Cu_x$ alloy is equal to 1 or 5 at. %, transformation temperatures decrease during 100-200 cycles and then slightly increase. If Cu concentration is equal to 10 at. %, transformation temperatures decreased during 500 cycles without saturation. At the same time, the absolute increment in the transformation temperature hardly depended on the Cu concentration.

- 2. An increase in the Cu concentration leads to alloy hardening that increases the yield limit for dislocation slip in the austenite phase more than 1.5 times. However, it hardly affects the thermal cycling stability in cast $Ti_{40.7}Hf_{9.5}Ni_{49.8-x}Cu_x$ alloys
- 3. The variation in the defect density on thermal cycling does not correlate with the yield limit for dislocation slip measured in samples before cycling. The defect density variation measured in the austenite state is comparable in all alloys. The maximum defect density variation in the martensite state is found in the Cu-5 alloy with the medium yield limit for dislocation slip. The minimum defect density variation is observed in Cu-1 alloy with the smallest dislocation yield limit.
- 4. The change in the defect density does not correlate with the variation in the transformation temperatures on thermal cycling. This shows that the variation in defect density is not the only reason for the weak cycling stability of the martensitic transformation temperatures on thermal cycling of the NiTi-based alloys.

CRediT authorship contribution statement

Natalia N. Resnina (DSC): conceptualization, writing – original draft; Sergey P. Belyaev (DSC): conceptualization, writing – review & editing; Andrey I. Bazlov (DSC): investigation; Alexei V. Sibirev (DSC): investigation; Irina V. Ponikarova (DSC): investigation; Marina E. Trofimova: investigation; Aleksei M. Ivanov (DSC): investigation; Rashid M. Bikbaev (DSC): investigation.

Conflict of interest

The authors declare that they have no conflict of interest.

References

- 1. Razov Al. Application of titanium nickelide-based alloys in engineering. *Phys. Met. Metal.* 2004;97(1): 97–126. 2. Jani JM, Leary M, Subic A, Gibson MA. A review of shape memory alloy research, applications and opportunities. *Mater. Design.* 2014;56: 1078–1113.
- 3. Priadko AI, Pulnev SA, Kovalev OO, Ilin IA. Rotary actuator control based on tensile force elements made of shape memory Cu–Al–Ni crystals when operated in a cyclic mode. *Materials Physics and Mechanics*. 2019;42(4): 407–414.
- 4. Tobushi H, Date K, Miyamoto K. Characteristics and development of Shape-memory alloy heat engine. *Journal of Solid Mechanics and Materials Engineering*. 2010;4(7): 1094–1102.
- 5. Otsuka K, Ren X. Physical metallurgy of Ti-Ni-based shape memory alloys. *Progress in Materials Science*. 2005;50(5): 511–678.
- 6. Miyazaki S, Igo Y, Otsuka K. Effect of thermal cycling on the transformation temperatures of Ti-Ni alloys. *Acta Metallurgica*. 1986;34(10): 2045–2051.
- 7. Furuya Y, Park YC. Thermal cyclic deformation and degradation of shape memory effect in Ti-Ni alloy. *Nondestructive Testing and Evaluation*. 1992;8–9(1–6): 541–554.
- 8. Matsumoto H. Transformation behaviour with thermal cycling in NiTi alloys. *Journal of Alloys and Compounds*. 2003;350(1–2): 213–217.

- 9. Eggeler G, Hornbogen E, Yawny A, Heckmann A, Wagner M. Structural and functional fatigue of NiTi shape memory alloys. *Materials Science and Engineering: A.* 2004;378(1–2): 24–33.
- 10. Resnina N., Belyaev S. Multi-stage martensitic transformations induced by repeated thermalcycling of equiatomic TiNi alloy. *Journal of Alloys and Compounds*. 2009;486(1-2):304-308.
- 11. Jones NG, Dye D. Martensite evolution in a NiTi shape memory alloy when thermal cycling under an applied load. *Intermetallics*. 2011;19(10): 1348–1358.
- 12. Pelton AR, Huang GH, Moine P, Sinclair R. Effects of thermal cycling on microstructure and properties in Nitinol. *Materials Science and Engineering: A.* 2012;532: 130–138.
- 13. Zhang J, Somsen C, Simon T, Ding X, Hou S, Ren S, Ren X, Eggeler G, Otsuka K, Sun J. Leaf-like dislocation substructures and the decrease of martensitic start temperatures: A new explanation for functional fatigue during thermally induced martensitic transformations in coarse-grained Ni-rich Ti–Ni shape memory alloys, *Acta Materialia*. 2012;60(5): 1999–2006.
- 14. Belyaev S, Resnina N, Sibirev A. Peculiarities of residual strain accumulation during thermal cycling of TiNi alloy. *Journal of Alloys and Compounds*. 2012;542: 37–42.
- 15. Kus K, Breczko T. Change in the transformation sequence due to stress-free thermal cycling of Ni-Ti shape memory alloy. *Materials Physics and Mechanics*. 2012;13: 64-69.
- 16 Churakova A, Gunderov D. Increase in the dislocation density and yield stress of the Ti50Ni50 alloy caused by thermal cycling. *Mater. Today: Proc.* 2017;4(3): 4732–4736.
- 17. Sibirev A, Resnina N, Belyaev S. Relationship between the variation in transformation temperatures, resistivity and dislocation density during thermal cycling of Ni50Ti50 shape memory alloy. *International Journal of Materials Research*. 2019;110(5): 387–392.
- 18. McCormick P, Liu Y. Thermodynamic analysis of the martensitic transformation in NiTi-II. Effect of transformation cycling. *Acta Metallurgica et Materialia*. 1994;42(7): 2407–2413.
- 19. Tong YX, Guo B, Chen F, Tian B, Li L, Zheng YF, Prokofiev EA, Gunderov DV, Valiev RZ. Thermal cycling stability of ultrafine-grained TiNi shape memory alloys processed by equal channel angular pressing. *Scripta Materialia*. 2012;67(1): 1–4.
- 20. Churakova A, Gunderov D. Microstructural and Mechanical Stability of a Ti-50.8 at. % Ni Shape Memory Alloy Achieved by Thermal Cycling with a Large Number of Cycles. *Metals*. 2020;10(2); 227.
- 21. Churakova A, Kayumova E, Gunderov D, Magomedova D. Interrelation of microstructure and kinetics of martensitic transformations in TiNi alloy in different structural states under thermal cycling conditions. *AIP Conf. Proc.* 2022;2533: 020049.
- 22. Resnina N, Belyaev S, Shelyakov A. Martensitic transformation in amorphous-crystalline Ti-Ni-Cu and Ti-Hf-Ni-Cu thin ribbons. *Eur. Phys. J. Spec. Top.* 2008;158: 21–26.
- 23. Denowh CM, Miller DA. Thermomechanical training and characterization of Ni-Ti-Hf and Ni-Ti-Hf-Cu high temperature shape memory alloys. *Smart Materials and Structures*. 2012;21(6); 065020.
- 24. Baradari S, Resnina N, Belyaev S, Nili-Ahmadabadi M. Martensitic phase transformation and shape memory properties of the as-cast NiCuTiHf and NiCuTiHfZr alloys. *Journal of Alloys and Compounds*. 2021;888: 161534.
- 25. Baradari S, Resnina N, Belyaev S, Nili-Ahmadabadi M. Cyclic Stability of Ni_{44.8}Cu₅Ti_{45.2}Hf₅ and Zr-Substituted Ni_{44.8}Cu₅Ti_{40.2}Hf₅Zr₅ Medium-Entropy Shape Memory Alloys. *Advanced Engineering Materials*. 2022;24(10): 2200106.
- 26. Li J, Yi X, Meng X, Qiao S, Cai W, Zhao L. Deposition and phase transformation behaviors of Ti-Ni-Hf-Cu quaternary shape memory alloy thin films. *Journal of Alloys and Compounds*. 2019;806: 33–39.
- 27. Resnina N, Belyaev S, Shelyakov A, Ubyivovk E, Ponikarova A, Stability of the B2 \leftrightarrow B19' martensitic transformation on thermal cycling of Ti-Hf-Ni-Cu thin ribbons. *Materials Letters*. 2024;357: 135770.
- 28. Salzbrenner RJ, Cohen M. On the Thermodynamics of Thermoelastic Martensitic Transformations. *Acta Metallurgica*. 1979;27: 739–748.
- 29. Wollants P, Roos JR, Delaey L. Thermally- and stress-induced thermoelastic martensitic transformations in the reference frame of equilibrium thermodynamics. *Progress in Materials Science*. 1993;37(3): 227–288. 30. Sibirev A, Ubyivovk E, Belyaev S, Resnina N. In situ transmission electron microscopy study of martensite boundaries movement on cooling and heating of the NiTi shape memory alloy. *Materials Letters*. 2022;319: 132267.

Accepted: December 5, 2024

Submitted: October 29, 2024

Revised: November 20, 2024

Creation of aluminum matrix composites reinforced with microand nanoparticles of titanium carbide with nickel coating and description of their hardening mechanisms

E.G. Zemtsova [□] (D. B.N. Semenov (D. N.F. Morozov), Yu.V. Sidorov,

V.K. Kudymov, V.M. Smirnov (1)

St. Petersburg State University, St. Petersburg, Russia

[™] ezimtsova@yandex.ru

ABSTRACT

During the high-temperature synthesis of carbide reinforced Al matrix composites, as a result of a chemical reaction between carbide particles and a metal matrix, aluminum carbide is formed, which embrittles the system. To eliminate the negative effect of aluminum carbide in the material, the dispersed phase of TiC was pre-metallized with a thin Ni layer. Our work also evaluates the effect of Ni-plated particles of TiC and aluminum nickelide, formed as a result of the chemical reaction of Ni with molten Al, on the hardening of the Al matrix composite. The mechanisms of hardening of the aluminum matrix composites with a dispersed phase of micro- and nanometer size are proposed. The analysis of the contributions of the above mechanisms to the hardening of the TiC reinforced Al composite considered in this article, shows that the main contribution to the hardening due to the low bulk concentration of reinforcing particles is provided by the dispersion hardening Orowan-Ashby mechanism and the dislocation mechanism caused by a thermal expansion coefficients mismatch between the matrix and reinforcing particles.

KEYWORDS

composite materials • ceramic nanoparticles • aluminum • mechanical properties

Funding. This work has been supported by the grant of the Russian Science Foundation, RSF 20-11-20083.

Acknowledgements. The research was carried out using the equipment of the resource centers of the St. Petersburg State University Scientific Park "X-ray Diffraction research methods" and "Nanotechnolog" and "Center for Innovative Technologies of Composite Nanomaterials".

Citation: Zemtsova EG, Semenov BN, Morozov NF, Sidorov YuV, Kudymov VK, Smirnov VM. Creation of aluminum matrix composites reinforced with micro- and nanoparticles of titanium carbide with nickel coating and description of their hardening mechanisms. Materials Physics and Mechanics. 2025;53(1): 68-77. http://dx.doi.org/10.18149/MPM.5312025_6

Introduction

It has been repeatedly noted that the main technological problems in the synthesis of composites containing ceramic particles and carbon additives are: the distribution of the reinforcing phase in the bulk composite; the strength of its adhesion to the matrix; chemical and structural stability of the reinforcing phase in the composite [1-5]. These tasks are solved by us first of all at the stage of the composite powder preparation.

During the high-temperature synthesis of carbide reinforced Al matrix composites, undesired aluminum carbide is formed, as a result of reaction between carbide particles and a metal matrix. Formed carbide embrittles the system and significantly reduces the plasticity of composites [6-8].



To minimize the negative impact, we introduced TiC into the Al matrix in the form of core-shell particles. The Ni shell minimizes the possibility of chemical bonding between C and Al and improves the particle wettability in the Al melt [9-12]. In this paper, we evaluate the effect of the Ni shell on the hardening of metal composites reinforced with core-shell particles, and experimental results are compared with the theoretical assessment.

There are many factors contributing to the experimentally observed hardening of metal matrix composites by solid particles with higher rigidity than the matrix material. The hardening depends, in particular, on the physical and mechanical properties of the reinforcing particles, their shape, concentration, and distribution over the matrix, as well as the presence of a bond at the particle-matrix interface.

When reinforcing the matrix with micro- or nanoparticles, the strength increase cannot be explained by known continuous models: the mixture rule, the Halpin-Tsai, Hashin-Shtrikman, Mura and other models [13]. The hardening mechanisms based on the involvement of dislocation models make it possible not only to explain qualitatively, but also to predict an increase in the strength properties of a metal matrix composite.

The improvement in the strength characteristics of reinforced materials, compared with pure Al, is due to the structural inhomogeneities that create additional resistance to the movement of dislocations. The main reason for the hardening is the creation of obstacles to the dislocations movement in the main lattice.

The observed hardening of composites with a metal matrix is the combination of several possible mechanisms [11-24]:

- 1. due to the efficient load transfer between the matrix and the reinforcing elements;
- 2. due to the elastic modules mismatch of the matrix materials and the inclusion;
- 3. due to the grain grinding of the matrix (Hall-Petch law);
- 4. Orowan hardening caused by the dispersed phase;
- 5. due to internal thermal stresses caused by a mismatch in the thermal expansion coefficients between the matrix and the carbide particles;
- 6. hardening caused by the appearance of an interfacial layer between the reinforcing particle and the matrix.

Which of these mechanisms are implemented in each specific case is determined by both the geometry, size and concentration of particles, and the conditions for introducing reinforcing particles into the matrix. The analysis of the contributions of the above mechanisms to the hardening of the TiC reinforced Al composite considered in this article, shows that the main contribution to the hardening due to the low bulk concentration of reinforcing particles is provided by the dispersion hardening Orowan-Ashby mechanism and the dislocation mechanism caused by a thermal expansion coefficients mismatch between the matrix and reinforcing particles.

Materials and Methods

Production of a bulk composite based on Al reinforced with nano-TiC

The of Al samples were cast on an induction vacuum compression casting machine UVLK-30A (Spark-Don LTD, Russia), equipped with an autonomous water cooling module MAVO-3. During the casting, we used tablets of material, consisting of dispersed Al matrix

and a reinforcing TiC phase. Composite tablets were obtained by mixing Al matrix particles with a reinforcing phase in dry mixing mode at room temperature, followed by pressing. Al was mixed with a dispersed reinforcing phase in ratios 99:1, 99:3, 95:5 wt. %.

Aluminum ASP-50 with a size of $50-80 \, \mu m$ was used as a matrix. As a reinforcing phase, core-shell TiC/Ni particles with a diameter of $20 \, \mu m$ and $200 \, nm$ were synthesized [14–28]. The difference in the method of Ni plating of TiC particles was to increase the thickness of the Ni coating on TiC surface by increasing the deposition cycles number to 3 [12].

The samples were melted in a vacuum melting mode with a pressure of less than 250 mbar under constant inert gas flow (argon). The flow of Ar throughout the entire melting and casting process provides minimized oxidation of the melt and its gas saturation. The minimum weight of the workpiece was chosen at 3.2 g. The casting temperature for Al raw materials was selected experimentally as 700 °C. Plates were made from the obtained samples on a spark-cutting machine to evaluate mechanical properties.

Characterization

The phase composition of the samples was monitored using XRD analysis on a Bruker "D2 Phaser" powder diffractometer. The surface defects of the samples were examined by optical microscopy. The structure of the composite material and elemental composition were studied using a scanning electron microscope Zeiss Merlin.

Mechanical tests, conducting tests for uniaxial tension

After a comprehensive study, samples were cut from the plates for uniaxial loading tests. Uniaxial stretching was performed on a Shimadzu AG–50kNX testing machine at room temperature, the deformation rate was $5\cdot10^{-4}$ s⁻¹. The deformation of the samples was controlled by a TRViewX 55S video extensometer. Bending tests were carried out in accordance with GOST 14019–80 "Metals and alloys. Methods of testing for bending".

Results and Discussion

To study the effect of the dispersed TiC phase with Ni nanostructures on the mechanical properties of an Al matrix composite, samples of the reinforcing phase with a core-shell structure were obtained after 3 cycles of Ni deposition. It should be borne in mind that the carbide phase is used for reinforcing an Al matrix composite at Al melting temperatures. So, for better TiC particles shielding from the Al matrix, the Ni shell must be thicker.

The morphology of the reinforcing phase particles and the surface of bulk sample obtained by casting was studied by a scanning electron microscopy (SEM) (Figs. 1 and 2). Figure 1 shows a micrograph of a 20 μ m TiC particle with Ni. A mixed type of Ni coating growth is observed. On the TiC surface, both Ni shell coating (Fig. 1(a)) and Ni agglomerates (Fig. 1(b)) form. Elemental analysis of the modified particles shows the presence of Ti, C and Ni. The carbon content is due to carbon tape that was used as a substrate for the samples analysis (Fig. 1(c)).

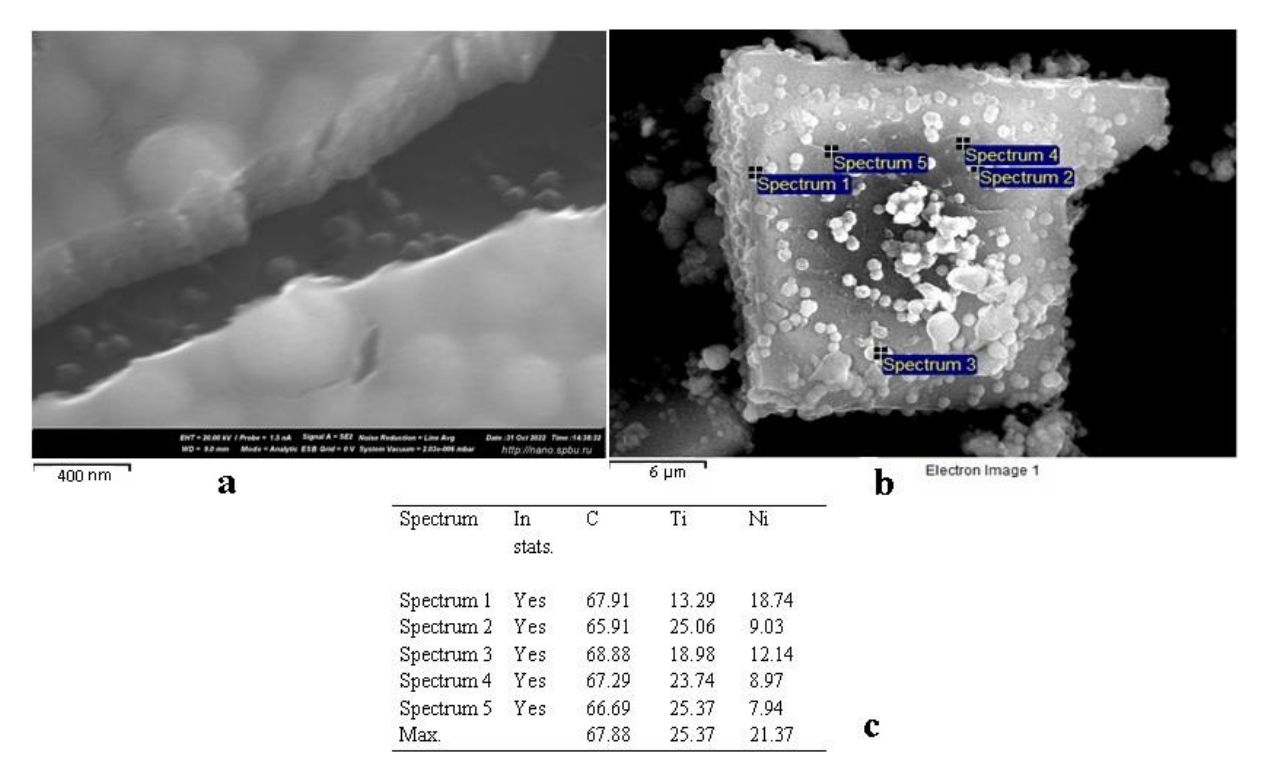


Fig. 1. Micrograph of TiC particles with Ni on the surface: (a) a section of the Ni shell on the TiC surface, (b) a TiC particle with Ni on the surface, (c) the elemental composition of the TiC surface

Figure 2 shows a micrograph of the composite sample surface with 5 % added reinforcing phase. The sample is nonporous. For a detailed study of the samples surfaces, the elemental composition at several surface points was evaluated simultaneously with microscopy. It can be seen from the microphotographs that the elemental sample composition corresponds to the expected one and consists of Al, Ti, C and Ni.

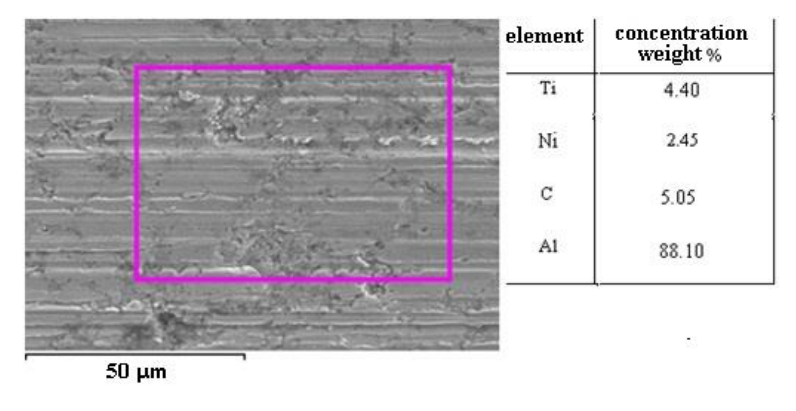


Fig. 2. Micrograph of a section of a composite Al sample with a 5 wt. % TiC/Ni

When obtaining bulk materials, the high temperature promotes the chemical reaction between carbide particles and the Al matrix, and undesired aluminum carbide can be obtained, which embrittles the system and reduces the strength characteristics and significantly reduces the plasticity of composites. XRD studies of samples using of a TiC-reinforced Al matrix composite with a Ni shell showed the absence of an aluminum carbide phase. The Al₃Ni phase was detected instead (Fig. 3) that, in opposite, leads to additional hardening [29,30].

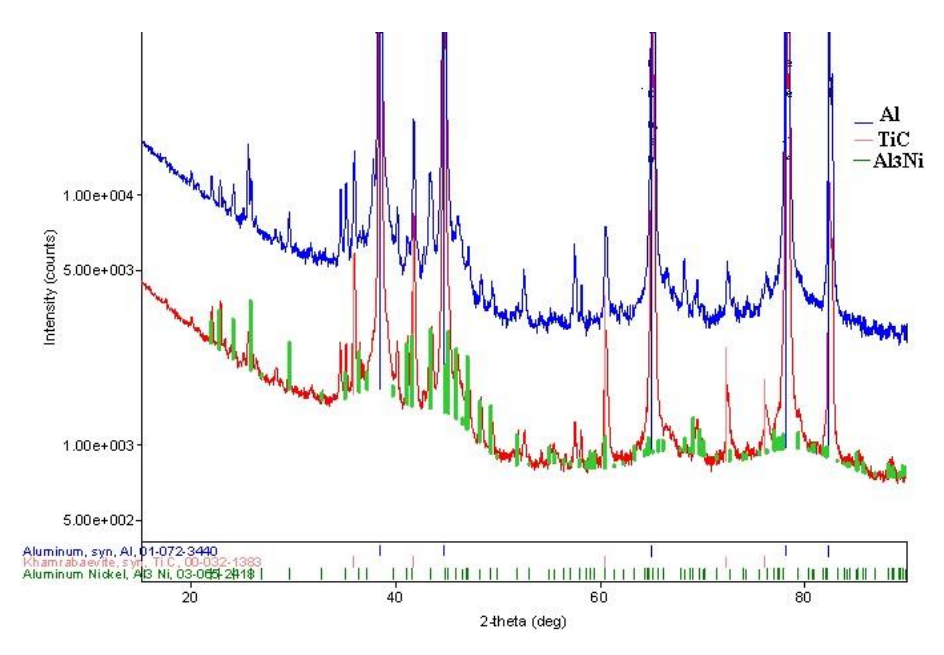


Fig. 3. Diffractogram of a bulk Al-TiC/Ni sample

The mechanical properties of Al matrix composites have been studied by uniaxial stretching. Mechanical tests were carried out at room temperature at the deformation rate $5 \cdot 10^{-4} \, \text{s}^{-1}$. From the samples obtained, double-sided blades with a working part size of $6 \times 2 \, \text{mm}^2$ were made on the ART 123 PRO electroerosion machine of NPK Delta–Test LLC. The ends of the blades were examined using a side-illuminated Micmed-6 microscope in order to control the samples integrity. All Al matrix composite samples obtained by injection molding show increased strength properties when tested for uniaxial tension (Fig. 4).

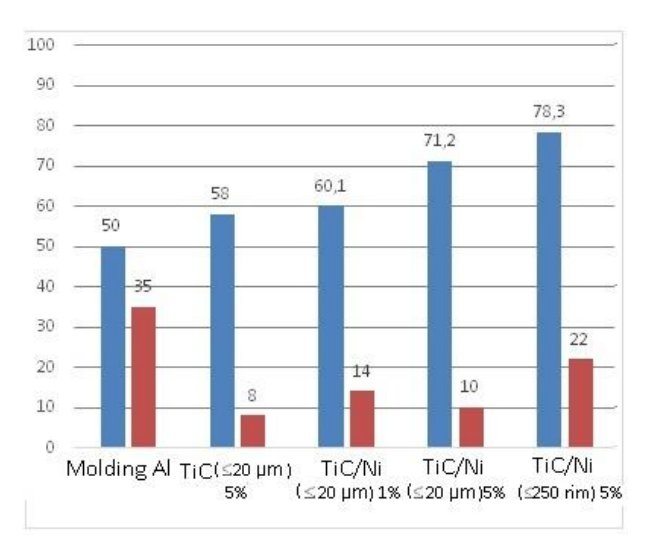


Fig. 4. Mechanical characteristics of Al matrix composites. Blue bars indicate the strength of the samples, red bars indicate the relative elongation of the samples

Al-based composites strengthened by Ni-plated TiC particles of both micron and nanometer sizes demonstrate higher strength characteristics compared with pure Al. This strength improvement is due to structural inhomogeneities that create additional

resistance to the dislocations movement. The increased effect of this mechanism can be observed during the transition from micron reinforcement particles to nanoscale ones.

Note that when cooling an Al composite reinforced with Ni-plated TiC particles from 600 to 20 °C, the reinforcing particles are in compression conditions, and the matrix material near the interface is under strong stretching conditions, which has a strong effect on the crack resistance of the composite and on plastic deformation. When the mixture melts, an aluminum nickelide layer forms at the TiC particles boundary. Upon cooling, microcracks arise in this layer, which cause a decrease in the plastic deformation area [27].

Mechanisms of hardening of Al matrix composite

Dispersion hardening mechanism

The presence of small-scale reinforcing particles in the metal matrix creates additional resistance to the dislocations movement through the matrix along its sliding planes. When colliding with a particle, moving dislocations first bend and then form a dislocation loop. This leads to an increase in the stress required for further dislocation movement, which increases the yield strength. The interaction between stress fields created by the looping of dislocations makes it difficult to further bend dislocations around particles. Therefore, a higher voltage is required to facilitate the dislocations movement, thereby increasing the composite strength.

Dispersion hardening by particles can be quantified using the Orowan-Ashby equation [17 – 21]:

$$\Delta\sigma_{Orow} = \frac{0.13G_m \, b}{\lambda} \ln\left(\frac{d_p}{2b}\right),\tag{1}$$

$$\Delta \sigma_{orow} = \frac{0.13G_m b}{\lambda} \ln \left(\frac{d_p}{2b} \right), \tag{1}$$

$$\lambda = d_p \left[\left(\frac{1}{2V_p} \right)^{1/3} - 1 \right], \tag{2}$$

where λ is the average distance between the particles, G_m is the shear modulus of the matrix material, for aluminum $G_m = 25.4 \cdot 10^9 \, \mathrm{MPa}$, $b = 0.286 \cdot 10^{-9} \, \mathrm{MPa}$ is the Burgers vector, d_p is a diameter of the reinforcing particle, V_p is a volumetric concentration of reinforcing particles.

The mechanism of deformation hardening caused by the discrepancy between the linear expansion coefficients of matrix materials and reinforcing particles

The strength increase of a metal matrix composite can be explained by matrix strengthening by creating a high dislocations density. While producing a metal matrix composite, thermal mismatch deformations are induced during cooling in the immediate vicinity of reinforcing particles due to the linear expansion coefficients difference between the matrix and the reinforcement. These mismatch thermal deformations change the internal stress state at the matrix-particle interface. To reduce the thermal effect and remove residual thermal stresses at the interface, the dislocations density near the interface of the particle matrix increases, which reduces the stored energy. As a result, the matrix undergoes deformation hardening near the interface and its strength increases. This hardening is quantified using the following equations [21–23]:

$$\Delta \sigma_{CTE} = M\beta G_m b \sqrt{\rho_{CTE}},\tag{3}$$

$$\rho_{CTE} = \frac{A\Delta\alpha\Delta T V_p}{bd_n(1-V_n)},\tag{4}$$

where ρ_{CTE} is the dislocations density generated by the linear expansion coefficients mismatch, M is the Taylor coefficient $M \approx 1$, β is a geometric constant, $\beta \approx 1.25$ for Al, A is a geometric constant (4 for equiaxed particles and 12 for extended ones), $\Delta \alpha$ is the linear expansion coefficients difference between reinforcing particle and matrix materials, ΔT is the difference between the synthesis temperature (in our case, the Al melting point) and room temperature.

These two mechanisms are used to evaluate the Al matrix hardening by TiC particles with a 20 μ m diameter, TiC particles with a 20 μ m diameter with a deposited 50 nm Ni layer and TiC particles with a diameter of 200 nm with a deposited 50 nm Ni layer.

Modeling of hardening by TiC and TiC/Ni particles

In the injection molding metal matrix composite obtaining approach, a reinforced with carbide particles, after cooling from the Al melting point to room temperature in the vicinity of the reinforcing particle-matrix boundary, the dislocation density increases significantly due to a linear expansion coefficients mismatch Eq. (4), which results in the composite hardening.

The main contribution to the hardening of a metal matrix composite reinforced with 20 µm TiC particles is provided by the dislocation hardening mechanism ($\Delta\sigma_{CTE}\approx 4.5$ MPa); the dispersion mechanism contribution is insignificant. When 20 µm TiC particles with a deposited 50 nm Ni layer, interact with molten Al, aluminum nickelide particles are formed, diffusing into molten Al. This assumption is confirmed by the diffractogram of a bulk composite Al – TiC/Ni (Fig. 3).

After cooling to room temperature, Ni₃Al forms an additional reinforcing phase along with TiC, which, despite its low concentration, makes a significant contribution to the metal composite hardening. At 1 wt. % of TiC/Ni, hardening due to Ni₃Al particles at their concentration of less than 0.01 vol. % TiC ~ 8.5 MPa, and at 5 wt. % of TiC/Ni, hardening due to Ni₃Al particles at their volume concentration in an Al matrix of less than 0.03 % $\Delta\sigma_{Ni3Al} \approx 18.5$ MPa.

Table 1. Com	position	of alum	inum matrix	based	composites

Matrix	Reinforcing phase	Reinforcing phase, %	σ_{V} , MPa exp.	σ_{V} , MPa calc.	Increment σ_V , %	Relative elongation
Cast Al 99.9%	-Cast Al		50	ı	-	35
Cast Al 95.5%	20 μm TiC 5 wt. %	5	58	54.	+15	8
Cast Al 99.0%	20 μm TiC/Ni 1 wt. %	1	60.1	60.5	+20	14
Cast Al 95.5%	20 μm TiC/Ni 5 wt. %	5	71.2	80.3	+42	10
Cast Al 95.5%	TiC/Ni (<i>d</i> ≤ 250 nm) 5 wt. %	5	78.3	88.2	+47	22

Considering that the hardening by carbide and aluminum nickelide particles are independent, the total hardening is determined by their sum [4]: $\Delta\sigma = \Delta\sigma_{TiC} + \Delta\sigma_{Ni3Al}$. At 1 wt. % of TiC/Ni, the total hardening is $\Delta\sigma \approx 10.5$ MPa, at 5 wt. % of TiC/Ni $\Delta\sigma \approx 30.4$ MPa. The theoretical hardening model correlates with the experimental results (Table 1).

When reinforced with 200 nm TiC particles coated with a 50 nm Ni layer, the Ni₃Al layer formed on the carbide particle surface does not diffuse into molten Al. These particles with a diameter of 250 nm are barriers to the dislocations movement, generating the metal composite hardening. Taking into account the mechanical properties of aluminum nickelide, this composite particle can be considered as homogeneous, attributing to it the Ni₃Al properties.

Estimating dispersion hardening Eq. (1) and dislocation hardening Eq. (3), we obtain $\Delta\sigma_{crow}=13.6$ MPa and $\Delta\sigma_{cre}=24.6$ MPa. The total hardening due to these two mechanisms $\Delta\sigma=\Delta\sigma_{crow}+\Delta\sigma_{cre}=38.2$ MPa corresponds to the experimental hardening (Table 1).

Conclusions

In conclusion, the use of core-shell TiC particles with a Ni shell in the production of Al matrix composites not only minimizes the possibility of chemical bonding between C and Al and improves the particle wettability in the Al melt, but also increases strength properties.

When reinforcing an Al matrix with micro-sized TiC particles with a nanoscale Ni layer at 3 vol. %, a strength increase of > 40 % is observed.

The analysis shows that for small concentrations of reinforcing carbide particles with a Ni shell on their surface, the main hardening mechanism involves the dislocation hardening caused by thermal expansion coefficients mismatch between the matrix and the carbide particles, and the dispersion mechanism.

CRediT authorship contribution statement

Elena G. Zemtsova [©]SC: writing – review & editing, writing – original draft; Boris N. Semenov [©]SCE: writing – original draft; Nikita F. Morozov ^{SCE}: data curation; Yuri V. Sidorov ^{SC}: writing – review & editing; Vladimir K. Kudymov ^{SCE}: data curation; Vladimir M. Smirnov [©]SCE: investigation, writing – original draft.

Conflict of interest

The authors declare that they have no conflict of interest.

References

- 1. Tolochko OV, Koltsova TS, Bobrynina EV, Rudskoy AI, Zemtsova EG, Kirichenko SO, Smirnov VM. Conditions for production of composite material based on aluminum and carbon nanofibers and its physic-mechanical properties. *Nanomaterials*. 2019;9(4): 550.
- 2. Choi HJ, Shin JH, Bae DH. Grain size effect on the strengthening behavior of aluminum-based composites containing multi-walled carbon nanotubes. *Composites Science and Technology*. 2011;71(15): 1699–1705.

- 3. Somashekar HM, Gowthama K, Suresha B. Microstructure, Mechanical Properties and Sliding Wear Behaviour of Silicon Carbide Reinforced Al 6026 Composites. *International Journal of Mechanical and Production Engineering Research and Development.* 2020;10(1): 259–270.
- 4. Mirza FA, Chen DL. A Unified Model for the Prediction of Yield Strength in Particulate-Reinforced Metal Matrix Nanocomposites. *Materials*. 2015;8(8): 5138–5153.
- 5. Van Aken DC, Krajewski PE, Vyletel GM, Allison JE, Jones JW. Recrystallization and grain growth phenomena in a particle-reinforced aluminum composite. *Metall Mater Trans A.* 1995;26: 1395–1405.
- 6. Rogov VA. Technology of structural materials. Nanotechnologies. Moscow: Yurait; 2019. (In Russian)
- 7. Thess A, Lee R, Nikolaev P, Dai H, Petit P, Robert J, Xu C, Lee YH, Kim SG, Rinzler AG, Colbert DT, Scuseria GE, Tomanek D, Fischer JE, Smalley RE. Crystalline Ropes of Metallic Carbon Nanotubes. *Science*. 1996;273(5274): 483–487.
- 8. Liao XZ, Serquis A, Jia QX, Peterson DE, Zhu YT, Xu HF. Effect of catalyst composition on carbon nanotube growth. *Applied Physics Letters*. 2003;82(16): 2694–2696.
- 9. Tjong SC. 8 Processing and Deformation Characteristics of Metals Reinforced with Ceramic Nanoparticles. In: Tjong SC. (eds.) *Nanocrystalline materials*. 2nd ed. Oxford: Elsevier; 2014. p.269–304.
- 10. Casati R, Vedani M. Metal matrix composites reinforced by nano-particles A review. *Metals*. 2014;4(1):65–83.
- 11. Zheng B, Smugeresky JE,. Zhou Y, Baker D, Lavernia EJ. . Microstructure and Properties of Laser-Deposited Ti6Al4V Metal Matrix Composites Using Ni-Coated Powder. *Metall Mater Trans A*. 2008;39(5): 1196–1205.
- 12. Zemtsova EG, Smirnov VM, Kozlova LA, Morozov PE, Yurchuk DV, Semenov BN, Morozov NF. Development of aluminum-based composite with two reinforcing modifiers (TiC/Ni, CNTs/Ni) with improved mechanical properties. *Materials Physics and Mechanics*. 2023;51(3): 9–19.
- 13. Dai LH, Ling Z, Bai YL. Size-dependent inelastic behavior of particle-reinforced metal-matrix composites. *Composites Science and Technology.* 2001;61(8): 1057–1063.
- 14. Mobasherpour I, Tofigh AA, Ebrahimi M. Effect of nano-size Al2O3 reinforcement on the mechanical behavior of synthesis 7075 aluminum alloy composites by mechanical alloying. *Mater. Chem. Phys.* 2013;138(2–3): 535–541.
- 15. Shivaraja HB, Kumar BP. Experimental determination and analysis of fracture toughness MMC. *International Journal of Science and Research (IJSR)*. 2014;3(7): 888–892.
- 16. Morozov NF, Semenov BN, Smirnov VM, Zemtsova EG.. Mechanical properties of metal-matrix composites reinforced with carbide structures. *Journal of Physics: Conference Series*. 2022;2231(1): 012003.
- 17. Zhang Z, Chen DL. Contribution of Orowan strengthening effect in particulate-reinforced metal matrix nanocomposites. *Materials Science and Engineering A*. 2008; 483–484: 148–152.
- 18. Ferguson JB, Lopez H, Kongshaug D, Schultz B, Rohatgi P. Revised Orowan Strengthening: Effective Interparticle Spacing and Strain Field Considerations. *Metallurgical and Materials Transactions A.* 2012;43(6): 2110–2115.
- 19. Kim CS, Sohn I, Nezafati M, Ferguson JB, Schultz BF, Rohatgi PK, Cho K. Prediction models for the yield strength of particle-reinforced unimodal pure magnesium (Mg) metal matrix nanocomposites (MMNCs). *J. Mater. Sci.* 2013;48: 4191–4204.
- 20. Ferguson JB, Schultz BF, Venugopalan D, Lopez HF, Rohatgi PK, Cho K, Kim CS. On the superposition of strengthening mechanisms in dispersion strengthened alloys and metal-matrix nanocomposites: Considerations of stress and energy. *Met. Mater. Int.* 2014;20: 375–388.
- 21. Zhang Z, Chen DL. Consideration of Orowan strengthening effect in particulate-reinforced metal matrix nanocomposites: A model for predicting their yield strength. *Scripta Materials*. 2006;54(7): 1321–1326.
- 22. Sahoo BP, Das D, Chaubey AK. Strengthening mechanisms and modelling of mechanical properties of submicron-TiB2 particulate reinforced Al 7075 metal matrix composites. *Materials Science and Engineering: A.* 2021;825: 141873.
- 23. Arsenault RJ, Shi N. Dislocation generation due to differences between the coefficients of thermal expansion. *Materials Science and Engineering*. 1986;81: 175–187.
- 24. Shi N, Arsenault RJ. Plastic Flow in SiC/A1 Composites-Strengthening and Ductility. *Annual Review of Materials Science*. 1994;24(1): 321–357.
- 25. Zemtsova EG, Yurchuk DV, Morozov PE, Korusenko PM, Kudymov VK, Smirnov VM. Features of the synthesis of the dispersed tic phase with nickel nanostructures on the surface to create an aluminum-based metal composite. *Nanomaterials*. 2021;11(10): 2499.
- 26. Morozov NF, Zemtsova EG, Kudymov VK, Morozov PE, Semenov BN, Yurchuk DV, Smirnov VM. Development of aluminum matrix composite with improved mechanical properties by the directional

regulation of the chemical composition of the reinforcing dispersed phase surface. *Izvestiya of Saratov University. Mathematics. Mechanics. Informatics.* 2024;24(1): 97–108. (In Russian)

- 27. Zemtsova EG, Morozov NF, Semenov, BN, Smirnov VM, Venatovskaya LA. Mechanical properties of aluminum matrix composite reinforced with titanium carbide. *Journal of Physics: Conference Series*. 2024;2817(1): 012014.
- 28. Zemtsova EG, Yurchuk DV, Sidorov YuV, Morozov NF, Semenov BN, Smirnov VM. Synthesis of metallic composite based on iron frame and SiC nanostructures and its strength properties. *Materials Physics and Mechanics*. 2020;46(1): 122–131.
- 29. Lefebvre W, Masquelier N, Houard J, Patte R,. Zapolsky H Tracking the path of dislocations across ordered Al3Zr nano-precipitates in three dimensions. *Scripta Materialia*. 2014;70: 43–46.
- 30. Xu N, Zong BY. Stress in particulate reinforcements and overall stress response on aluminum alloy matrix composites during straining by analytical and numerical modeling. *Computational Materials Science*. 2008;43(4):1094–1100.

Submitted: October 8, 2024 Revised: October 23, 2024 Accepted: November 13, 2024

EBSD on bainitic steel to assess parent austenite state after multipass hot rolling: Textural analysis versus reconstruction of prior grains

A.A. Zisman ^{1,2} , N.Yu. Zolotorevsky ², D.A. Petrov ³, S.N. Petrov ¹

ABSTRACT

Owing to inter-phase orientation relationship, EBSD analysis of martensitic or bainitic steel enables reconstruction of prior grains. Thus, assessment of the treatment conditions remains possible even if the chemical etching cannot properly reveal the parent structure. However, such an approach is hardly applicable to the industrial modes of multi-pass rolling. Unlike a single thickness reduction, small strains per pass followed by a kind of annealing in inter-pass pauses cause specific mechanisms of austenite recrystallization so that the latter becomes difficult to be assessed in morphological terms. At the same time, the textural analysis enables estimation of the parent state using whether the texture of reconstructed austenite or the measured transformation texture. When tested on low carbon bainitic steel, both methods lead to close estimates of the parent texture and thus support each other.

KEYWORDS

austenite • bainite • martensite • martensite • hot rolling • prior grains • transformation texture • EBSD

Funding. This work has been supported by the grant of the Russian Science Foundation, RSF 22-19-00627.

Citation: Zisman AA, Zolotorevsky NYu, Petrov DA, Petrov SN. EBSD on bainitic steel to assess parent austenite state after multi-pass hot rolling: Textural analysis versus reconstruction of prior grains. *Materials Physics and Mechanics*. 2025;53(1): 78–88.

http://dx.doi.org/10.18149/MPM.5312025_7

Introduction

According to orientation relationships (OR) pronounced in martensitic and bainitic steels [1-3], the transformation texture measured at room temperature is indicative of the proportion between deformation and recrystallization components in the *parent* texture. Thus, the hot rolling effect on austenite states before the direct quenching keeps detectable regardless of the prior grain morphology. Such an advantage is very important for low carbon steels where a chemical etching to image prior grains is rather laborious and not always efficient. However, the considered textural method originally based on X-ray diffraction (XRD) data [4,5] did not attract due regard because of some limitations considered in our previous article [6]. Instead, to assess a shape of prior grains, the latter are commonly reconstructed from EBSD data [7-14] with allowance for a certain OR.

Avoiding the reconstruction of austenite grains, use of EBSD data to assess the parent texture rather than structure greatly simplifies computations while averaging out local measurement errors [6]. Besides, it allows to get rid of the above-mentioned shortcomings inherent in XRD technique. These advantages particularly gain in



¹ NRC "Kurchatov Institute" – CRISM "Prometey", St. Petersburg, Russia

² Peter the Great St. Petersburg Polytechnic University, St. Petersburg, Russia

³ Institute for Problems in Mechanical Engineering of the Russian Academy of Science, St. Petersburg, Russia

[™] zolotorevsky@phmf.spbstu.ru

significance in the general case where deformed and recrystallized austenite fractions can turn out comparable so that the grain morphology is hard to quantify. Apart from these reasons, a principal limitation of the morphological estimate appears in the *multipass* modes of industrial hot rolling. In this case, a combination of concurrent recrystallization mechanisms during the sequence of strains followed by a kind of annealing in pauses between them notably weakens the effect of rolling conditions on grain shapes [15–19]. Regardless of related explanations [16,18] remaining a subject of dispute, the considered regularity in itself supports the alternative textural approach to parent states of steel.

Following [5], to evaluate specific contributions to the transformation texture appearing from deformation and recrystallization components of the parent texture, we will make use of the virtual Bain relationship [20] since various actual ORs generally spread around it. With orientations expressed by Euler angles (φ_1 , φ and φ_2), Figure 1 illustrates the above-mentioned orientation transformations by respective ODF sections at φ_2 = 45°. Unlike a strong influence of presumed OR on the grain reconstruction [7–10], such an implicit allowance for variations of real OR will not notably affect assessments of the parent orientation statistics. Moreover, determination of any presumably precise OR is not realistic because the result depends on an analyzed EBSD area and can vary even within prior grains [21,22]. This ambiguity particularly aggravates at deformed grains owing to the orientation inhomogeneity in their substructures [23]. In this case the reconstruction has to rely on some intuitive compromise between the locality of OR and its significance suggesting a large enough analyzed domain.

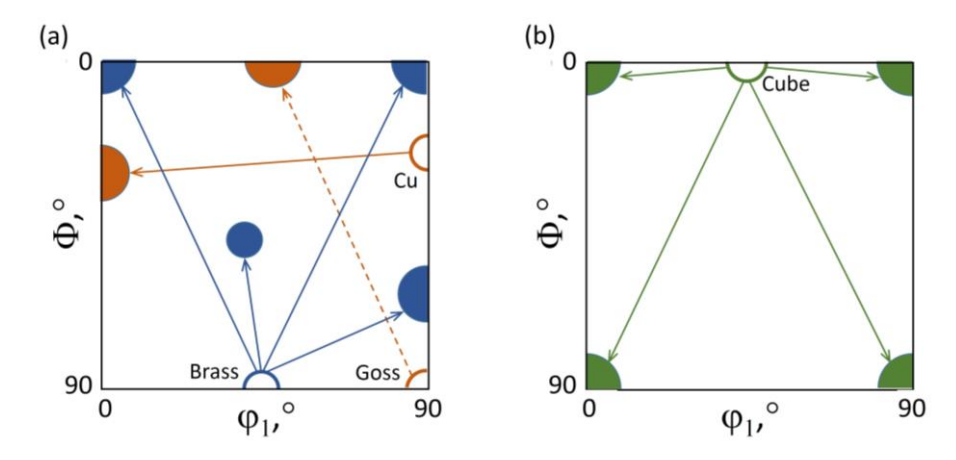


Fig. 1. Sections of ODF at φ_2 = 45° illustrating the transformation of main texture components according to the Bain OR for (a) deformed and (b) recrystallized states of hot rolled austenite. Parent and transformed components are represented by empty and filled circles, respectively

To quantify austenite states formed in multi-pass hot rolling, measured textural parameters should be compared with reference values corresponding to certain recrystallization degrees as confirmed by independent methods. In the present work both the completely deformed and recrystallized states of austenite will be prepared by single passes of hot rolling in a medium carbon martensitic steel where specific shapes of prior grains are easy to reveal by etching. Despite a different chemical composition of this material, it admits the method calibration as far as the Bain relationship approximates

both its OR and that of the considered bainitic steel. Anyway, this difference is insignificant relative to those of model FCC alloys [4,24,25] used to mimic the parent phase of hot rolled martensitic or bainitic steel.

Since the proposed treatment of EBSD data suggests a simple alternative to the currently popular grain reconstruction, we will compare respective assessments of the parent austenite states. The comparison is possible as far as shapes of prior grains are restored together with their orientations [7-11] and resulting statistics of them represents the parent texture. The latter mostly averages out local errors sensitive to the presumed OR and hence can implicitly verify use of the Bain relationship that provides a virtual center for various experimental OR.

Materials and Methods

To analyze influence of multi-pass hot rolling modes on the austenite state of low carbon bainitic steel (wt. %: 0.08C, 0.21Si, 0.34Mn, 2.6[Ni+Cu], 0.59[Cr+Mo], 0.038[V+Nb]), its slabs of 250 mm thickness reheated to 1200 °C, were rolled at gradually diminishing temperatures to the thickness of 18 mm before the direct quenching in a sprinkler installation. Keeping these conditions, the rolling modes still could vary in strains and temperatures at the finish stage. Limiting consideration to its last five passes, we will compare modes B_1 and B_2 providing there average thickness reductions per pass of 16 and 14 % at average temperatures of 913 and 977 °C, respectively. According to previous experiments [6], B_1 results in a stronger work hardening of austenite that elevates the transformation start temperature and hence provides softer bainite unlike the more lath-like bainite of B_2 . Additionally, in order to obtain a bainitic state with a weakened rolling texture, a sample of B_2 was reheated to 950 °C and quenched in water. Therefore, the initial texture has been dissipated by way of $\alpha-\gamma-\alpha$ transformation. This mode has been marked as B_3 .

As noted in the introduction and further confirmed in this paper, effects of the multipass rolling, hard to analyze in terms of the grain morphology, still are perceptible by the material texture. The latter in turn satisfactorily complies with grain shapes after a *single* rolling pass [4,26] so that revealed parent structures enable the calibration of textural parameters. To make use of this expedient, we will consider medium carbon martensitic steel (wt. %: 0.35C, 0.3Si, 1.8[Ni+Mn], 0.75[Cr+Mo], 0.04[V+Nb], 0.003B) since its prior grains are easy to image by etching in Marshall's reagent [27] at room temperature. Samples of this reference material reheated to 1150 °C have been hot rolled by single passes to a thickness reduction of 35 % at temperatures 900 and 1100 °C. According to [26], the whole parent phase of this steel proves to be deformed or fully recrystallized at the lower or the higher rolling temperature, respectively.

Sections of the samples prepared by usual metallographic procedures were then subjected to electrolytic polishing in perchloric acid-ethanol solution at 0 °C. Using SEM Lyra 3-XM at an accelerating voltage of 20 kV, EBSD orientation data are collected by Channel 5 software at various scanning steps. Textures of martensitic and bainitic steels were composed over areas of 2.25 and 3 mm², respectively, with a step of about 1 μ m. Then, the step was refined to 0.1 or 0.5 μ m for the bainitic and martensitic steel, respectively, in order to reconstruct prior grains. Treatment of the orientation data,

including the reconstruction of austenite texture and structure, was conducted using MTEX toolbox [12] for MatLab.

Results and Discussion

Martensitic steel hot rolled by single pass

Revealed by the chemical etching on martensitic steel, structures of its parent austenite after single passes of hot rolling at different temperatures are shown in Fig. 2(a,b). The distinction between deformed and recrystallized prior grains is apparent here owing to their flattened and equiaxed shapes, respectively. Results of the grain reconstruction from EBSD represented in Fig. 2(c,d) satisfactorily comply with the images in Fig. 2(a,b). Moreover, a recrystallized state indicated in Fig. 2(b) by the grain shape is additionally justified in Fig. 2(d) by the orientation uniformity, that is, by the absence of substructure within reconstructed grains.

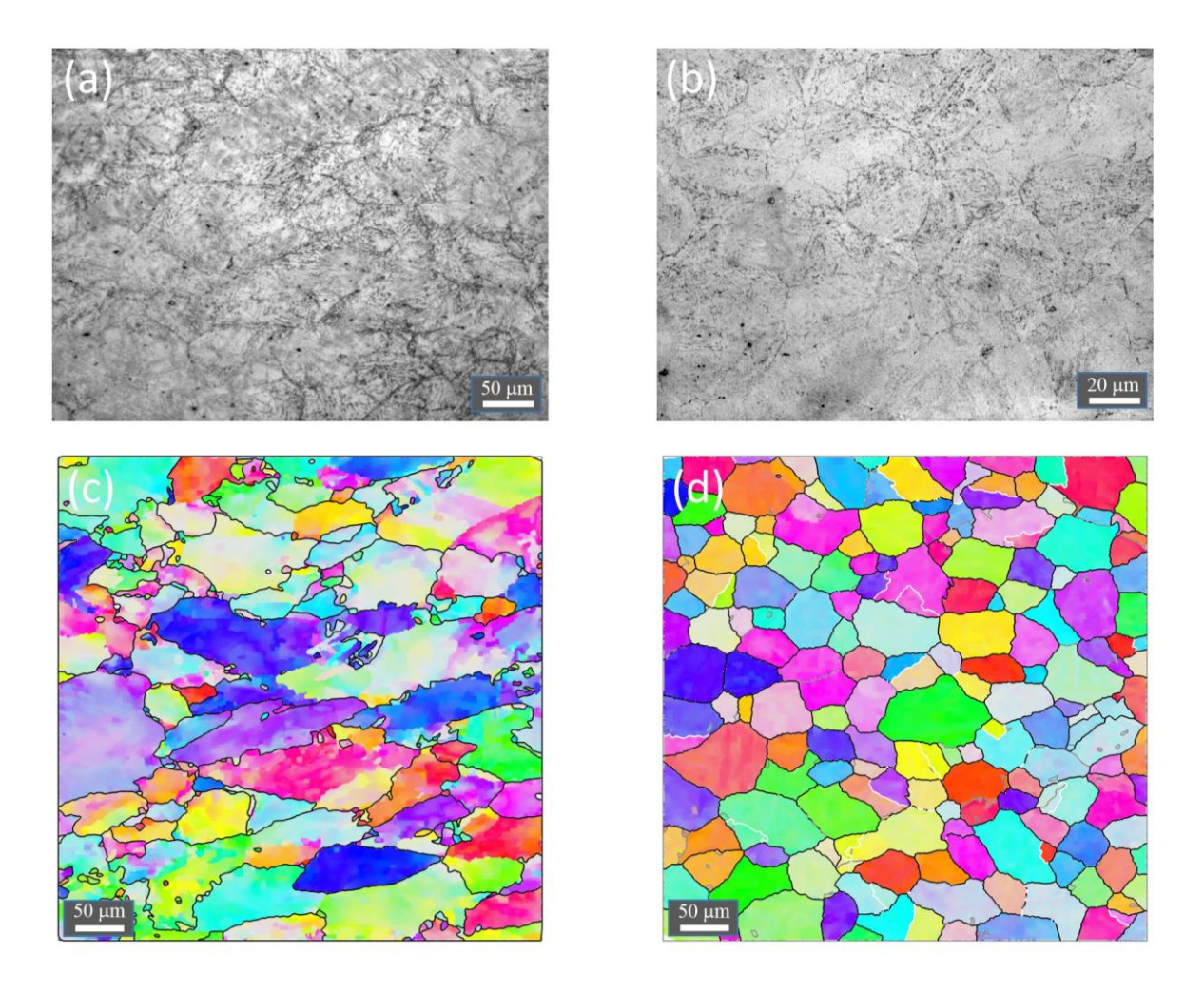


Fig. 2. Deformed (a,c) and recrystallized (b,d) parent structures of martensitic steel hot rolled by a single pass: image of prior grains revealed by chemical etching (a,b) and respective orientation (IPF) maps reconstructed from EBSD data (c,d). Coloring of boundaries on the orientation maps: low angle – gray; random high angle – black; twin – white

Figure 3 shows the (110) pole figures obtained for two structural states of the martensitic steel (the transformation textures) and the (111) pole figures computed for the reconstructed austenite. Note that, as long as $\{110\}$ planes of α phase are approximately parallel to the $\{111\}$ of γ phase in accordance with the inter-phase OR [1], close correlation between the (110) pole figures for the martensite texture and the (111) pole figures for the prior austenite texture exists [4].

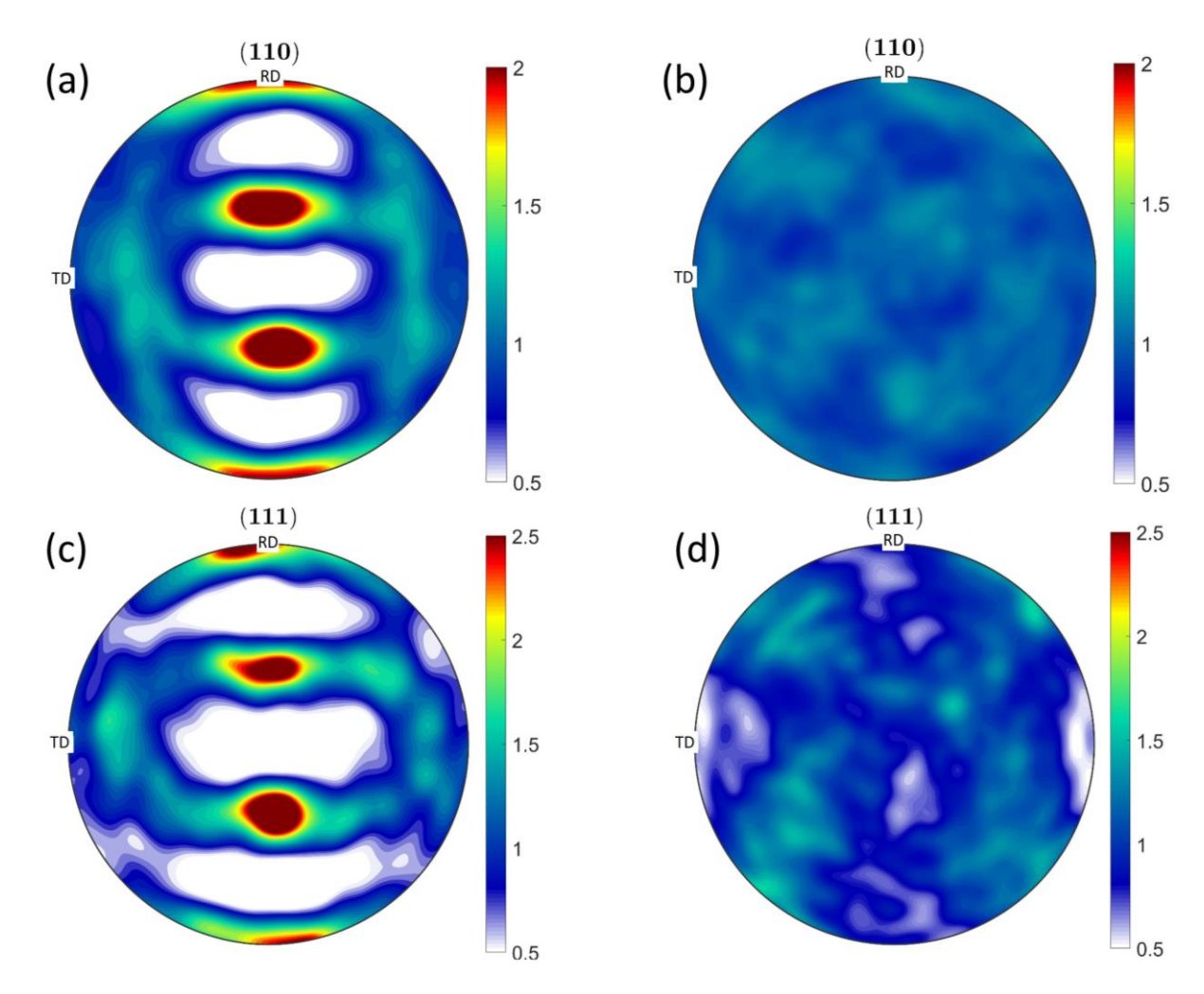


Fig. 3. Pole figures for measured transformation textures of martensitic steel (a,b) and its reconstructed parent textures (c,d). Figures (a,c) and (b,d) correspond to the deformed (M1) and recrystallized (M2) states of parent austenite, respectively

More detailed and unambiguous representation of texture is given by the orientation distribution function (ODF) [28]. Figure 4 represents ODF sections ($\varphi_2 = 45^\circ$) for the considered textures. In the deformed state, Fig. 4(c), austenite texture have strong Cu and Brass components (see Fig. 1), whereas the texture of recrystallized state, Fig. 4(d), is significantly dissipated and contain Cube component. Therefore, the textures confirm our above conclusions made on the basis of structure appearance.

To sum up this subsection, after the hot rolling by the single pass both the shapes of prior grains (whether revealed by etching or reconstructed from EBSD data) and the related textures of steel lead to similar assessments of the parent austenite states,

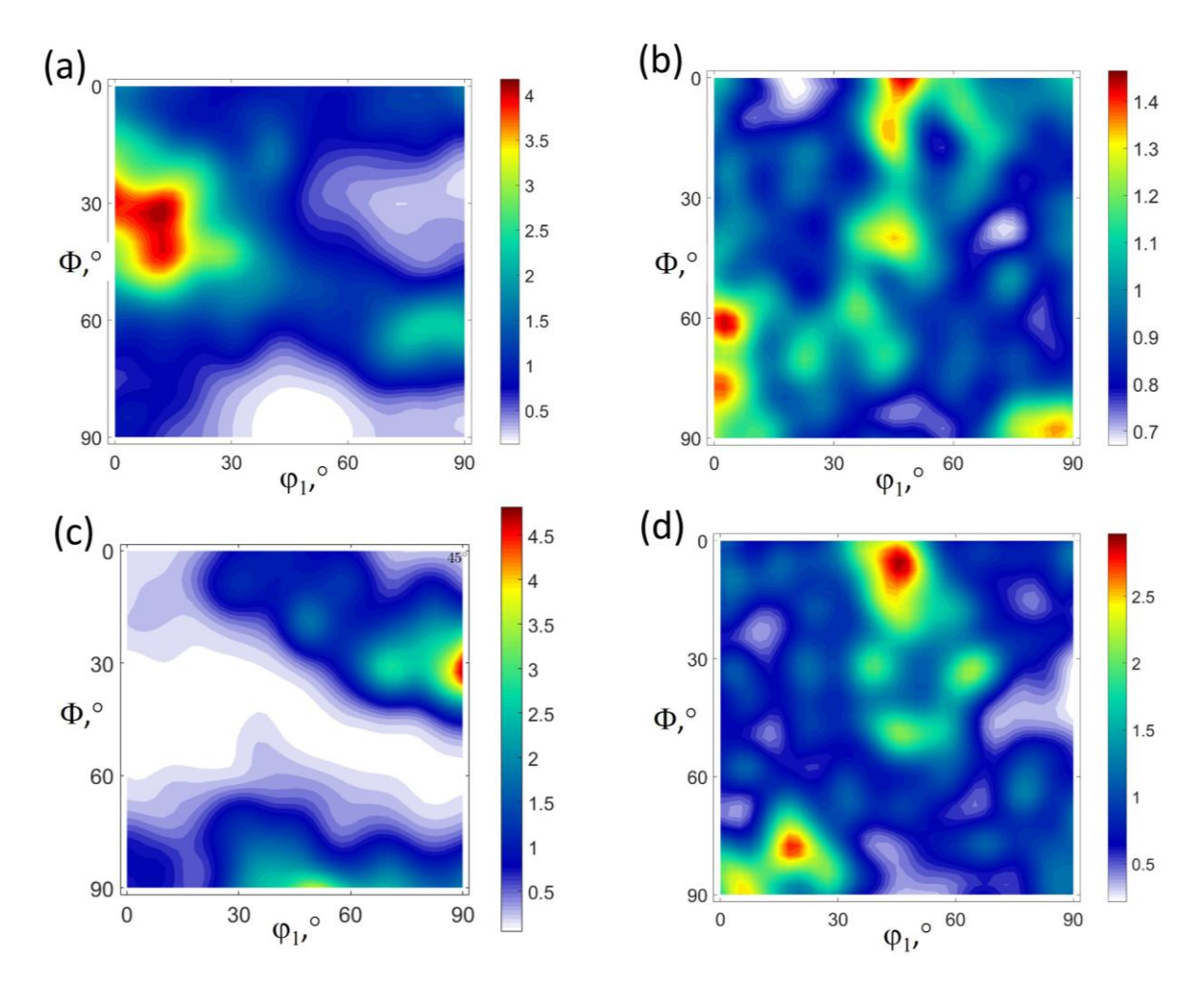


Fig. 4. Sections of ODF at φ_2 = 45° for the measured transformation textures of martensitic steel (a,b) and its reconstructed parent textures (c,d). Figures (a,c) and (b,d) correspond to the deformed and recrystallized states of parent austenite, respectively

namely, the first is deformed while the second is completely recrystallized. These two states are further used to calibrate textural data on bainitic steel.

Bainitic steel hot rolled by industrial multi-pass mode

Figure 5 shows the structure of prior austenite reconstructed in the cases termed B_1 , B_2 and B_3 . The latter case (Fig. 5(c)) is not in dispute since here we have austenite grains created during reverse α to γ transformation. The structures presented in Fig. 5(a,b), however, are rather difficult to interpret. Actually, in the case of mode B_1 one can see highly distorted grain boundaries as well as a misoriented substructure inside grains. At the same time, the flattening of grains that one might expect in the deformed state, is not observed. For the mode B_2 , the austenite grains are less distorted that seems to indicate a greater contribution of recrystallization. However, this contribution is difficult to assess quantitatively.

The pole figures obtained on bainitic steel (Fig. 6) demonstrate that the industrial hot rolling modes mostly lead to the rolling texture, stronger in B_1 and weaker in B_2 . In the case of B_3 , where the texture is very weak, the subtle signs of the rolling texture,

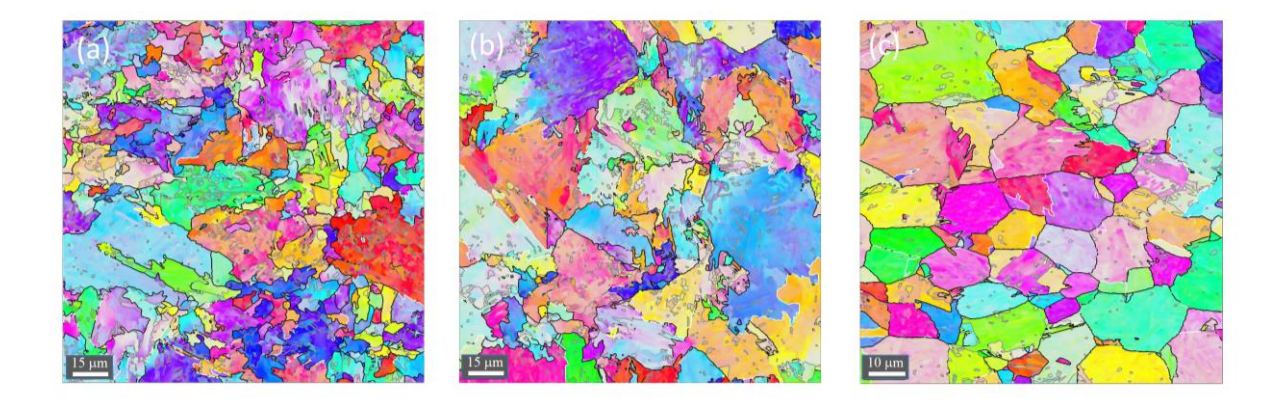


Fig. 5. Prior austenite grains reconstructed from EBSD data on bainitic steel subjected to regimens (a) B_1 , (b) B_2 and (c) B_3 . Coloring of boundaries on the orientation maps: low angle – gray; random high angle – black; twin – white

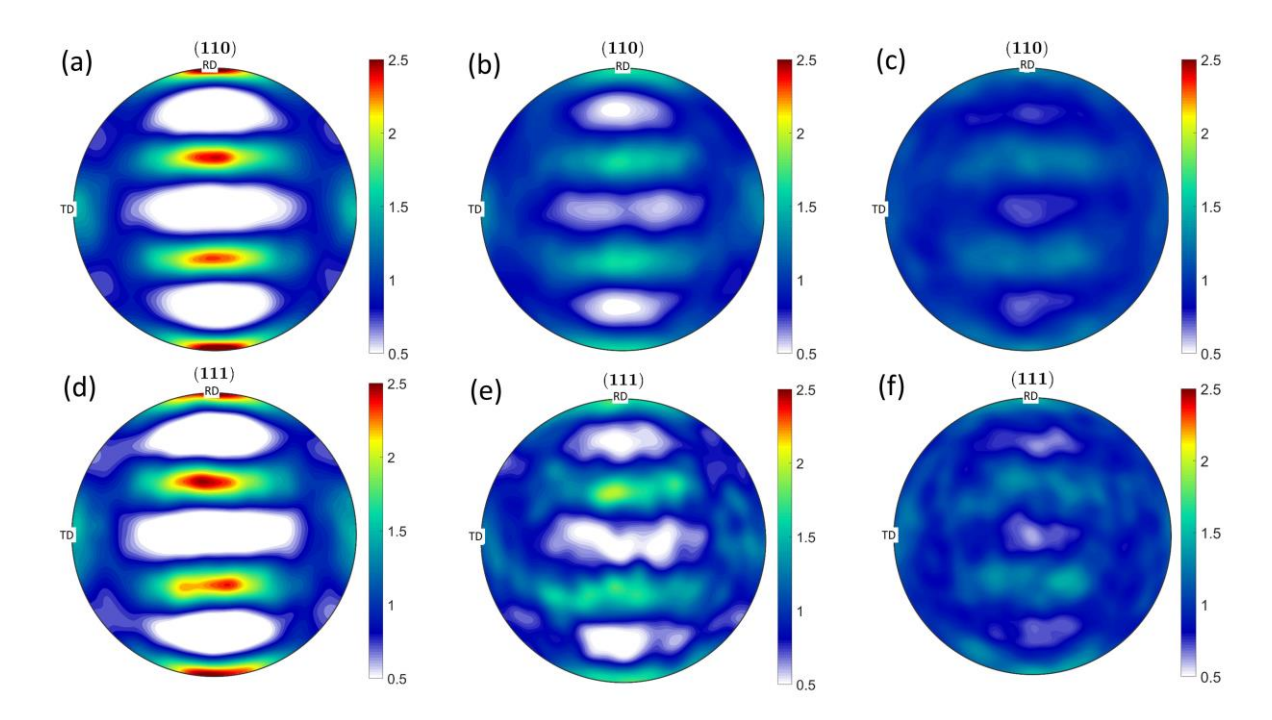


Fig. 6. Pole figures for measured transformation textures of bainitic steel (a,b,c) and its reconstructed parent textures (d,e,f). Figures (a,d), (b,e) and (c,f) correspond, respectively to the regimens B_1 , B_2 and B_3

which remain visible after $\alpha-\gamma-\alpha$ transformation, are due to a "texture memory" peculiar to bainitic steels [29].

Consider now the ODF sections (Fig. 7). For B_1 , the intensities of transformed Cu and Brass components in Fig. 7(a) are close to those for the not-recrystallized austenite¹ of the martensitic steel (see Fig. 4(a)) that indicate a deformed state of austenite in this case. The reconstructed texture confirms this suggestion in view of the strong Cu and Brass components. At the same time, a Cube component also takes place in Fig. 7(d). Though

¹ The intensities of main texture components are even stronger than in the case of martensite, apparently because of the larger accumulated strain during hot rolling [6].

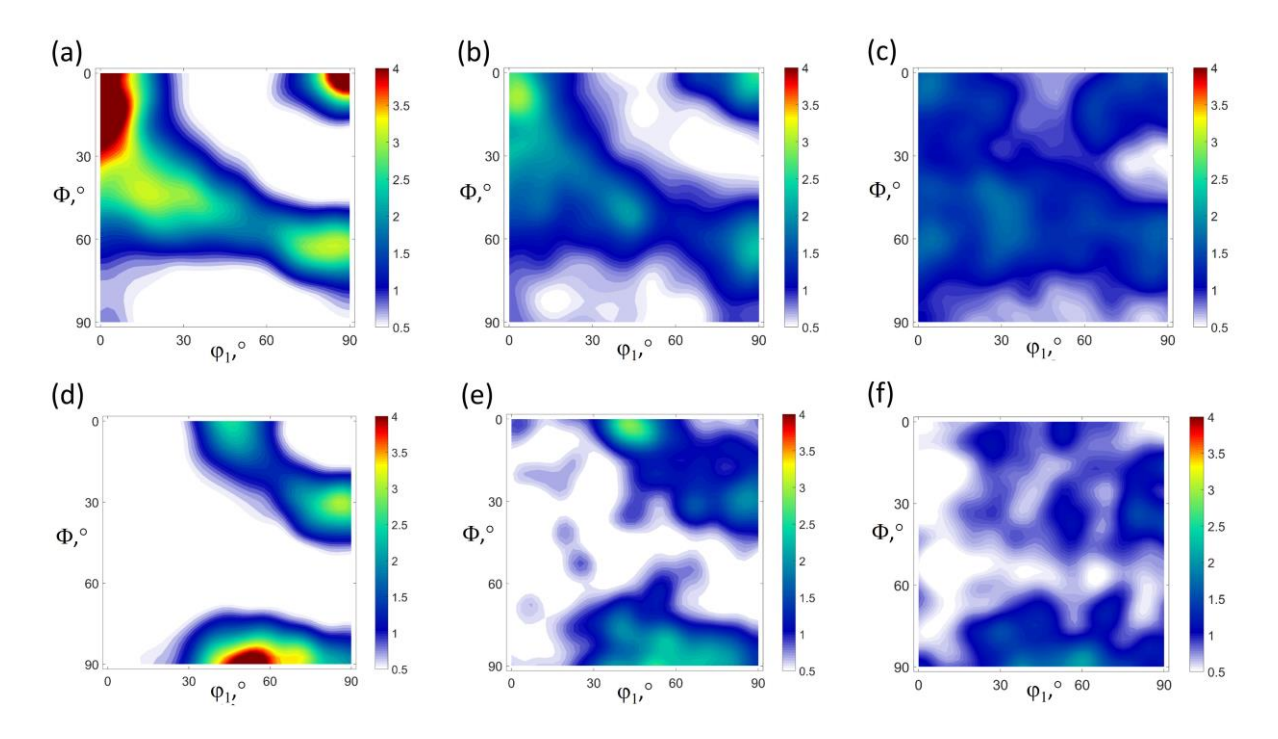


Fig. 7. Sections of ODF at φ_2 = 45° for the measured transformation textures of bainitic steel (a,b,c) and its reconstructed parent textures (d,e,f). Figures (a,d), (b,e) and (c,f) correspond, respectively, to the regimens B₁, B₂ and B₃

very weak, it indicates, together with the morphological features of austenite grains (Fig. 5(a)), an occurrence of certain recrystallization. The conservation of pronounced rolling texture in the samples of bainitic steel allows us to assume that those recrystallization is associated mostly with local migration of grain boundaries, similar to what happens during continuous recrystallization [30]. A deformation texture is known to mostly retain during such a structural transformation, while a strengthening of Cube component may be caused by a preferential growth of Cube-oriented regions [31].

For B_2 , the texture components related to the rolling are considerably weaker than for B_1 , both in the transformation and parent textures, while the Cube component is stronger. This confirms an increased contribution of recrystallization to the austenite structure formation during this mode of hot rolling.

Therefore, it turned out that, in the case of multi-pass rolling of bainitic steel, the textural analysis enables to assess structural state of parent austenite more unambiguously than the reconstruction of austenite grains. Moreover, not only the reconstructed austenite texture but even the transformation texture gives this possibility. With regard of this finding, a simple scalar parameter is suggested and verified in the next section for quantification of those assessment.

Quantification of austenite states in textural terms

To introduce a single scalar [26] indicative of the whole texture, we will allow only for two components of the latter, which are unambiguous and most strong. Specifically, at the deformed state of parent austenite (Fig. 1(a)) they are Brass and Copper components, whereas in the respective transformation texture the transformed Copper and the right

lower constituent of transformed Brass should be considered. Accumulation of rolling strains is then expressed by textural parameter

$$t=0.5(p_1+p_2)/r-1,$$
 (1)

where p_1 and p_2 are probability densities averaged within 15° deviations from virtual centers of the two considered components and r is probability density in case of the random orientation distribution [32]. Note that austenite recrystallization, if any, is also reflected by t insofar far as probabilities of all texture components sum to unity. Derived from measured transformation textures and statistics of the reconstructed prior grain orientations, the considered parameters are listed in Table 1 with subscripts α and γ , respectively. In turn, states B_1-B_3 of bainite follow the gradual texture weakening in accordance with strain degree stored in austenite before its transformation.

Table 1. Characteristics of austenite states as derived from the transformation (α) and parent (γ) textures of steel

Parent	Textural	parameter	Recrystallization degree, %		
state	t_{lpha}	t_{γ}	R_{lpha}	R_{γ}	
M_1	3.7	3.8	0*	0*	
M ₂	0.7	-0.1	100*	100*	
B ₁	4.0	3.6	0	5	
B ₂	2.5	2.0	40	46	
B ₃	1.6	1.6	-	-	

^{*}Calibration according to the grain morphology

Let the completely deformed and recrystallized austenite states appear at $t \ge t_d$ and $t \le t_r$, respectively, where reference t_α and t_γ are found by metallographic methods. Then, using a kind of the lever rule as proposed in [26], the recrystallization degree is roughly evaluated by:

$$R = \begin{cases} 1, & t \le t_r \\ 0, & t \ge t_d \\ (t_d - t)/(t_d - t_r), & t_r < t < t_d \end{cases}$$
 (2)

To discriminate between transformation (measured) and parent (reconstructed) textures in what follows, corresponding estimates of t and R will have appropriate subscripts. As to t_d and t_r , they are determined in previously considered special states M_1 and M_2 , respectively. Concerning mode B_3 , values $R_\alpha = 70$ % and $R_\gamma = 57$ % formally calculated according to Eq. (2) have not been placed in Table 1, since a true recrystallization did not occur in this case. According to the listed results, the two compared methods satisfactorily correspond to each other. Thus, plausible assessments of the parent state are possible without the reconstruction of prior grains. Obviously, rapidly developing methods of reconstruction remain in demand since *morphology* of the austenite structure undoubtedly affects the kinetics of transformation during subsequent cooling. In this regard, a simplified approach based on the Bain relationship finds one more application as the tool to verify grain reconstruction algorithms in textural terms.

Conclusions

Characterization of parent austenite in the samples of bainitic steel treated by multi-pass hot rolling has been performed using EBSD analysis of bainite as well as EBSD-based

reconstruction of parent austenite. The reconstruction of austenite structure has showed that considerable recrystallization proceeded during last passes of the rolling. However, this is not a usual "discontinuous" recrystallization [31], which includes nucleation of new grains and their growth at the expense of neighboring deformed grains. Judging from both textural and structural analysis, the observed mode of recrystallization is mostly reduced to the local migration of boundaries, similar to the continuous recrystallization of heavily deformed metals.

In spite of apparent occurrence of recrystallization, it is difficult to assess its degree in multi-passed hot rolling from the reconstructed austenite structure. At the same time, such an assessment can be made based on the crystallographic texture. To do this, we have introduced a scalar parameter dependent on the intensity of main texture components. To calibrate this textural parameter, a martensitic steel in two conditions has been used; in the first condition the parent austenite was deformed while in the second it was completely recrystallized. Such an analysis can be performed based on the transformation texture or the reconstructed austenite texture, and these two methods were shown to agree satisfactorily. Thus, assessment of the parent austenite state is possible even without the reconstruction of prior grains.

CRediT authorship contribution statement

Conflict of interest

The authors declare that they have no conflict of interest.

References

- 1. Kurdjumov G, Sachs Z. Uber den machanismus der stahlhartung. Zeitschrift für Physic. 1930;64: 325 343.
- 2. Greninger AB, Troyano AR. The mechanism of martensite formation. JOM. 1949;1: 590 598.
- 3. Wassermann G. Einfluß der $\alpha-\gamma$ -Umwandlung eines irreversiblen Nickelstahls auf Kristallorientierung und Zugfestigkeit. *Archiv für das Eisenhüttenwesen.* 1933;6(8): 347–351.
- 4. Brown EL, Deardo AJ. On the origin of equiaxed austenite grains that result from the hot rolling of steel. *Metallurgic and Materials Transactions A.* 1981;12: 39–47.
- 5. Jonas JJ. Transformation textures associated with steel processing. In: Haldar A, Suwas S, Bhattacharjee D. (eds.) *Microstructure and Texture in Steels*. London: Springer; 2009. p.3–17.
- 6. Zisman AA, Petrov SN, Zolotorevsky NY, Yakovleva EA. Effect of industrial hot rolling mode on microstructure and properties of low carbon bainitic steel. *Materials Physics and Mechanics*. 2023;51(6): 54–64.
- 7. Miyamoto G, Iwata N, Takayama N, Furuhara T. Mapping the parent austenite orientation reconstructed from the orientation of martensite by EBSD and its application to ausformed martensite. *Acta Materialia*. 2010;58(19): 6393–6403.
- 8. Bernier N, Bracke L, Malet L, Godet S. An alternative to the crystallographic reconstruction of austenite in steels. *Materials Characterization*. 2014;89: 23–32.
- 9. Abbasi Majid, Kim DI, Nelson TW, Abbasi Mehrdad. EBSD and reconstruction of pre-transformation microstructures, examples and complexities in steels. *Materials Characterization*. 2014;95: 219–231.
- 10. Eres-Castellanos A, Morales-Rivas L, Jimenez JA, Caballero FG, Garsia-Mateo C. Effect of ausforming on the macroand micro-texture of bainitic microstructures. *Metallurgical and Materials Transactions: A.* 2021;52: 4033–4052.

- 11. Shibata A, Miyamoto G, Morito Sh, Nakamura A, Moronaga T, Kitano H, Gutierrez-Urrutia I, Hara T, Tsuzaki K. Substructure and crystallography of lath martensite in as-quenched interstitial-free steel and low-carbon steel. *Acta Materialia*. 2023;246: 118675.
- 12. Niessen F, Nyyssönen T, Gazder A, Hielscher R. Parent grain reconstruction from partially or fully transformed microstructures in MTEX. *Journal of Applied Crystallography*. 2022;55(1): 180–194.
- 13. Hielscher R, Nyyssönen T, Niessen F, Gazder A. The variant graph approach to improved parent grain reconstruction. *Materialia*. 2022;22: 101399.
- 14. Taylor M, Smith AD, Donoghue JM, Burnett TL, Pickering E. *In-situ Heating-Stage EBSD Validation of Algorithms for Prior-Austenite Grain Reconstruction in Steel [Data Set]*. Zenodo; 2023.
- 15. Qiu C, Xu R, Xu X, Ma S. Finite element simulation of multi-pass rolling of a pure aluminum target under different rolling routes and methods. *Metals*. 2024;14(8): 845.
- 16. Lin X, Zou X, An D, Krakauer BW, Zhu M. Multi-scale modeling of microstructure evolution during multipass hot-rolling and cooling process. *Materials*. 2021;14(11): 2947.
- 17. Jiang JF, Liu YZ, Xiao GF, Wang Y, Ju YN. Effect of pass reduction on microstructure, mechanical properties and texture of hot-rolled 7075 alloy. *Materials Characterization*. 2019;147, 324–339.
- 18. Xiao XD, Zhang QZ, Li YJ, Qin FM. Effect of deformation pass on softening mechanism and microstructure of 7085 alloy. *Materials Science and Technology*. 2023;39(4): 509–518.
- 19. Sun P, Yang H, Huang R, Zhang Y, Zheng S, Li M, Koppala S. The effect of rolling temperature on the microstructure and properties of multi pass rolled 7A04 aluminum alloy. *Journal of Materials Research and Technology*. 2023;25: 3200–3211.
- 20. Bain EC. The nature of martensite. Trans. AIME. 1924;70: 25-35.
- 21. Germain L, Gey N, Humbert M. Reconstruction of deformed parent grains from microstructure inherited by phase transformations. *Scripta Materialia*. 2019;158: 91–94.
- 22. Hayashi T, Morito S, Ohba T. Local distribution of orientation relationship and microstructure evolution of lath martensite in an ultra-low-carbon steel. *Scripta Materialia*. 2020;180: 1–5.
- 23. Cayron C, Baur A, Logé RE. Intricate morphologies of laths and blocks in low-carbon martensitic steels. *Materials and Design*. 2018;154: 81–95.
- 24. Taylor AS, Cizek P, Hodgson PD. Orientation dependence of the substructure characteristics in a Ni 30Fe austenitic model alloy deformed in hot plane strain compression. *Acta Materialia*. 2012;60(4): 1548 1569.
- 25. Poddar D, Cizek P, Beladi H, Hodgson PD. The evolution of microbands and their interaction with NbC precipitates during hot deformation of a Fe-30Ni-Nb model austenitic steel. *Acta Materialia*. 2015;99: 347-362. 26. Zisman AA, Zolotorevsky NY, Petrov SN. Texture analysis of hot rolled martensitic and bainitic steels by electron
- backscatter diffraction to quantify parent austenite states. *Steel Research International*. 2024:95(7): 2300901.
- 27. Benscoter A, Perricone M, Marshall's reagent: origins, modifications, and new applications. *Microscopy and Microanalysis*. 2005;11(S02): 76–77.
- 28. Bunge H-J. *Texture analysis in materials science. Mathematical methods.* Cuvillier Verlag: Göttingen; 1993.
- 29. Hutchinson B, Kestens LAI. Origins of texture memory in steels. In: Rollett AD. (ed.) *Applications of Texture Analysis*. Hoboken, New Jersey: John Wiley & Sons; 2008. p.281–290.
- 30. Sakai T, Belyakov A, Kaibyshev R, Miura H, Jonas JJ. Dynamic and post-dynamic recrystallization under hot, cold and severe plastic deformation conditions. *Progress in Materials Science*. 2014;60: 130–207.
- 31. Rollett A, Humphreys FJ, Rohrer GS, Hatherly M. *Recrystallization and related annealing phenomena*. 2nd ed. Elsevier; 2004.
- 32. Engler O, Randle V. *Introduction to texture analysis: macrotexture, microtexture, and orientation mapping.* Taylor and Francis Group; 2010.

Submitted: March 12, 2024 Revised: June 4, 2024 Accepted: July 31, 2024

Structural changes in a commercial Al-Cu alloy during hot equal channel angular pressing

O.S. Sitdikov [™] (i)

Institute for Metals Superplasticity Problems of RAS, Ufa, Russian Federation

[™] sitdikov.oleg@imsp.ru

ABSTRACT

The evolution of the structure of aluminum alloy 2219 ingot during equal channel angular pressing (ECAP) to a cumulative strain of e=12 at 475 °C (\sim 0.8 $T_{\rm m}$) was studied. It was found that the structural changes during hot ECAP were determined by the action of two main structural processes. In the early stages of ECAP (e=1-3), the alignment of the initial grains in the pressing direction was mainly accompanied by the formation of a dynamically equilibrated subgrain structure. However, upon reaching a critical strain ($e \approx 3-4$), grain fragmentation by deformation/microshear bands started with a subsequent gradual increase in the number of bands and their misorientation, leading to grain refinement. As a result, a heterogeneous bimodal grain structure was formed after e=12, consisting of about 50 % new grains of about 10 μ m size and residual fragments of the initial grains containing subgrains. It was concluded that grain refinement during hot ECAP occurred by the mechanism of continuous dynamic recrystallization.

KEYWORDS

aluminium alloy 2219 • equal channel angular pressing • ECAP • microstructural evolution • grain refinement **Funding**. The research was supported by the Ministry of Science and Higher Education of the Russian Federation within the framework of the state assignment of IMSP RAS

Acknowledgements: The author is grateful to Prof. T. Sakai (UEC Tokyo, Japan) and Drs. A. Belyakov and R. Kaibyshev (BSU, Russia) for fruitful discussions that contributed to this study. Some experimental results were obtained in the joint research with I.A. Mazurina and I.S. Oleneva.

Citation: Sitdikov OS. Structural changes in a commercial Al-Cu alloy during hot equal channel angular pressing. *Materials Physics and Mechanics*. 2025;53(1): 89–108. http://dx.doi.org/10.18149/MPM.5312025_8

Introduction

The problem of obtaining bulk ultrafine-grained (UFG) materials (grain size less than 1 μ m) is of considerable interest to researchers working in the field of materials science and solid state physics [1–5]. This is due to the range of high physical and mechanical properties that can be achieved, allowing such materials to be widely used in practical applications [2,3]. In order to form a UFG structure in bulk billets, severe plastic deformation (SPD) methods, such as equal channel angular pressing (ECAP) [1–5], accumulative roll bonding [1,2,5], multidirectional isothermal forging [1–3,5], etc. are often used. In addition, these methods can also be considered as an effective "scientific tool" for obtaining knowledge about the structural changes that occur during large strain deformations [1,4,5].

At present, both the characteristics of the above-mentioned SPD methods and the properties of the UFG-structured semi-finished products obtained by such methods have been quite well studied [1-35]. In particular, a large number of studies have been devoted



to the analysis of changes in the structure of aluminum alloys, which are typical materials with high stacking fault energy. It has been shown in [4,6,8,12-21,24,26,31] that in these alloys SPD can cause fragmentation of the initial grains with the formation of dislocation boundaries with medium angular misorientation ($\Theta \approx 5-15^{\circ}$), which are the boundaries of deformation bands. With increasing strain, the number and misorientation of these boundaries increase, leading to the formation of new ultrafine grains surrounded mainly by high-angle boundaries ($\Theta \ge 15^{\circ}$) at relatively high strains. It has been concluded that the formation of new grains in this case is due to the occurrence of continuous dynamic recrystallization (cDRX) [11,12,15,16,21,26].

However, detailed studies of the microstructure evolution during SPD in aluminum and its alloys have usually been limited to the temperature range from 20 to 250-300 °C ($T \le 0.6T_m$), i.e. they have been performed under conditions of so-called cold or warm deformation [1,4,6-8,10-24,27,28,31]. At the same time, they were carried out much less frequently under conditions of hot deformation at higher temperatures ($T \approx 0.7-0.8T_m$). This can be explained both by the technical difficulties of implementing SPD schemes under isothermal conditions at high temperatures (e.g. in the ECAP process) and by the decrease in practical interest in materials where the size of the resulting grains no longer belonged to the UFG range. Accordingly, the use of SPD schemes at such high temperatures has generally been recommended only for processing hard-to-deform and/or brittle materials. As a result, there remains a significant gap in the understanding of the nature and characteristics of structure formation at large strains and high temperatures [35].

For example, it has been shown in [11,26] that the same grain refinement mechanism associated with grain fragmentation due to deformation banding can occur at different temperatures during both warm and hot deformation. In the case of Al-Mg alloys with transition metals (such as Al 1570) [26], this mechanism led to the formation of new grain structures with similar angular characteristics regardless of processing temperature. In a number of cases, grain refinement accelerated with increasing temperature, particularly in high-strength complex-alloyed alloys of the 7XXX series [12,18]. In other materials, however, an increase in temperature may suppress grain refinement or alter the dominant mechanisms of structure formation, such as in Al, Al-Cu alloys, and some steels [6,9,10,13,16,19,23,29,30,32]. Therewith, possible variants of material behavior during hot deformation were the transition from fragmentation-related cDRX to either geometric-type dynamic recrystallization or discontinuous dynamic recrystallization [13,25,27,29,30]. It has also been suggested that in the high-temperature region, the process of grain refinement due to the development of deformation bands may be replaced by the evolution of more homogeneous deformation-induced subgrain structures associated with the progressive rotation of individual subgrains and their transformation into new grains. Thus, the question of the mechanisms and patterns of new grain formation during hot deformation remains open (and covered by rather insufficient information in the literature).

The objective of this work was to analyze the microstructural changes during ECAP of the aluminum alloy 2219 at 475 °C (about $0.8T_m$). Previous studies [15,16,33] have shown that ECAP at temperatures of 250–475 °C leads to the formation of new grains after high strains (e = 10-12). However, the evolution of the microstructure has been

studied in detail mainly during warm deformation at 250 °C [15], while the features of the structural changes at the highest temperature (475 °C) have been insufficiently investigated and only partially presented in previous publications [16,33]. In the present work, additional studies of the microstructure at this temperature as a function of strain were carried out in order to identify the main mechanisms and factors influencing grain refinement during hot working of the aluminum alloy.

Materials and methods

Commercial aluminum alloy AA2219 with the following chemical composition Al-6.4Cu-0.3Mn-0.18Cr-0.19Zr-0.06Fe (wt. %) was produced by the semi-continuous casting method. The alloy was homogenized at a temperature of 530 °C for 6 h, followed by cooling in a furnace to obtain an equilibrium phase composition.

The workpieces for ECAP, in the form of rods 20 mm in diameter and 100 mm in length were cut parallel to the ingot axis. ECAP was performed under isothermal conditions at a temperature of 475 °C using a die with an L-shaped channel configuration with internal and external angles of φ = 90° and ψ = 0°, respectively. This configuration provided a true equivalent strain e of approximately 1 per pass [6]. The workpieces were deformed to e = 12 using the route A (i.e., without rotation between passes). The deformation was performed in a hydraulic press with a ram speed of 6 mm/s. According to [36], this resulted in an average effective strain rate of 3 s⁻¹. To fix the formed microstructure, the pressed parts were cooled in water after each pass and then heated for 45 min before the next pass. The average time interval between the start of deformation in each pass and the immersion of the workpiece in water after pressing was about 1.5 min. Some additional time for the workpiece in the die was due to the typical features of the ECAP process, where the workpiece after pressing is pushed out of the channel by the next workpiece inserted into the die. The structure of the workpieces subjected to ECAP was analyzed in a longitudinal section parallel to the pressing direction (PD).

Metallographic analysis was carried out using optical microscopy (OM) after etching the samples in Keller's standard reagent. For scanning electron microscopy (SEM) with electron backscatter diffraction (EBSD) analysis, the samples were electropolished in a solution of 80 % C₂H₅OH, 12 %, 2n-butoxyethanol, 8 % HClO₄ at room temperature. EBSD analysis was performed using Hitachi S-4300H and TESCAN MIRA3 LMH field emission scanning electron microscopes equipped with OIM Analysis™ and HKL Channel 5 software, respectively [37,38]. The investigated areas were scanned with a step size of 1.5 µm. In the EBSD maps of the reconstructed structures, different colors corresponded to different crystallographic orientations according to the standard green (110) / red (100) / blue (111) triangle, and intercrystallite boundaries with low $(2 \le \theta < 5^\circ)$, medium $(5 \le \theta < 15^\circ)$ and high ($\theta \ge 15^{\circ}$) angular misorientations were marked with thin white, thin dark gray and thick black lines, respectively. Boundaries with misorientations less than 2° were not considered. Distributions of misorientations of deformation-induced (sub)grain boundaries were obtained from the EBSD data both for the entire scanned area and for selected areas (using the standard "structure cropping" and/or "subset selection" options of the EBSD software [37,38]), as described in more detail below. The average grain size in the formed fine-grained regions was estimated using the line-intercept method. The

width of the deformation bands (the average distance between the nearest band boundaries) was measured perpendicular to the direction of their preferred orientation. The volume fraction of fine grains $V_{\rm fg}$ was determined by the point-counting method. Thin foils for transmission electron microscopy (TEM) were obtained by electropolishing at a temperature of -28°C in a solution of 30 % HNO₃ and 70 % CH₃OH using a TenuPol-5 double-jet polisher and examined with a JEOL 2000EX TEM microscope.

Results and Discussion

Initial structure

After homogenization, the alloy matrix was represented by equiaxed grains with diameters ranging from 100 to 400 μ m (Fig. 1(a)). Several types of second phases were identified in the structure [39–41]: T-phase dispersoids (Al₂₀Cu₂Mn₃) in the form of plates up to 200 nm long, as well as spherical precipitates of Al₇Cr and Al₃Zr with sizes of 80 and 20 nm, respectively (Fig. 1(b)). Larger precipitates of the main strengthening phase Θ (Al₂Cu) were also observed, uniformly distributed within the grains and in the boundary regions (Fig. 1). It is known that precipitates of the Al₃Zr phase can be both coherent and incoherent with the matrix after homogenization [40]. According to the analysis in [39], almost 90 % of the Al₃Zr dispersoids in the studied alloy were incoherent.

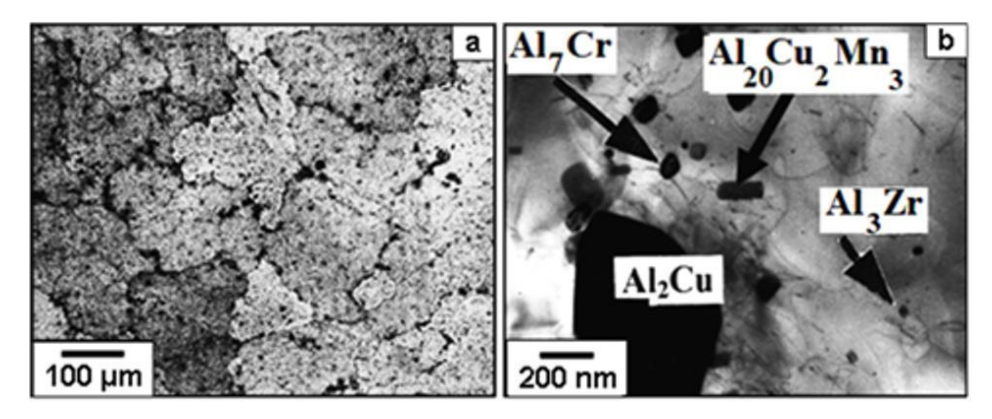


Fig. 1. Initial structure of alloy 2219 after homogenization: (a) OM; (b) TEM

Structure formed during ECAP

A typical alloy structure formed during ECAP is shown in Figs. 2 and 3. At $e \le 4$, pressing along route A mainly resulted in a change in the shape of the initial grains, which were elongated in the pressing direction (PD) according to simple shear [4,5] (Fig. 2(a)). As a result, after e = 4 (Fig. 2(b)), a non-uniform microstructure was observed in the material, containing large elongated grains in the interior of which a well-developed substructure was formed, as judged by the etching patterns. In some areas, these grains acquired wavy boundaries (see for example the upper part of Fig. 2(b)) and were sometimes replaced by chains of smaller and more equiaxed crystallites, as can be seen in the attached higher magnification image in the lower left corner of Fig. 2(b).

With a further increase in the number of passes (e = 4-12), the character of the microstructural evolution changed significantly (Fig. 3). Namely, new fine grains began

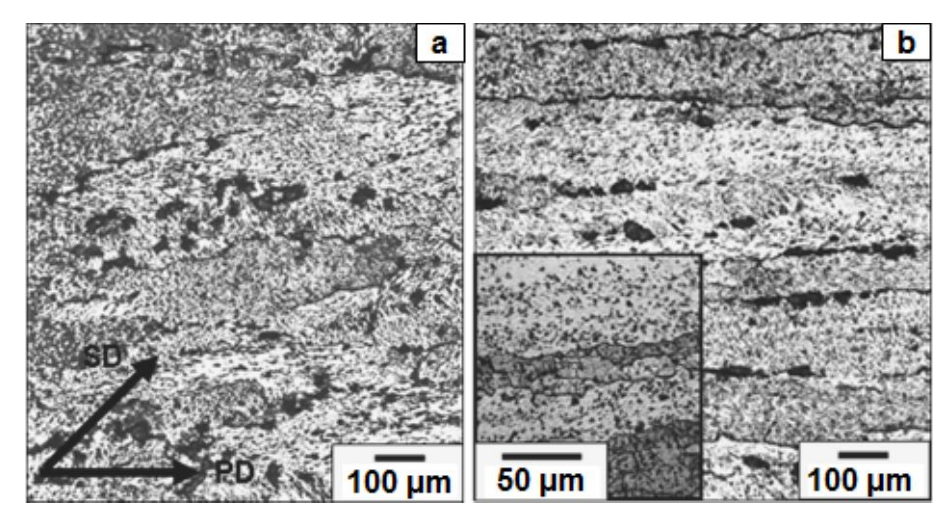


Fig. 2. OM-images of microstructure of alloy 2219 after ECAP at T = 475 °C to: (a) e = 2, (b) e = 4. Hereafter, SD is the main shear direction, PD is the pressing direction during ECAP

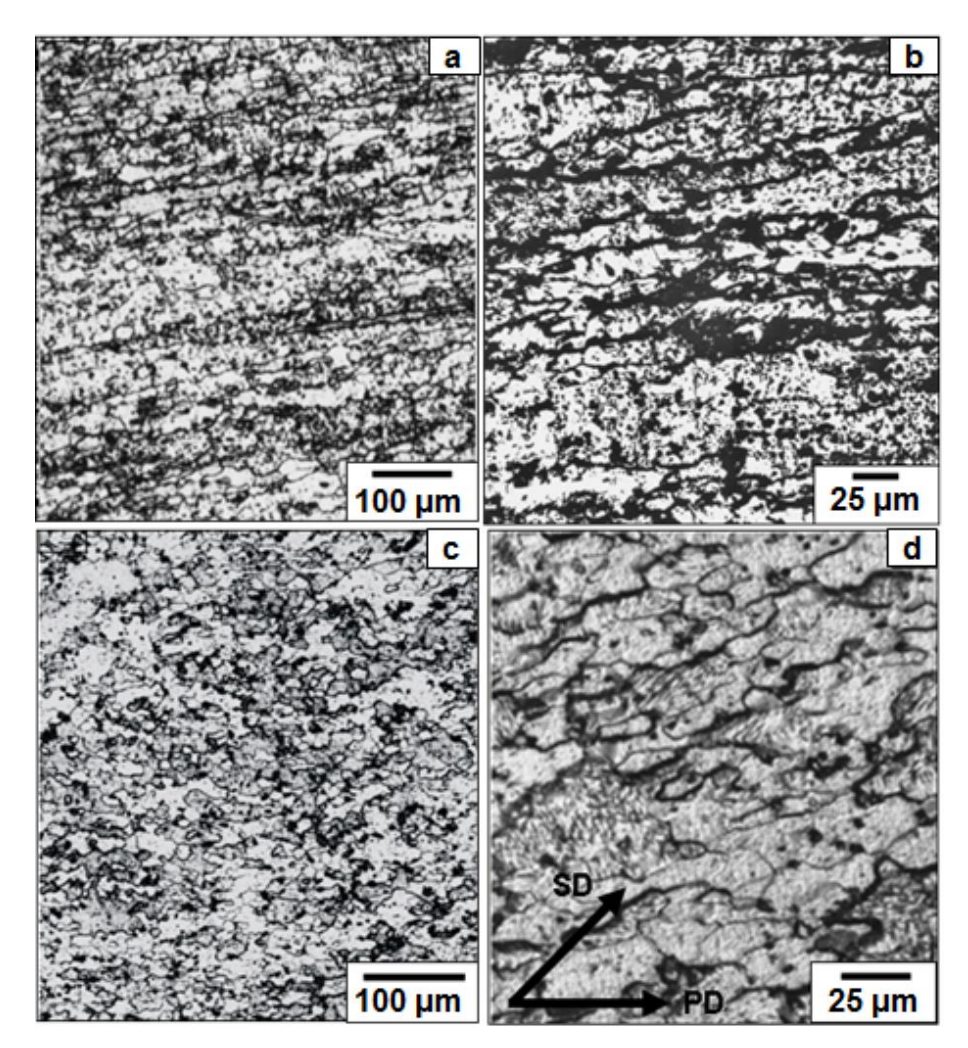


Fig. 3. OM-images of microstructure of alloy 2219 after ECAP at T = 475 °C to: (a,b) e = 8, (c,d) e = 12

to form within the large grains and the coarse-grained microstructure was gradually replaced by regions of a new fine-grained structure. After e = 8-12, a mixed bimodal structure was observed in the alloy, consisting of colonies of fine grains and larger fragments of the initial grains aligned in the PD (Fig. 3(a,c)). At higher magnification it

can be seen that the grains were refined mainly by the formation of banded structures at the mesolevel and fragmentation of the initial grains (Fig. 3(b)). After e = 12, most of the new small grains had an elongated shape and common boundaries within the bands, which were predominantly oriented along the main shear direction (SD) during ECAP, i.e. at an angle of about 45° with respect to the PD (Fig. 3(d)). The observed evolution of the alloy microstructure can be quantitatively characterized by the change in the volume fraction of new fine grains (V_{fg}) during ECAP (Fig. 4). Up to e = 3, V_{fg} did not exceed 5 %, but began to increase rapidly at $e \ge 4$. However, even at such a high strain as e = 12, the volume fraction of fine grains reached relatively low values, barely exceeding 50 %.

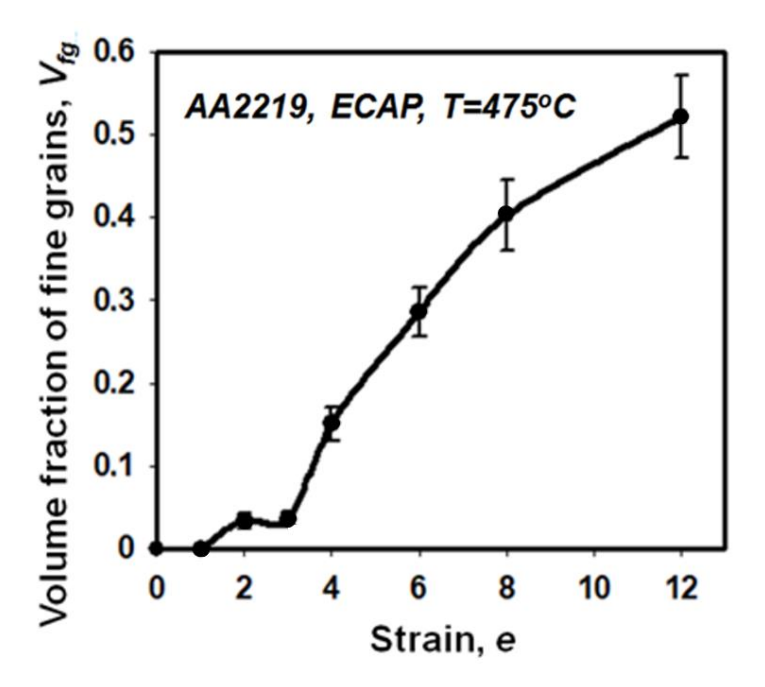


Fig. 4. Strain dependence of the volume fraction of new fine grains formed in alloy 2219 during ECAP at T = 475 °C

EBSD (Figs. 5–7) and TEM (Fig. 8) were used to examine the deformation structures formed during ECAP in more detail. Figure 5 shows that in the early stages of ECAP (e=1-3), a network of low angle boundaries was formed within the initial grains. These boundaries were uniformly distributed in the matrix and were mainly associated with the formation of a homogeneous subgrain structure due to the occurrence of dynamic polygonization [42–45]. In addition, after e=1, extended subboundaries with low and medium angular misorientations oriented at angles from 0 to 15° relative to the PD were observed in individual grains (Fig. 5(a)). The formation of these boundaries, as judged by the local change in color contrast within the grains, was accompanied by significant lattice rotations. This allowed them to be classified as deformation bands resulting from strain localization [4,6,17,24,26,34,46].

It is well known that deformation bands can form in a material when fewer than five independent slip systems required for uniform deformation are active [1,17,44–46]. These include the so-called primary deformation bands [14,17,24,34], which show fairly clear boundaries on EBSD maps and can develop at the macro- and mesolevel (i.e. at the level of several initial grains) in the early stages of ECAP. However, it was quite surprising

to observe their formation in an alloy with an fcc lattice at a temperature of $0.8\,T_{\rm m}$, when a priori at least five slip systems should be active in most grains. Probably, the formation of deformation bands during hot ECAP was caused by plastic restrictions in some grains due to the requirements of their compatible deformation with neighboring grains [1,11,12,14–17,20,44], which occurred independently of the processing temperature, and/or was a result of deformation localization during ECAP due to the peculiarities of their orientation with respect to the main shear plane [4–6]. It should be noted that after their formation such deformation bands could exist in the alloy even at high temperatures due to stabilization of the dislocation structure by precipitates of second phases [12,21,22,27,43], mainly dispersoids (see Figs. 1 and 8).

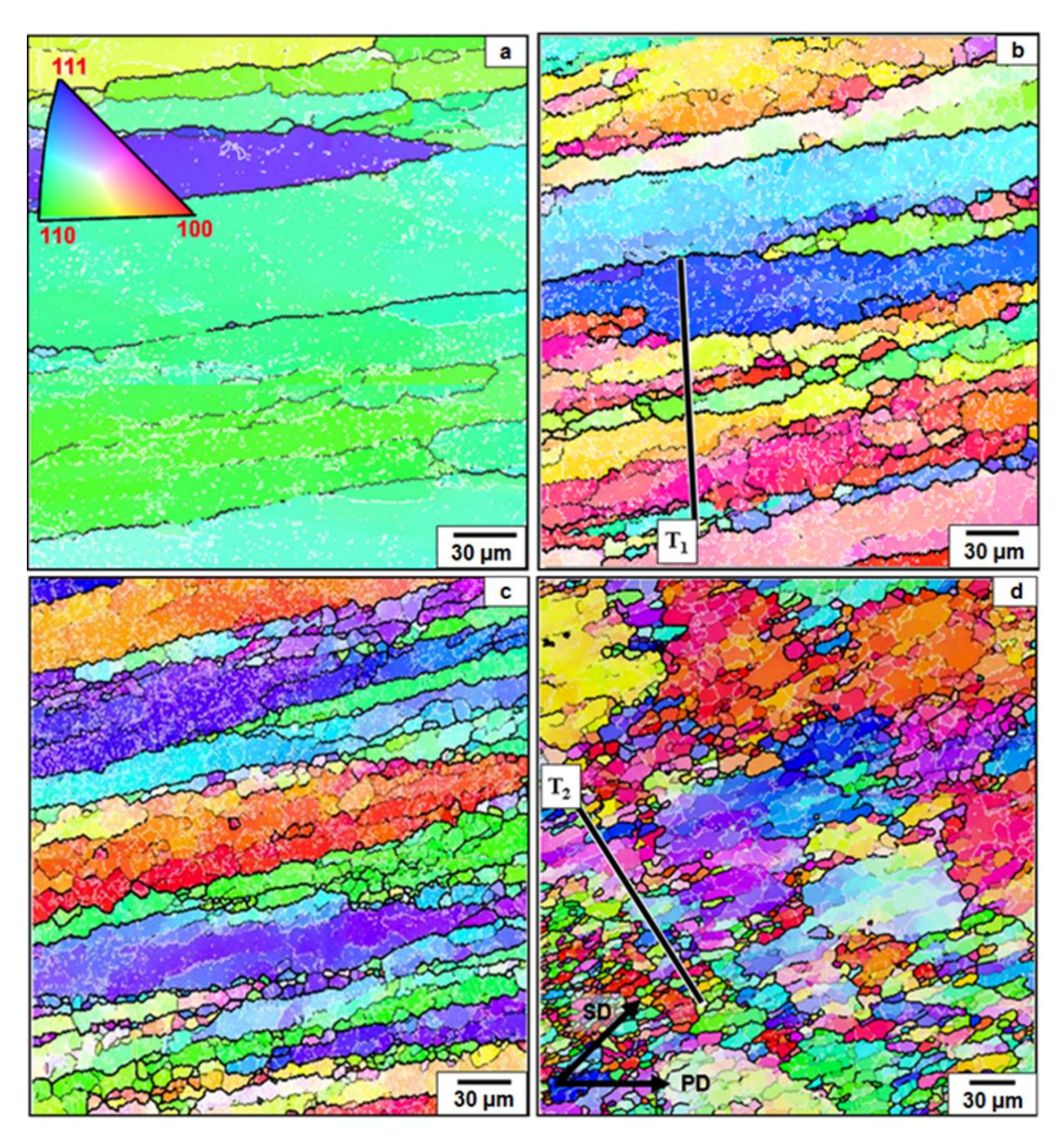


Fig. 5. Typical EBSD maps of alloy 2219 after ECAP at T = 475 °C to: (a) e = 1, (b) e = 2, (c) e = 3, (d) e = 6

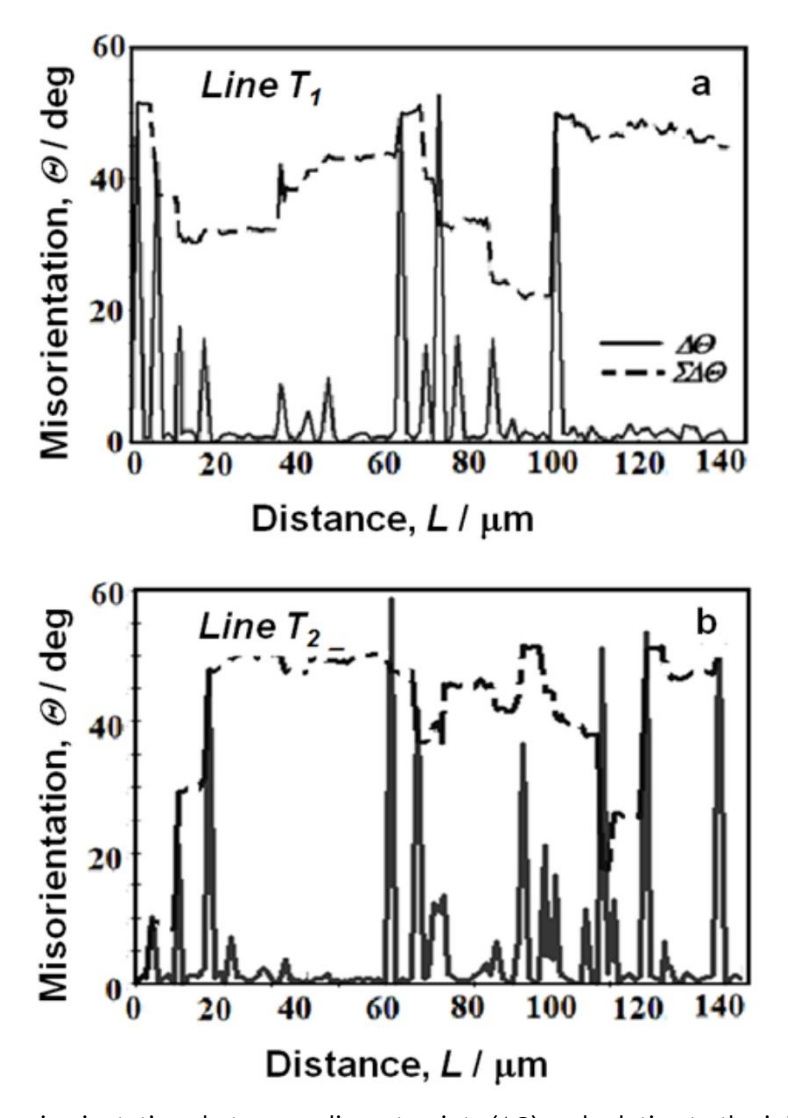


Fig. 6. Change in misorientations between adjacent points ($\Delta\Theta$) and relative to the initial point ($\Sigma\Delta\Theta$) along test lines T_1 and T_2 in Fig. 5

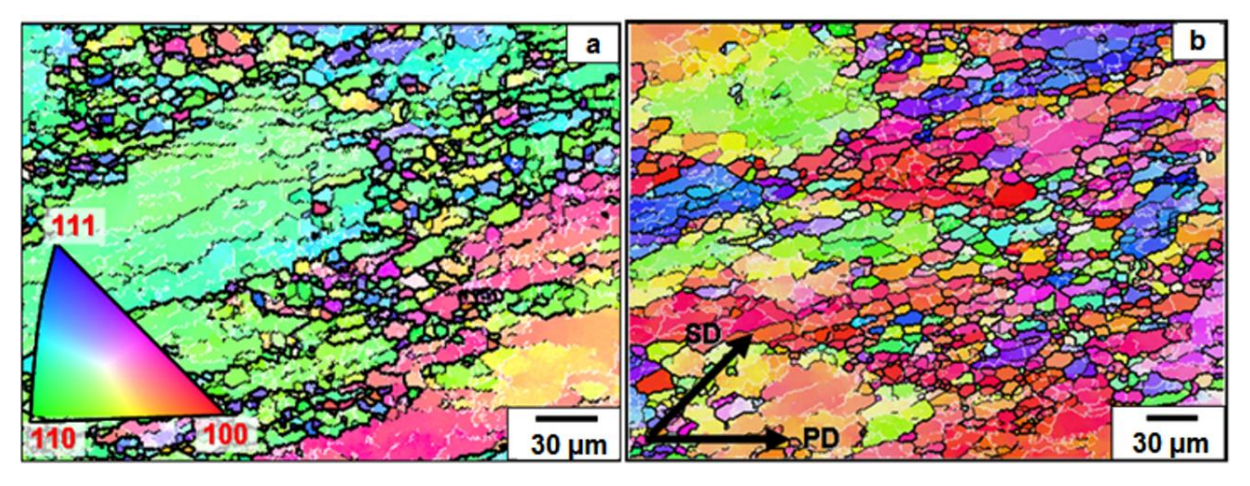


Fig. 7. EBSD maps of alloy 2219 after ECAP at T = 475 °C to: (a) e = 8, (b) e = 12

It is known from the literature that during cold and warm deformation of aluminum alloys, once formed, deformation bands remain permanent elements of the structure, in contrast to cells/subgrains which are of an "incidental" nature [42,44], i.e. they are

continuously repolygonized during deformation. Accordingly, under simple shear during cold ECAP, the band boundaries, like the boundaries of the initial grains, gradually align along the PD with increasing strain, leading to an additional increase in the number of longitudinal intercrystallite boundaries [4,6,8,13,17,21,24,34]. Similar structural changes were observed in the early stages of hot ECAP of this alloy (Fig. 5). Namely, at e = 2-3, single grains containing deformation bands were transformed into fibers elongated along the PD, outlined by alternating longitudinal boundaries of bands with medium to high angular misorientations and boundaries of the initial grains (Fig. 5(b,c)). The width of such crystallites at the strains considered was significantly smaller than the average distance between the longitudinal boundaries of the initial deformation band-free grains [25]. In subsequent passes, the misorientation of the deformation band boundaries increased and the distance between them decreased. Note that some of these thinner fibers were replaced by chains of equiaxed grains with a close (judging by the color contrast on the EBSD maps) crystallographic lattice orientation and approximately the same transverse size as the fibers themselves. This suggests that new grains could form in place of the deformation bands as a result of a mechanism similar to geometric dynamic recrystallization [25,33,42,43]. Thus, during ECAP, the fiber boundaries became serrated (see Figs. 2 and 5) due to the surface tension of the subgrain boundaries formed during dynamic polygonization [43]. As the distance between fiber boundaries decreased during deformation, opposite boundary segments could come into contact and annihilate each other, leaving more equiaxed fine grains in the structure [25,43].

The conclusion about the occurrence of geometric dynamic recrystallization during high-temperature ECAP of the studied alloy was also based on the results of microstructural observations in a previous work [33]. However, from the subsequent detailed study of the transformation of a similar coarse-grained structure during ECAP in another alloy [25], it should be noted that at e < 3-4 the distance between the boundaries of most of the initial grains remains quite large for the widespread implementation of geometric dynamic recrystallization. At such relatively low strains, this mechanism could only take place in single grains containing deformation bands. Accordingly, the fraction of new grains formed by this mechanism was only a few percent (Fig. 4).

Another feature of the deformation structure of this alloy, although not as noticeable in the early stages of pressing, has been associated with grain fragmentation due to the development of deformation bands at a lower scale (within individual grains), such as microshear bands [4,12,17,24,47]. The EBSD analysis data in Fig. 6 illustrate typical distributions of lattice misorientations between neighboring points ($\Delta\Theta$) and relative to the starting point ($\Sigma\Delta\Theta$) along the test lines T_1 and T_2 drawn within several initial grains in Fig. 5(b) (for e=2) and Fig. 5(d) (for e=6), respectively. Figure 6(a) shows that the misorientation values at e=2 vary mainly randomly from 2 to 5°, corresponding to the intersection of line T_1 with uniformly distributed subgrain boundaries [42–44]. Some peaks with $\Delta\Theta$ greater than 40°, located at a distance of about 40–60 µm from each other, may correspond to the boundaries of the initial grains.

Note, however, that in some regions within the grains, the misorientations reached modal values from 5 to \geq 15° with an average spacing between them of about 10–20 µm, and the cumulative misorientation in the same regions changed discontinuously within 10–15°. These peaks indicated the formation of deformation band boundaries similar to

microshear bands, resulting in "rigid" local rotations and shears in the crystal lattice [6,12,17,24,46,47]. The TEM results also support these data. Figure 8(a) shows that at e=2, elongated crystallites of a non-equilibrium, almost rectangular shape are formed in the material, which may be a consequence of the formation and mutual crossing of the boundaries of the deformation bands [34]. Figure 8(b), taken at a higher magnification, shows that the formation of some such boundaries causes significant displacements and shears in the forming dislocation structure. It can therefore be concluded that these boundaries are the boundaries of microshear bands that develop on the micro- and mesoscale and lead to fragmentation of the initial grains even in the second ECAP pass [17,24,34].

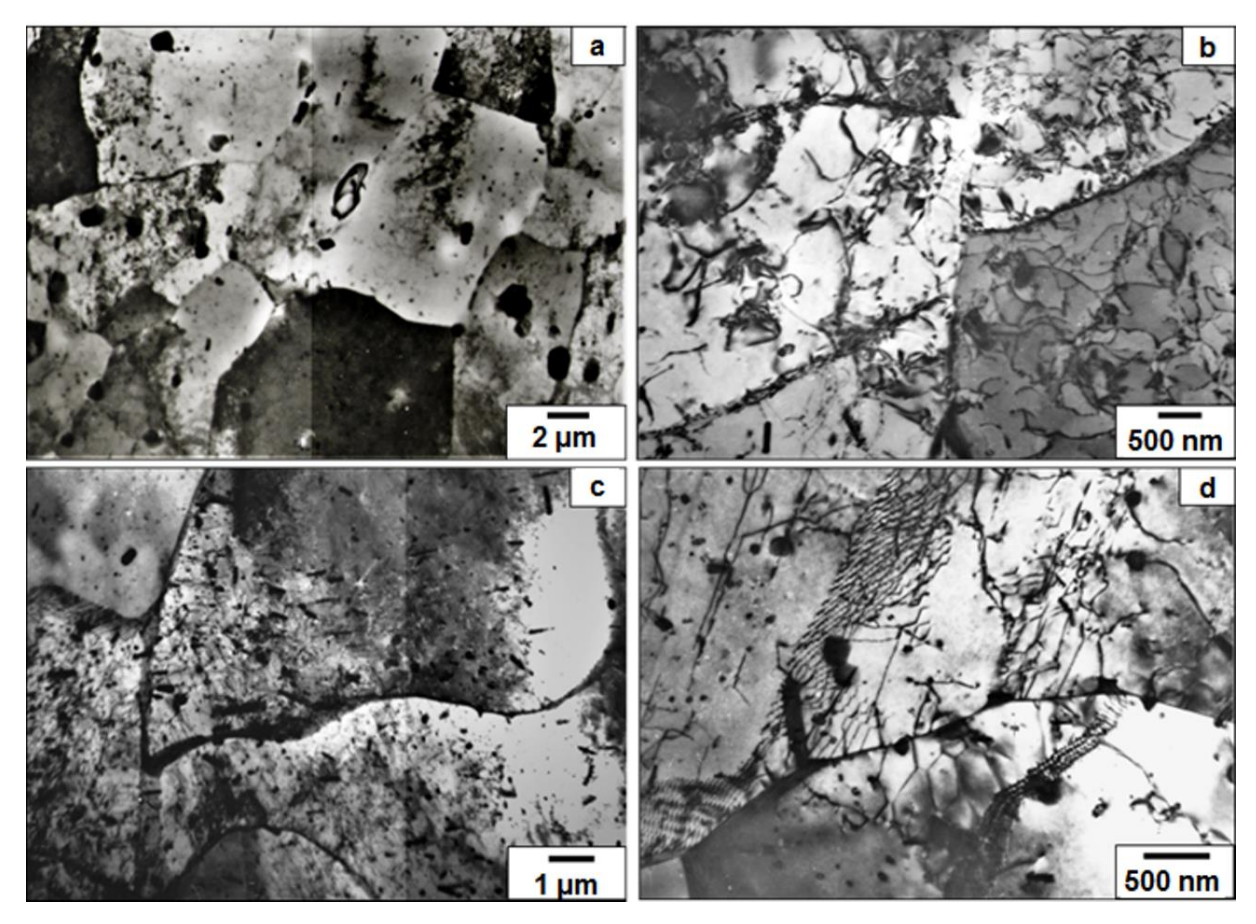


Fig. 8. Typical fine structure of alloy 2219 after ECAP at T = 475 °C to: (a,b) e = 2, (c,d) e = 12

As shown in Fig. 6(b), the number and misorientation of the medium-angle boundaries increased somewhat with increasing strain. Therewith, the EBSD maps clearly showed deformation/microshear bands oriented parallel to SD (i.e. at an angle of 45° to PD), which became one of the main features of the substructure at e = 6 (see Fig. 5(d)). Note that such behavior of the alloy is characteristic of lower deformation temperatures [17,24,34]. Thus, during cold or warm ECAP, microshear bands were formed within the grains regardless of their initial crystallographic orientation [15,17,21,24,34]. In this case, the formation of microshear bands acted as the main structural prerequisite for introducing significant misorientations into the interior of the grains and led to their refinement [17,34,47]. As a result, new grains were formed by fragmentation of the initial

grains during mutual intersection of microshear bands with a subsequent increase in their number and boundary misorientation [12,15].

It has been suggested that the formation of shear bands may be due to a complex interaction of crystal lattice defects and is associated with the involvement of as-formed dislocation structures (lamellar and/or cellular banded) in the ongoing deformation [24,34,48,49]. Accordingly, the development of microshear bands (with subsequent grain refinement) could begin only after certain strains are reached, when stress concentration and/or localization of plastic flow would be sufficient to create such heterogeneous structures. It can be assumed that during hot deformation of this alloy, when the plastic flow was relatively uniform at the micro- and mesolevel during the initial ECAP passes, the formation of microshear bands and grain fragmentation occurred only in localized areas, without being noticeable throughout the sample (Figs. 2,4,5(a-c)). Therefore, only weak signs of strain localization and grain refinement were observed in the range 1 < e < 4. Accordingly, considering only this strain range, it could be concluded that the main process of structure formation during hot deformation of aluminum alloy is the formation of dynamically equilibrium subgrain structure [43-45].

Meanwhile, the results of this work showed that the formation of new fine grains under the present deformation conditions was simply "delayed" until $e \ge 4$, i.e., until microshear bands began to develop extensively in the alloy structure. Thus, in Fig. 5(d), it is evident that at e = 6 new fine grains were formed along the deformation/microshear bands oriented in the SD. And with further deformation to e = 8-12 (Fig. 7), these grains continued to appear following the propagation and development of the bands, i.e. new grains were formed in fragmented regions at the intersection of the bands. In other regions of the material, where deformation bands practically did not form, low-angle (subgrain) boundaries prevailed (see the segment on line T_2 at a distance of 20 to 60 μ m, left side of Fig. 6(b)). In this case, individual large fragments of the initial grains containing subgrains remained even at large strains (Fig. 7(b)).

It should be noted that even at such a high strain as e = 12, the fine structure of the alloy revealed by TEM still contained crystallites of predominantly non-equilibrium rectangular shape with angles in triple junctions close to 90° (Fig. 8(c,d)). The formation of such crystallites, as at lower strains, was apparently caused by the intersection of deformation bands. Strong interaction of deformation-induced boundaries and lattice dislocations with second phase particles present in the alloy was also observed. As mentioned above, the latter could effectively restrict the migration of boundaries and the rearrangement of dislocations over large distances, preventing the relaxation of the accumulated deformation energy and thereby creating conditions for the formation of a new fine-grained structure even during hot deformation. On the other hand, the observed curved/wavy grain boundaries (Fig. 8(c)) and the formation of flat dislocation walls inside the grains (Fig. 8(d)) indicated that due to the high rate of diffusion processes during high temperature ECAP, limited grain boundary migration and dislocation rearrangement over short distances often occurred. Such processes facilitated the rapid transformation of deformation band boundaries from dislocation walls to more balanced and flat high angle boundaries and the formation of new fine grains with more equiaxed shape [34].

Analysis of microstructural parameters

Figure 9 shows the minimum width of deformation bands and the average size of new grains formed in fine-grained regions as a function of strain. The width of the deformation bands was measured from the profiles of misorientations along the test lines plotted on the EBSD maps perpendicular to these bands, as the average distance between neighboring boundaries with misorientations from 5 to 15° (see e.g. Fig. 6). Both parameters quickly decreased to e=6 and remained approximately constant at high strains, slightly exceeding 10 µm. The grain size was close to the width of the bands, indicating that the formation of new grains at high strains was mainly controlled by the evolution of the deformation bands. In other words, the formation of new grains was associated with the fragmentation of the initial grains due to the formation of deformation bands and/or microshear bands and their subsequent transformation into new grains [12,15].

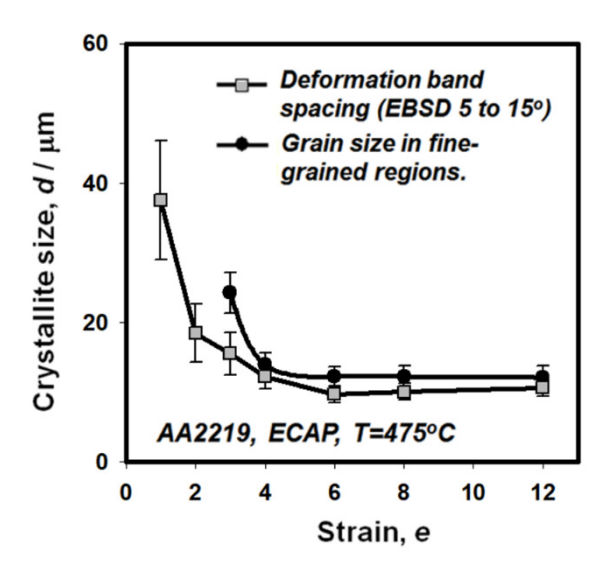


Fig. 9. Strain dependencies of the crystallite size and the width of deformation bands measured in different regions of alloy 2219 after ECAP at T = 475 °C

Changes in the distribution of intercrystallite boundary misorientations averaged over all regions of the forming deformation structures (i.e. obtained from the entire EBSD maps) are shown in Fig. 10 depending on strain. The plots of the dependence of the angular parameters of the structure, such as the average misorientation of the crystallite boundaries, Θ_{av} , and the fraction of high angle boundaries, f_{HABs} , are shown in Fig. 11 and are denoted by white squares and dotted lines. At e = 1-4 (Fig. 10(a-c)), the misorientation spectra were characterized by the maximum boundary distribution density in the low and medium angle ranges up to 15°, and the high angle misorientations in these spectra apparently corresponded mainly to the boundaries of the initial grains. In this case, the evolution of the primary deformation bands undoubtedly had an additional effect on the misorientation spectrum, causing some shift of their average values towards larger angles.

¹ The grain size was determined at $e \ge 3$, since at lower strains the deformation-induced crystallites revealed by EBSD were not completely surrounded by high-angle boundaries (see Fig. 5).

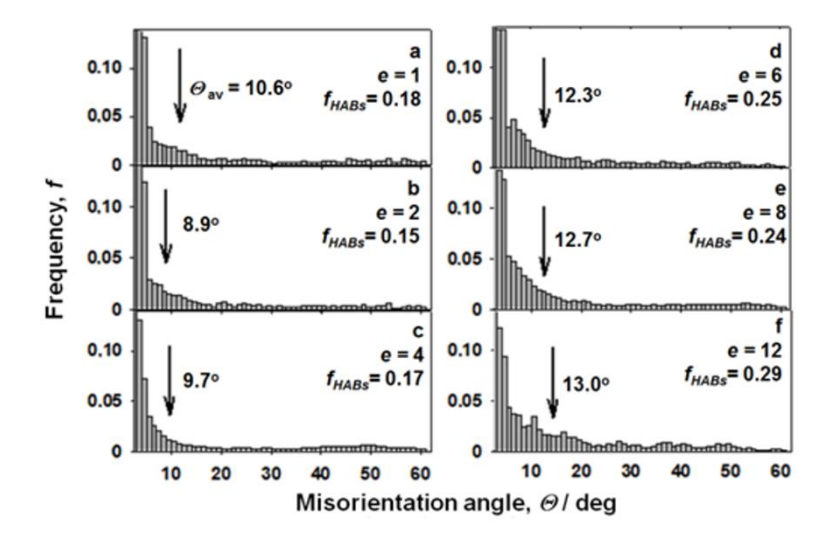


Fig. 10. Changes in the distribution of misorientations of (sub)grain boundaries developing in the structure of alloy 2219 during ECAP at T=475 °C

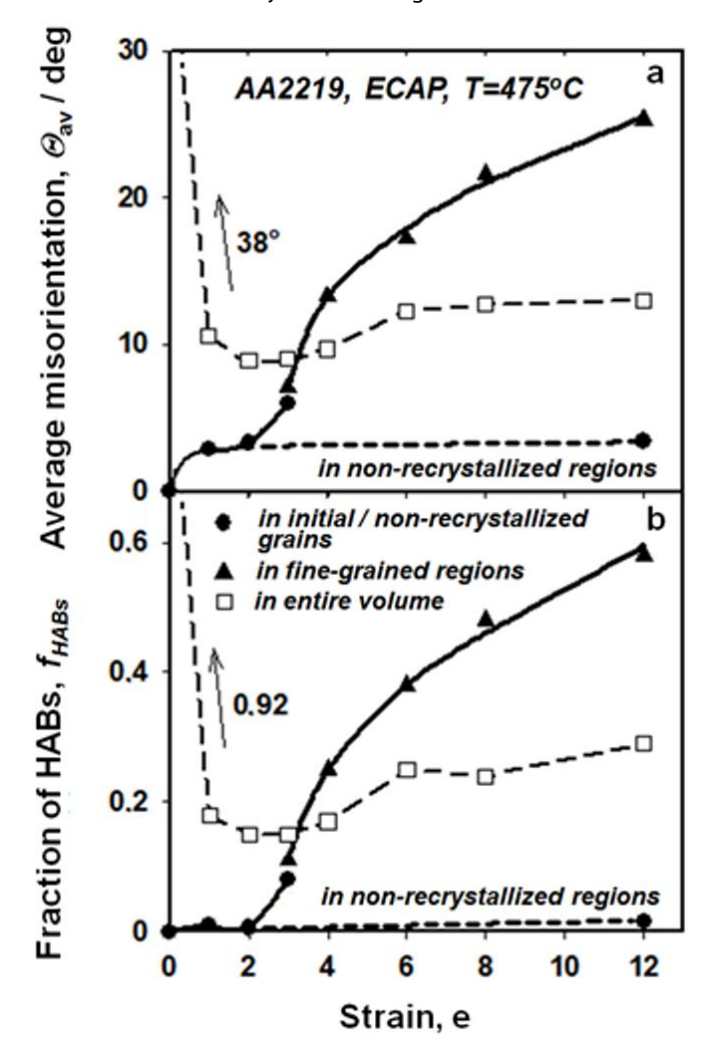


Fig. 11. Changes in (a) the average misorientation of deformation-induced boundaries and (b) the fraction of high-angle boundaries (HABs) formed in different regions of alloy 2219 during ECAP at T = 475 °C

However, this practically did not change the shape of the obtained dependencies, since in the early stages of deformation a large number of low angle boundaries were

simultaneously formed in the initial grains, which generally led to a sharp decrease in the average crystallite boundary misorientation and the fraction of high angle boundaries (Fig. 11). At strains e > 4, the fraction (fractional density) of medium angle boundaries increased, a new peak appeared in the distributions at 5° (Fig. 10(d)), while the spectrum of misorientations expanded towards larger angles (Figs. 10(d,e)), which was accompanied by an increase in Θ_{av} and f_{HABs} (Fig. 11). This was associated with the intense formation of microshear bands and new grains. However, the angular parameters of the whole structure increased slowly, and at strains e = 6-12 a tendency to "saturation" of Θ_{av} and f_{HABs} was observed at relatively low values of about 13° and 0.30, respectively.

At the same time, it seems that the change in the average values of the angular parameters of the microstructure calculated for the entire volume of the material does not always adequately reflect the physical nature of the processes occurring. This is due to the heterogeneity of the structure of the material, which leads to significant differences in the data obtained from different regions, making the use of averaged parameters for the assessment of structural changes ineffective. For example, in a number of studies in the initial stages of SPD, as well as in this alloy, a decrease in the average values of the angular parameters of the structure calculated for the entire volume of the material was observed. However, to the best of the author's knowledge, the corresponding mechanisms of structure formation leading to a decrease in (sub)grain boundary misorientation during deformation have not yet been identified [35]. The decrease in the mean values occurred only due to the formation of a large number of new low angle boundaries in the original polycrystal and was the result of averaging their misorientations with the misorientations of the boundaries of the initial grains. It should be noted that the nature of the dependence of the angular parameters of the structure on the deformation in the early stages of SPD has not yet been determined. Some researchers extrapolate the graphs of Θ_{av} =f(e) dependencies to zero values, representing a straight line (without any experimental confirmation) directly proportional to the growth of misorientations at the early stages of deformation [29,45]. However, this approach seems to be too simple.

The deformation microstructures in alloy 2219, even at e = 12, remained mixed and belonged to two main types:

- 1. colonies of fine grains, mainly with high angle boundaries;
- 2. fragments of deformed initial grains containing subgrains.

Therefore, for a more objective analysis of the data obtained from the EBSD maps, it was advisable to analyze their evolution separately in each of the developing regions.

First, the internal regions of large initial grains were identified and analyzed using standard software procedures for EBSD analysis [37,38]. This allowed the influence of initial boundaries and developing deformation bands on the microstructure parameters to be excluded. In this case, the misorientation spectra at strains e < 3 also showed maxima at angles less than 5° (Fig. 12(a,b)), but without contributions from grain boundary misorientations in the high angle region. This resulted in constant "low angle" values of microstructural parameters, forming a "plateau" 2 at $\Theta_{av} \approx 3.0-3.5$ ° and $f_{HABS} \approx 0$

² In a number of studies [11,12,18,19] such "plateaus" can also be observed in the "averaged over all regions" dependence of the structural parameters of alloys in which the initial grain size was relatively large and/or the subgrain size was relatively small, and accordingly the contribution of the initial grain boundaries to the average values of the developing microstructural parameters was not as sensitive.

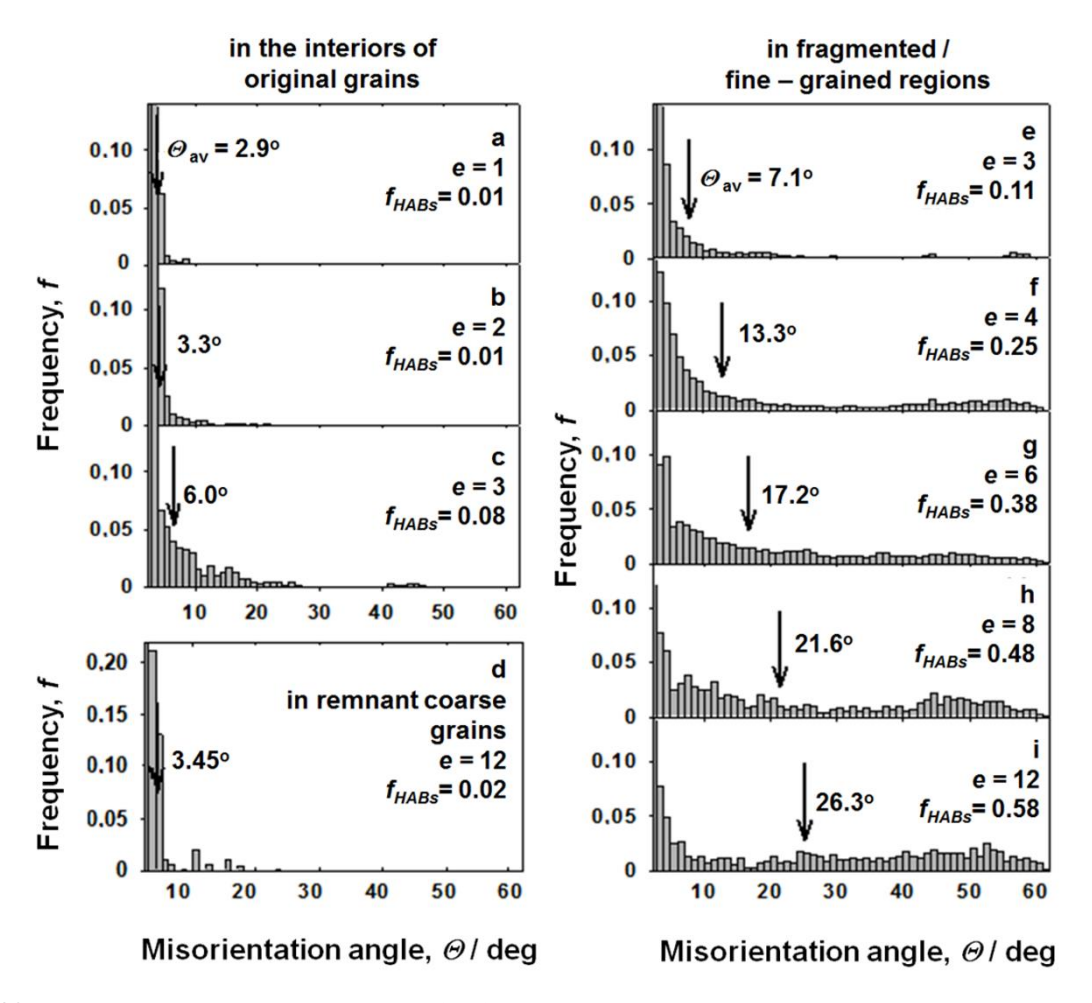


Fig. 12. Distributions of misorientations of (sub)grain boundaries formed in different regions of alloy 2219 during ECAP at T = 475 °C: (a-c) inside the initial grains (e = 1-3); (d) inside the remnant non-recrystallized grains (e = 12); (e-i) in fragmented/fine-grained regions (e = 3-12)

in the early stages of deformation (see graphs indicated by black circles and solid lines in Fig. 11). Contrary to the average characteristics of the microstructure, these plateaus obtained for the "selected" structure could be associated with a certain "incubation period" preceding the formation of new grains [11,12].

Figure 5 shows that the plateaus obtained are mainly related to the formation of a subgrain structure. This structure, similar to the cellular structures formed during cold deformation [4,17,24], can be classified as an "incidental" structure [43]. However, it should be noted that this structure is one of the most characteristic in the early stages of ECAP of this alloy, so its analysis can be important in understanding and describing the characteristics of the structural behavior during high temperature SPD.

It can be assumed that this structure corresponds to the so-called dynamic equilibrium subgrain structure, formed during "conventional" warm or hot deformation of materials with high stacking fault energy as described in [42,44,45]. Microstructural observations [42–45] have shown that these materials undergo dynamic recovery (polygonization) rather than dynamic recrystallization during high temperature deformation. In the early stages of deformation, the rates of formation and annihilation of defects in the crystal structure gradually equalize and a dynamic equilibrium is

0.S. Sitdikov

reached, leading to a "steady-state" of plastic flow when the parameters of the (sub)grain structure do not further change. However, it should be noted that most traditional deformation schemes, such as rolling or compression, limit the maximum relative strain to about 90-95 %, which corresponds to e=2.5-3.0. Therefore, comparing these values with the data presented in Figs. 10-12, it can be assumed that studies of the structural behavior of some materials with high stacking fault energy have only been performed at strains within the limits indicated by the plateau. In other words, before noticeable changes at the grain structure level begin to occur in the material (Fig. 4). This suggests that grain refinement at high temperature in some aluminum alloys requires higher strains, which is only possible with SPD.

For example, after the critical strain e = 2-3 was exceeded, medium angle boundaries began to form along with subgrain boundaries in alloy 2219 (Fig. 12(c)). This was accompanied by a rapid increase in Θ_{av} to medium angle values (Fig. 11) and a more than twofold decrease in the distance between deformation bands (Fig. 9). The latter suggests that in the midst of the development of a dynamically equilibrium subgrain structure at the indicated strains, localization of plastic flow occurred, leading to the intensive formation of new deformation bands, which caused fragmentation of the initial grains containing subgrains (Figs. 5–8).

On the other hand, misorientation distributions similar to those shown in Fig. 12(a,b) were also obtained by analyzing the structure developing in the inner parts of large fragments of the initial grains retained in the alloy even at e=12 (Figs. 11 and 12(d)). The graphs marked with black round dots and dashed lines in Fig. 11 show that the fraction of high-angle boundaries and the average misorientation angle of intercrystallite boundaries in these grains after high strains remained approximately the same as in the early stages of ECAP, i.e. about zero and $3-4^\circ$, respectively. This indicates that in the absence of grain fragmentation and refinement during deformation banding, the subgrain structure with low-angle boundaries remains dominant (dynamically balanced and stable) throughout the SPD process and does not transform into a new grain structure even at very high strains. Thus, strain localization and deformation banding is a necessary condition for the formation of new fine grains.

It is noteworthy that at high temperature, the plastic deformation proceeded uniformly, and high deformation gradients did not develop in the remaining large fragments due to the weak influence of the surrounding fine-grained matrix. In this matrix, the deformation energy was almost dissipated due to dynamic recovery and grain boundary sliding [11,12]. At the same time, the subgrains in the remaining fragments corresponded to the "dynamically equilibrium subgrain structure" that was formed in the early stages of plastic flow and maintained its "dynamically equilibrium" state in all areas with relatively uniformly progressing deformation.

In turn, the misorientation spectra obtained for the fragmented/fine-grained regions often showed peaks corresponding to low and medium angle boundaries with misorientations from 2 to 10° (Fig. 12(e,f)) in the early stages of deformation, which gradually expanded to higher angles with increasing strain amidst a noticeable decrease in the fraction of medium angle boundaries (Figs. 12(g-i)). This indicates that the medium angle boundaries (of microshear bands) introduced into the structure were predominantly transformed into boundaries of new grains. It should be noted that the values of the

average misorientation and the fraction of high angle boundaries in the fragmented/fine-grained regions increased significantly faster with increasing deformation, reaching higher values ($\Theta_{av} = 25^{\circ}$ and $f_{HABs} = 0.6$) at e = 12 (see graphs represented by black triangles and solid lines in Fig. 11) than in the whole material.

At the same time, the dependencies of the angular microstructural parameters on the deformation in the fragmented/fine-grained regions at the studied temperature of 475 °C were close to the dependencies previously obtained for the same alloy at lower ECAP temperatures of 250 and 300 °C, when new ultrafine grains were formed practically throughout the volume of the material [15,16]. This allows us to assume that the same grain refinement mechanism operated in the alloy regardless of the deformation temperature, associated with the localization of deformation and the formation of deformation bands with the subsequent formation of new grains [4,6,17,34,48]. However, the rate and completeness of this process depended on the deformation temperature. At higher temperatures, more uniform dislocation slip (controlled by their climb) and higher rates of dynamic recovery led to the formation of deformation bands in a smaller volume of the material and their development at higher strains [27,50]. Consequently, a smaller number of new grains were formed in the alloy at the same strains. Thus, it can be concluded that grain refinement during SPD of this alloy was controlled by both athermal processes, such as mechanically induced local lattice rotations and deformation banding, and thermally activated processes associated with homogenization of dislocation slip and acceleration of dynamic recovery with increasing temperature.

Another important conclusion from the analysis of the microstructural parameters (Figs. 4,9 and 11) was that the size of the new crystallites formed in place of microshear bands remained practically constant at medium and high strains, while the misorientation of their boundaries gradually increased. Thus, the crystallites formed during deformation increased their misorientation and were transformed *in-situ* into new fine grains without any noticeable growth. It is known that such features of structure evolution are characteristic of deformation-induced continuous reactions of the cDRX type [44]. Thus, it can be argued that the formation of new grains during hot ECAP of this 2219 aluminum alloy, as well as in a number of other aluminum alloys during high-temperature SPD [11,12,26,44], occurred as a result of cDRX.

Conclusions

In this paper, the microstructure evolution of cast aluminum alloy 2219 (Al-6.4Cu-0.3Mn-0.18Cr-0.19Zr-0.06Fe (wt. %)) was investigated during ECAP by route A at 475°C (\sim 0.8 $T_{\rm m}$) to a total strain of e = 12. The main results can be summarized as follows.

1. The OM data showed that after hot deformation up to strains of e=4, the alloy structure mainly contained large initial grains aligned in the pressing direction according to the simple shear scheme. At higher strains, new fine grains started to form and the coarse-grained microstructure was gradually replaced by a mixed bimodal structure consisting of fine grains and larger fragments of the initial grains. The size and volume fraction of new grains in such a structure at e=12 were about 10 μ m and 50 %, respectively. The results obtained indicate the need to achieve large strains to refine the grains during hot working of this alloy.

106 O.S. Sitdikov

2. SEM and TEM studies, including electron backscatter diffraction analysis, showed that the main structural changes in the early stages of ECAP (e = 1-2) were associated with the formation of a nearly homogeneous "dynamically equilibrium" subgrain structure with lowangle boundary misorientation ($\theta < 5^{\circ}$) inside the grains. Its formation was due to homogeneous slip and dislocation rearrangement typical of hot deformation of aluminum alloys under conditions of high dynamic recovery rate. This structure was maintained inside the non-recrystallized grains over the whole range of strains studied, giving an approximately constant average misorientation of the intercrystallite boundaries of 3-4°. 3. Grain refinement during high-temperature ECAP was associated with the development of non-uniform deformation, leading to the formation of various types of deformation bands with medium-angle ($5 \le \theta < 15^{\circ}$) misorientation of boundaries against the background of the equilibrium subgrain structure. Thus, as a result of deformation localization at the macro/meso level in the initial stages of ECAP, primary deformation bands oriented at an angle of up to 10-15° to the pressing axis developed in some initial grains. With further deformation, they increased their misorientation to high-angles $(\theta \ge 15^{\circ})$ and were aligned along the pressing axis together with the initial grains. This resulted in a rapid decrease in the distance between high-angle boundaries in the transverse direction in some grains, followed by the onset of geometric dynamic recrystallization.

4. Another and more pronounced mechanism of grain refinement was associated with microshear bands oriented along the shear plane during ECAP, which were formed after the critical strain of about e = 2-3. During the subsequent ECAP, a gradual refinement of the initial grains occurred by the mechanism of their fragmentation, where new fine grains were formed by mutual intersection of microshear bands developed in different passes, with a subsequent increase in their number and misorientations. This led to the formation of a microstructure with an average misorientation of the intercrystallite boundaries of about 23°. 5. Analysis of the dependence of the microstructural parameters on strain showed that grain refinement in alloy 2219 during hot ECAP occurred by the mechanism of cDRX.

CRediT authorship contribution statement

Oleg Sh. Sitdikov (DSC): writing – review & editing, writing – original draft.

Conflict of interest

The author declares that he has no conflict of interest.

References

- 1. Humphreys FJ, Prangnell PB, Bowen JR, Gholinia A, Harris C. Developing stable fine-grain microstructures by large strain deformation. *Philosophical Transactions of the Royal Society A: Mathematical Physical and Engineering Sciences*. 1999;357(1756): 1663–1681.
- 2. Edalati K, Bachmaier A, Beloshenko VA, Beygelzimer Y, Blank VD, Botta WJ, Bryła K et al. Nanomaterials by severe plastic deformation: Review of historical developments and recent advances. *Materials Research Letters*. 2022;10(4): 163–256.
- 3. Mulyukov RR, Imayev RM, Nazarov AA, Imayev MF, Imayev VM. *Superplasticity of ultrafine grained alloys: Experiment, theory, technologies.* Moscow: Nauka; 2014. (In Russian)

2004;50(5): 613-617.

- 4. Beyerlein IJ, Tóth LS. Texture evolution in equal-channel angular extrusion. *Progress in Materials Science*. 2009;54(4): 427–510.
- 5. Segal V. Review: Modes and processes of severe plastic deformation (SPD). *Materials*. 2018;11(7): 1175.
- 6. Segal V. Equal channel angular extrusion: from macromechanics to structure formation. *Materials Science and Engineering: A.* 1999;271(1–2): 322–333.
- 7. Yamashita A, Yamaguchi D, Horita Z, Langdon TG. Influence of pressing temperature on microstructural development in equal-channel angular pressing. *Materials Science and Engineering: A.* 2000;287(1): 100–106.
- 8. Gholinia A, Prangnell PB, Markushev MV. The effect of strain path on the development of deformation structures in severely deformed aluminium alloys processed by ECAE. *Acta Materialia*. 2000;48(5): 1115–1130.
- 9. Chakkingal U, Thomson PF. Development of microstructure and texture during high temperature equal
- channel angular extrusion of aluminium. *Journal of Materials Processing Technology*. 2001;117(1–2):169–177. 10. Wang YY, Sun PL, Kao PW, Chang CP. Effect of deformation temperature on the microstructure developed in commercial purity aluminum processed by equal channel angular extrusion. *Scripta Materialia*.
- 11. Goloborodko A, Sitdikov O, Kaibyshev R, Miura H, Sakai T. Effect of pressing temperature on fine-grained structure formation in 7475 aluminum alloy during ECAP. *Materials Science and Engineering: A.* 2004;381(1–2): 121–128.
- 12. Sitdikov O, Sakai T, Goloborodko A, Miura H, Kaibyshev R. Grain refinement in coarse-grained 7475 Al alloy during severe hot forging. *Philosophical Magazine*. 2005;85(11): 1159–1175.
- 13. Popovic M, Verlinden B. Microstructure and mechanical properties of Al-4·4 wt-%Mg alloy (AA5182) after equal channel angular pressing. *Materials Science and Technology*. 2005;21(5): 606–612.
- 14. Werenskiold JC, Roven HJ. Microstructure and texture evolution during ECAP of an AlMgSi alloy: Observations, mechanisms and modeling. *Materials Science and Engineering: A.* 2005;410–411: 174–177.
- 15. Mazurina I, Sakai T, Miura H, Sitdikov O, Kaibyshev R. Grain refinement in aluminum alloy 2219 during ECAP at 250°C. *Materials Science and Engineering: A.* 2008;473(1–2): 297–305.
- 16. Mazurina I, Sakai T, Miura H, Sitdikov O, Kaibyshev R. Effect of deformation temperature on microstructure evolution in aluminum alloy 2219 during hot ECAP. *Materials Science and Engineering: A.* 2008;486(1–2): 662–671.
- 17. Huang Y, Prangnell PB. Orientation splitting and its contribution to grain refinement during equal channel angular extrusion. *Journal of Materials Science*. 2008;43(23–24): 7273–7279.
- 18. Sitdikov O, Sakai T, Miura H, Hama C. Temperature effect on fine-grained structure formation in high-strength Al alloy 7475 during hot severe deformation. *Materials Science and Engineering: A.* 2009;516(1–2): 180–188.
- 19. Mazurina I, Sakai T, Miura H, Sitdikov O, Kaibyshev R. Partial grain refinement in Al-3%Cu alloy during ECAP at elevated temperatures. *Materials Transactions*. 2009;50(1): 101–110.
- 20. Subbarayan S, Roven HJ, Chen YJ, Skaret PC. Microstructure evolution in pure aluminium processed by equal channel angular pressing at elevated temperature. *International Journal of Materials Research*. 2013;104(7): 630–636.
- 21. Sitdikov O, Avtokratova E, Sakai T. Microstructural and texture changes during equal channel angular pressing of an Al-Mq-Sc alloy. *Journal of Alloys and Compounds*. 2015;648: 195–204.
- 22. Gazizov M, Malopheyev S, Kaibyshev R. The effect of second-phase particles on grain refinement during equal-channel angular pressing in an Al-Cu-Mg-Ag alloy. *Journal of Materials Science*. 2015;50(2): 990–1005.
- 23. Shaeri MH, Shaeri M, Ebrahimi M, Salehi MT, Seyyedein SH. Effect of ECAP temperature on microstructure and mechanical properties of Al–Zn–Mg–Cu alloy. *Progress in Natural Science: Materials International.* 2016;26(2): 182–191.
- 24. Huang Y. Substructural alignment during ECAE processing of an Al-0.1Mg aluminium alloy. *Metals.* 2016;6(7): 158. 25. Sitdikov OSh. Microstructure evolution in high-temperature equal channel angular pressing of Al-3%
- Cu alloy. *Physical Mesomechanics*. 2017;20(2): 95–109.

 26. Sitdikov O, Garipova R, Avtokratova E, Mukhametdinova O, Markushev M. Effect of temperature of isothermal multidirectional forging on microstructure development in the Al-Mg alloy with nano-size
- aluminides of Sc and Zr. *Journal of Alloys and Compounds*. 2018;746: 520–531.

 27. Sitdikov OS, Avtokratova EV, Zagitov RR, Markushev MV. Influence of the temperature of equal-channel angular pressing on fine-grain structure formation in the alloy Al-3% Cu. *Letters on Materials*. 2021;11(3): 332–337.
- 28. Baig M, Seikh AH, Rehman AU, Mohammed JA, Hashmi FH, Ragab SM. Microstructure evaluation study of Al5083 alloy using EBSD technique after processing with different ECAP processes and temperatures. *Crystals*. 2021;11(8): 862.
- 29. Yanushkevich Z, Belyakov A, Kaibyshev R. Microstructural evolution of a 304-type austenitic stainless steel during rolling at temperatures of 773–1273K. *Acta Materialia*. 2015;82: 244–254.

108 O.S. Sitdikov

30. Gholizadeh R, Terada D, Shibata A, Tsuji N. Strain-dependence of deformation microstructures in ultra-low-C IF steel deformed to high strains by torsion at elevated temperatures. *Nano Materials Science*. 2020;2(1): 83–95.

- 31. Jagadeesh C, Shivananda NH, Ramesh S, Praveen TR. Effect of multi-directional forging on the evolution of microstructural and mechanical properties of lightweight Al-Cu-Li alloy AA2050. *Journal of Materials Engineering and Performance*. 2023;32: 11118–11132.
- 32. Dolzhenko P, Tikhonova M, Odnobokova M, Kaibyshev R, Belyakov A. Ultrafine-grained stainless steels after severe plastic deformation. *Metals*. 2023;13(4): 674.
- 33. Kaibyshev R, Mazurina I, Sitdikov O. Geometric dynamic recrystallization in an AA2219 alloy deformed to large strains at an elevated temperature. *Materials Science Forum*. 2004;467–470: 1199–1204.
- 34. Sitdikov O, Avtokratova E, Markushev M, Sakai T. Structural characterization of binary Al-Cu alloy processed by equal channel angular pressing at half of the melting point. *Metallurgical and Materials Transactions A.* 2023;54: 505–525.
- 35. Carreño F. Predicting ECAP misorientation evolution and its influence on superplasticity for an Al-Zn-Mg-Cu alloy. *Materials Research Proceedings*. 2023;32: 189–196.
- 36. Kim HS. Evaluation of strain rate during equal-channel angular pressing. *Journal of Materials Research*. 2002;17(01): 172–179.
- 37. OIM Analysis Tutorials PDF Scribd. Available from: https://www.scribd.com/document/351952255/OIM-Analysis-Tutorials-pdf
- 38. Channel 5 (Oxford Instruments HKL A/S 2007). Available from: https://alabama.app.box.com/s/6r4atfrtolhxh9dh1xk6twgutpr73dpi
- 39. Kaibyshev R, Sitdikov O, Mazurina I, Lesuer DR. Deformation behavior of a 2219 Al alloy. *Materials Science and Engineering: A.* 2002;334(1–2): 104–113.
- 40. Davis JR. *ASM Handbook: Nonferrous alloys and special-purpose materials. Vol. 2.* 10th ed. Ohio, USA: ASM International; 1990.
- 41. Belov NA, Akopyan TK, Shurkin PK, Korotkova NO. Comparative analysis of structure evolution and thermal stability of commercial AA2219 and model Al-2 wt%Mn-2 wt%Cu cold rolled alloys. *Journal of Alloys and Compounds*. 2021;864: 158823.
- 42. Blum W, McQueen HJ. Dynamics of recovery and recrystallization. Materials Science Forum. 1996;217 222: 31 42.
- 43. Blum W, Zhu QS, Merkel R, McQueen HJ. Evolution of grain structure in hot torsion of Al-5Mg-0.7Mn (AA5083). *Materials Science Forum*. 1996;217–222: 611–616.
- 44. McQueen HJ, Blum W. Recovery and recrystallization in aluminum alloys: Fundamentals and practical applications. In: *Proceedings of the 6th International Conference on Aluminium Alloys*. 1998. p.99–112.
- 45. McQueen HJ, Spigarelli S, Kassner ME, Evangelista E. *Hot deformation and processing of aluminum alloys*. 1st ed. Boca Raton: CRC Press; 2011.
- 46. Kuhlmann-Wilsdorf D. "Regular" deformation bands (DBs) and the LEDS hypothesis. *Acta Materialia*. 1999;47(6): 1697–1712.
- 47. Hurley PJ, Humphreys FJ. The application of EBSD to the study of substructural development in a cold rolled single-phase aluminium alloy. *Acta Materialia*. 2003;51(4): 1087–1102.
- 48. Wang J, Kang S-B, Kim H-W. Shear features during equal channel angular pressing of a lamellae eutectic alloy. *Materials Science and Engineering: A.* 2004;383(2): 356–361.
- 49. Utyashev FZ, Raab GI. Influence of large and severe plastic deformation mechanisms on structure formation in metals. *Materials Letters*. 2021;302:130241.
- 50. Duckham A, Knutsen RD, Engler O. Influence of deformation variables on the formation of copper-type shear bands in Al-1Mg. *Acta Materialia*. 2001;49(14): 2739–2749.

Submitted: November 20, 2024

Revised: February 4, 2025 Accepted: February 12, 2025

Effect of high pressure torsion and annealing on the microstructure and microhardness of Inconel 718 produced by selective laser melting

K.S. Mukhtarova ¹, R.V. Shakhov ², Sh.Kh. Mukhtarov ²

ABSTRACT

Comparative study of Inconel 718 nickel-base superalloy produced by selective laser melting (SLM) and conventional technology was carried out. The SLM Inconel 718 microstructure consists of γ grains, surrounded by δ phase plates and small carbides. γ'' and γ' precipitates were present within the γ subgrains. The δ phase plates are mainly located along grain boundaries like in conventional Inconel 718. The γ grains consist of columnar and equiaxed subgrains. Study of microstructure showed that the columnar subgrains in their turn consisted of equiaxed subgrains. The SLM material features a developed substructure in γ grains, and dispersed precipitates, oxides along subgrain boundaries. SLM Inconel 718 and conventional Inconel 718 were subjected to high pressure torsion (HPT), which resulted in microstructure refining down to nanocrystalline size and partial dissolution of Nb containing γ'' and δ phases. δ phase particles were revealed more clearly after subsequent annealing at the temperature close to aging temperature like in conventional superalloy. Nanostructure of SLM Inconel 718 formed by HPT had duplex (γ + δ) structure and was found to be thermally stable at 600 °C during 2 h. Annealing of the SLM Inconel 718 led to superior microhardness (956.46 HV), which was slightly higher than that of the conventional superalloy.

KEYWORDS

nickel-based superalloy • microstructure • grain • boundary • selective laser melting • severe plastic deformation high pressure torsion • nanostructure • annealing • microhardness

Funding. The reported study was accomplished according to the state assignment of IMSP RAS (No. 124022900106-9). **Acknowledgements.** The research was carried out using the equipment of the shared services center of the Institute for Metals Superplasticity Problems of Russian Academy of Sciences "Structural and Physical-Mechanical Studies of Materials".

Citation: Mukhtarova KS, Shakhov RV, Mukhtarov ShKh. Effect of high pressure torsion and annealing on the microstructure and microhardness of Inconel 718 produced by selective laser melting. *Materials Physics and Mechanics*. 2025;53(1): 109–116.

http://dx.doi.org/10.18149/MPM.5312025_9

Introduction

The nickel-base superalloy Inconel 718, which can be exposed to high mechanical and thermal stresses, is commonly used in rocket and aircraft engines [1-3]. The phase composition, heat treatment and production technique determine its performance characteristics. For instance, selective laser melting (SLM) is a particular technique of rapid prototyping, 3D printing, or Additive Manufacturing (AM) designed to melt and fuse metallic powders with a high power-density laser [4-11]. SLM produces solid, simple or geometrically complex objects having a number of layers [4-7,11-13]. The AM process results in the formation of a complex heterogeneous microstructure, characterised by the



¹ Eötvös Loránd University, Budapest, Hungary

² Institute for Metals Superplasticity Problems of RAS, Ufa, Russia

[™] shamilm@imsp.ru

precipitation of dispersed strengthening phases and oxides. This is due to the combination of multiple heating and rapid cooling during the manufacturing process [4,8,10,14–18]. Consequently, the microstructure of the SLM material differs from that of materials produced by conventional methods. The microstructure is comprised of contained columnar and cellular grains, as observed in previous studies [19–21]. The microstructure of conventional superalloy subjected to severe plastic deformation by high pressure torsion (HPT) has been refined to nanoscale [22,23]. HPT can enhance the diffusion and dissolution of precipitates [23]. The microstructure and microhardness of SLM Inconel 718 and the conventional alloy subjected to HPT and annealing were compared in this paper.

Materials and Methods

Inconel 718 Ni-based superalloy, produced by SLM, was received in the form of a bar with a square cross-section measuring $11 \times 11 \times 73 \text{ mm}^3$, which was built vertically. The SLM scanning parameters, including laser power, scanning speed, layer thickness, and the distance between the scanning tracks of the laser beam, were selected to minimize porosity in the produced material. Table 1 shows the chemical composition of Inconel 718 Ni-based superalloy produced by SLM. The chemical composition of the superalloy was specified in the material's technical specifications, and its major elemental concentrations were confirmed using an energy-dispersive X-ray spectroscopic analysis (EDS, Aztec, Oxford Instruments). The samples 8 mm in diameter and 0.7 mm in thickness were cut from the SLM alloy. These small discs were processed by HPT on 5 revolutions at room temperature [24] and subsequently annealed at 600 °C for 2 h.

Table 1. The chemical composition of the SLM Inconel 718 alloy (wt. %)

Cr	Fe	Мо	Со	Al	Ti	Nb	C	В	Ni
19.8	18.4	3.4	0.1	0.6	1.0	5.9	0.04	0.03	base

The microstructure investigation was carried out with the use of scanning electron microscopy (SEM) in backscattering electron (BSE) mode. The electron backscattered diffraction (EBSD) analysis performed with a scan-step of 1 μm was carried out by Tescan Mira-3. Channel 5 processing software was applied for EBSD analysis. JEM-2000EX provided transmission electron microscopy. The samples and foils were polished at 50V with an electrolyte consisting of 10 % perchloric acid and 90 % butanol. Axiovert 100A and a microhardness tester MNT-10 with a 100 g load and 10 second time-lag were used for Vickers microhardness tests.

Results and Discussion

The microstructure of SLM Inconel 718

The BSE cross section image of superalloy Inconel 718 in as-built SLM condition is represented in Fig. 1(a). The microstructure consists of coarse and fine γ grains. The size of γ grains is about 20–100 µm. γ grains contain columnar and equiaxed subgrains (Fig. 1(a,b)) [25,26]. The plates of the δ (orthorhombic D0_a structure) phase, small carbides

and, probably oxides, are located at the γ grain boundaries. Columnar subgrains consist of submicrocrystalline equiaxed subgrains of about 0.5 μ m. Dispersed γ'' (tetragonal D0₂₂ structure) and γ' (cubic L1₂ structure) particles are precipitated in γ subgrains (Fig. 1(c,d)), like in conventional superalloy [27]. The diffraction pattern of the SLM alloy at Fig. 1(e) shows the existence of Ni-based (γ phase, (331)), orthorhombic Ni₃Nb (δ phase, (313)), body-centered tetragonal Ni₃Nb (γ'' phase, (301)), and Ni₃Al (γ' phase, (222)). EBSD analysis of the initial microstructure, earlier performed in [28], showed that high-angle grain boundaries accounted for 26 %.

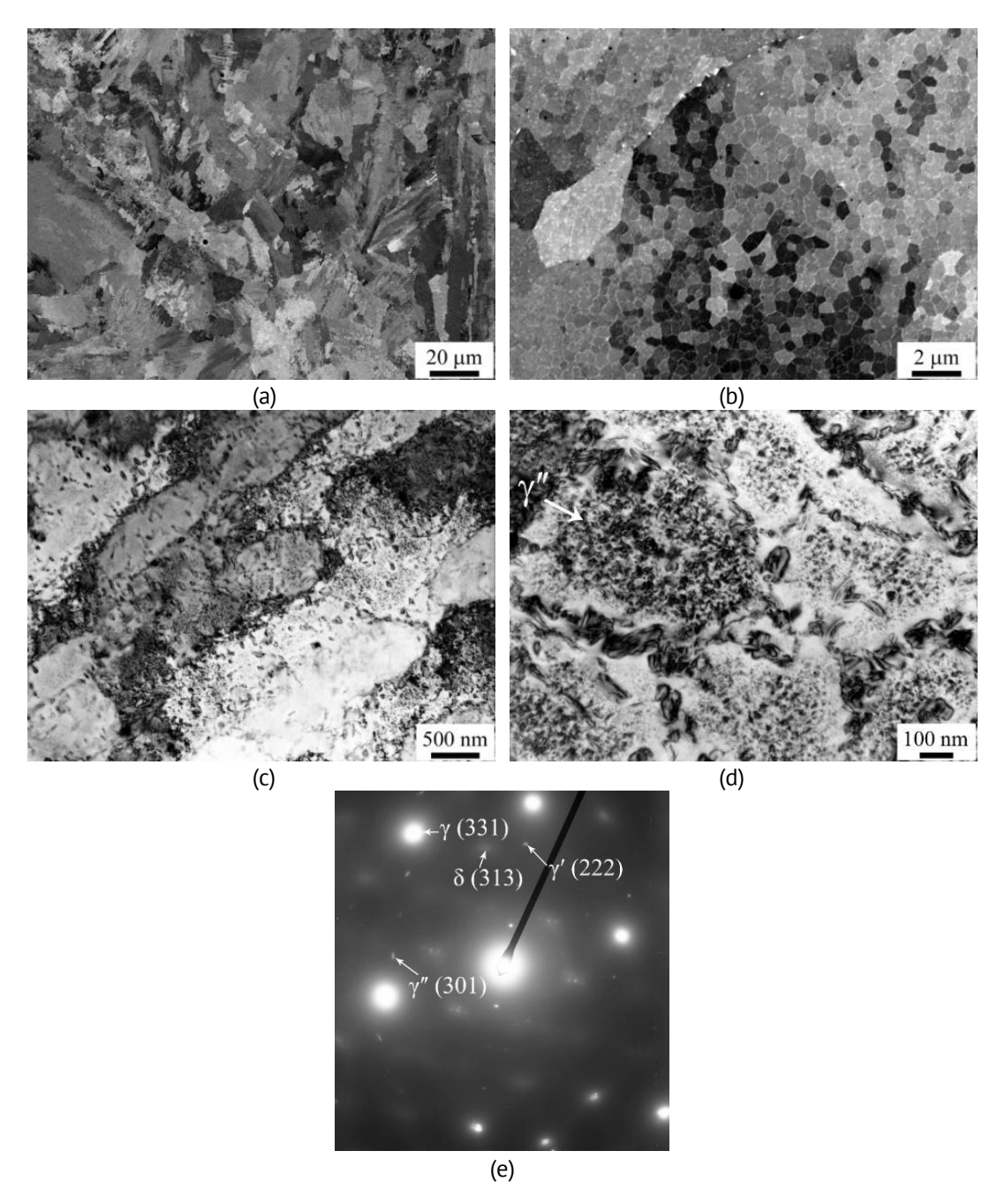


Fig. 1. The microstructure of SLM Inconel 718: BSE images of columnar subgrains and of equiaxed subgrains (a,b); transmission electron microscopy (TEM) images of submicrocrystalline subgrains (c,d); the diffraction pattern of the whole area of Fig. 1(d)

The microstructure of SLM Inconel 718 subjected to HPT

Figure 2 shows BSE and TEM images of SLM Inconel 718 subjected to HPT. The γ grain size in this condition was about 30 nm which is akin to that of conventional alloy subjected to HPT [22,23]. It is well known that the volume fraction of γ' precipitates in conventional Inconel 718 alloy is less than 5 %, γ'' precipitates is less than 25 % [29], and δ phase is about 16 % [30]. Really a large amount of dispersed precipitates as δ phase, carbides and oxides of the SLM alloy is unlikely to dissolve in γ matrix during HPT. Dispersed particles, probably fine carbides or oxides were visible in Fig. 2(a). The diffraction pattern of the alloy after HPT of TEM image Fig. 2(b) showed the existence of orthorhombic Ni₃Nb (δ phase, (211)), as well as Ni-based γ phase, (200). Probably metastable γ'' phase and γ' phase are almost completely dissolved during HPT as in the conventional superalloy subjected to the same treatment [23].

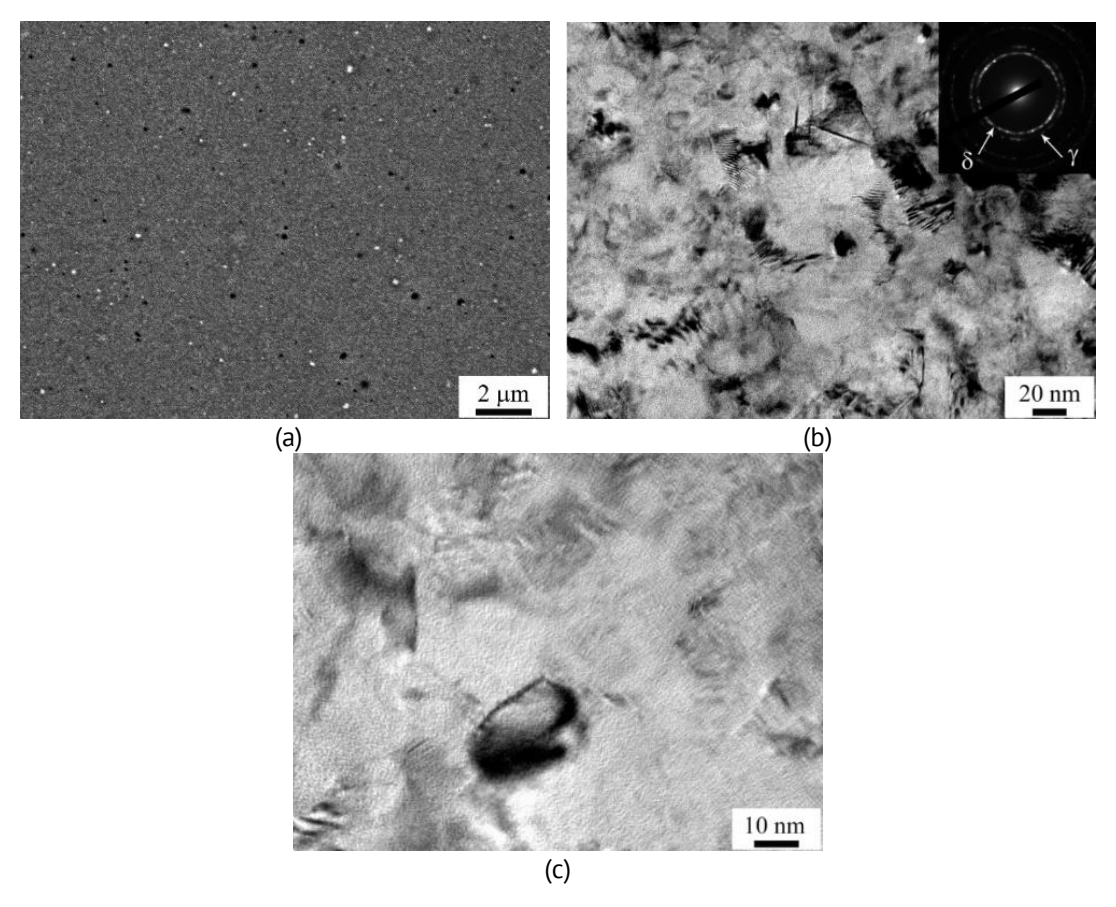


Fig. 2. Microstructure of SLM Inconel 718 subjected to HPT: BSE image (a), TEM images (b, c) with electron diffraction pattern (b)

The microstructure of SLM Inconel 718 subjected to annealing

Figure 3 shows the BSE images and the EBSD orientation map of SLM Inconel 718 after annealing at 600 °C for 2 h. The quantity of δ phase precipitates, carbides and oxides increased along the grain and subgrain boundaries during annealing (Fig. 3(a,b)). The microstructure contains coarse and fine γ grains. The γ grains also exhibited the presence of both columnar and equiaxed subgrains, while the γ grain size remained unaltered in comparison to the as-built condition (Fig. 1(a,b)). The EBSD orientation map shows that

the quantity of low angle boundaries decreased (Fig. 3(c)) and the fraction of high angle boundaries increased during annealing up to 69 % (Fig. 3(d)). The Σ 3 twin boundaries were not identified in either the BSE images or the misorientation – angle distribution for grain boundaries (about 60°) after annealing (Fig. 3).

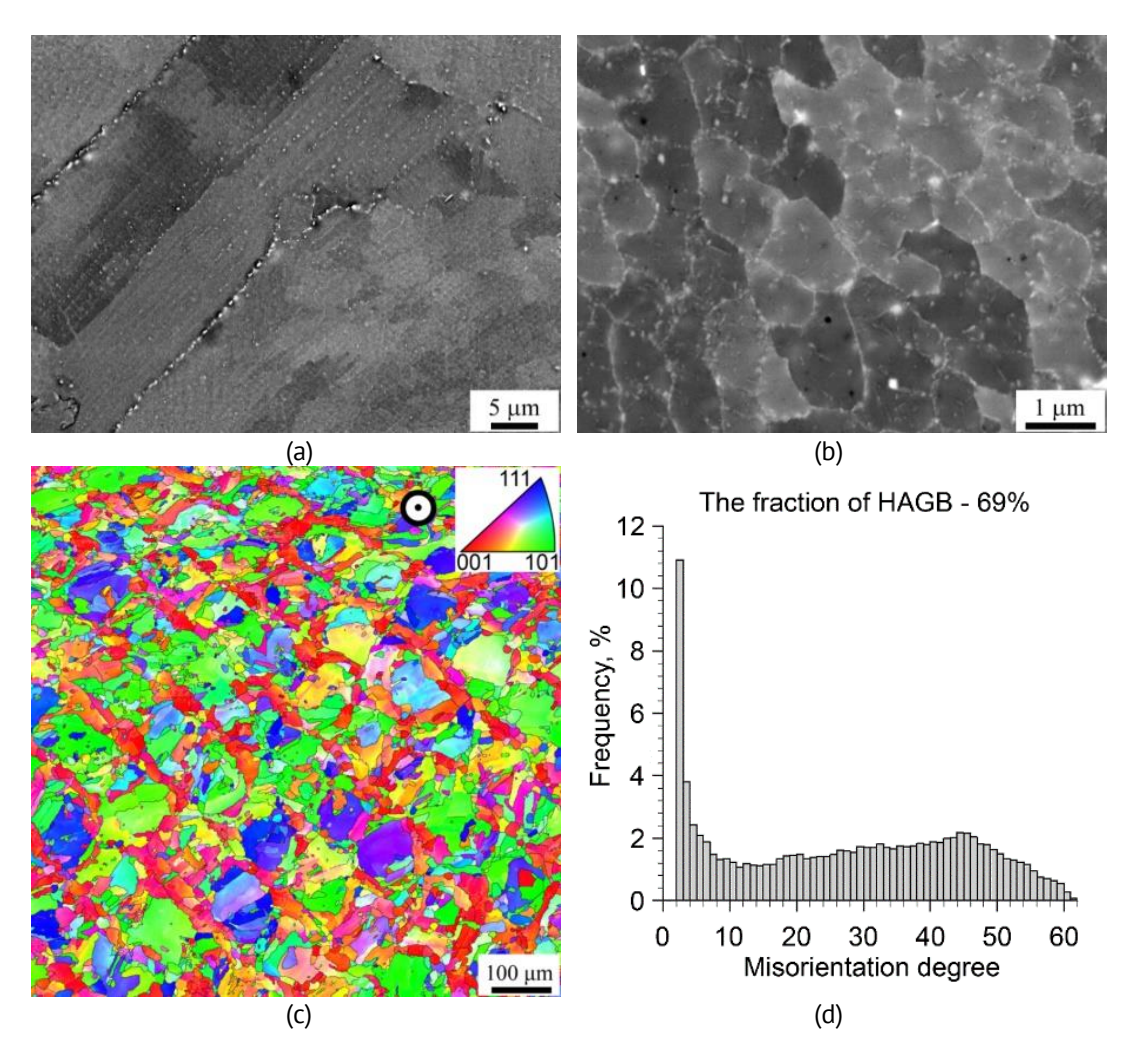


Fig. 3. The microstructure of SLM Inconel 718 after annealing at 600 °C for 2 hours: BSE images (a,b), EBSD normal-direction (inverse-pole-figure) orientation map (c) and corresponding misorientation angle distribution for grain boundaries (d), and the circle in (c) indicates the plane is perpendicular to the build direction

The microstructure of SLM Inconel 718 subjected to HPT and annealing

Figure 4 represents the TEM images of the sample subjected to HPT and annealing at 600 °C for 2 hours. The average size of γ grains increased from 30 to 50 nm. The diffraction pattern of the SLM alloy subjected to HPT and annealing exhibited the presence of the orthorhombic δ phase (412) and the γ phase (220), as observed in Fig. 4(b). γ phase and δ phase precipitates were revealed in the microstructure. The γ'' precipitates were dissolved in the γ matrix during HPT and subsequently precipitated during annealing by additional δ -phase particles. HPT and annealing of the SLM alloy resulted in the microstructure similar to that of the conventional superalloy subjected to the same treatment [22,23].

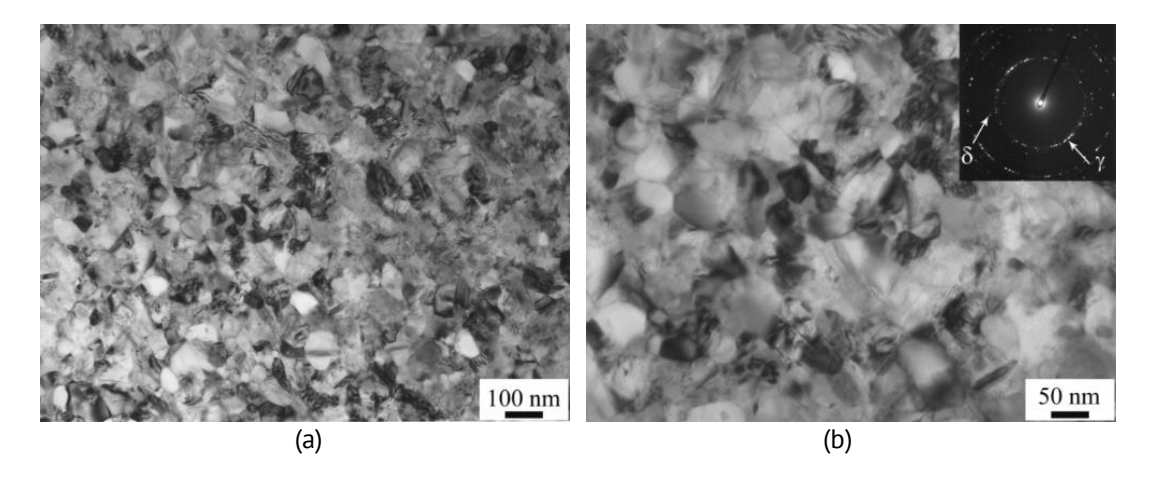


Fig. 4. The microstructure of SLM Inconel 718 subjected to HPT and annealing at 600 °C for 2 hours: TEM images (a,b) with electron diffraction pattern (b)

Effect of HPT and annealing on the microhardness

The microhardness (HV) of SLM and conventional Inconel 718 in different conditions is represented in Table 2. The SLM superalloy that was the subject of this investigation exhibited a microhardness of 530.23 ± 19.37 HV, which is higher than the microhardness of 432 ± 12 HV reported in [31]. Annealing at 600 °C for two hours did not impact the microhardness of the SLM alloy, due to the previous treatment of the alloy being carried out at a higher temperature via laser melting, followed by cooling. As shown in [32], the γ'' phase in SLM alloy is precipitated at temperatures of 700 °C and above. It can be reasonably assumed that the annealing temperature of 600 °C was too low to precipitate the γ'' phase in the SLM alloy. Indeed, the minimum aging temperature for Inconel 718 alloy is typically 620 °C [33]. The conventional superalloy microhardness is observed to decrease to 477.21 HV as a consequence of a reduction in dislocation density following hot forging and subsequent annealing. Better microhardness after HPT is related with microstructure refinement down to the nanocrystalline level. The observed increase in microhardness following subsequent annealing is likely attributable to the precipitation of the δ phase and the onset of polygonization that occurred prior to recrystallization [34]. The microhardness of SLM Inconel 718 is higher than that of the conventional alloy, probably due to dispersed oxides and carbides in the SLM alloy at the grain boundaries [35].

Table 2. Microhardness (HV) of SLM Inconel 718 and conventional Inconel 718 subjected to different treatment

Conditions	Inconel 718	SLM Inconel 718
Initial	547.57 ± 25.49	530.23 ± 19.37
Annealing at 600 °C	477.21 ± 19.37	528.19 ± 12.24
HPT	637.30 ± 39.77	721.93 ± 26.51
HPT+annealing at 600 °C	866.73 ± 42.83	956.46 ± 25.49

Conclusions

1. The stable δ phase precipitates present in the SLM Inconel 718 alloy did not fully dissolve during HPT, and their presence was more clearly discernible following annealing at 600 °C for 2 h.

- 2. The mean size of γ grains increased from 30 to 50 nm during annealing at 600 °C for 2 h of the SLM Inconel 718 alloy subjected to HPT on five revolutions.
- 3. The SLM Inconel 718 processed by HPT on five revolutions and annealed at 600 °C for 2 h show the higher microhardness (956.46 HV) than conventional one (866.73 HV), and in both cases was achieved in due to additional precipitation by dispersed δ phase.

CRediT authorship contribution statement

Kamilla Sh. Mukhtarova (DSC): investigation, writing – original draft, data curation; Shamil Kh. Mukhtarov ٧. conceptualization, writing - review & editing.

Conflict of interest

The authors declare that they have no conflict of interest.

References

- 1. Schafrik R, Sprague R. Superalloy technology a perspective on critical innovations for turbine engines. Key Engineering Materials. 2008;380: 113-134.
- 2. Special Metals Corporation. INCONEL alloy 718. Available from: https://www.specialmetals.com/documents/ technical-bulletins/inconel/inconel-alloy-718.pdf [Accessed 20th November 2024].
- 3. Maslov AA, Nazarov AY, Khusainova AM, Ramazanov KN. Y-Al-O Coating Grown on Inconel 718 Alloy. Physics of Metals and Metallography. 2024;125: 1609–1614.
- 4. DebRoy T, Wei HL, Zuback JS, Mukherjee T, Elmer JW, Milewski JO, Beese AM, Wilson-Heid A, De A, Zhang W. Additive manufacturing of metallic components – Process, structure and properties. Progress in Materials *Science.* 2018;92: 112–224.
- 5. Yap CY, Chua CK, Dong ZL, Liu ZH, Zhang DQ, Loh LE, Sing SL. Review of selective laser melting: Materials and applications. Applied Physics Reviews. 2015;2(4): 041101.
- 6. Oliveira JP, Santos TG, Miranda RM. Revisiting fundamental welding concepts to improve additive manufacturing: from theory to practice. *Progress in Materials Science*. 2020;107: 100590.
- 7. Körner C. Additive manufacturing of metallic components by selective electron beam melting a review. International Materials Reviews. 2016;61(5): 361–377.
- 8. Tucho WM, Cuvillier P, Sjolyst-Kverneland A, Hansen V. Microstructure and hardness studies of Inconel 718 manufactured by selective laser melting before and after solution heat treatment. Materials Science and Engineering: A. 2017;689: 220-232.
- 9. Kuo YL, Kakehi K. Influence of powder surface contamination in the Ni-based superalloy Alloy718 fabricated by selective laser melting and hot isostatic pressing. Metals. 2017;7(9): 367.
- 10. Lu Y, Wu S, Gan Y, Huang T, Yang C, Junjie L, Lin J. Study on the microstructure, mechanical property and residual stress of SLM Inconel-718 alloy manufactured by differing island scanning strategy. Optics & Laser Technology. 2015;75: 197-206.
- 11. Polozov IA, Borisov EV, Sufiiarov VSh, Popovich AA. Selective laser melting of copper alloy. Materials *Physics and Mechanics.* 2020;43(1): 65–71.
- 12. Murr LE, Martinez E, Amato KN, Gaytan SM, Hernandez J, Ramirez DA, Shindo PW, Medina F, Wicker RB. Fabrication of metal and alloy components by additive manufacturing: examples of 3D materials science. Journal of Materials Research and Technology. 2012;1(1): 42-54.
- 13. Popovich AA, Sufiiarov VSh, Borisov EV, Polozov IA, Masaylo DV. Design and manufacturing of tailored microstructure with selective laser melting. *Materials Physics and Mechanics*. 2018;38(1): 1–10.
- 14. Raza T, Andersson J, Svensson LE. Microstructure of selective laser melted Alloy 718 in as-manufactured and post heat treated condition. *Procedia Manufacturing*. 2018;25: 450–458.
- 15. Gong X, Wang X, Cole V, Jones Z, Cooper K, Chou K. Characterization of Microstructure and Mechanical Property of Inconel 718 From Selective Laser Melting. In: ASME 2015 International Manufacturing Science

- and Engineering Conference: Volume 1: Processing, 8–12 June 2015, Charlotte, North Carolina, USA. American Society of Mechanical Engineers; 2015. MSEC2015-9317, V001T02A061.
- 16. Popovich AA, Sufiiarov VSh, Polozov IA, Borisov EV. Microstructure and mechanical properties of Inconel 718 produced by SLM and subsequent heat treatment. *Key Engineering Materials*. 2015;651–653: 665–670.
- 17. Raghavan S, Zhang B, Wang P, Sun CN, Nai MLS, Li T, Wei J. Effect of different heat treatments on the microstructure and mechanical properties in selective laser melted INCONEL 718 alloy. *Materials and Manufacturing Processes*. 2017;32(14): 1588–1595.
- 18. Mukhtarova KS, Shakhov RV, Mukhtarov SK, Smirnov VV, Imayev VM. Microstructure and mechanical properties of the Inconel 718 superalloy manufactured by selective laser melting. *Letters on Materials*. 2019;9(4): 480–484.
- 19. Wei W, Xiao JC, Wang CF, Cheng Q, Guo FJ, He Q, Wang MS, Jiang SZ, Huang CX. Hierarchical microstructure and enhanced mechanical properties of SLM-fabricated GH5188 Co-superalloy. *Materials Science & Engineering A*. 2022;831: 142276.
- 20. Zeng Q, Wang K, Lu S, Lu C, Wang Z, Zhou T. Evolution of the microstructure and multi-objective optimization of the tensile properties of GH3625 superalloy by selective laser melting. *Journal of Materials Research and Technology.* 2023;24: 8826–8848.
- 21. Liu H, Han S, Lan Y, Zhao W, Zhang C, Li Q. The effect of direct aging treatment on microstructure and mechanical properties of the GH4099 superalloys produced by selective laser melting. *Journal of Alloys and Compounds*. 2024;1007: 176493.
- 22. Sauvage X, Mukhtarov S. Microstructure evolution of a multiphase superalloy processed by severe plastic deformation. *IOP Conference Series: Materials Science and Engineering*. 2014;63: 012173.
- 23. Mukhtarov ShKh, Sauvage X. Microstructure and microhardness of a nanostructured nickel-iron based alloy. *Materials Science Forum.* 2011;683: 127–135.
- 24. Gunderov DV, Asfandiyarov RN, Raab GI, Churakova AA, Astanin VV. Method for slippage evaluation at various stages of high-pressure torsion and its application to Fe-0.1%C. *Letters on Materials*. 2021;11(4): 416–421.
- 25. Zhou S, Liu L, Yang Y, Lv P. Effect of heat treatment on the microstructure and recrystallization of an SLM nickel-based superalloy. *Materials Today Communications*. 2024;39: 109253.
- 26. Wang H, Wu D, Xiao F, Quan G, Liu B. Influence of heat treatment temperature on grain structures and properties of a Ni-based superalloy fabricated via selective laser melting. *Materials Today Communications*. 2024;41: 110673.
- 27. Burke MG, Miller MK. Precipitation in Alloy 718: A combined AEM and APFIM investigation. In: Loria EA. (eds.) *Superalloys 718, 625 and Various Derivatives.* Warrendale PA: The Minerals, Metals & Materials Society; 1991. p. 331–350. 28. Shakhov R, Mukhtarova K. Nb rich precipitates in Inconel 718 produced by selective laser melting. *Letters on Materials.* 2018;8(1): 105–109.
- 29. Yang L, Chang KM, Mannan S, deBarbadillo J. A new DTA approach for verifying precipitate solvus in Inconel alloy 718. In: Loria EA. (eds.) *Superalloys 718, 625, 706 and Various Derivatives*. Warrendale PA: The Minerals, Metals & Materials Society; 1997. p. 353–365.
- 30. Moyye DP, Satheesh Kumar SS, Nagarajan D, Balasundar I. Microstructural evolution and mechanical behavior during isothermal multiaxial forging of nickel-based Superalloy SUPERNI 718. To be published in *Journal of Materials Engineering and Performance*. [Preprint] 2024. Available from: doi.org/10.1007/s11665-024-09249-1
- 31. Protatskaya AA, Sharipova SR. The effect of heat treatment on the structure of the SLM of the Inconel 718 alloy. *Materials. Technologies. Design.* 2022;4(2): 46–51.
- 32. Ghaemifar S, Mirzadeh H. Precipitation kinetics of gamma double prime phase during direct aging treatment of Inconel 718 superalloy additively manufactured by selective laser melting. *Journal of Materials Research and Technology*. 2023;27: 4248–4255.
- 33. Chen B, Zhuo L, Xie Y, Huang S, Wang T, Yan T, Gong X, Wang Y. Comparative study on microstructure, mechanical and high temperature oxidation resistant behaviors of SLM IN718 superalloy before and after heat treatment. *Journal of Materials Research and Technology*. 2024;31: 1535–1546.
- 34. Mukhtarov ShKh. Effect of grain size on the superplastic behavior of a nanostructured nickel-based superalloy. *Materials Science Forum.* 2009;633–634: 569–575.
- 35. Sheinerman AG. Strengthening of nanocrystalline alloys by grain boundary segregations. *Materials Physics and Mechanics*. 2022;50(2): 193–199.

Submitted: August 24, 2024 Revised: October 2, 2024 Accepted: October 30, 2024

Mechanical and durability properties of sustainable composites derived from recycled polyethylene terephthalate and enhanced with natural fibers: a comprehensive review

A. Kumar [™], R. Bedi [©]

National Institute of Technology Jalandhar, Jalandhar (Punjab), India

[™] ajayk.me.19@nitj.ac.in

ABSTRACT

Pursuing sustainable and environment-friendly materials has spurred a paradigm shift in composite materials, with an increasing focus on composite materials with natural fibers as reinforcement. An indepth study of composites crafted from natural fibers and recycled polyethylene terephthalate (rPET) as matrix is presented in this comprehensive review. The cellulosic fibers offer an eco-friendly alternative to synthetic reinforcements with attributes such as high tensile strength, low density, easy availability in abundance at low cost, and biodegradability. When incorporated into composites, they improve the mechanical behavior, and there is less material consumption, making it preferable for lightweight applications. Conversely, using rPET represents an innovative step in addressing the environmental challenges of using traditional petroleum-based plastics. The rPET matrix, derived from the chemical recycling of used PET bottles, is a promising material for developing environmentally conscious composites. The discussion includes mechanical properties and extends to the durability behavior of these composites, evaluating their resistance to moisture, UV radiation, and temperature variations: durability, resistance to deterioration, and performance of the composite materials under actual situations. The review concludes by exploring current challenges and limitations, highlighting areas for future research and development.

KEYWORDS

sustainability • NFRCs • rPET • mechanical performance • surface modification • durability behavior

Citation: Kumar A, Bedi R. Mechanical and durability properties of sustainable composites derived from recycled polyethylene terephthalate and enhanced with natural fibers: a comprehensive review. *Materials Physics and Mechanics*. 2025;53(1): 117–142.

http://dx.doi.org/10.18149/MPM.5312025_10

Introduction

This article aims to thoroughly analyze the durability and mechanical performance of composite materials, specifically those incorporating natural fibers with rPET (recycled polyethylene terephthalate) as the matrix. The integration of natural fibers with rPET holds great promise in enhancing the overall properties of composite materials while addressing concerns related to ecological impact and resource depletion. Using natural fibers as reinforcements in polymer composites has gained widespread focus due to their renewable nature, low environmental footprint, and favorable mechanical properties. These plant-based fibers offer unique combinations of strength, stiffness, and lightness, making them attractive candidates for reinforcing polymer matrices. This review explores the diverse range of natural fibers, emphasizing their intrinsic attributes that add to the mechanical performance of polymeric composites. In parallel, the focus on rPET as a matrix material adds another layer of sustainability to the composite system. rPET is a



versatile and recyclable matrix option chemically derived from virgin PET bottles. The compatibility between natural fibers and rPET offers a synergistic effect, leveraging the strengths of both components and potentially mitigating the environmental issues interrelated with traditional crude oil-based matrices. The mechanical performance of composite materials is a critical aspect influencing their suitability for various applications. This review delves into the mechanical performance of rPET-based composites utilizing fibers from natural resources. Durability is another pivotal factor determining the practicality and longevity of composites. Natural fiber-reinforced rPET composites are scrutinized for their resistance to aging or degradation in different conditions such as water, moisture, UV radiation, temperature variations, etc. The assessment will extend beyond short-term effects to address the long-term stability and resistance to degradation, offering insights into the durability of these composites in realworld conditions. The aim is to identify existing challenges, pose avenues for future research, and present an overview of the recent developments in green composites. Despite the remarkable progress made in the field, certain obstacles still need to be addressed, including issues related to fiber-matrix interactions, processing techniques, and exploring novel natural fibers. The concluding section provides a roadmap for future research, urging a collective effort to overcome these challenges and further propel the adoption of natural fiber-reinforced rPET composites in engineering and manufacturing applications. In essence, this review sets the stage for a deeper understanding of the mechanical properties and durability aspects of natural fiber-reinforced rPET composites, aiming to contribute to the broader discourse on sustainability and drive innovation



Fig. 1. Types of plant-based natural fibers. Reprinted with permission from [1], © Elsevier 2022

in pursuing a more ecologically responsible future. Traditional composite materials, often reliant on synthetic reinforcements, face scrutiny due to their environmental impact and limited sustainability. Plant or animal-sourced fibers offer a promising solution as reinforcement materials in composites. The motivation for exploring natural fiber-reinforced composites stems from the desire to reduce reliance on non-renewable resources and mitigate environmental concerns. Recycled PET, chemically derived from used PET bottles, emerges as a significant matrix material in this review. Its unique properties, including versatility, recyclability, and compatibility with natural fibers, contribute to composites' overall sustainability and performance.

Fibers from natural resources

Natural fibers come directly from plants, animals, or minerals (Fig. 1). These fibers can be turned into thread, filaments, or rope and are used for making composite materials. Many researchers have shown interest in using natural fibers, which are available in abundance. It has also been economically investigated that integrating farm waste into composite manufacturing is advantageous for applications where products are subjected to environmental degradation [2–4].

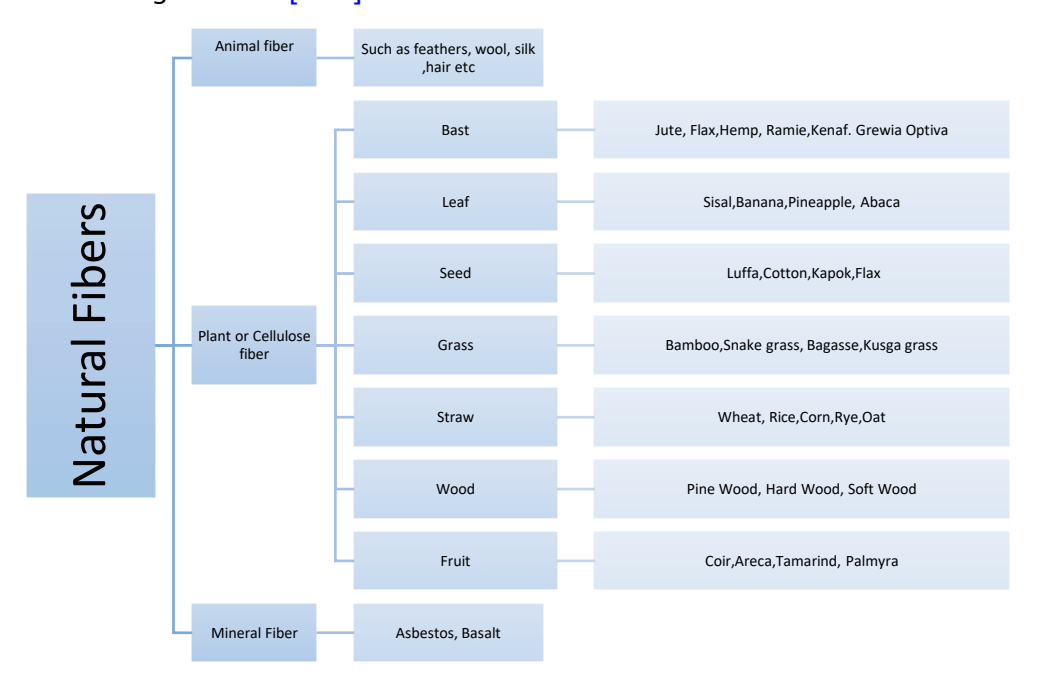


Fig. 2. Categorization of fibers from natural resources. Based on [2]

Classification of natural fibers

The fibers from natural resources can be grouped into three broad categories (Fig. 2):

- 1. animal fiber: animal fibers include wool, feathers, hair/fur, and bird feathers;
- 2. plant or cellulose fiber: flax, cotton, kenaf, sisal, jute, and hemp are examples of plant fiber;
- 3. mineral fiber: asbestos, ceramic fibers, and basalt fibers are naturally occurring mineral fibers.

Composition of natural fibers

Plant fibers primarily comprise cellulose, hemicellulose, pectin, lignin, natural waxes, and other compounds soluble in water. Even though these fibers belong to the same family or kind, their chemical composition varies based on the fiber's source, affecting its mechanical behavior and other properties. The variation in properties is also noticed for the same natural fibers (Fig. 3) depending upon the type of soil they were cultivated, the amount of water and sun received by them, the amount of fertilizer or other chemicals used during the growing stage, the seasonal variation during growth and harvesting for a particular year, i.e., some of the reasons for variability in the properties of same natural fibers are beyond human control as they are cultivated in fields but not produced in factories.

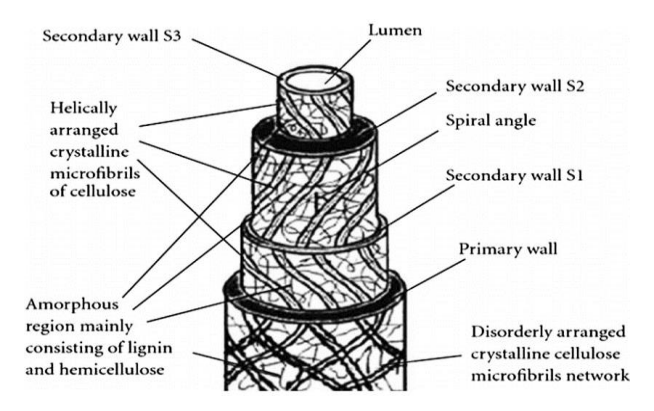


Fig. 3. Natural fiber cell wall's structural organization. Reprinted with permission from [3], © Elsevier 2001

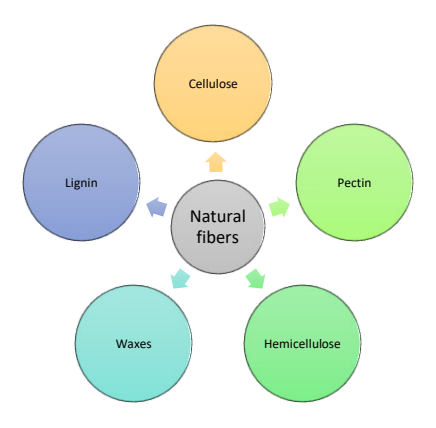


Fig. 4. Constituents of plant-based fibers. Based on [9]

Plant fibers are often known as lingo cellulosic structures containing cellulose, hemicellulose, and lignin [4]. Cellulose is an unbranched macromolecule present in all fiber cell chemical compositions. The amount of cellulose in a plant fiber can substantially impact its functionality and performance in many applications, hemicellulose is a multi-branched polysaccharide polymer composed of sugars which binds cellulose and lignin and in some way also improves the stiffness as well as strength of plant fibers [5]. In the textile and paper industry, bast and jute are favored due to their outstanding cellulose content. Lignin in the plant cell is the second-most found polymer after cellulose. It is a unique biomacromolecule that is highly branched and doesn't have a clear fundamental structure. Plant tissue and individual fibers (Fig. 4) get their stiffness

and strength from the lignin (Table 1). It also protects the carbohydrates and sugars from chemical and microbial attack [6-8].

Table 1 . Chemical	composition of	plant-based natural	fibers (wt	. %)	[10]	
---------------------------	----------------	---------------------	------------	------	------	--

Fiber	Cellulose	Hemicellulose	Lignin	Pectin	Waxes
Hemp	70-75	17.5-22.5	3.7-5.7	0.9-1.0	0.7-0.8
Jute	60-71	13.5-20.5	12-14	0.2-0.3	0.4-0.5
Ramie	68-76	13-16.5	0.6-0.8	1.9-2.0	0.2-0.3
Nettle	86	4.0	5.4	0.6	3.1
Sisal	67-78	10-14	8-11	10	10-22
Pineapple	80-83	15-20	8-12	1-3	8-15
Cotton	85-90	5.7	0.7-1.6	1.0	20-30
Coir	36-43	0.15-0.25	41-45	5.2-16.0	30-49

Merits and demerits of fibers from nature

One of the primary motivations for incorporating natural fibers in composite materials is their renewable nature and eco-friendly characteristics. Unlike synthetic fibers, natural fibers are sourced from readily available raw materials, contributing to sustainability. Cultivating these fibers requires less energy and results in lower carbon footprints than synthetic reinforcements. The biodegradability of natural fibers further enhances their environmental appeal, reducing the long-term impact on ecosystems.

Merits

Natural fiber's intrinsic properties, such as low density, low cost, easy availability, high toughness, strength, stiffness, outstanding acoustic and thermal insulating capabilities, and high electrical resistance combined with minimum health impact and comparable mechanical performance, make them suitable candidates for composite manufacturing. They also have a low adverse effect on cutting tools and machines [11]. Traditionally, rice and wheat straw fibers were used to strengthen mud bricks, which are still used in various applications (Fig. 5).

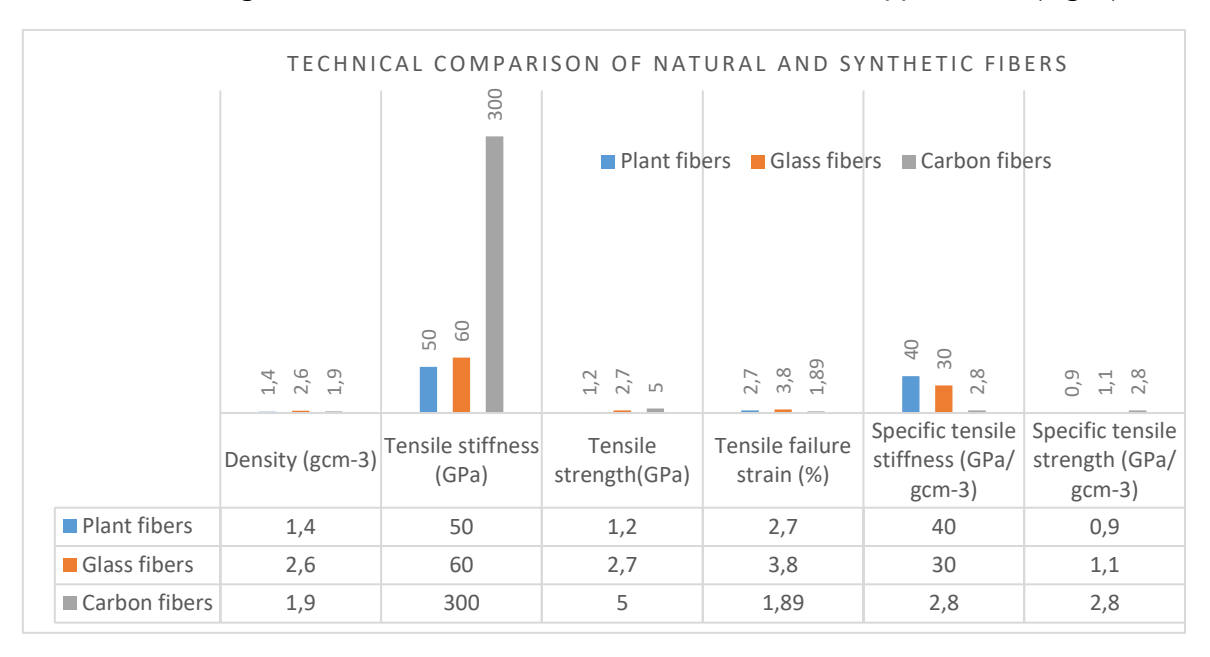


Fig. 5. Comparison (average values) of standard natural and synthetic fibers. Based on [12]

Demerits

Despite their numerous benefits, natural fibers have drawbacks, such as poor compatibility and the matrix's non-uniform wetting of the fibers, high moisture absorption, and deterioration due to heat during manufacturing. These make them unsuitable for various composite applications [13]. One of the problems experienced due to poor wetting of the hydrophilic natural fibers by hydrophobic organic polymer matrix is weak adhesion at the reinforcement-matrix interface [14]. Therefore, the natural fibers need surface treatment before the composite is made from them. Several treatments and techniques are available to modify the surface of natural fibers to form a strong bond between the fibers and matrix. For example, mercerization, also called alkali treatment, is a chemical process used to clean and alter the surface of plant-based fibers to increase interfacial adhesion with the matrix [15]. Some of the merits and demerits of natural fibers are listed below (Fig. 6).



Fig. 6. Merits and demerits of natural fibers. Based on [16]

Comparison of natural and synthetic fibers

The comparative analysis of natural and synthetic fibers (Fig. 7) reveals significant differences in environmental impact, mechanical properties, and applications. Natural fibers, such as jute and flax, are increasingly favored for their eco-friendliness and lower greenhouse gas emissions, while synthetic fibers like polyester are associated with higher environmental costs.

Despite the advantages of natural fibers, challenges still need to be addressed, such as variability in quality and performance compared to synthetic alternatives. Balancing these factors is crucial for their use in composites.

The interfacial adhesion between natural fibers and polymer matrixes (Fig. 8) is crucial for enhancing composites' mechanical strength and overall characteristics. This adhesion facilitates effective stress transfer, which is essential for the all-around performance of the composite material. Interdiffusion, electrostatic adhesion, and mechanical interlocking contribute to adequate bonding [25]. Coating fibers with acrylic resins can significantly enhance interfacial shear strength, improving load transfer [26]. Chemical treatments and surface roughening of fibers have increased compatibility with polymer matrices [27,28]. However, natural fibers often exhibit poor moisture resistance

Table 2. Comparison of natural and synthetic fibers

·	Natural fibers	Synthetic fibers		
Environmental	These generally exhibit lower environmental	Synthetic fibers contribute		
impact	impacts across various categories, including fossil	significantly to Eco-toxicity		
Impact	resource scarcity and global warming potential.	and require extensive		
		energy for production [17].		
	Natural fiber-reinforced composites demonstrate	These provide superior		
Mechanical	favorable mechanical properties, such as high	strength and durability but		
properties	flexibility and lower weight, making them suitable	at a higher environmental		
	for non-structural applications [18].	cost [19].		
	These are hydrophilic, leading to higher moisture	Synthetic fibers maintain		
	absorption, which can compromise durability, but at	structural integrity under		
Durability aspects	the same time, natural fibers are biodegradable and	varying environmental		
Durability aspects	more sustainable, making them preferable in eco-	conditions [22].		
	conscious applications despite their lower			
	durability [20,21].			
	Natural fibers are increasingly used in sustainable	Synthetic fibers dominate		
Applications	construction and automotive sectors.	in high-performance		
Applications		applications due to their		
		enhanced properties [23].		

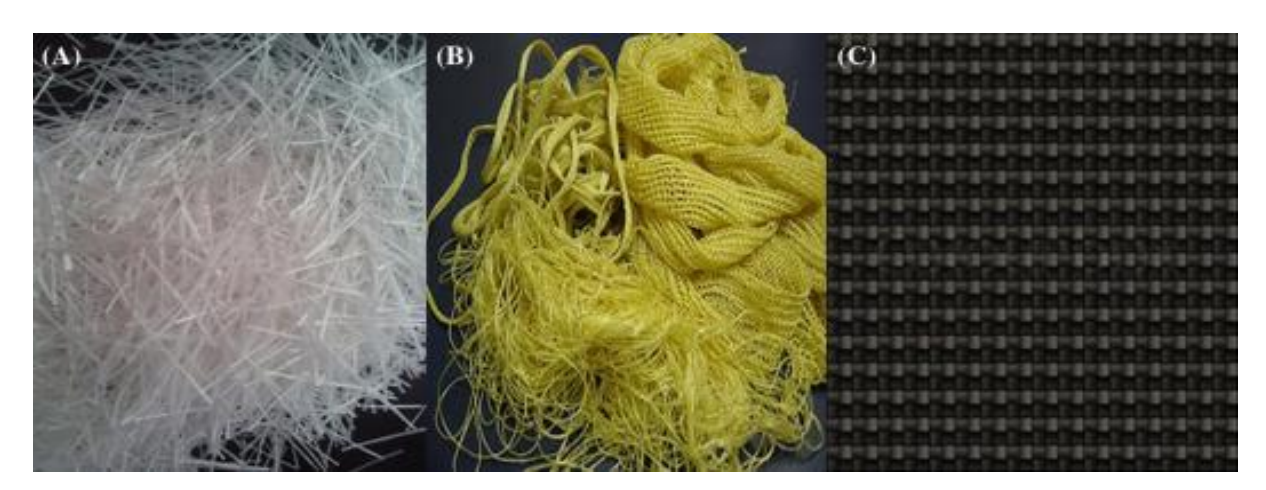


Fig. 7. Displaying synthetic fibers (A) glass, (B) kevlar, and (C) carbon fibers.

Reprinted with permission from [24], © Elsevier 2017

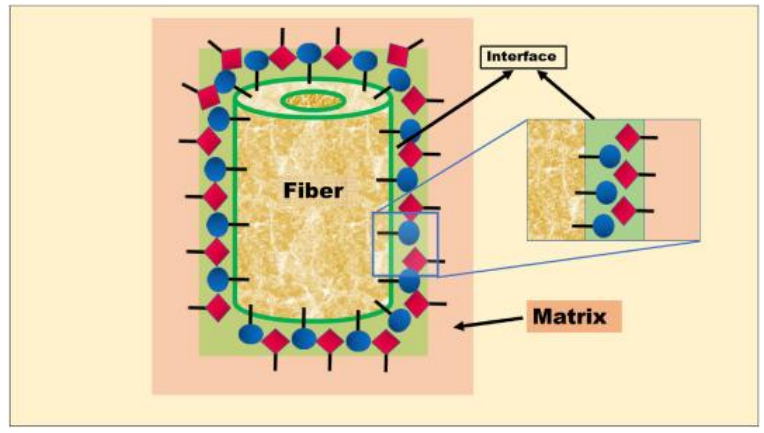


Fig. 8. Interfacial chemical bonding mechanisms between fiber and matrix. Reprinted with permission from [29], © Elsevier 2022

and variability, leading to weak fiber-matrix adhesion [28]. Addressing these challenges through strategic modifications can lead to composites with superior mechanical performance.

While enhancing interfacial adhesion is vital for improving composite strength, it is also essential to consider the balance between fiber properties and matrix characteristics to achieve optimal performance in various applications.

Surface modification of natural fibers

Naturally found fibers are polar and hydrophilic [30], whereas the polymer matrix is hydrophobic, which results in poor interface bonding between the two. Due to this weak adhesion at the interface of cellulosic fiber and the polymer matrix, the overall performance of the fabricated composites is compromised [31,32]. Plant-based fiber surfaces can be surface-treated to improve their hydrophilic nature [33]. Treated natural fibers improve bonding at the fiber interface and the matrix, enhancing stress transferability [34]. The adherence of plant fibers to the inorganic matrix can be enhanced by (i) altering the top layer of the fibers, (ii) altering the polymer matrix, or (iii) altering both. Surface modification with physical methods such as plasma, ultrasound, ultraviolet light, and treatment with chemicals like silane, alkali, acetylation, benzoylation, and sodium chloride helps to improve the bonding of plant-based fibers with polymer matrix [35,36].

Surface modification by physical methods

Physical modification procedures like plasma treatment attempt to roughen the plant-based fibers' surface and remove surface contaminants such as oils, waxes, and pectin to increase the mechanical bonding of fiber with the matrix [12]. The Ultraviolet treatment improves the polarity of the fiber surface, resulting in enhanced wettability by the matrix and overall strength of the composite [37,38]. The fiber-beating increases fiber surface area, defibrillation, and mechanical interlocking, improving the strength of natural fibers [39].

Corona and plasma treatments

The corona treatment raises the surface energy and oxides on the plant fibers' surface, making it blend more efficiently with the polymer matrix [40]. Plasma treatment alters the surface of plant-based fibers by eliminating poorly connected surface layers and generating new functional groups [41].

Surface modification by chemical methods

The chemical treatment removes unwanted constituents in plant fibers, such as hemicellulose, waxes, lignin, and pectin, improving matrix adhesiveness's overall physical and chemical characteristics [42]. A study by Maya Jacob John and Rajesh D. Anandjiwala reports that lignocellulosic fibers are naturally polar and water-loving, but most thermoplastics aren't polar; mixing them is hard. Another problem with using natural fibers to make durable composites is that they aren't very resistant to bacteria and mounds, making them prone to rotting and causing significant issues when shipping, storing, and

making composites. Chemical treatments can fix most of these problems associated with natural fibers, making them suitable for composites with polymer matrix [43].

NaOH treatment

Treatment with alkali, such as mercerization, is one of the easiest, most cost-efficient, and most effective methods for enhancing plant-based fiber adherence to the polymer matrix. This approach uses sodium hydroxide (NaOH) to alter the cellulose composition of natural fibers [44]. The fibers' surfaces become clean and homogeneous. An optimal alkali concentration should be attained, as substantial concentrations can weaken and destroy the fibers. The diameter of the fibers is decreased at an optimum alkali concentration, resulting in improved adhesion of fibers with matrix due to enhanced fiber surface area and improved aspect ratio [45].

The equation below shows the reaction of plant-based fiber with NaOH:

Fiber – OH + NaOH = Fiber – O – Na +
$$H_2O$$
.

The surface roughness of sisal fibers was significantly increased after alkali treatment, resulting in fibers with lower diameters, most likely due to eliminating noncellulosic chemicals. Furthermore, sisal fibers treated with NaOH solution produced somewhat greater contact angles with water drops, implying enhancement in wettability with hydrophobic polymer matrices [46,47]. Studies have shown that alkali treatment increases the proportion of amorphous cellulose at the expense of crystalline cellulose and removes hydrogen bonding in the network structure [48,49]. Huda et al. [50] discovered that the NaOH-treated pineapple leaf fibers reinforced PLA composites had better mechanical qualities than the untreated leaf composites. Edeerozey et al. [51] found that 6 % NaOH was optimal for superior mechanical attributes compared to stock kenaf fibers. Fiore et al. [52] calculated the effect of NaOH treatment on the mechanical performance of kenaf fiber-reinforced epoxy composites, stating that the treated composite had better mechanical properties, according the Nurul Munirah Abdullah and Ishak Ahmad [53] prepared coconut fiber/polyester composite using alkali, silane, and silane on alkalized fibers to increase the adhesion between coconut fiber and polyester resin. The tensile characteristics of coconut fiber were significantly improved by surface treatment.

Additionally, it was noted that composites made using treated fibers had less water absorption capacity than untreated fiber composites. Overall, the current literature [54] suggests that treating plant-based fibers with alkali concentrations of 5 to 8 % improves the mechanical behavir of the composites.

Silane treatment

In this method, silane coupling agents cover micropores on the fiber surface. Silane (SiH_4) is an inorganic compound in nature is made up of both hydrophilic and hydrophobic compounds connected to the silicon molecule, which can be thickened by adding a coagulant agent to make silanol (SiOH) groups (Fig. 9) and subsequently siloxane bridges [55].

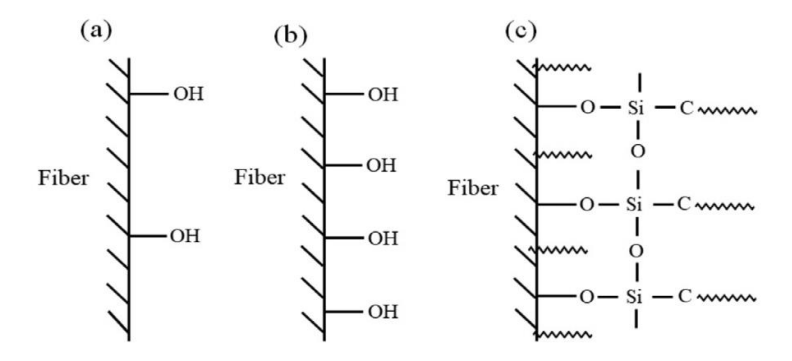


Fig. 9. Schematic showing how chemicals interact with the fiber when it is (a) untreated, (b) treated with NaOH, and (c) treated with Silane. Reprinted with permission from [56], © Elsevier 2020

In a research conducted by Y. Liu et al. [57], fibers from corn waste were treated with silane solution. Silane's effects on the chemical, morphological, and mechanical properties of Corn Stalk Fibre (CSF) and CSF-reinforced polymer composites were studied. Pull-out tests confirmed the improved interfacial adhesion between silane-treated sisal fiber and matrix; silane-treated fibers had higher interfacial shear strength than untreated fibers.

Peroxide treatment

Researchers from diverse fields have investigated treating natural fibers with peroxide and the mechanical characteristics of polymer composites reinforced with these peroxide-treated fibers (Fig. 10). Free radicals are created when the peroxide breaks down: RO + Cellulose - H = R - OH + Cellulose.

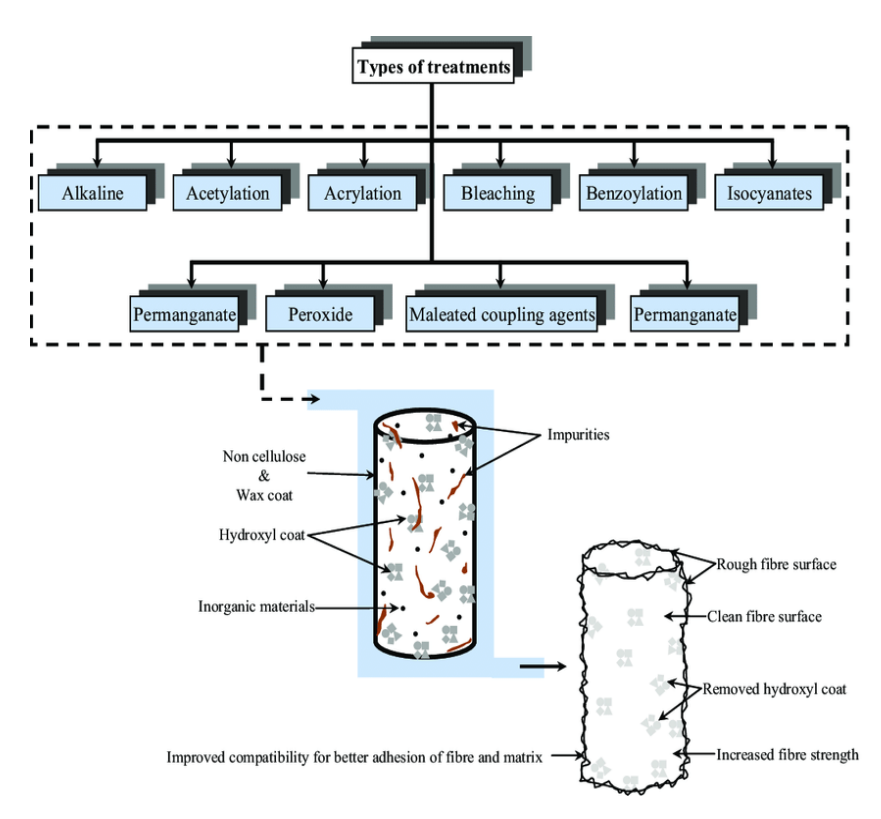


Fig. 10. Changes in the surface of cellulosic fiber after various treatments. Reprinted with permission from [58], © Elsevier 2015

Benzoylation treatment

Benzoyl chloride is also used in modifying the surface of natural fibers. This includes benzoyl ($C_6H_5C=0$), which is responsible for lowering the hydrophilicity of the plant fiber and improving bonding with the polymer matrix. Joseph et al. [59] used NaOH and benzoyl chlorite (C_6H_5COCl) solution for surface modification of sisal fibers and reported improved hydrophobicity. Mixing two or more chemicals for surface treatment, such as alkali with silane, improves mechanical properties better than just one treatment. Chemical agents like maleic anhydride grafted polypropylene (MAGP) and zein also improve flexural strength [60]. A study [61] investigated the influence of different surface chemical treatments (Fig. 11) on the mechanical characteristics and durability of jute fiber-reinforced epoxy composites (JFRECs). It was discovered that the combined chemical treatment is far better than individual treatments. Water absorption rates for composites with chemically treated fibers were lower than those for untreated fiber composites.

Other miscellaneous treatments

In composites reinforced with natural fibers, various chemical treatments are used to modify the surface of the fibers, but on the other hand, inadequate treatment with chemicals could damage the structure of the natural fibers, thereby considerably decreasing their mechanical properties [62]. R. Sepe et al. [63] reported that both tensile and flexural strengths of composites

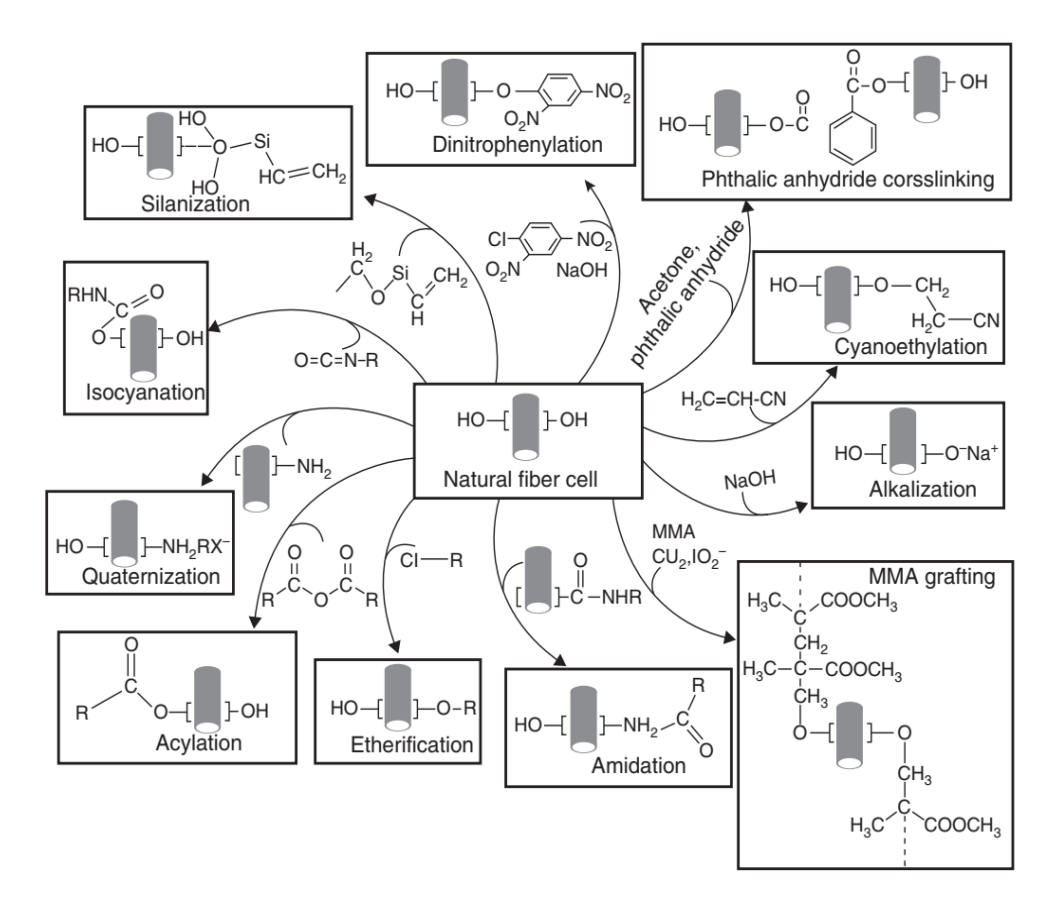


Fig. 11. Basic chemistry of surface modification treatments of plant fibers. Reprinted with permission from [10], © Elsevier 2015

reinforced with hemp fibers improved when these fibers were treated with (3Glycidyloxypropyl) trimethoxysilane. The effect of an eco-friendly chemical treatment consisting of a 10 % solution of sodium bicarbonate on the resistance to aging in some marine conditions of epoxy-based composites reinforced with flax and jute fibers was studied by V. Fiore et al. [64]. The samples prepared were put in a salty and foggy spray environment for around 60 days. The experimental campaign showed that the sodium bicarbonate treatment makes plant-based fibers and epoxy matrix stick together in a better way, which helps treated laminates retain their flexural properties better than untreated laminates during salt fog exposure. M. Bayart et al. [65] investigated the adhesion at the interface of surface-treated flax fibers and polylactic acid (PLA) utilizing lignin and tannin, which are eco-friendly polyphenolic chemicals generated from the waste of paper industries. The findings demonstrated that the interfacial strength of composites was significantly increased by using a coating of solutions containing 1 % (wt/V) tannin/lignin. Tannin demonstrated improved compatibility with PLA and flax fibers, increasing the composites' ultimate flexural strength and interlaminar shear strength by 17 % and 29 %, respectively. Research work was carried out by A. L. N. Inácio et al. [66] to test the mechanical and thermal aspects of composite materials with bamboo fiber-reinforced recycled talc-filled PP/EPDM that has been grafted with maleic anhydride (PP-q-MAH). The composite was held at 90 °C for seven days in a chamber with hot air moving through it. Improvements in tensile strength, flexural strength, and fatigue life were noticed (Fig. 12).

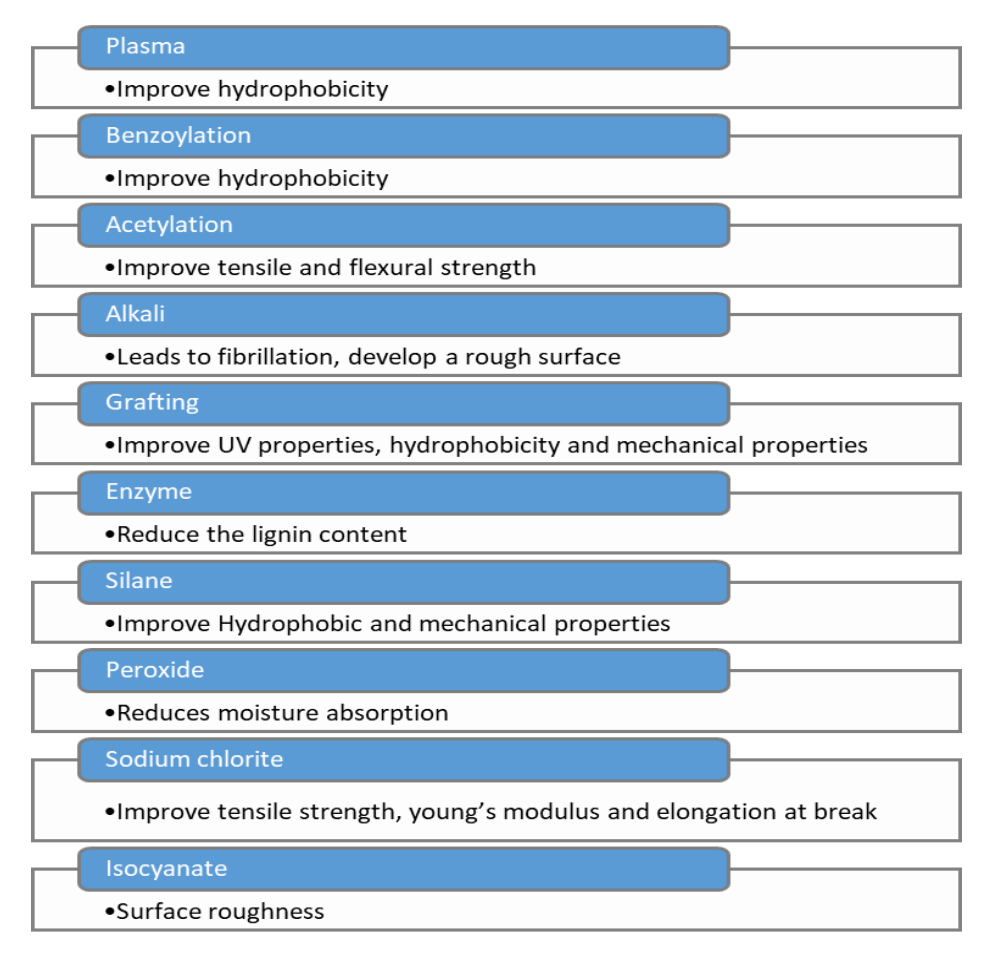


Fig. 12. Effect of various surface treatments on natural fibers. Based on [67]

S. Satapathy and R.V.S. Kothapalli [68] fabricated composites based on recycled high-density polyethylene (RHDPE) / fly ash cenospheres (FACS)/banana fiber (BF) to enhance the commercial value of these waste products. Maleic anhydride-grafted HDPE (MA-g-HDPE) was also used as a compatibilizer to promote the dispersion of fibers within the polymer matrix and the compatibility of the matrix with fillers. The addition of 7.5 wt. % FACS, 30 wt. % BF, and three wt. % MAg-HDPE to the RHDPE matrix improved the tensile strength by 17 %, the tensile modulus by 188 %, the flexural strength by 38 %, the flexural modulus by 159 %, and the hardness by 37 %. The surface of raw natural fibers can be modified by various treatments to improve the bonding of these fibers with the polymer matrix.

Recycled PET as matrix material

The matrix material in composite structures is pivotal in calculating the composite's overall performance, durability, and sustainability. Polyethylene terephthalate (PET) (Fig. 13) is a popular technical polymer. Because of its multiple vital characteristics it is used in household items, textiles [69], and single-use bottles such as water, cold drinks, juices, etc. PET or polyethylene terephthalate is a functional polymer with many applications, and the market for PET goods has been gradually rising in recent years. This has resulted in a considerable amount of non-biodegradable PET waste [70], which poses significant threat to the environment due to pollution and depletion of resources. PET waste does not decay and can take hundreds of years in the environment. Single-use plastic in the form of PET significantly contributes to garbage in landfills. Moreover, PET is derived from fossil fuels, especially crude oil, and as such, extensive use of PET means more resource depletion and negative environmental consequences. Therefore, the safe method of mitigating the harmful impacts of PET waste is to encourage and improve recycling efforts. Various recycling systems have emerged to address the pollution caused by PET [71]. PET waste can be recycled mechanically and chemically (Fig. 14), with glycolysis being the most successful [72].

Fig. 13. Chemical structure of PET. Based on [73]

Consequently, we need to increase waste collection activities and establish efficient recycling processes, promoting a circular plastics economy and decreasing the amount of plastic garbage entering the environment. One solution that holds promise is chemical recycling, which could turn PET waste back into valuable raw materials and reduce the negative environmental impacts associated with the disposal of plastic waste. The recycled resin (rPET), thus derived from chemical recycling, has properties akin to those of virgin PET and can be used as a matrix for manufacturing composite materials. Recycled PET exhibits excellent processability, allowing for ease of manufacturing and

compatibility with various reinforcement materials. Understanding the molecular structure, processing methods, and fundamental characteristics of rPET is crucial for comprehending its role within the composite system.

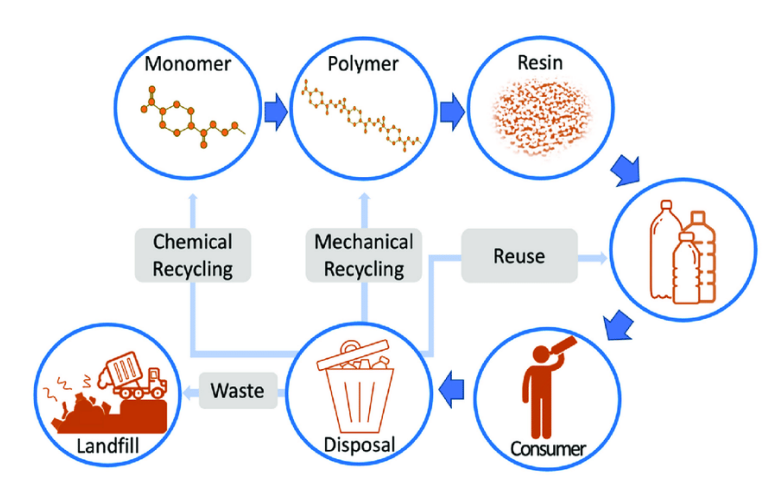


Fig. 14. Life cycle of a typical PET product [74]. Reproduced with the kind permission from https://www.mdpi.com/openaccess#Permissions

Advantages of rPET as matrix material

Recycled PET brings several advantages (Fig. 15), making it a sought-after matrix material for natural fiber-reinforced composites:

- 1. versatility: rPET can be tailored to meet specific application requirements by adjusting its chemical composition and processing parameters. This versatility allows for the formulation of composites with a wide range of mechanical and thermal properties;
- 2. process ability: The ease of processing rPET facilitates various manufacturing techniques, including injection molding, vacuum bagging, infusion, compression molding, and extrusion. This processability contributes to the efficiency and scalability of composite production;
- 3. mechanical performance: rPET offers commendable mechanical properties, including tensile strength, toughness, and resistance to wear. These characteristics enhance the overall mechanical performance of composites, especially when combined with natural fiber reinforcements.

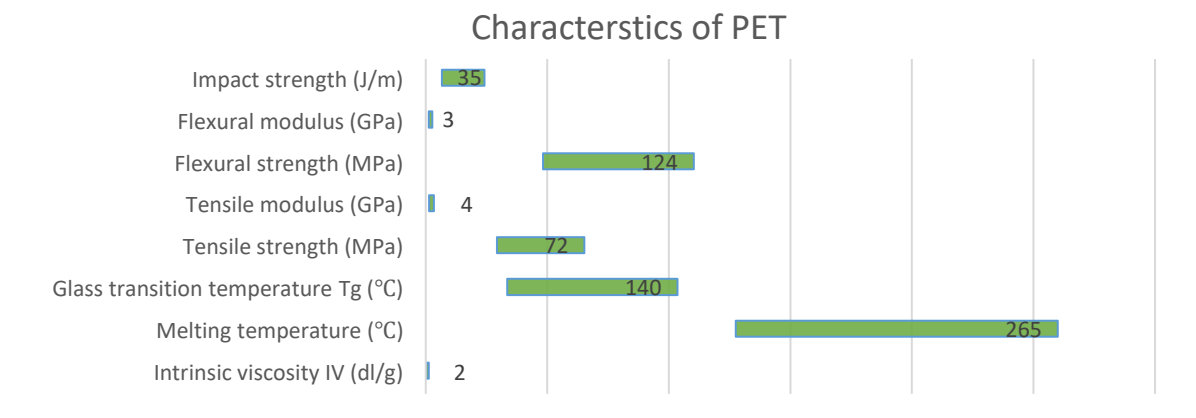


Fig. 15. Properties of PET (polyethylene terephthalate). Based on [75]

Several polymer matrix composites utilize recycled polyethylene terephthalate (RPET) as the matrix material. This also implements the EU's mandate, which requires all plastic packaging to be recyclable or reused by 2030 [76].

Mechanical and durability properties of natural fiber reinforced composites based on recycled PET

Composites based on recycled PET and reinforced with wood flour and polymeric cobalt were aged by Przemysław P. Aczkowski et al. [77] and found that the mechanical performance of the composites decreased drastically as the amount of wood increased. Composites lost their shine and became more brittle as they aged. In a work by J. Mikes [78], the reinforcing impact of basalt fibers and talc powder on recycled PET was examined using the rheometric system, tensile tests, and DSC, comparing the processing and usability characteristics of reinforced composites to those of an unreinforced matrix showed improvement.

A. Dehghani et al. [79] developed a composite based on recycled polyethylene terephthalate (rPET) reinforced with surface-treated 5 % NaOH at 100 °C for one h, date palm leaf fiber (DPLF). Dynamic mechanical analysis (DMA) showed that adding DPLF to the rPET matrix made the composites more robust, the crystallization temperature rose, and the composites were more crystalline. E. Corradini et al. [80] examined composites made from recycled PET and bagasse fiber from sugarcane, the composites' interfacial behavior was studied, it was reported that the bagasse sugarcane fiber reinforcement decreased the tensile strength and elongation of PET but had no effect on the tensile modulus. A study by M.E. Cinar and F. Kar [81] sought to create composite materials using marble dust and PET (polyethylene terephthalate) bottles. In a screwed extruder, marble dust is combined with PET waste particles to create a composite material. Vickers hardness values increased together with the rise in the marble ratio in composite material structure. After a particular ratio (25 % marble dust), it was seen that particle size has significant impact on hardness. Composites were fabricated from unsaturated polyester resin (UPR), which has been synthesized from recycled polyethylene terephthalate (PET) and empty fruit bunch fibers (EFB), as reported by C. Tan et al. [82]. The effects of treating EFB's surface with silane, sodium hydroxide solution (NaOH) and maleic anhydride (MA) were investigated. The testing findings revealed that the chemically modified EFB had more excellent tensile and impact strength than untreated EFB. The silane treatment had the best results, followed by the MA and NaOH treatments, which raised the tensile strength by approximately 21, 18, and 13 %, respectively. It was also reported that treating EFB fibers with these chemicals increased their interfacial bonding with the polymer matrix compared to neat UPR/EFB composites. Sara Madadi Ardekani et al. [83] studied the mechanical and chemical characteristics of recycled PET (rPET) composites reinforced with recycled newspapers to ascertain the impact of NPF. The impact strength of rPET was dramatically increased by adding SEBS-g-MA (10 phr). With adding more fiber, the Young's and flexural moduli improved, and at 5 wt. % fiber loading, the tensile and flexural strengths displayed the most significant values.

In a study by R. Passos et al. [84], different plasticizer mixes were employed to reduce the Tm of recycled PET, allowing the materials to be processed at a temperature much below the melting point of the neat polymer. Without a plasticizer, this temperature

is high enough to cause considerable breakdown of the lignocellulosic sisal fiber. Furthermore, the inclusion of plasticizers reduced the melt viscosity of PET, which resulted in increased wetting of the fibers by the polymer. Additionally, the content of the fiber, surface treatment of the fiber, compatibilizers, recycled plastic, etc., affect the qualities of natural fiber-reinforced rPET composite as a whole [85]. The development of a composite filled with wood flour (WF) based on a PP/r-PET blend was reported by Dairi et al. [86] morphological, mechanical, and physical properties were studied and reported that higher WF loading decreased mechanical properties in PP/r-PET/WF composites except for flexural and tensile modulus due to WF clumping and weak interfacial adhesion. However, with MAPP, these composites showed improved tensile and flexural strength and modulus, as MAPP promoted even WF distribution and better adhesion. Additionally, while higher WF content increased water absorption, adding MAPP reduced it by improving PP-WF adhesion and reducing voids. Uncoated and epoxycoated kenaf fiber reinforced recycled polyethylene terephthalate (rPET) composites at weight percentages of 5, 10, and 15 % by M.M. Owen et al. [87]. DSC and TGA were utilized to analyze the composites' thermal phase and decomposition. Coated kenaf composites were thermally stable, showing no fiber degradation. Mechanical characteristics of coated kenaf composites were better than untreated and improved with fiber content. In a work by P. Chaiwutthinan et al. [88], WPCs were made by combining rPET and PBAT with 5-30 % wood flour (WF). The results showed improvement in impact strength and elongation compared to neat rPET at 5-15 wt. % WF of WPCs. The 20-30 wt. % WF composites showed greater tensile strength than the clean blend. In research by S.T. Mosavi-mirkolaei et al. [89], recycled HDPE/LDPE blends were strengthened with PET microfibrils to make composites. The results reported improvement in the crystallinity of the plastics (HDPE and LDPE) in these wood plastic composites with the addition of PET microfibrils, E-GMA, and WF. The mechanical properties of the WPCs with PET and E-GMA also improved.

Y. Martinez Lopez et al. [90] aimed to fabricate a wood-plastic composite board sawdust, high-density polyethylene, thermoplastic polyethylene terephthalate, polypropylene, and calcium carbonate were raw materials. The results showed better physical and mechanical properties. Ahmad et al. [91] prepared sawdust/UPR composite and investigations into the effects of treatment with alkali, filler content, and filler size on mechanical properties and water absorption of the composites revealed that mechanical strength of composites increased with increasing filler contents, the particle size of the sawdust significantly influenced the mechanical parameters with smaller sawdust providing higher strength and modulus which may be attributed to increased surface area for filler-matrix interaction.

Recycled high-density polyethylene (HDPE) and recycled polyethylene terephthalate (rPET) reinforced with rice husk (RH) composites were fabricated by R. S. Chen et al. [92]. Dimensional stability, swelling, and mechanical behavior of these composites were evaluated as functions of bio-filler content both water absorption and swelling indicated a linear rise with RH concentration. The composites' thickness experienced the most swelling, followed by their width and length. Compatibilized recycled polymer blend rPB-based composites showed less water absorption and dimensional instability than neat rPB-based composites. I. Ahmad and T.M. Mei [93]

prepared a UPR composite reinforced with sawdust from rubber wood with 10 % NaOH treatment. Researchers looked at how the surface treatment and amount of filler affected the composite's mechanical properties and how much water it could hold. The results show that the tensile modulus increased as the filler amount increased. The alkali treatment made the rubber wood sawdust stick better to the UPR matrix and improved the mechanical properties. The flooring tiles based on recycled PET reinforced with natural fibers meet the required compression strength. They may be utilized as possible candidate materials as they are light in weight, economical, and environmentally friendly [94]. I. Ahmad and A. Ramli [95] produced UPR composite based on recycled PET reinforced with sawdust. The results show that as the amount of sawdust filler treated with alkali went up, the tensile strength and bending strength came down as the filler is hydrophilic; adding it makes the composites absorb more water.

Applications, challenges and limitations

The use of plant and animal-sourced natural fibers as reinforcing materials in polymer composites has been investigated around the globe. Natural fibers are becoming increasingly popular for cost-effective buildings and transportation [96]. These polymer composites, which have natural fibers as reinforcement, have the potential to be used in various applications (Fig. 16, 17) and are viable alternatives to synthetic fiber-reinforced polymer composites. As the general public becomes more concerned about the environmental difficulties caused by non-degradable and non-recyclable materials, the industry prefers the shift to natural fibers [97]. To do this, the US and Europe have given specific rules about vehicles that have completed their useful lives. The European Commission put into place the "European Guidelines 2000/53/EG", which said that by 2005, 85 % of an automobile's weight should be recyclable. By 2015, this number rose to 95 %. This kind of law is a big reason NFRCs are becoming more popular.

POTENTIAL APPLICATION AREAS

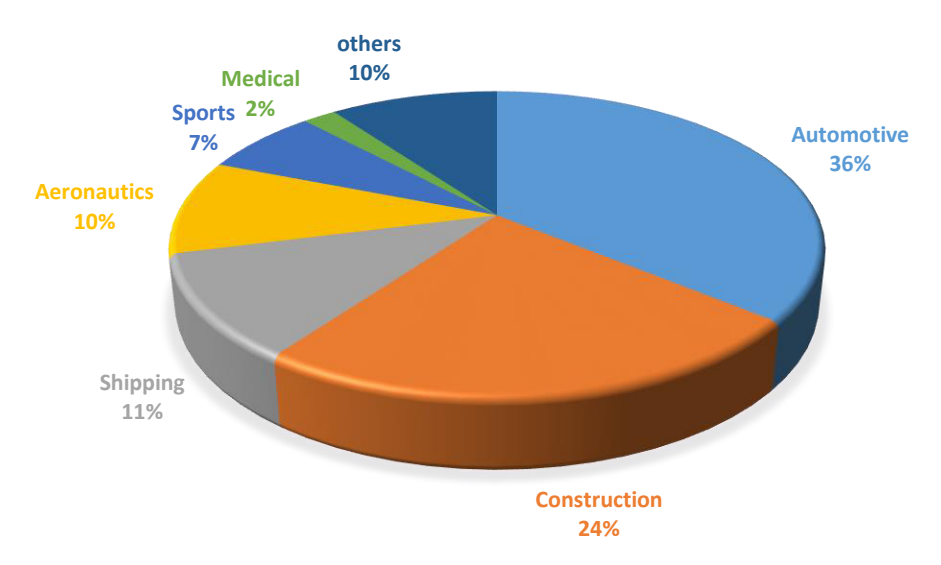


Fig. 16. Application potential of NFRCs. Based on [104]

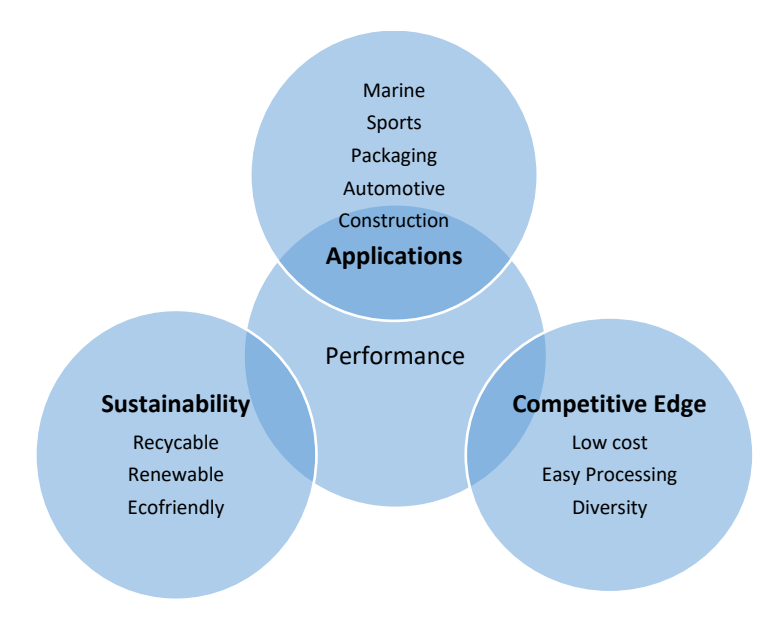


Fig. 17. The performance of commercial success for NFPCs. Based on [105]

Polymers based on natural fibers have been used in many car models over the past 20 years, initially in Europe and then in North America. These include boot liners, sun visors, oil and air filters, rear seat backs, exterior underfloor paneling, internal engine covers, door panels, trays, utility racks, and console panels [98]. At the same time, we can reduce our reliance on crude oil by building more fuel-efficient cars, not just by putting efficient engines in them but also by making them lighter so that they need less fuel [99]. Strength and safety must not be compromised to reduce vehicle weight. High-strength materials are usually heavier. It seems more complicated to achieve good strength with lightweight materials than conventional ones. The only practical approach is to use plant-based materials, which might replace steel. The automotive industry is using plant-based materials to make car components [100].

The avenues of application of natural fiber-reinforced composites are growing at a pace in a large number of engineering and multidisciplinary areas [101] owing to their intrinsic properties such as low specific weight, comparatively high strength, relatively low production cost, resistance to corrosion, and fatigue NFRCs are widely used in automotive applications, structural components, packaging, building, electronic and electrical industries, aircraft, sports and recreational equipment, boats, machinery, office supplies, etc. [102].

Compared with composites reinforced with synthetic fibers such as glass fibers, it was found that composites with natural fibers were better for industrial use. Also, because natural fibers are now seeing a place in different engineering and construction industries, it helps rural areas grow their economies [103].

NFPCs have also been employed as a replacement for synthetic fiber (Fig. 18) in the aircraft sector for interior paneling, goods for funeral and packaging items, railings of ships and boats, packaging cases for laptops, mobile phones, and other lightweight electronic items and toys [6]. Bamboo culms are interconnected to form a multi-culm composite part to withstand heavy loads and provide sustainable green building resources [105]. A study carried out by Saxena et al. [106] revealed that Indian railways make floor and roof panels, berths, walls, and modular toilets in the coaches using natural

fibers, which is essential for getting high speeds, low power consumption, less weight, less inertia, decreased wear of the tracks and other things. Swamy et al. [107] examined fiber usage from the areca plant as reinforcement in polymer composites. They discovered it to be an excellent acoustic material for structural applications. Maheswari et al. [108] suggested that composites made from high-density polyethylene (HDPE) reinforced with Borassus can be utilized in various secondary structural applications and as suitable packaging materials.

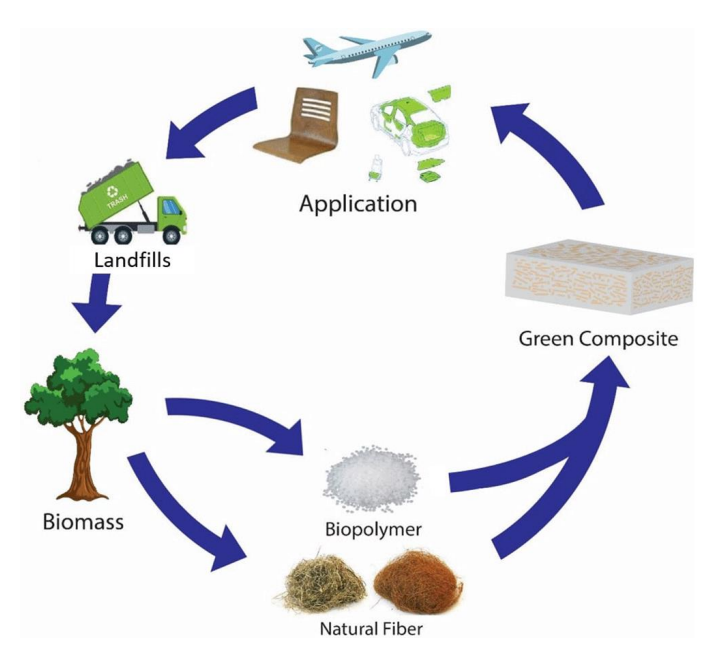


Fig. 18. Life cycle of green composites [109]. Reproduced with the kind permission from https://materialsopenresearch.org/about/policies/#licenses

Furthermore, some researchers fabricated cellular beams and plates reinforced with fibers from jute, hemp, and flax plants based on unsaturated polyester matrix as loadbearing structural members, demonstrating that NFRCs can be used as load-bearing members in structural applications [110]. Ghavami [111] used bamboo fiber to produce structural concrete parts. Rethinam and Sivaraman [112] examined the acoustic qualities of areca plant fiber and found it better than plywood, making it more suitable for furniture applications. Board made out of banana fiber is a potential substitute for plywood and medium-density boards made of wood [113]. RH-filled composites will likely be used in building and construction as alternatives to other materials because they are light and inexpensive [114]. Zawawi et al. [115] conducted a microwave property comparison study on PLA composites reinforced with plant-based fibers to assess their potential as alternatives to typical printed circuit boards (PCBs) for electronic industries. They reported that kenaf/PLA and RH/PLA composites can be used for microwave applications. Wind and solar energy are the most popular renewable energy sources that are being looked at as alternatives to oil-based energy sources. The cost of making the molds for the parabolic trough collector (PTC) makes it expensive. In these situations, adding plantbased fibers is an excellent way to make up for the overall cost of the composite materials. It was recently shown that the price of trough collectors can be reduced by adding natural fibers [116]. Carbon and glass fiber hybrids are the most used turbine

blade fillers. Price and weight are the key disadvantages of carbon and glass fibers. Utilizing comparably less expensive fillers that are significantly lighter than carbon fibers can increase the efficiency of wind turbines. A recent study indicated that it is possible to substitute 20–30 % of carbon fibers in turbine blade composites (Fig. 19) with basalt fibers without adversely affecting the composite's characteristics [117].

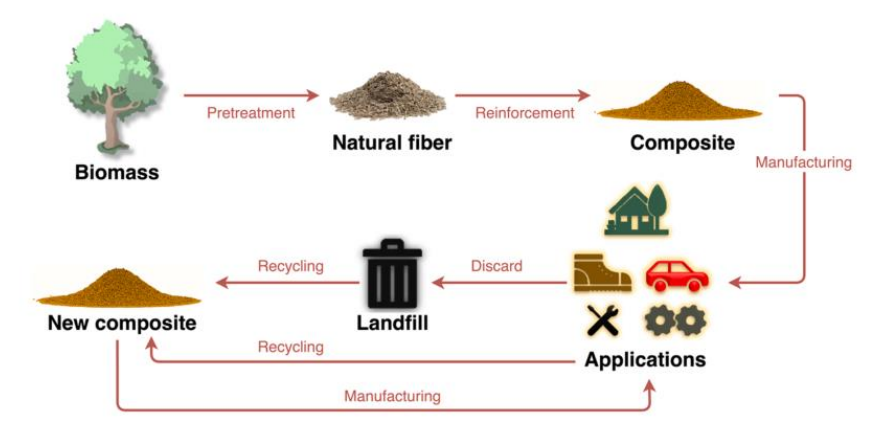


Fig. 19. Recycling natural fiber-reinforced composites toward a circular economy. Reprinted with permission from [118], © Elsevier 2022

One of the primary challenges in natural fiber-reinforced composites lies in achieving optimal interactions at the fiber-matrix interface [119]. The composite's effectiveness heavily depends on the strength and compatibility of this interface. More studies that explore methods to enhance interfacial adhesion, such as surface treatments, coupling agents, and modifications to the matrix formulation, are needed. Understanding the challenges of achieving a solid interface is essential for overcoming mechanical performance limitations and ensuring these composites' longevity. The processing techniques employed in fabricating natural fiber-reinforced rPET composites are crucial in determining their mechanical properties and overall performance. Challenges arise in achieving uniform fiber dispersion, minimizing defects, and optimizing processing parameters to ensure the desired material characteristics. While traditional natural fibers like jute, flax, hemp, and kenaf exhibit favorable properties, their availability, processing, or mechanical performance limitations pose challenges. Exploration of novel natural fibers is needed to address these limitations. Research efforts focusing on alternative natural fibers with unique characteristics are required, shedding light on the potential for diversifying fiber options and overcoming inherent challenges associated with existing choices. The environmental impact of natural fiber-reinforced rPET composites, while generally having a lower carbon footprint than traditional materials, introduces challenges to sustainability and end-of-life considerations. Addressing the environmental impact of composite materials is integral to ensuring their alignment with broader sustainability goals and minimizing their ecological footprint. By understanding the intricacies of interactions at the fiber-matrix interface, refining processing techniques, exploring novel natural fibers, and considering environmental factors, researchers and practitioners can pave the way for overcoming these challenges.

Conclusions

In exploring the mechanical performance and durability behavior of natural fiberreinforced rPET composites, this review has uncovered valuable insights into the promising realm of sustainable materials. The interfacial adhesion, compatibility, and interaction of the fiber with the matrix play a crucial role in NFRC's mechanical behavior. Various issues are associated with using natural fibers as reinforcement in polymer composites. As such, more research is required, focusing on parameters like stiffness in composites, moisture effects, fatique and creep life, physical degradation, and less longterm stability. These composites have outstanding structural qualities, and more research is needed to analyze the performance of natural fiber composite materials in impact loading. Compared to virgin PET, rPET degrades during recycling, resulting in inferior mechanical characteristics. Mixing rPET with virgin PET, polyamide, polycarbonate, and other materials may address the mechanical performance loss of rPET. Combining rPET with additives like chain extender, polypropylene, polyethylene, polyamide, and polycarbonate enhances the blend's properties, reduces environmental waste, and slows the spread of contaminants. Hybridization using several natural (and synthetic) fiber reinforcements has emerged as a viable composite manufacturing avenue. Furthermore, it can enhance mechanical behavior and durability. External and load-bearing applications for NFRCs have significantly grown, but more research is needed to broaden their use range, including improvements in the hydrothermal environment and durability. Future research and development must focus on developing eco-friendly materials with adequate qualities to replace synthetic polymer composites in emerging new application areas. This review discussed natural fibers, their types, surface modification of fibers, physical and mechanical properties, advantages, and disadvantages. Due to their durability, renewable nature, and fully or partially recyclable qualities, research on natural fiber-based composite materials has expanded in recent years. The automobile and space sectors are the most pushing composites, which have been reinforced with natural fiber manufacturing components that are non-structural and semi-structural. Other major industries, such as sports, medicine, furniture, and packaging materials, also adopt natural fiber composites.

CRediT authorship contribution statement

Ajay Kumar: writing – review & editing, writing – original draft; conceptualization and data curation; **Raman Bedi Sc**: supervision and review of entire manuscript.

Conflict of interest

The authors declare that they have no conflict of interest.

References

- 1. Sriram M, Aswin Sidhaarth KR. Various properties of natural and artificial fibers with cementitious composites in hybrid form A review. *Mater Today Proc.* 2022;60: 2018–2025.
- 2. Rajeshkumar G, Seshadri SA, Devnani GL, Sanjay MR, Siengchin S, Maran JP, Al-Dhabi NA, Ponmurugan K, Valan Arasu M, Sivarajasekar N, Ronaldo Anuf A. Environment-friendly, renewable and sustainable poly

lactic acid (PLA) based natural fiber reinforced composites – A comprehensive review. *Journal of Cleaner Production*. 2021;310: 127483.

- 3. Rong MZ, Zhang MQ, Liu Y, Yang GC, Zeng HM. The effect of fiber treatment on the mechanical properties of unidirectional sisal-reinforced epoxy composites. *Composites Science and Technology*. 2001;61(10): 1437–1447.
- 4. Fuqua MA, Huo S, Ulven CA. Natural fiber-reinforced composites. *Polymer Reviews*. 2012;52(3–4): 259–320.
- 5. Reddy N, Yang Y. Biofibers from agricultural byproducts for industrial applications. *Trends in Biotechnology*. 2005;23(1): 22–27.
- 6. Ho M, Wang H, Lee J, Ho C, Lau K, Leng J, Hui D. Critical factors on manufacturing processes of natural fibre composites. *Composites Part B.* 2012;43(8): 3549–3562.
- 7. Hameed N, Salim NV, Hanley TL, Sona M, Fox BL, Guo Q. Individual dispersion of carbon nanotubes in epoxy via a novel dispersion-curing approach using ionic liquids. *Physical Chemistry Chemical Physics*. 2013;15(28): 11696–703.
- 8. Kalia S, Dufresne A, Cherian BM, Kaith BS, Averous L, Njuguna J, Nassiopoulos E. Cellulose-based bio-and nanocomposites: A review. *Int J Polym Sci.* 2011;11: 2011.
- 9. Faruk O, Bledzki AK, Fink HP, Sain M. Progress report on natural fiber reinforced composites. *Macromol Mater Eng.* 2014;299(1): 9–26.
- 10. Gurunathan T, Mohanty S, Nayak SK. A review of the recent developments in biocomposites based on natural fibres and their application perspectives. *Composites Part A.* 2015;77: 1–25.
- 11. Singha AS, Thakur VK. Mechanical properties of natural fibre reinforced polymer composites. *Bull Mater Sci.* 2008;31: 791–799.
- 12. Shah DU. Developing plant fibre composites for structural applications by optimising composite parameters: a critical review. *J Mater Sci.* 2013;48: 6083–6107.
- 13. Kalia S, Kaith BS, Kaur I. Pretreatments of Natural Fibers and their Application as Reinforcing Material in Polymer Composites A Review. *Polymer Engineering and Science*. 2009;49(7): 1253–1272.
- 14. Reddy PV, Krishnudu DM, Prasad PR, Reddy RVS. A Study on Alkali Treatment Influence on Prosopis Juliflora Fiber-Reinforced Epoxy Composites. *Journal of Natural Fibers*. 2021;18(8): 1094–1106.
- 15. Boopathi L, Sampath PS, Mylsamy K. Investigation of physical, chemical and mechanical properties of raw and alkali treated Borassus fruit fiber. *Composites Part B.* 2012;43(8): 3044–3052.
- 16. Jawaid M, Khalil HPSA. Cellulosic/synthetic fibre reinforced polymer hybrid composites: A review. *Carbohydrate Polymers*. 2011;86(1): 1–18.
- 17. Gonzalez V, Lou X, Chi T. Evaluating Environmental Impact of Natural and Synthetic Fibers: A Life Cycle Assessment Approach. *Sustainability*. 2023;15(9): 7670.
- 18. Singh S, Gupta PK. Natural Fiber-Reinforced Polymer Composite: A Review. In: *Manufacturing and Processing of Advanced Materials*. Bentham Science Publisher; 2023. p.141–153.
- 19. de Azevedo ARG, Cruz ASA, Marvila MT, de Oliveira LB, Monteiro SN, Vieira CMF, Fediuk R, Timokhin R, Vatin N, Daironas M. Natural Fibers as an Alternative to Synthetic Fibers in Reinforcement of Geopolymer Matrices: A Comparative Review. *Polymers*. 2021;13(15): 2493.
- 20. Bichang'a DO, Aramide FO, Oladele IO, Alabi OO. A Review on the Parameters Affecting the Mechanical, Physical, and Thermal Properties of Natural/Synthetic Fibre Hybrid Reinforced Polymer Composites. *Advances in Materials Science and Engineering*. 2022;2022(1): 1–28.
- 21. Mohd Bakhori SN, Hassan MZ, Mohd Bakhori N, Jamaludin KR, Ramlie F, Md Daud MY, Abdul Aziz S. Physical, Mechanical and Perforation Resistance of Natural-Synthetic Fiber Interply Laminate Hybrid Composites. *Polymers*. 2022;14(7): 1322.
- 22. Khan SH, Rahman MZ, Haque MR, Hoque ME. Characterization and Comparative Evaluation of Structural, Chemical, Thermal, Mechanical, and Morphological Properties of Plant Fibers. In: Khiari R, Jawaid M, Belgacem MN. (eds.) *Annual Plant: Sources of Fibres, Nanocellulose and Cellulosic Derivatives. Composites Science and Technology.* Singapore: Springer; 2023. p.1–45.
- 23. Al-Maharma AY, Patil SP, Markert B. 33–Environmental impact analysis of plant fibers and their composites relative to their synthetic counterparts based on life cycle assessment approach. In: Rangappa SM, Puttegowda M, Parameswaranpillai J, Siengchin S, Gorbatyuk S. (eds.) *The Textile Institute Book Series. Advances in Bio-Based Fiber.* Woodhead Publishing; 2022. p.741–781.
- 24. Saba N, Jawaid M. 3–Epoxy resin based hybrid polymer composites. In: Thakur VK, Thakur MK, Pappu A. (eds.) *Hybrid Polymer Composite Materials*. Woodhead Publishing; 2017. p.57–82.

- 25. Mohammed MM, Rasidi M, Mohammed AM, Rahman RB, Osman AF, Adam T, Betar BO, Dahham OS. Interfacial bonding mechanisms of natural fibre-matrix composites: An overview. *BioResources*. 2022;17(4): 7031–7090. 26. Vargas J, Jalalvand M, Meza JM. Improving interfacial shear strength of fique fibres using an acrylic coating. *Science Progress*. 2023;106(4): 1–18.
- 27. Pattnaik SS, Behera AK, Das N. Spectroscopic Analysis of Interfacial Adhesion in Natural Fibre Polymer Composites. In: Krishnasamy S, Hemath KM, Parameswaranpillai J, Mavinkere RS, Siengchin S. (eds.) *Interfacial Bonding Characteristics in Natural Fiber Reinforced Polymer Composites. Composites Science and Technology.* Singapore: Springer; 2024. p.79–96.
- 28. Ermeydan MA. New Methodologies to Improve the Interfacial Interaction in Natural Fibre Polymer Composites. In: Krishnasamy S, Hemath KM, Parameswaranpillai J, Mavinkere RS, Siengchin S. (eds.) *Interfacial Bonding Characteristics in Natural Fiber Reinforced Polymer Composites. Composites Science and Technology.* Singapore: Springer; 2024. p.23–45.
- 29. Mohammed M, Rahman R, Mohammed AM, Adam T, Betar BO, Osman AF, Dahham OS. Surface treatment to improve water repellence and compatibility of natural fiber with polymer matrix: Recent advancement. *Polymer Testing*. 2022;115: 107707.
- 30. Lilholt H, Lawther J. 1.10 Natural Organic Fibers. In: Kelly A, Zweben C. (eds.) *Comprehensive Composite Materials*. Pergamon; 2000. p.303 325.
- 31. Faruk O, Bledzki AK, Fink H peter, Sain M. Progress in Polymer Science Biocomposites reinforced with natural fibers: 2000–2010. *Progress in Polymer Science*. 2012;37: 1552–1596.
- 32. Qian S, Wang H, Zarei E, Sheng K. Effect of hydrothermal pretreatment on the properties of moso bamboo particles reinforced polyvinyl chloride composites. *Composites Part B.* 2015;82: 23–29.
- 33. Ardanuy M, Claramunt J, Toledo Filho RD. Cellulosic fiber reinforced cement-based composites: A review of recent research. *Construction and Building Materials*. 2015;79: 115–128.
- 34. Shih YF, Chang WC, Liu WC, Lee CC, Kuan CS, Yu YH. Pineapple leaf/recycled disposable chopstick hybrid fiber-reinforced biodegradable composites. *Journal of the Taiwan Institute of Chemical Engineers*. 2014;45(4): 2039–2046. 35. Bledzki AK, Gassan J. Composites reinforced with cellulose based fibres. *Progress in Polymer Science*. 1999;24: 221–274.
- 36. Bledzki AK, Reihmane S, Gassan J. Properties and modification methods for vegetable fibers for natural fiber composites. *J Appl Polym Sci.* 1996;59: 1329–1336.
- 37. Gassan J, Gutowski VS. Effects of corona discharge and UV treatment on the properties of jute-fibre expoxy composites. *Composites Science and Technology*. 2000;60(15): 2857–2863.
- 38. Di Benedetto RM, Gelfuso MV, Thomazini D. Influence of UV radiation on the physical-chemical and mechanical properties of banana fiber. *Materials Research*. 2015;18(2): 265–272.
- 39. Beg MDH, Pickering KL. Mechanical performance of Kraft fibre reinforced polypropylene composites: Influence of fibre length, fibre beating and hygrothermal ageing. *Composites Part A.* 2008;39(11): 1748–1755.
- 40. Sreekala MS, Kumaran MG, Joseph S, John MJ, Thomas S. Oil Palm Fibre Reinforced Phenol Formaldehyde Composites: Influence of Fibre Surface Modifications on the Mechanical Performance. *Applied Composite Materials*. 2000;(7): 295–329.
- 41. Young RA. Activation and Characterization of Fiber Surfaces for Composites. *Emerging Technologies for Materials and Chemicals from Biomass.* 1992;9: 115–135.
- 42. Thiruchitrambalam M, Alavudeen A, Athijayamani A, Venkateshwaran N, Perumal AE. Improving mechanical properties of banana/kenaf polyester hybrid composites using sodium laulryl sulfate treatment. *Materials Physics and Mechanics*. 2009;8(2): 165–173.
- 43. Ali A, Shaker K, Nawab Y, Jabbar M, Hussain T, Militky J, Baheti V. Hydrophobic treatment of natural fibers and their composites—A review. *Journal of Industrial Textiles*. 2018;47(8): 2153–2183.
- 44. Ray D, Sarkar BK, Rana AK, Bose NR. Mechanical properties of vinylester resin matrix composites reinforced with alkali-treated jute fibres. *Composites Part A.* 2001;32(1): 119–127.
- 45. Walker JCF. Primary Wood Processing: Principles and Practice. Springer Dordrecht; 2006.
- 46. Orue A, Jauregi A, Labidi J, Eceiza A, Arbelaiz A. The effect of surface modifications on sisal fiber properties and sisal/poly (lactic acid) interface adhesion. *Composites Part B.* 2014;73: 132–138.
- 47. Orue A, Eceiza A, Peña-Rodriguez C, Arbelaiz A. Water uptake behavior and young modulus prediction of composites based on treated sisal fibers and poly(lactic acid). *Materials*. 2016;9(5): 400.
- 48. Morrison WH, Archibald DD, Sharma HSS, Akin DE. Chemical and physical characterization of water- and dew-retted flax fibers. *Industrial Crops and Products*. 2000;12(1): 39–46.

140 A. Kumar, R. Bedi

49. Misra S, Misra M, Tripathy SS, Nayak SK, Mohanty AK. The influence of chemical surface modification on the performance of sisal-polyester biocomposites. *Polymer Composites*. 2002;23(2): 164–170.

- 50. Huda MS, Drzal LT, Mohanty AK, Misra M. Effect of chemical modifications of the pineapple leaf fiber surfaces on the interfacial and mechanical properties of laminated biocomposites. *Composite Interfaces*. 2008;15(2–3): 169–191.
- 51. Edeerozey AMM, Akil H, Azhar AB, Ariffin MIZ. Chemical modification of kenaf fibers. *Materials Letters*. 2007;61(2007): 2023–2025.
- 52. Fiore V, Bella GD, Valenza A. The effect of alkaline treatment on mechanical properties of kenaf fibers and their epoxy composites. *Composites Part B.* 2015;68: 14–21.
- 53. Abdullah NM, Ahmad I. Potential of using polyester reinforced coconut fiber composites derived from recycling polyethylene terephthalate (PET) waste. *Fibers and Polymers*. 2013;14(4): 584–590.
- 54. Narayana VL, Rao LB. A brief review on the effect of alkali treatment on mechanical properties of various natural fiber reinforced polymer composites. *Materials Today: Proceedings*. 2021;44(1): 1988–1994.
- 55. Koohestani B, Khodadadi-Darban A, Darezereshki E, Mokhtari P, Yilmaz E, Yilmaz E. The influence of sodium and sulfate ions on total solidi fi cation and encapsulation potential of iron-rich acid mine drainage in silica gel. *Journal of Environmental Chemical Engineering*. 2018;6(2): 3520–3527.
- 56. Kumar A, Bedi R, Singh B. Mechanical properties of composite materials based on waste plastic A review. *Materials Today: Proceedings*. 2020;26(2): 1293–1301.
- 57. Liu Y, Lv X, Bao J, Xie J, Tang X, Che J, Ma Y, Tong J. Characterization of silane treated and untreated natural cellulosic fibre from corn stalk waste as potential reinforcement in polymer composites. *Carbohydrate Polymers*. 2019;218: 179–187.
- 58. Nirmal U, Hashim J, Megat Ahmad MMH. A review on tribological performance of natural fibre polymeric composites. *Tribology International*. 2015;83: 77–104.
- 59. Joseph K, Mattoso LHC, Toledo Filho RD, Thomas S, Carvalho LH, Pothan LA, Kala S, James B. Natural Fiber Reinforced Thermoplastic Composites. In: Frollini E, Leao AL, Mattoso LHC. (eds.) *Natural Polymers and Agrofibers Composites*. San Carlos: Embrapa; 2000. p.159–201.
- 60. Sood M, Dwivedi G. Effect of fiber treatment on flexural properties of natural fiber reinforced composites: A review. *Egyptian Journal of Petroleum*. 2018;27(4): 775–783.
- 61. Dilfi A, Balan A, Bin H, Xian G, Thomas S. Effect of surface modification of jute fiber on the mechanical properties and durability of jute fiber-reinforced epoxy composites. *Polymer Composites*. 2018;39(S4): E2519–E2528.
- 62. Orue A, Eceiza A, Arbelaiz A. Pretreatments of Natural Fibers for Polymer Composite Materials. In: Kalia S. (eds.) *Lignocellulosic Composite Materials*. Cham: Springer; 2018. p.137–175.
- 63. Sepe R, Bollino F, Boccarusso L, Caputo F. Influence of chemical treatments on mechanical properties of hemp fiber reinforced composites. *Composites Part B.* 2018;133: 210–217.
- 64. Fiore V, Sanfilippo C, Calabrese L. Influence of sodium bicarbonate treatment on the aging resistance of natural fiber reinforced polymer composites under marine environment. *Polymer Testing*. 2019;80: 106100.
- 65. Bayart M, Adjalle K, Diop A, Ovlaque P, Barnabe S, Robert M, Elkoun S. PLA/flax fiber bio-composites: effect of polyphenol-based surface treatment on interfacial adhesion and durability. *Composite Interfaces*. 2020;28(3): 287–308. 66. Inacio ALN, Nonato RC, Bonse BC. Mechanical and thermal behavior of aged composites of recycled PP/EPDM/talc reinforced with bamboo fiber. *Polymer Testing*. 2018;72: 357–363.
- 67. Ali A, Shaker K, Nawab Y, Jabbar M, Hussain T, Militky J, Baheti V. Hydrophobic treatment of natural fibers and their composites—A review. *Journal of Industrial Textiles*. 2018;47(8): 2153–2183.
- 68. Satapathy S, Kothapalli RVS. Mechanical, Dynamic Mechanical and Thermal Properties of Banana Fiber/Recycled High Density Polyethylene Biocomposites Filled with Flyash Cenospheres. *J Polym Environ*. 2018;26: 200–213.
- 69. Ciobanu RC, Aradoaei M, Caramitu AR, Ion I, Schreiner CM, Tsakiris V, Marinescu V, Hitruc EG, Aflori M. Special Packaging Materials from Recycled PET and Metallic Nano-Powders. *Polymers*. 2023;15(15): 3161.
- 70. Chen R, Deng S, Cui T, Duan S, Jia Q, Zhang L. Progress in recycling and reutilization of waste polyethylene terephthalate. *Progress in Rubber, Plastics and Recycling Technology.* 2024;40(1): 77–97.
- 71. Muringayil Joseph T, Azat S, Ahmadi Z, Moini Jazani O, Esmaeili A, Kianfar E, Haponiuk J, Thomas S. Polyethylene terephthalate (PET) recycling: A review. *Case Studies in Chemical and Environmental Engineering*. 2024;9: 100673.
- 72. Bhanderi KK, Joshi JR, Patel JV. Recycling of polyethylene terephthalate (PET Or PETE) plastics An alternative to obtain value added products: A review. *Journal of the Indian Chemical Society*. 2023;100(1): 100843.

- 73. Dutt K, Soni RK. A review on synthesis of value added products from polyethylene terephthalate (PET) waste. *Polym. Sci. Ser. B.* 2013;55: 430–452.
- 74. Benyathiar P, Kumar P, Carpenter G, Brace J, Mishra DK. Polyethylene Terephthalate (PET) Bottle-to-Bottle Recycling for the Beverage Industry: A Review. *Polymers*. 2022;14(12): 2366.
- 75. Singh AK, Bedi R, Kaith BS. Composite materials based on recycled polyethylene terephthalate and their properties A comprehensive review. *Composites Part B.* 2021;219: 108928.
- 76. Almahri G, Madi K, Alkaabi F, Badran Y, Shehadeh K, ElHassan A, Ahmed W, Alzahmi S. Characterization of Hybrid FRP Composite Produced from Recycled PET and CFRP. *Polymers*. 2023; 15(13): 2946.
- 77. Pączkowski P, Puszka A, Gawdzik B. Green Composites Based on Unsaturated Polyester Resin from Recycled Poly(Ethylene Terephthalate) with Wood Flour as Filler—Synthesis, Characterization and Aging Effect. *Polymers*. 2020;12(12): 2966.
- 78. Kracalik M, Pospisil L, Slouf M, Mikesova J, Sikora A, Simonik J, Fortelny I. Recycled poly(ethylene terephthalate) reinforced with basalt fibres: Rheology, structure, and utility properties. *Polymer Composites*. 2008;29(4): 437–442.
- 79. Dehghani A, Madadi Ardekani S, Al-Maadeed MA, Hassan A, Uzir Wahit M. Mechanical and thermal properties of date palm leaf fiber reinforced recycled poly (ethylene terephthalate) composites. *Materials and Design*. 2013;52: 841–848.
- 80. Corradini E, Ito EN, Marconcini JM, Triveno Rios C, Agnelli JAM, Mattoso LHC. Interfacial behavior of composites of recycled poly(ethyelene terephthalate) and sugarcane bagasse fiber. *Polymer Testing*. 2009;28(2): 183–187.
- 81. Cinar ME, Kar F. Characterization of composite produced from waste PET and marble dust. *Construction and Building Materials*. 2018;163: 734–741.
- 82. Tan C, Ahmad I, Heng M. Characterization of polyester composites from recycled polyethylene terephthalate reinforced with empty fruit bunch fibers. *Materials and Design*. 2011; 32: 4493–4501.
- 83. Ardekani SM, Dehghani A, Al-Maadeed MA, Wahit MU, Hassan A. Mechanical and thermal properties of recycled poly(ethylene terephthalate) reinforced newspaper fiber composites. *Fibers and Polymers*. 2014;15: 1531–1538.
- 84. Oliveira Santos R, Castro DO, Ruvolo-Filho AC, Frollini E. Processing and thermal properties of composites based on recycled PET, sisal fibers, and renewable plasticizers. *J. Appl. Polym. Sci.* 2014;131(12): 40386.
- 85. Cruz-Salgado J, Alonso-Romero S, Zitzumbo-Guzman R, Dominguez-Dominguez J. Optimization of the Tensile and Flexural Strength of a Wood-PET Composite. *Ingenieria Investigacion y Tecnologia*. 2015;16(01): 105–112.
- 86. Dairi B, Djidjelli H, Boukerrou A, Migneault S, Koubaa A. Morphological, mechanical, and physical properties of composites made with wood flour-reinforced polypropylene/recycled poly(ethylene terephthalate) blends. *Polymer Composites*. 2015;38(8): 1749–1755.
- 87. Owen MM, Ishiaku US, Danladi A, Dauda BM, Romli AZ. The effect of surface coating and fibre loading on thermo-mechanical properties of recycled polyethylene terephthalate (RPET)/epoxy-coated kenaf fibre composites. *AIP Conf. Proc.* 2018;1985 (1): 030002.
- 88. Chaiwutthinan P, Pimpong A, Larpkasemsuk A, Chuayjuljit S, Boonmahitthisud A. Wood plastic composites based on recycled poly(ethylene terephthalate) and poly(butylene adipate-co-terephthalate). *Journal of Metals, Materials and Minerals.* 2019;29(2): 87–97.
- 89. Mosavi-Mirkolaei ST, Najafi SK, Tajvidi M. Physical and Mechanical Properties of Wood-Plastic Composites Made with Microfibrillar Blends of LDPE, HDPE and PET. *Fibers and Polymers*. 2019;20: 2156–2165.
- 90. Lopez YM, Paes JB, Gustave D, Goncalves FG, Mendez FC, Theodoro Nantet AC. Production of wood-plastic composites using cedrela odorata sawdust waste and recycled thermoplastics mixture from post-consumer products—A sustainable approach for cleaner production in Cuba. *Journal of Cleaner Production*. 2020;244: 118723.
- 91. Ahmad I, Mosadeghzad Z, Daik R, Ramli A. The effect of alkali treatment and filler size on the properties of sawdust/UPR composites based on recycled PET wastes. *J. Appl. Polym. Sci.* 2008;109(6): 3651–3658.
- 92. Chen RS, Ahmad S, Gan S. Rice husk bio-filler reinforced polymer blends of recycled HDPE/PET: Three-dimensional stability under water immersion and mechanical performance. *Polymer Composites*. 2016;39(8): 2695–2704.
- 93. Ahmad I, Mei TM. Mechanical and Morphological Studies of Rubber Wood Sawdust-Filled UPR Composite Based on Recycled PET. *Polymer-Plastics Technology and Engineering*. 2009;48(12): 1262–1268.
- 94. Chaka KT, Ahmed FE, Zegeye LH, Worku BG. Compressive Strength of Floor Tile Composites from Recycled PET Reinforced with Natural Fibers. *Journal of Natural Fibers*. 2022;20(1): 2146249.
- 95. Mosadeghzada Z, Ahmad I, Daika R, Ramli A, Jalaludin Z. Preparation and properties of acacia sawdust/UPR composite based on recycled PET. *Malaysian Polymer Journal*. 2009;4(1): 30–41.

142 A. Kumar, R. Bedi

96. Kumar S, Manna A, Dang R. A review on applications of natural Fiber-Reinforced composites (NFRCs). *Materials Today: Proceedings.* 2022;50(5): 1632–1636.

- 97. Witayakran S, Smitthipong W, Wangpradid R, Chollakup R, Clouston PL. Natural Fiber Composites: Review of Recent Automotive Trends. In: Hashmi S, Choudhury IA. (eds.) *Encyclopedia of Renewable and Sustainable Materials*. Elsevier; 2017. p.166–174.
- 98. Pickering KL, Efendy MGA, Le TM. A review of recent developments in natural fibre composites and their mechanical performance. *Composites Part A.* 2016;83: 98–112.
- 99. Sinha AK, Narang HK, Bhattacharya S. Mechanical properties of natural fibre polymer composites. *Journal of Polymer Engineering*. 2017;37(9): 879–895.
- 100. Khan MZR, Srivastava SK, Gupta MK. Tensile and flexural properties of natural fiber reinforced polymer composites: A review. *Journal of Reinforced Plastics and Composites*. 2018;37(24): 1435–1455.
- 101. Mohammed L, Ansari MNM, Pua G, Jawaid M, Islam MS. A Review on Natural Fiber Reinforced Polymer Composite and Its Applications. *Int J Polym Sci.* 2015;2015(1): 243947.
- 102. Pecas P, Carvalho H, Salman H, Leite M. Natural fibre composites and their applications: A review. *Journal of Composites Science*. 2018;2(4): 66.
- 103. Ashik KP, Sharma RS. A Review on Mechanical Properties of Natural Fiber Reinforced Hybrid Polymer Composites. *Journal of Minerals and Materials Characterization and Engineering*. 2015;3: 420–426.
- 104. Vaisanen T, Das O, Tomppo L. A review on new bio-based constituents for natural fiber-polymer composites. *Journal of Cleaner Production*. 2017;149: 582–596.
- 105. Bahtiar ET, Denih A, Rama Putra G. Multi-culm bamboo composites as sustainable materials for green constructions: section properties and column behavior. *Results in Engineering*. 2023;17: 100911.
- 106. Srinivasakumar P. Sisal and its Potential for Creating Innovative Employment Opportunities and Economic Prospects. *IOSR Journal of Mechanical and Civil Engineering*. 2013;8(6): 01–08.
- 107. Swamy RP, Kumar GCM, Vrushabhendrappa Y, Joseph V. Study of areca-reinforced phenol formaldehyde composites. *Journal of Reinforced Plastics and Composites*. 2004;23(13): 1373–1382.
- 108. Maheswari CU, Reddy KO, Muzenda E, Shukla M, Rajulu AV. A Comparative Study of Modified and Unmodified High-Density Polyethylene/Borassus Fiber Composites. *International Journal of Polymer Analysis and Characterization*. 2013;18(6): 439–450.
- 109. Molla A, Moyeen AA, Mashfiqua Mahmud R, Haque MJ. Plant fiber-reinforced green composite: A review on surface modification, properties, fabrications and applications. *Materials Open Research*. 2024;3: 6.
- 110. Kumar R, Ul Haq MI, Haq U, Raina A, Anand A, Industrial applications of natural fibre-reinforced polymer composites—challenges and opportunities. *International Journal of Sustainable Engineering*. 2018;12(3): 212–220.
- 111. Ghavami K. Bamboo as reinforcement in structural concrete elements. *Cement and Concrete Composites*. 2005;27(6): 637–649.
- 112. Rethinam P, Sivaraman K. Arecanut (Areca catechu. L)—Present status and future strategies. *Indian Journal Arecanut, Spices Medica Plants.* 2001;3(2): 35–50.
- 113. Saravana Bavan D, Mohan Kumar GC. Potential use of natural fiber composite materials in India. *Journal of Reinforced Plastics and Composites*. 2010;29(24): 3600 3613.
- 114. Arjmandi R, Hassan A, Majeed K, Zakaria Z. Rice Husk Filled Polymer Composites. *International Journal of Polymer Science*. 2015;2015(1): 798–829.
- 115. Zawawi NA, Ismail A, Abdan K, Mahdi MA. Investigation on the microwave properties of kenaf and rice-husk fiber reinforced pla composite utilizing one-port coaxial transmission line reflection method. *Key Engineering Materials*. 2011;471–472: 868–873.
- 116. Reddy KS, Singla H. Optimization of woven jute/glass fibre-reinforced polyester hybrid composite solar parabolic trough collector. *IOP Conf. Series: Materials Science and Engineering.* 2017;222(1): 012016.
- 117. Chikhradze NM, Marquis FDS, Abashidze GS. Hybrid fiber and nanopowder reinforced composites for wind turbine blades. *Journal of Materials Research and Technology.* 2015;4(1): 60–67.
- 118. Zhao X, Copenhaver K, Wang L, Korey M, Gardner DJ, Li K, Lamm ME, Kishore V, Bhagia S, Tajvidi M, Tekinalp H, Oyedeji O, Wasti S, Webb E, Ragauskas AJ, Zhu H, Peter WH, Ozcan S. Recycling of natural fiber composites: Challenges and opportunities. *Resources, Conservation and Recycling*. 2022;177: 105962.
- 119. Xia C, Wang K, Dong Y, Zhang S, Shi SQ, Cai L, Ren H, Zhang H, Li J. Dual-functional natural-fiber reinforced composites by incorporating magnetite. *Composites Part B*. 2016;93: 221–228.

Accepted: January 22, 2025

Submitted: December 9, 2024

Revised: December 20, 2024

The influence of brombutyl and divinylstyrene caoutchoucs, sevilen on the properties of seawater-resistant rubber

E.N. Egorov [™] (D), N.I. Kol'tsov (D)

I.N. Ulyanov Chuvash State University, Cheboksary, Russia

[™] enegorov@mail.ru

ABSTRACT

The effect of bromobutyl caoutchouc BBK-232, sevilene 11808-340, divinylstyrene caoutchoucs DSSK-628V and SKMS-30ARK on the rheometric characteristics of the rubber mixture, physical, mechanical, operational and dynamic properties of rubber used for the manufacture of seawater-resistant products are studied. Along with the listed ingredients, the rubber mixture contained a vulcanizing agent - sulfur; vulcanization accelerators - 2,2'-dibenzothiazole disulfide, diphenylguanidine; vulcanization activators - zinc white, stearin; antioxidant - naphtham-2; fillers - technical carbons P 514 and P 803, natural chalk; polymer filler - trans-polynorbornene; softeners - rosin, petroleum polymer resin "Shinplast", factice; plasticizer - petroleum bitumen. It was found that rubber based on DSSK-628V and BBK-232 couutchoucs with their mass ratio of 75:25 not containing sevilen 11808-340 has better rheometric, physical-mechanical, dynamic properties and resistance to sea water.

KEYWORDS

physical-mechanical, operational and dynamic properties • bromobutyl caoutchouc • sevilen • rubber divinylstyrene caoutchous • rheometric • sea water

Citation: Egorov EN, Kol'tsov NI. Stydy of the influence of brombutyl and divinylstyrene caoutchoucs, sevilen on the properties of seawater-resistant rubber. *Materials Physics and Mechanics*. 2025;53(1): 143–149. http://dx.doi.org/10.18149/MPM.5312025_11

Introduction

In industrial production, rubber is one of the widely used polymeric materials that underlie the manufacture of products used in various fields of activity, including products with high dynamic properties. Special requirements are imposed on such rubbers, since they must have good dynamic properties and be resistant to the effects of sea water. Such rubbers are usually prepared on the basis of general-purpose and special-purpose caoutchoucs [1-3]. In [4-14], it was established that the use of combinations of caoutchoucs of different nature is one of the promising ways to create rubbers with improved dynamic properties. In [15,16], it was shown that rubbers based on combinations of caoutchoucs of different polarity (polar butadiene-nitrile SKN 4065 and non-polar butadiene-methylstyrene SKMS-30ARK and butyl rubber BK-1675) with additives of trans-polynorbornene, sevilene 11808-340 [15], polyisobutylene P-200 with sevilene 11808-340 [16], as well as rubbers containing polyisobutylene [17-20], sevilene [21-27] and based on halobutyl caoutchoucs [28-33], are characterized by fairly high dynamic properties. In this regard, the aim of this work is to study the influence of bromobutyl caoutchouc BBK-232 and sevilene 11808-340, as well as divinylstyrene caoutchoucs DSSK-628V and SKMS-30ARK on the properties of rubber used for the manufacture of products used in sea water.



144 E.N. Egorov, N.I. Kol'tsov

Materials and Method

The rubber mixture under study included the following caoutchoucs and ingredients: SKMS-30 ARK, DSSK-628V and BBK-232 caoutchoucs; sevilen 11808-340; vulcanizing vulcanization accelerators 2,2'-dibenzothiazole diphenylquanidine; vulcanization activators - zinc white, stearic acid; antioxidant naphtham-2; fillers - carbon black P 514, carbon black P 803, natural chalk; polymer filler - trans-polynorbornene; softeners - rosin, Shinplast petroleum polymer resin, factis, petroleum bitumen. The rubber mixture was prepared on a laboratory mill LB 320 160/160 at a roll temperature of 60-70 °C for 25 min. The rheometric characteristics of the rubber mixture were studied on a rheometer MDR 3000 Basic by Mon Tech at 150 °C for 30 min in accordance with ASTM D2084-79. Standard samples for determining the physical and mechanical properties were vulcanized at a temperature of 150 °C for 30 min in a vulcanization press type P-V-100-3RT-2-PCD. The main characteristics of the vulcanizates were determined in accordance with the standards current in the rubber industry: elastic-strength properties were determined according to GOST 270-75; Shore A hardness - according to GOST 263-75; tear resistance - according to GOST 262-93; change in conventional tensile strength, relative elongation at break and hardness after exposure to sea water (8 % aqueous solution of sea salt) - according to GOST 9.030-74 (method B); change in mass after exposure to sea water - according to GOST 9.030-74 (method A). Dynamic parameters (tangent of the angle of mechanical losses) of vulcanizates of different variants of rubber compound were studied at a temperature of 30 °C on a Metravib VHF 104 dynamic mechanical analyzer in the "tension-compression" deformation mode (degree of deformation 0.01 %) and a frequency of 1000 Hz.

Results and Discussion

The efficiency of using bromobutyl caoutchoc BBK-232, sevilen 11808-340, divinylstyrene caoutchocs DSSK-628V and SKMS-30ARK was assessed by the kinetic (rheometric) properties of the rubber mixture, physical and mechanical properties and changes in these parameters after exposure to sea water, as well as the dynamic properties of the vulcanizates. The variants of the studied rubber mixture containing caoutchocs SKN-4045, DSSK-628V, BBK-232 and sevilen in different quantities are given in Table 1. Figure 1 shows the vulcanization curves for different rubber compound variants.

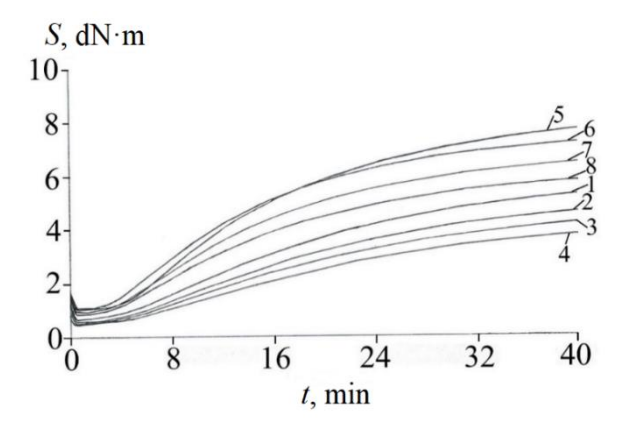


Fig. 1. Vulcanization curves of rubber compound (curve numbers correspond to variant numbers)

Table 1. Variants ai	nd	rheometric properties of rubber mixture

Caoutchoucs,	Variants							
sevilen, indicators	1	2	3	4	5	6	7	8
BBK-232, mass	25.0	25.0	25.0	25.0	25.0	25.0	25.0	25.0
parts	23.0	23.0	23.0	23.0	23.0	23.0	23.0	23.0
SKMS-30ARK,	75.0	75.0	75.0	75.0	-	-	-	-
mass parts								
DSSK-628V, mass	_	_	_	_	75.0	75.0	75.0	75.0
parts			_		7 3.0	7 3.0	75.0	7 3.0
Sevilen 11808-	_	5.0	10.0	15.0	-	5.0	10.0	15.0
340, mass parts								
Rheometric properties								
S _{max} , dN⋅m	5.27	4.62	4.21	3.80	7.69	7.20	6.46	5.79
S _{min} , dN·m	0.86	0.74	0.69	0.63	1.33	1.34	1.18	1.09
t _s , min	13.46	15.31	16.91	19.48	9.13	8.38	9.54	10.71
<i>t</i> ₉₀ , min	31.09	31.41	31.60	32.21	29.75	27.64	28.77	29.18

Note: S_{max} and S_{min} are the maximum and minimum torques; t_{s} and t_{90} are the start and optimum times of vulcanization.

Table 1 shows the results of studies of rheometric parameters for different variants of the rubber compound, as shown in Fig. 1. As can be seen, an increase in the content of sevilene 11808-340 in variants 1-4 of the rubber compound based on SKMS-30ARK caoutchouc and variants 5-8 of the rubber compound based on DSSK-628V caoutchouc leads to a decrease in the maximum and minimum torques, while the times of the onset and achievement of the vulcanization optimum increase. Equal-mass replacement of SKMS-30ARK (variants 1-4) with DSSK-628V (variants 5-8) leads to an improvement in the rheometric, and, consequently, technological properties of the rubber compound.

The results of studies of the physical and mechanical properties of the vulcanizates of the rubber compound are shown in Table 2. It follows from the data in Table 2 that with equal-mass replacement of SKMS-30ARK with DSSK-628V, there is an increase in the conventional tensile strength, hardness and tear resistance, a decrease in the values of relative elongation at break and rebound elasticity of vulcanizates. An increase in the content of sevilen leads to a decrease in the values of conventional tensile strength, hardness and tear resistance, an increase in the values of relative elongation at break and rebound elasticity of vulcanizates. The best physical and mechanical properties are possessed by the vulcanizate of variant 5 of the rubber mixture containing a combination of DSSK-628V and BBK-232 caoutchoucs in a mass ratio of 75:25.

The results of the study of rubber resistance to the effects of sea water are also presented in Table 2, from which it follows: changes of the physical and mechanical properties and the degree of swelling of vulcanizates based on DSSK-628V caoutchouc are less than those based on SKMS-30ARK caoutchouc; an increase in the content of sevilene leads to an increase in these indicators of vulcanizates; which are generally small and do not exceed 6 % for physical and mechanical indicators and 0.6 % for the degree of swelling. From the results of studies of the dynamic properties of vulcanizates presented in Table 2 it follows: vulcanizates based on DSSK-628 caoutchouc, in comparison with vulcanizates based on SKMS-30ARK caoutchouc, have higher values of the tangent of the angle of mechanical losses and lower values of the modulus of

146 E.N. Egorov, N.I. Kol'tsov

elasticity; the introduction of sevilene leads to a decrease in the tangent of the angle of mechanical losses and an increase in the modulus of elasticity; The best dynamic properties are possessed by the vulcanizate of variant 5 of the rubber mixture, based on DSSK-628V and BBK-232 caoutchoucs with their mass ratio of 75:25.

Table 2. Physical, mechanical and dynamic properties of vulcanizates

Indicators	Variants								
	1	2	3	4	5	6	7	8	
f_p , MPa	5.2	5.0	4.7	4.3	5.0	5.2	5.1	4.9	
ε_p , %	560	580	590	620	400	410	420	440	
<i>H</i> , units Shore A	54	52	51	50	55	56	54	52	
B, kN/m	27	26	25	22	25	32	29	26	
<i>S</i> , %	31	30	29	27	16	21	20	19	
Changes in physical and mechanical properties of vulcanizates after exposure to sea water at 23°C for 30 days									
Δf_{p} , %	+1.9	+2	+2.4	+2.6	+1.7	+1.6	+1.9	+2.2	
$\Delta \varepsilon_{p}$, %	-3.6	-3.9	-4.5	-5.3	-3.2	-3.5	-4.7	-5.6	
Δ <i>H</i> , units Shore A	+4	+3	+3	+1	+4	+4	+3	+2	
Degree of swelling of vulcanizates after exposure to an 8 % aqueous solution of sea salt at 23 °C for 7 days									
Δm, %	0.50	0.46	0.53	0.54	0.26	0.24	0.27	0.30	
Dynamic properties of vulcanizates of rubber compound									
<i>E'</i> ·10 ⁻⁷ , Pa	2.18	2.26	2.25	2.14	2.32	2.78	2.81	2.8	
$tg\delta$	0.304	0.292	0.284	0.282	0.555	0.476	0.454	0.442	

Note: f_p is a conventional tensile strength, ε_p is a relative elongation at break, H is hardness, B is a tear resistance, Δf_p , $\Delta \varepsilon_p$, Δm are relative changes in conventional tensile strength, relative elongation at break and weight after keeping rubber in sea water, ΔH is a difference in rubber hardness before and after keeping in sea water, E' is the elastic modulus, $tq\delta$ is a tangent of mechanical loss angle.

Conclusions

The influence of bromobutyl caoutchouc BBK-232, sevilen 11808-340, divinylstyrene caoutchoucs SKMS-30ARK and DSSK-628V on the rheometric, physical-mechanical, operational and dynamic properties of rubber was studied. It was found that the best rheometric, physical-mechanical, dynamic properties and stability in sea water are possessed by rubber based on a combination of caoutchoucs DSSK-628V (75.0 parts by weight) and BBK-232 (25.0 parts by weight), not containing sevilen 11808-340.

CRediT authorship contribution statement

Evgeniy N. Egorov DSC: writing – review & editing, writing – original draft, conceptualization, investigation; **Nikolay I. Kol'tsov DSC**: writing – review & editing, writing – original draft, conceptualization, supervision, data curation.

Conflict of interest

The authors declare that they have no conflict of interest.

References

- 1. Nafeesa MS, Azura AR. The Influence of Different Types of Rubber on Curing Behaviour and Dynamic Properties of Rubber Compound. *Journal of Physics: Conference Series*. 2018;1082: 012010.
- 2. Nobari Azar FA, Karimzadeh Naghshineh A, Sen M. Preparation and characterization of natural rubber–based new elastomers for high-damping base isolation systems. *Journal of Elastomers and Plastics*. 2022;54(6): 959–974.
- 3. Lei T, Zhang Y-W, Kuang D-L, Yang Y-R. Preparation and Properties of Rubber Blends for High-Damping-Isolation Bearings. *Polymers*. 2019;11(8): 1374.
- 4. Qin R, Huang R, Lu X. Use of gradient laminating to prepare NR/ENR composites with excellent damping performance. *Materials and Design*. 2018; 149: 43–50.
- 5. Zhao X, Yang J, Zhao D, Lu Y, Wang W, Zhang L, Nishi T. Natural rubber/nitrile butadiene rubber/hindered phenol composites with high-damping properties. *International Journal of Smart and Nano Materials*. 2015;6(4): 239–250.
- 6. Dharmaraj MM, Chakraborty BC, Begum S. The effect of graphene and nanoclay on properties of nitrile rubber/polyvinyl chloride blend with a potential approach in shock and vibration damping applications. *Iranian Polymer Journal*. 2022;31: 1129–1145.
- 7. Akyüz S, Darı ME, Esiyok YE, Ermeydan MA. Effects of NR/SBR ratio on mechanical properties and artificial mechanical performance of anti-vibration bushings. *Iranian Polymer Journal*. 2021;30: 1317–1328.
- 8. Lu X, Huang R, Li H, Long J, Jiang Z. Preparation of an elastomer with broad damping temperature range based on EPDM/ENR blend. *Journal of Elastomers and Plastics*. 2017;49(8): 758–773.
- 9. Egorov EN, Kol'tsov NI. Influence of glass fibers on the physico-mechanical and performance properties of rubber based on general and special purpose caoutchoucs. *Materials Physics and Mechanics*. 2024;52(1): 126–131.
- 10. Egorov EN, Sandalov SI, Kol'tsov NI. Study of the influence of dispersed fillers on properties of rubber for gaskets of rail fastening. *Materials Physics and Mechanics*. 2023;51(6): 119–126.
- 11. Nabil H, Ismail H, Ratnam CT. (2014). Simultaneous Enhancement of Mechanical and Dynamic Mechanical Properties of Natural Rubber/Recycled Ethylene-Propylene-Diene Rubber Blends by Electron Beam Irradiation. *International Journal of Polymer Analysis and Characterization*. 2014;19(3): 272–285.
- 12. Nabil H, Ismail, H, Azura AR. Optimization of accelerators on curing characteristics, tensile, and dynamic mechanical properties of (natural rubber)/(recycled ethylene-propylene-diene-monomer) blends. *Journal of Vinyl and Additive Technology*. 2014;21(2): 79–88.
- 13. Marzocca AJ, Mansilla MA. Dynamic mechanical properties in natural rubber/styrene-butadiene rubber blends: The local strain behavior in the glass transition region. *Polymer Engineering and Science*. 2023;63(5): 1471–1480.
- 14. Egorov EN, Salomatina EV, Vassilyev VR, Bannov AG, Sandalov SI. Effect of Polynorbornene on Physico-Mechanical, Dynamic, and Dielectric Properties of Vulcanizates Based on Isoprene, α-Methylstyrene-Butadiene, and Nitrile-Butadiene Rubbers for Rail Fasteners Pads. *Journal of Composites Science*. 2023;7(8): 334.
- 15. Egorov EN, Ushmarin NF, Sandalov SI, Kol'tsov NI. Research of operational and dynamic properties of rubber for products working in sea water. *ChemChemTech.* 2020;63(11): 96–102. (In Russian)
- 16. Egorov EN, Ushmarin NF, Sandalov SI, Kol'tsov NI, Voronchikhin VD. Investigation of the dynamic properties of seawater-resistant rubber. *Journal of Siberian Federal University. Chemistry.* 2021;14(1): 38–44.
- 17. Egorov EN, Ushmarin NF, Salomatina EV, Matyunin AN. The effect of polyisobutylene on physical-mechanical, operational, dielectric and dynamic properties of rubber for laying rail fasteners. *ChemChemTech.* 2022;65(5): 94–102. (In Russian)
- 18. Xia L, Li C, Zhang X, Wang J, Wu H, Guo S. Effect of chain length of polyisobutylene oligomers on the molecular motion modes of butyl rubber: Damping property. *Polymer*. 2018;141: 70–78.
- 19. Wu J, Huang G, Wang X, He X, Zheng J. Detecting different modes of molecular motion in polyisobutylene and chlorinated butyl rubber by using dielectric probes. *Soft Matter*. 2011;7(19): 9224–9230.
- 20. Giller CB, Roland CM. Strength Enhancement in Miscible Blends of Butyl Rubber and Polyisobutylene. *Macromolecules*. 2013;46(7): 2818–2822.
- 21. He X, Qu M, Shi X. Damping properties of ethylene-vinyl acetate rubber/polylactic acid blends. *Journal of Materials Science and Chemical Engineering*. 2016;4(3): 15.
- 22. Yu Z, Wang C, Zhang X, Zhao Y, Wen S, Zhang ZX. Controlled damping ethylene-vinyl acetate copolymer/styrene ethylene butylene styrene foam in wide temperature range prepared by supercritical nitrogen. *Polymer Engineering and Science*. 2023;63(10): 3429–3432.

148 E.N. Egorov, N.I. Kol'tsov

23. Raksaksri L, Chuayjuljit S, Chaiwutthinan P, Boonmahitthisud A. Vinyl acetate ethylene copolymer and nanosilica reinforced epoxidized natural rubber: Effects of sulfur curing systems on cure characteristics, tensile properties, thermal stability, dynamic mechanical properties and oil resistance. *Journal of Vinyl and Additive Technology*. 2019;25(s2): E28–E38.

- 24. Nadal A, Segura J, Juliá E, Gadea JM, Montava I. Evaluation of acoustic and dynamic behaviour of ethylene vinyl acetate panels. *Materials Science and Engineering Technology*. 2019;50(1): 14–24.
- 25. Singla RK, Zafar MT, Maiti SN, Ghosh AK. Physical blends of PLA with high vinyl acetate containing EVA and their rheological, thermo-mechanical and morphological responses. *Polymer Testing*. 2017;63: 398–406. 26. Zia-ul-Haq M, Wu J, Haq ZU, Peng Z, Zhang Y. Enhanced mechanical, thermal performance and kinetics of thermal degradation of silicone rubber/ethylene–vinyl acetate copolymer/halloysite nanoclay nanocomposites compatibilized by ethylene–acrylic acid copolymer. *Journal of Polymer Research*. 2023;30: 306.
- 27. Sadeghi-Askari A, Tavakoli M. Optimization of mechanical and dynamic-mechanical properties of electron beam irradiation of reclaimed tire rubber/poly (ethylene-co-vinyl acetate) nanocomposite by design of experiment. *Iranian Polymer Journal*. 2023;32: 417–431.
- 28. Cao R, Zhao X, Zhao X, Wu X, Li X, Zhang L. Bromination modification of butyl rubber and its structure, properties and application. *Industrial and Engineering Chemistry Research*. 2019;58(36): 16645–16653.
- 29. Chen B, Dai J, Song T, Guan Q. Research and Development of High-Performance High-Damping Rubber Materials for High-Damping Rubber Isolation Bearings: A Review. *Polymers*. 2022;14(12): 2427.
- 30. Behera PK, Kumar A, Mohanty S, Gupta VK. Overview on Post-Polymerization Functionalization of Butyl Rubber and Properties. *Industrial and Engineering Chemistry Research*. 2022;61(46): 16910–16923.
- 31. Chen J, Wang J, Li S, Xiang K, Song S. Pyridine terminated polyurethane dendrimer/chlorinated butyl rubber nanocomposites with excellent mechanical and damping properties. *Chinese Journal of Chemical Engineering*. 2023;53: 211–221
- 32. Pan Y, Wang J, Yang S. Preparation of novel damping layered silicates and its application in chlorinated butyl rubber (CIIR) composites. *Polymer-Plastics Technology and Materials*. 2019;59(4): 385–397.
- 33. Liu Z, Wang K, Wu Y, Zhang H, Hao T, Qi H, Liu B. A Novel Method to Characterize the Damping Capacity of EPDM/CIIR Blends Using Vibrating Rubber Balls. *Polymers*. 2024;16(11): 1447.

Submitted: February 29, 2024 Revised: January 15, 2025 Accepted: January 26, 2025

Preparation and characterization of geopolymer/activated carbon composite materials used as a bone substitute material

A. Moonphukhiao¹, B. Samran², S. Chaiwichian¹

- ¹ Rajamangala University of Technology Isan Sakonnakhon Campus, Phangkon, Sakonnakhon, Thailand
- ² Nakhon Phanom University, Muang District, Nakhon Phanom, Thailand

ABSTRACT

Geopolymer/activated carbon composite materials were successfully prepared using alkaline activator solution to be a binder. The physical and mechanical properties of as-prepared samples were characterized through X-ray diffraction, scanning electron microscopy, transmission electron microscopy, Fourier transform infrared spectrometry and compressive strength techniques. Results revealed that geopolymer/activated carbon composite materials exhibited amorphous phase and spherical-like and plate-like morphologies. Fourier transform infrared spectrometry results indicated that after the geopolymerization reaction, the band at 977 cm⁻¹ was shifted to lower wavenumber (975 cm⁻¹). This might be attributed to the interaction of aluminum atoms and the formation of higher cross-linking in silicate geopolymer structure. The compressive strength of geopolymer/activated carbon composite materials decreased with increasing amount of activated carbon in geopolymer. It was found that the concentration of 0.001 mol. % activated carbon introduced into geopolymer gave the highest strength compared with other samples.

KEYWORDS

geopolymer • activated carbon • alkaline activator • geopolymerization reaction

Acknowledgements. The authors would like to gratefully thank the Department of Science and Mathematics, Faculty of Industry and Technology, Rajamangala University of Technology Isan, Phangkon, Sakon Nakon for support.

Citation: Moonphukhiao A, Samran B, Chaiwichian S. Preparation and characterization of geopolymer/activated carbon composite materials used as a bone substitute material. *Materials Physics and Mechanics*. 2025;53(1):150–158. http://dx.doi.org/10.18149/MPM.5312025 12

Introduction

A significant component of the human body consists of 206 bones. Each bone has different internal and external structures, such as leg bones, arm bones, hip bones, etc. [1,2]. However, these bones may not remain throughout a person's life, as they can be affected by various factors, such as accidents, bone diseases, and bone deterioration [2,3]. To date, artificial bones or bone substitute materials have become crucial in addressing bone-related issues. As a result, many researchers have focused on the development of artificial bones to create efficient bone substitute materials and to improve production technologies for faster and more accurate procedures. Artificial bones or bone substitute materials are typically made from various metals, such as stainless steel, titanium, titanium-cobalt alloys, and others [4], which can suffer from corrosion during long-term use. To overcome this limitation, researchers have been seeking alternative materials to replace metals. Geopolymer, first synthesized by Davidovits in the 1970s [5–7], is classified as an inorganic polymer. It is well-known as a green pozzolanic material,



[™] saranyou530531117@gmail.com

produced using waste materials as aluminosilicate sources combined with an alkaline activator solution [8–13]. Geopolymers are significant alternative materials and have drawn substantial interest in biomedical applications to replace metals due to their desirable properties, such as low greenhouse gas emissions, corrosion resistance and environmental sustainability [11,14,15]. However, a limitation of pure geopolymer is its low compressive strength. To address this issue, numerous efforts have focused on incorporating porous materials into geopolymer to improve its compressive strength. Recently, porous materials, such as zeolite and activated carbon, have gained popularity for enhancing the mechanical properties of geopolymers [16]. Activated carbon, in particular, is a naturally derived porous material widely used in industry as an adsorbent and catalyst for waste and gas purification [16,17]. Additionally, activated carbon possesses important mechanical properties, such as resistance to abrasion and attrition, making it suitable for integration with geopolymer to enhance its compressive strength.

In this study, geopolymer/activated carbon composite materials were prepared by using an alkaline activator solution as a binder, with activated carbon added to the geopolymer solution to form the composite. Furthermore, we investigated the effect of varying concentrations of activated carbon in the geopolymer on the mechanical properties, with the aim of utilizing these materials in biomedical applications in the future. The chemical properties of all the prepared samples were characterized using X-ray diffraction (XRD), scanning electron microscopy (SEM), transmission electron microscopy (TEM), and Fourier transform infrared spectroscopy (FTIR).

Materials and Methods

Activated carbon was made of coconut shell by using potassium hydroxide (KOH) as an activating agent during chemical activation process. Firstly, the natural coconut shell was cleanly washed with deionized water to eliminate the contaminant. The coconut shell was then dried at 80 °C for 24 h in an electric oven to remove the water content. Next, the coconut shell was heated at 200 °C to form charcoal. The as-prepared charcoal was ground into small pieces and soaked in 6M KOH solution to generate porous volume. Then, the obtained suspension was filtered and washed with deionized water until pH 7 by using a centrifuge to split the particle and solution. Finally, the as-prepared activated carbon particles were dried in an electric oven at a temperature of 80 °C for 24 h and then heated at the calcination temperature of 600 °C for 1 h.

Geopolymer was prepared by using kaolin, CaO, NaOH and Na₂SiO₃ as precursor. First of all, kaolin was heated at 600 °C within 2 h to form metakaolin. Then, 2:1:1:1 of metakaolin, CaO, NaOH and Na₂SiO₃, respectively, was slowly dissolved in 25 ml of deionized water until becoming homogeneous solution. The as-prepared suspension was poured in the mold and dried at room temperature for 24 h. Finally, geopolymer for bone substitute materials was heated at 550 °C for 6 h.

Geopolymer/activated carbon composite materials were prepared by using NaOH as alkaline activator to activate geopolymer. 2:1:1:1 of metakaolin, CaO, NaOH and Na $_2$ SiO $_3$, respectively, was dissolved in 25 ml of deionized water with vigorously magnetic stirrer till homogeneous solution. Then, the previously prepared activated carbon powders were added into the geopolymer solution with different mole ratios of 0.001 and 0.003 %

together with continuously magnetic stirring for 30 min. Next, the obtained suspension was poured in the mold, and then dried at room temperature overnight to construct a bone substitute material. The samples were finally heated at the high temperature of 550 °C for 6 h by a furnace.

The identification of phase structure of all samples was measured using X-ray diffraction (XRD, Philips X'Pert MPD, Thailand) with CuK α radiation (0.15418 nm) at the 20 range of 10° to 80°. The morphology structure of as-prepared samples was studied via scanning electron microscopy (SEM, JEOL JSM-6335F, Thailand) technique. The microstructure and actual particle size of samples were investigated by using transmission electron microscopy (TEM, JEOL JEM-2010, Thailand) technique. The structural characterization and functional group identification of samples were analyzed by using Fourier transform infrared spectroscopy (FTIR, PerkinElmer Sciencific, Thailand) technique.

The mechanical property of all samples in the hardened state was carried out by compressive strength. The compressive strength of prismatic samples with dimensions of $150 \times 30 \times 30 \text{ mm}^3$ was studied in accordance with the ASTM C105 standard.

Results and Discussion

Figure 1 shows the result of X-ray diffraction (XRD) patterns of geopolymer, activated carbon, geopolymer/activated carbon with different activated carbon mole ratios of 0.001 and 0.003 %. The XRD patterns of activated carbon showed a broad peak appearing at 20 of 24.15° and 43.44°, corresponding to the (002) and (100) plans in amorphous carbon [18,19]. In part of XRD pattern of geopolymer, the peak was located at 20 of 21.78°, 26.80°, 50.28° and 60.51°, which can be indexed as quartz phase [7], whereas the peak was detected at 20 of 13.51°, 34.07° and 42.04°, which can be assigned to mullite phase [7]. Furthermore, the sharp peak was located at 20 of 23.73°, which can be identified as

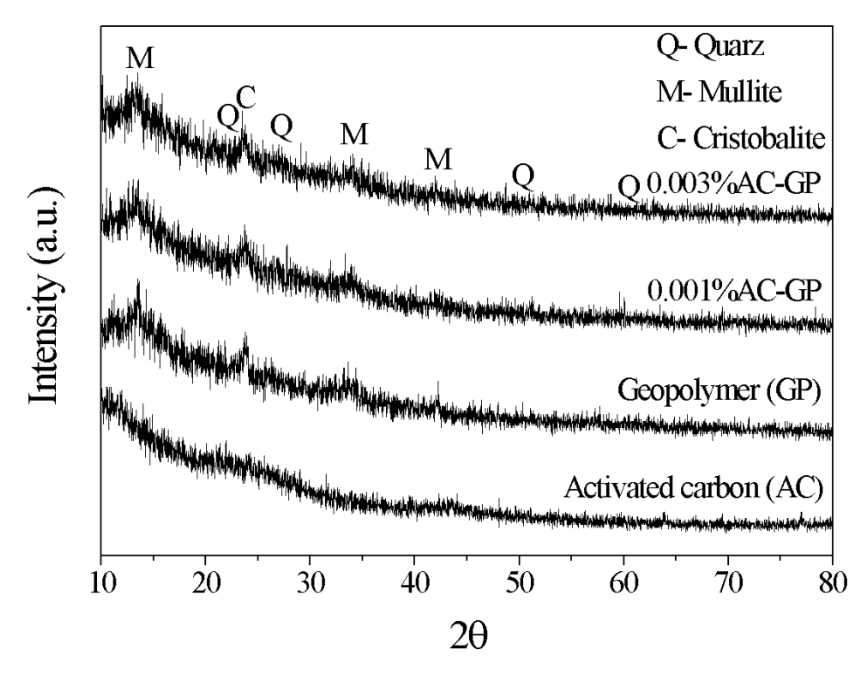


Fig. 1. XRD patterns of geopolymer, activated carbon, geopolymer/activated carbon with different activated carbon mole ratios of 0.001 and 0.003 %

the cristobalite phase in silica [7,20]. Moreover, it was found that the absence of alumina peak showed in XRD pattern, indicating that the alumina in geopolymer was in the amorphous phase [21]. For geopolymer/activated carbon with different activated carbon mole ratios of 0.001 and 0.003 %, the XRD peak was similar to pure geopolymer, which can be inferred that the addition of activated carbon content into geopolymer had no effect on the phase transition of geopolymer. In addition, it can be clearly observed that no activated carbon peak was emerged on geopolymer/activated carbon composite materials, owing to a very low content of activated carbon added into geopolymer.

The morphology of geopolymer, activated carbon, geopolymer/activated carbon with different activated carbon mole ratios of 0.001% and 0.003% was investigated through scanning electron microscopy (SEM), as shown in Fig. 2. Results showed that the morphology of geopolymer exhibited spherical-like structure, with average particle size of 50 to 100 nm approximately, as displayed in Fig. 2(a). Meanwhile, the activated carbon morphology was plate-like structure together with some pores distributed on the surface of activated carbon [22]. The size of pore diameters was about 1.4 to 1.9 μ m corresponding to the macropore classification [23,24], as shown in Fig. 2(b). For composite materials, the morphology was consisted of the structures of geopolymer and activated carbon in composite materials, as represented in Fig. 2 (c,d).

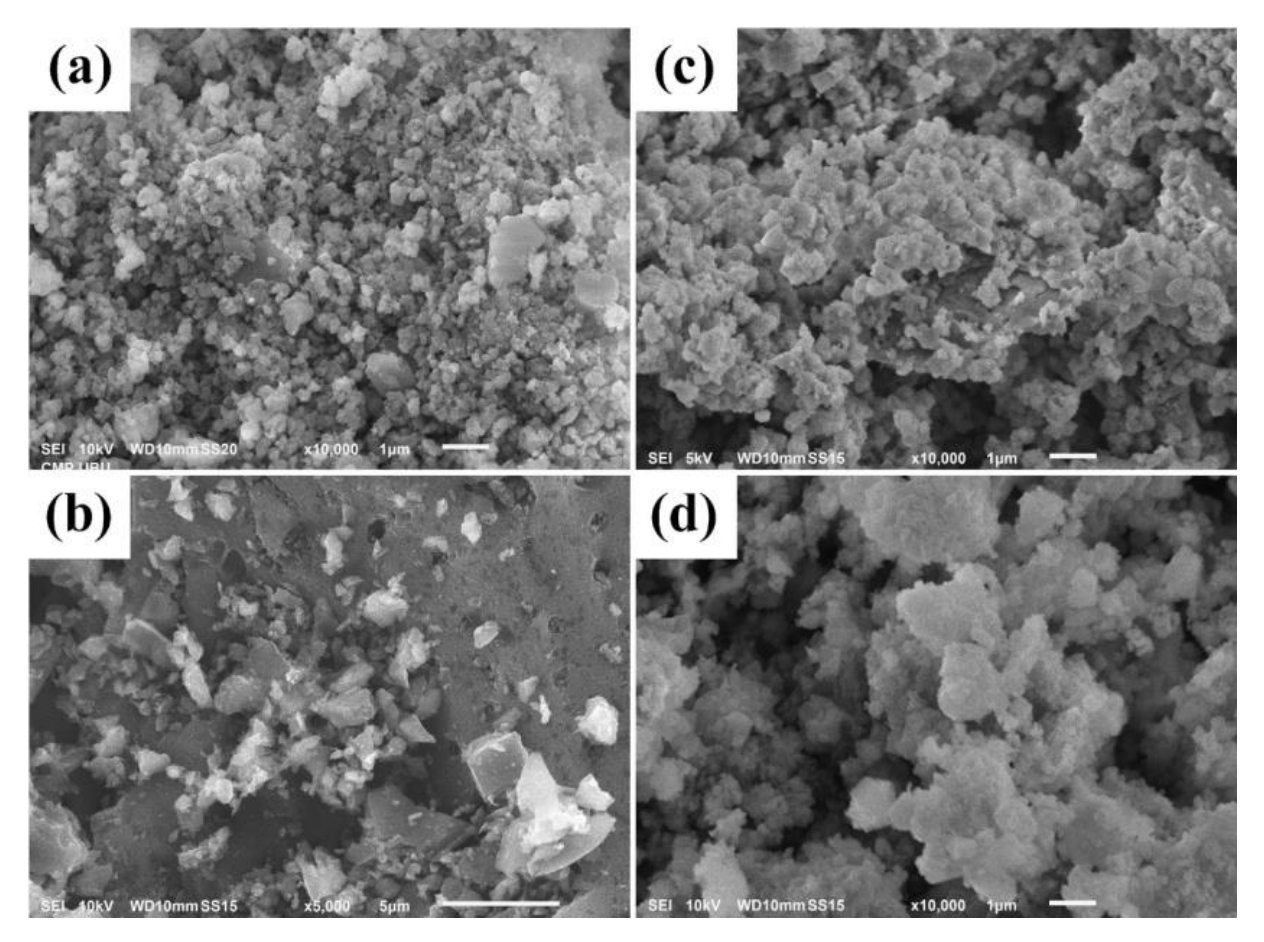


Fig. 2. SEM images of (a) geopolymer, (b) activated carbon and geopolymer/activated carbon with different activated carbon mole ratios of (c) 0.001 and (d) 0.003 %

To confirm the microstructure and particle size of geopolymer, activated carbon, geopolymer/activated carbon with different activated carbon mole ratios of 0.001% and 0.003%, transmission electron microscopy (TEM) was used, as shown in Fig. 3. The results of TEM image of geopolymer were spherical-like structure, with the average particle size of about 50 to 100 nm, as displayed in Fig. 3(a). In Figure 3 (b), TEM images of activated carbon were plate-like structure together with particle size of 20 to 100 nm approximately. For the composite materials, TEM images were composed of spherical-like and plate-like structures, as illuminated in Fig. 3(c,d). Therefore, it can be confirmed that the presence of activated carbon was in the geopolymer/activated carbon composite materials.

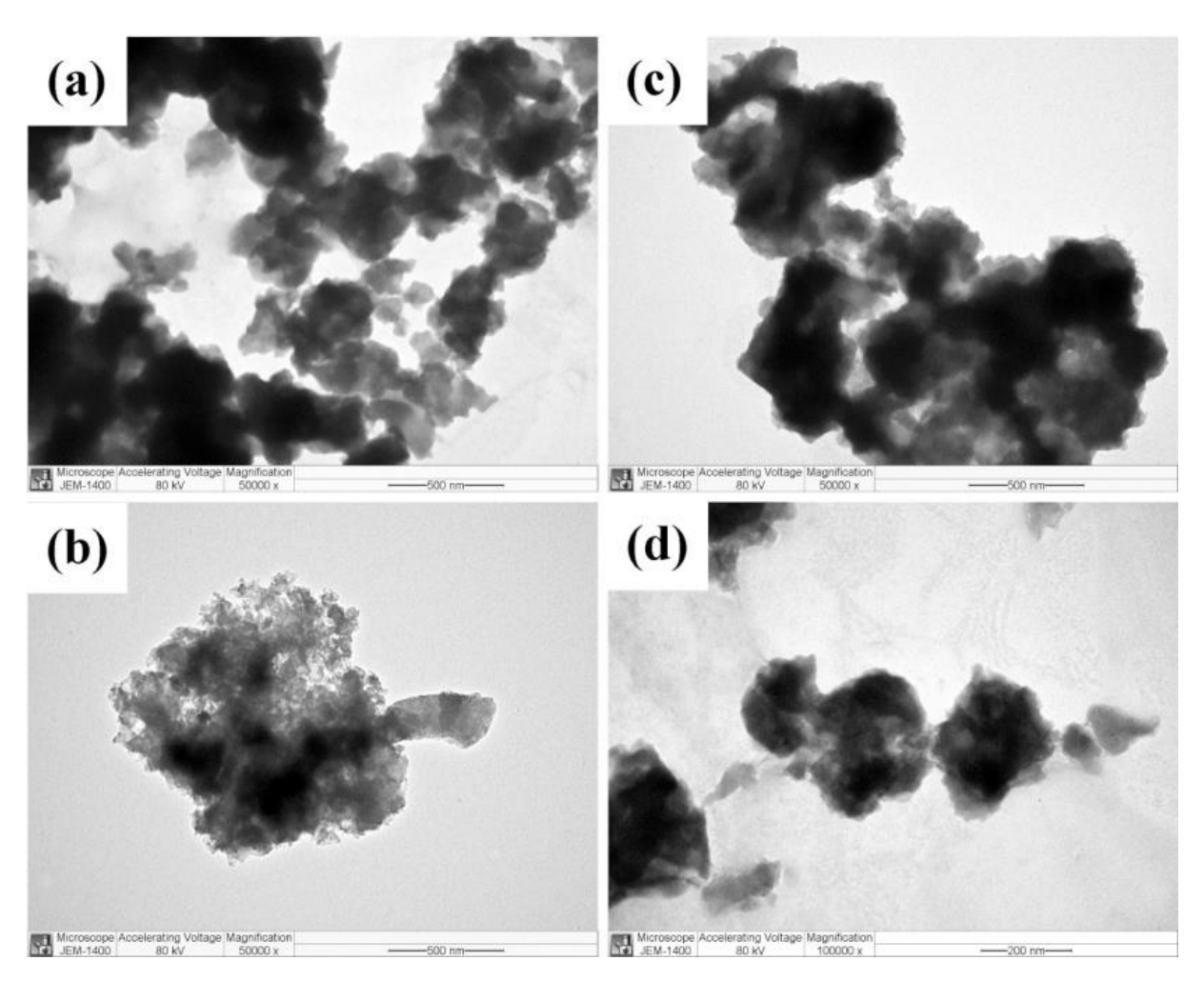


Fig. 3. TEM images of (a) geopolymer, (b) activated carbon and geopolymer/activated carbon with different activated carbon mole ratios of (c) 0.001 and (d) 0.003 %

The chemical structure and functional group of activated carbon, geopolymer and geopolymer/activated carbon with different activated carbon mole ratios of 0.001 and 0.003 % were studied by using Fourier transform infrared spectroscopy (FT-IR), as presented in Fig. 4. FT-IR spectra of activated carbon showed absorption bands at 3442 cm⁻¹, which might be due to the –OH stretching vibration [22]. The peaks occurred at 1558 cm⁻¹ could be attributed to the N-H deformation vibration, C=C group or C=O stretching vibration in carbon [25], while the peaks at 2361 and 1208 cm⁻¹ could be

due to the N-H and C-O stretching vibrations, respectively [25]. For FT-IR spectra of geopolymer, the peaks appeared at 3406 and 1443 cm⁻¹ were ascribed to the O-H stretching vibration of absorbed H₂O molecules and C-O stretching vibration of CO₃²⁻ groups [26,27]. The peaks located at 977 cm⁻¹ and 866 cm⁻¹ were characterized as the Si-O-T (where T is tetrahedral Si or Al) asymmetric stretching vibration in geopolymer and O-C-O stretching vibration [28,29], respectively. The part of the peaks at 687 cm⁻¹ to 425 cm⁻¹ was corresponded to the Si-O-Si and Al-O-Si symmetric stretching vibrations, indicating the formation of amorphous aluminosilicate materials in geopolymer [30-32]. In part of FT-IR spectra of geopolymer/activated carbon with different activated carbon mole ratios of 0.001 and 0.003 %, the peaks were similar to the geopolymer. Furthermore, it can be observed that the peaks of geopolymer and /activated carbon composite materials occurred at 977 cm⁻¹ were shifted to the lower wavenumbers (975 cm⁻¹) after geopolymerization reaction [33,34]. The shifting and reduction of peaks in the geopolymer and /activated carbon composite materials might be due to the interaction of aluminum atoms and the formation of poly (sialate-siloxo) chain in geopolymer structure [34,35].

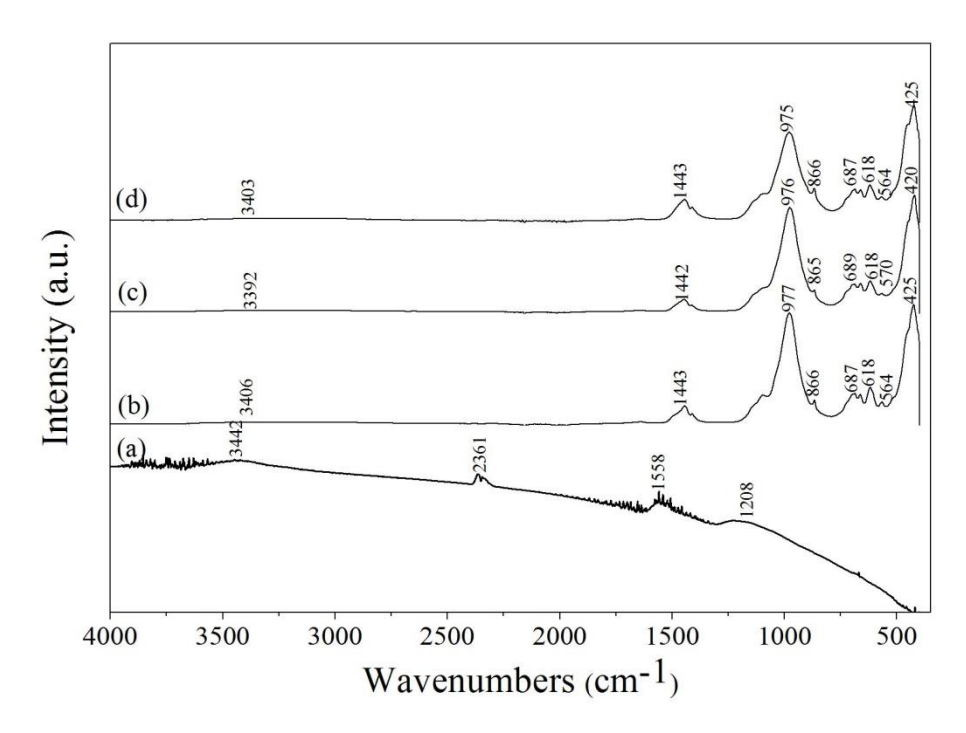


Fig. 4. FT-IR spectra of activated carbon, geopolymer and geopolymer/activated carbon with different activated carbon mole ratios of 0.001 and 0.003 %

The compressive strengths of geopolymer and geopolymer/activated carbon composite materials with different activated carbon mole ratios of 0.001 and 0.003 % were shown in Fig. 5. From experimental results, the compressive strength of geopolymer was 12.79 MPa, while the geopolymer/activated carbon composite materials with different activated carbon mole ratios of 0.001 and 0.003 % were 16.09 and 10.93 MPa, respectively. The obtained results were found that the concentration of 0.001 mol. % activated carbon added into the geopolymer showed the highest strength. While the concentration of 0.003 mol. % activated carbon was introduced into the geopolymer, the

strength of geopolymer was decreased. Therefore, it was concluded that the concentration of activated carbon added into geopolymer had an effect on the strength of geopolymer, the 0.001 mol.% activated carbon loaded into the geopolymer was a suitable concentration to function as a bone substitute material in the future.

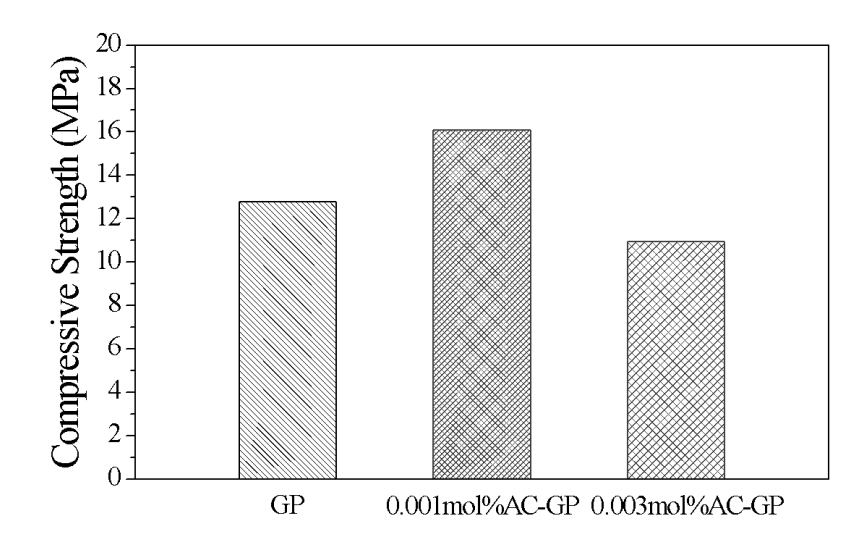


Fig. 5. Compressive strength of geopolymer and geopolymer/activated carbon composite materials with different activated carbon mole ratios of 0.001 and 0.003 %

Conclusions

In summary, geopolymer/activated carbon composite materials were successfully synthesized from metakaolin using a NaOH alkaline activator solution as a binder. The resulting geopolymer/activated carbon composite materials exhibited an amorphous phase. The composite materials consisted of spherical-like geopolymer and plate-like activated carbon, with an average particle size ranging from 20 to 100 nm. The FTIR band of the geopolymer/activated carbon composite materials, after the geopolymerization reaction, shifted slightly from 977 to 975 cm⁻¹. This shift could be attributed to the interaction of the functional groups of aluminum atoms and the increased cross-linking within the geopolymer structure. The sample with 0.001 % activated carbon demonstrated the highest strength compared to the other samples.

CRediT authorship contribution statement

A. Moonphukhiao: writing – review & editing; **Buagun Samran** Sc: writing – original draft; **Saranyoo Chaiwichian** Sc: writing – review & editing; writing – original draft; investigation.

Conflict of interest

The authors declare that they have no conflict of interest.

References

- 1. Florencio-Silva R, da Sasso GRS, Sasso-Cerri E, Simões MJ, Cerri PS. Biology of bone tissue: Structure, function, and factors that influence bone cells. *BioMed Research International*. 2015;1: 421746.
- 2. Ricciotti L, Apicella A, Perrotta V, Aversa R. Geopolymer materials for bone tissue applications: recent advances and future perspectives. *Polymers*. 2023;15(5): 1087.
- 3. Huang H, Liu X, Wang J, Suo M, Zhang J, Sun T, Wang H, Liu C, Li Z. Strategies to improve the performance of polyetheretherketone (PEEK) as orthopedic implants: from surface modification to addition of bioactive materials. *Journal of Materials Chemistry B.* 2024:12(19): 4533–4552.
- 4. Rodriguez J, Mónica Mandalunis P. A review of metal exposure and its effects on bone health. *Journal of Toxicology*. 2018;2018(1): 4854152.
- 5. Swanepoel JC, Strydom CA. Utilization of fly ash in a geopolymeric material. *Applied Geochemistry*. 2002;17(8): 1143–1148.
- 6. Davidovits J. Geopolymers: inorganic polymeric new materials. *Journal of Thermal Analysis and Calorimetry*. 1991;37(8): 1633–1656.
- 7. Hwang CL, Huyn TP. Effect of alkali-activator and rice husk ash content on strength development of fly ash and residual rice husk ash-based geopolymers. *Construction and Building Materials*. 2015;101: 1–9.
- 8. Cui YF, Qu SH, Bao JW, Zhang P. Bond performance of steel bar and fly ash-based geopolymer concrete in beam end tests. *Polymers*. 2020;14: 2012.
- 9. Baqi HJ. Assessment of the Effects of Boron Nitride Nanoplatelets Reinforcement on the Physical and Mechanical Properties of the Geopolymer Prepared by Natural Kaolinite: An in Vitro Study. *Dental Hypotheses*. 2024:15(1):11–13.
- 10. Kudłacik-Kramarczyk S, Drabczyk A, Figiela B, Korniejenko K. Geopolymers: Advanced Materials in Medicine, Energy, Anticorrosion and Environmental Protection. *Materials*. 2023:16(23): 7416.
- 11. Jamaludin L, Razak RA, Abdullah MMAB, Vizureanu P, Bras A, Imjai T, Sandu AV, Abd Rahim SZ, Yong HC. The suitability of photocatalyst precursor materials in geopolymer coating applications: a review. *Coatings*. 2022;12(9): 1348.
- 12. Radhi HAA, Ahmad MA. Biological Test of Porous Geopolymer as a Bone Substitute. *Journal of Medicinal and Chemical Sciences*. 2023;6: 710–719.
- 13. Provis JL, Duxson P, van Deventer JSJ. The role of particle technology in developing sustainable construction materials. *Advanced Powder Technology*. 2010;21(1): 2–7.
- 14. Casagrande Paim T, Bertaco I, Naasani LS, Buchner S, Kovářík T, Hájek J, Wink MR. Hierarchically porous bioceramics based on geopolymer-hydroxyapatite composite as a novel biomaterial: Structure, mechanical properties and biocompatibility evaluation. *Applied Materials Today*. 2023:33: 101875.
- 15. Kriven WM, Leonelli C, Provis JL, Boccaccini AR, Attwell C, Ducman VS, Ferone C, Rossignol S, Luukkonen T, Van Deventer JSJ, Emiliano, JV, Lombardi JE. Why geopolymers and alkali-activated materials are key components of a sustainable world: A perspective contribution. *Journal of the American Ceramic Society*. 2024:107(8): 5159–5177.
- 16. Pimraksa K, Setthaya N, Thala M, Chindaprasirt P, Murayama M. Geopolymer/Zeolite composite materials with adsorptive and photocatalytic properties for dye removal. *Plos one.* 2020;15(10): e0241603. 17. Wang X, Hu Z, Chen Y, Zhao G, Liu Y, Wen Z. A novel approach towards high-performance composite photocatalyst of TiO_2 deposited on activated carbon. *Applied Surface Science.* 2009;255: 3953–3958.
- 18. Xing BL, Shi CL, Zhang CX, Yi GY, Chen LJ, Guo H, Huang GX, Cao JL. Preparation of TiO₂/Activated Carbon Composites for Photocatalytic Degradation of RhB under UV Light Irradiation. *Journal of Nanomaterials*. 2016;2016(1): 8393648.
- 19. Lee HM, Lee BH, An KH, Park SJ, Kim BJ. Facile preparation of activated carbon with optimal pore range for high butane working capacity. *Carbon Letters*. 2020;30: 297 305.
- 20. Xu W, Lo TY, Memon SA. Microstructure and reactivity of rich husk ash. *Construction and Building Materials*. 2012;29: 541–547.
- 21. He J, Jie Y, Zhang J, Yu Y, Zhang G. Synthesis and characterization of red mud and rice husk ash-based geopolymer composites. *Cement* and *Concrete Composites*. 2013;37: 108–118.
- 22. Moyo M, Nyamhere G, Sebata E, Guyo U. Kinetic and equilibrium modelling of lead sorption from aqueous solution by activated carbon from goat dung. *Desalination and Water Treatment*. 2016;57(2): 765–775.

- 23. Wang YW, Duan YH, Liang X, Tang L, Sun L, Wang RR, Wei SH, Huang HN, Yang PH, Hu HN. Hierarchical porous activated carbon derived from coconut shell for ultrahigh-performance supercapacitors. *Molecules*. 2023;28(20): 7187. 24. Wang Y, Lu W, Xu X, Pang F, Feng X, Zhang X, Zeng Y, Yang Z, Wang R, Yang P. Ternary-doped hierarchical porous carbons derived from durian kernel as electrode materials for efficient energy storage devices. *Diamond and Related Materials*. 2022;130: 109451.
- 25. Liu Y, Liu XH, Dong WP, Zhang LL, Kong Q, Wang WL. Efcient adsorption of sulfamethazine onto modifed activated carbon: a plausible adsorption mechanism. *Scientific Reports*. 2017;7: 12437.
- 26. Azhar NSDM, Zainal FF, Abdullah MMAB. Bonding and phases analysis of geopolymer materials. *IOP* Conference *Series: Materials Science and Engineering*. 2020;957: 012052.
- 27. Mužek MN, Svilović S, Zelić J. Fly ash-based geopolymeric adsorbent for copper ion removal from wastewater. *Desalination* and *Water Treatment*. 2014;52: 2519–2526.
- 28. Bakharev T. Resistance of geopolymer materials to acid attack. *Cement and Concrete Research.* 2005;35(4):658–670. 29. Guo X, Pan X. Effects of steel slag on mechanical properties and mechanism of fly ash-based geopolymer. *Journal of Materials in Civil Engineering.* 2020;32(2): 04019348.
- 30. Villa C, Pecina ET, Torres R, Go'mez L. Geopolymer synthesis using alkaline activation of natural zeolite. *Construction and Building Materials*. 2010;24(11): 2084–2090.
- 31. Maiti M, Sarkar M, Maiti S, Malik MA, Xu S. Modification of geopolymer with size controlled TiO₂ nanoparticle for enhanced durability and catalytic dye degradation under UV light. *Journal of Cleaner Production*. 2020;255: 120183.
- 32. Sindhunata Van Deventer JSJ, Lukey GC, Xu H. Effect of curing temperature and silicate concentration on fly-ash-based geopolymerization. *Industrial & Engineering Chemistry Research*. 2006;45: 3559–3568.
- 33. Van Jaarsveld JGS, Van Deventer JSJ. Effect of the alkali metal activator on the properties of fly ashbased geopolymers. *Industrial & Engineering Chemistry Research*. 1999;38: 3932–3941.
- 34. Chen L, Wang Z, Wang Y, Feng J. Preparation and properties of alkali activated metakaolin-based geopolymer. *Materials*. 2016;9(9): 767.
- 35. Cheng-Yong H, Yun-Ming L, Abdullah MMAB, Hussin K. Thermal resistance variations of fly ash geopolymers: foaming responses. *Scientific Reports*. 2017;7(1): 45355.

Accepted: January 22, 2025

Submitted: December 9, 2024

Revised: December 20, 2024

Magnetism of the hybrid SiC/Si structure grown on silicon surface

V.V. Romanov ¹, N.I. Rul' ¹, V.E. Gasumyants ¹, I.D. Venevtsev ¹, K.B. Taranets ¹, A.V. Korolev ², S.A. Kukushkin ³, A.V. Osipov ³, N.T. Bagraev ⁴

ABSTRACT

A low-dimensional hybrid structure of silicon carbide grown on silicon by the vacancy method of coordinated substitution of atoms based on the measurements of its magnetic characteristics – magnetic susceptibility and magnetization is studied. The measurements were carried out on the Quantum Design MPMS XL SQUID (superconducting quantum interferometer), M.N. Mikheev Institute of Metal Physics of the Ural Branch of the Russian Academy of Sciences, Ekaterinburg, and Faraday Balance (Faraday method), Peter the Great St. Petersburg Polytechnic University, St. Petersburg. The results of magnetization field dependences measurement, carried out by two experimental setups, clearly confirm the reliability of the obtained results. **KEYWORDS**

hybrid structure • silicon carbide • VMCSA • magnetic properties • superconducting quantum interferometer Faraday method • magnetization

Funding. S.A. Kukushkin and A.V. Osipov carried out their part of work within the framework of the state assignment of the Institute of Problems of Mechanical Engineering of the Russian Academy of Sciences N^{Ω} FFNF-2021-0001 of the Ministry of Science and Higher Education.

Acknowledgements. The synthesis of the hybrid SiC/Si structure was performed using the unique specific equipment "Physics, Chemistry and Mechanics of Crystals and Thin films" of the Institute of Problems of Mechanical Engineering of the Russian Academy of Sciences, St. Petersburg. The authors are sincerely grateful to A.S. Grashchenko for his help in synthesizing the SiC/Si sample under study.

Citation: Romanov VV, Rul' NI, Gasumyants VE, Venevtsev ID, Taranets KB, Korolev AV, Kukushkin SA, Osipov AV, Bagraev NT. Magnetism of the hybrid SiC/Si structure grown on silicon surface. *Materials Physics and Mechanics*. 2025;53(1): 159–164.

http://dx.doi.org/10.18149/MPM.5312025_13

Introduction

Silicon carbide is of an interest to researchers because it possesses a wide range of qualities that determine the possibilities of its practical application [1-5]. Currently, the technology of obtaining both bulk crystals and thin SiC layers [6-8] is actively developing, which obviously requires the involvement of a wide range of experimental research methods, the results of which can be used as a basis for modeling its physical properties [9-15].

A fundamentally new method for monocrystalline silicon carbide (SiC) on silicon (Si) growth called the method of coordinated substitution of atoms (MCSA) was discovered [16,17]. The SiC growth by the MCSA method is carried out due to the interaction of a



¹ Peter the Great St. Petersburg Polytechnic University, St. Petersburg, Russia

² Institute of Metal Physics, Ural Division of the RAS, Ekaterinburg, Russia

³ Institute for Problems of Mechanical Engineering RAS, St. Petersburg, Russia

⁴ loffe Institute, St. Petersburg, Russia

[™] rul.nickolai@mail.ru

gaseous carbon (CO) with the Si surface at temperatures exceeding 1000 °C. The interaction reaction proceeds in several stages, which distinguishes it from the reactions used in classical method of growing SiC on Si [18,19]. The MCSA method was significantly improved in [20,21], resulting in the development of a new method, namely, the vacancy method of coordinated substitution of atoms (VMCSA).

In the present work, we demonstrate the results of the study of magnetic properties of a SiC structure grown by VMCSA technology on a silicon surface. The choice of magnetic research methods is justified by their high informativeness, which is provided, first of all, by measuring field and temperature dependences of static magnetic susceptibility and magnetization in wide range of magnetic fields and temperatures. Here we discuss the results of measuring the field dependences of the investigated structure, mainly at room temperature.

Materials and Methods

On a Faraday Balance setup based on the MGD 312 FG spectrometer, measurements were performed at room temperature in the range of magnetic fields up to 11 kOe, where the magnetic field was varied in steps of 5 Oe, by the Faraday method in automatic mode. The Faraday method is used to measure the magnetic characteristics of material samples, the linear dimensions of which do not exceed 3 mm, in an inhomogeneous magnetic field, the gradient of which is created by pole pieces of a special shape. The obtained field dependence of the sample magnetization is a sequence of measurement results recorded when the system reaches thermodynamically equilibrium states. The force of interaction of the sample with the magnetic field was measured using Microbalance MTB 10-8 high-precision scales with an accuracy of 10^{-7} g, which determined the error of measuring the magnetic susceptibility of a sample weighing up to 100 mg as 10^{-8} cm³/g.

The relationship between the force acting on the sample in a magnetic field, the field characteristics, and the static magnetic susceptibility of the sample is given by a well-known equation:

$$F(H,T) = m \cdot \chi \cdot H \cdot dH/dz,\tag{1}$$

where χ is the specific static magnetic susceptibility having the inverse density dimension, H is the external magnetic field strength, dH/dz is the magnetic field gradient along the vertical axis z, and m is the mass of the sample measured on laboratory scales with the 10^{-5} g accuracy.

When analyzing the array of obtained data, the magnetic susceptibility or magnetization of the sample was considered to have changed if their determining force of interaction with the external magnetic field differed from the previous value by at least 10^{-7} g, after which the results of measurements were discussed and interpreted. Thus, the Faraday Balance setup makes it possible to measure the magnetic characteristics of low-dimensional structures at high temperatures, generally speaking, at room temperature and above, in weak magnetic fields.

The joint use of experimental techniques applied in the study, firstly, made it possible to expand the temperature intervals and ranges of external magnetic fields in which the sample was placed, complementing each other. And, secondly, to evidentially consider and resolve the question of the reliability of the obtained results, based on the

comparison of the obtained data in the intervals of magnetic fields and temperatures realized at both setups.

Results and Discussion

The interpretation of the experiments performed on SQUID (Fig. 1) via superconducting quantum interferometer [22,23] and by the Faraday method [24] on Faraday Balance setup can be based on the consideration of different additive contributions to the sample magnetization due to the composition and presence of defects in the grown hybrid structure. In addition, the magnetization curves exhibit oscillations that, when interpreted, can be grouped together to reveal general patterns characteristic of the nanostructures under study.

When analyzing the results of sample measurements on a superconducting quantum interferometer, it is necessary to take into account that the technique implemented at the SQUID setup does not allow, due to a large hardware error in relatively weak fields, less than 2 kOe, to reveal features in the magnetization behavior of the structure under study. At the same time, in magnetic fields up to 25 kOe at temperatures from 5 to 350 K the applied technique allows minimizing the instrument error and measuring with high accuracy the field dependences of magnetic characteristics of the studied samples.

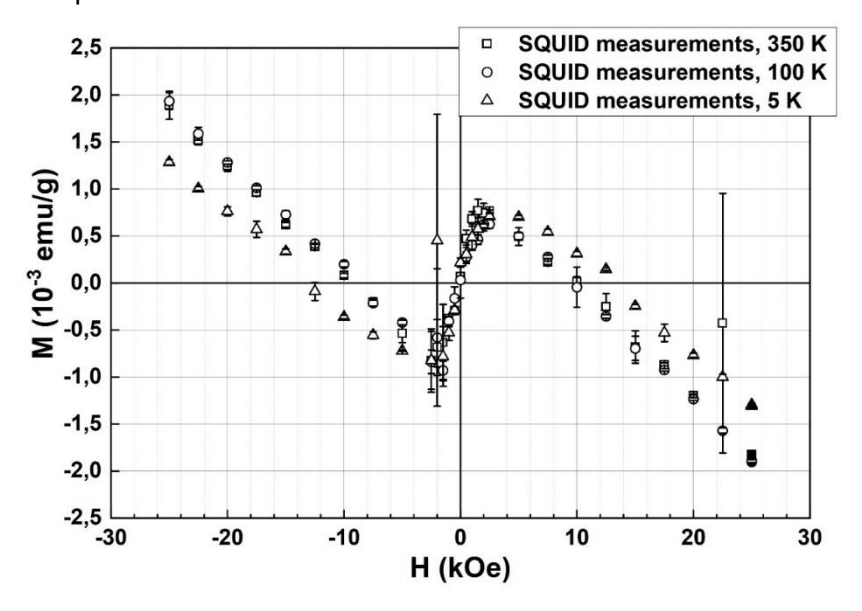


Fig. 1. Field dependences of the magnetization of the SiC/Si hybrid structure grown by the vacancy method of coordinated substitution of atoms measured on the Quantum Design MPMS XL SQUID at temperatures of 5, 100, and 350 K, respectively

High-field measurements performed at helium temperatures on SQUID, in particular, showed that the diamagnetism of SiC layers grown on the silicon crystal surface by VMCSA cannot be described solely by additive contributions of the substrate and the low-dimensional structure grown on it, but requires a different interpretation that takes into account the modification of the internal structure of the latter – structural transformations during the transition from bulk to low-dimensional crystals, and depends on the growth conditions.

Once again, we note that hybrid structures grown by VMCSA on the silicon surface and formally defined as low-dimensional silicon carbide layers, differs significantly [25-27] from SiC crystals due to specially realized growth conditions.

We will not dwell on the discussion of the studies conducted on the superconducting quantum interferometer, since we have devoted a separate publication to a detailed description of the experimental SQUID method [28], the processing of the data obtained during the measurement and their interpretation with respect to the structures under study.

The results obtained in the experiment at the Faraday Balance setup are displayed in Fig. 2, which also shows the field dependences of the magnetization of the low-dimensional structure of the silicon-silicon carbide hybrid grown by the vacancy method of coordinated substitution of atoms measured at the SQUID setup. The above dependences clearly demonstrate the possibilities and advantages of both methods.

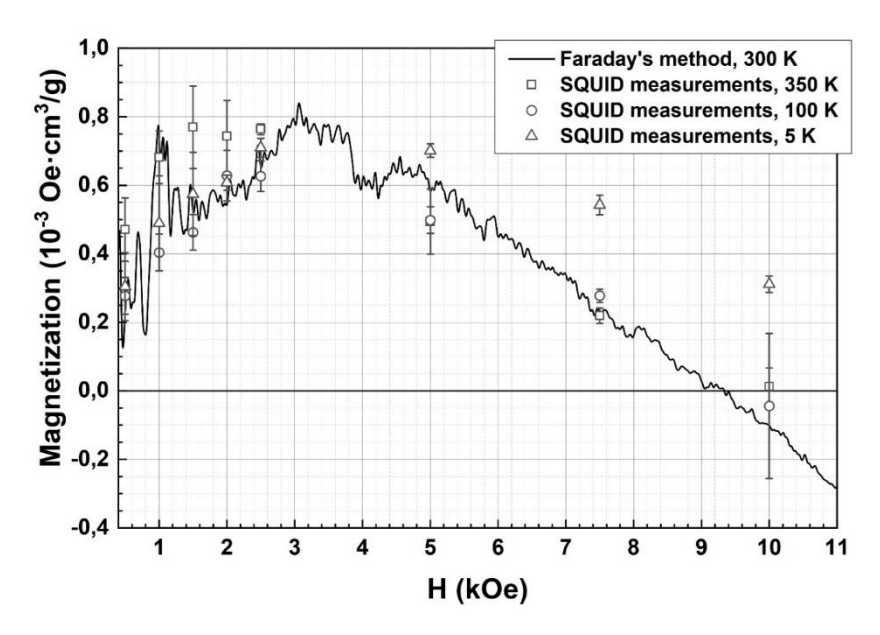


Fig. 2. Field dependence of the magnetization of the SiC/Si hybrid structure grown on the silicon surface obtained by the Faraday method at 300 K (solid curve) in comparison with the results of measurements at the SQUID setup

The analysis of the obtained results shows that in fields less than 2 kOe at room temperature the field dependence of magnetization obtained by the Faraday method is the most informative. Thus, measurements at room temperature in weak magnetic fields at the Faraday Balance at quasi-continuous variation of the external magnetic field (in the range up to 1.5 kOe with a step of 1 Oe) demonstrate oscillations of magnetization, which are combined into groups and, apparently, can be interpreted as a macroscopic quantum de Haas – van Alphen effect [29–31], related to the most direct methods of measuring the charge carriers effective mass [32], and the Aharonov-Bohm effect [33,34], the periodicity of oscillations in which may contain information about charge carriers, the detailed analysis of which we assume to carry out in a separate publication.

Conclusions

The field dependences of the magnetization of the SiC/Si hybrid structure grown by the vacancy method of coordinated substitution of atoms, obtained by two complementary experimental methods have been studied.

The correlation of results of measurements carried out at room temperature in the range of external magnetic field strength up to 11 kOe, realized by two experimental setups, clearly confirm the reliability of the obtained results.

In conclusion, it should be noted that the development and creation of VMCSA technology made it possible to grow hybrid structures based on silicon carbide, exhibiting magnetic properties due not only to a decrease in dimensionality, but, first of all, to the technology of their growth, which was established in this study.

CRediT authorship contribution statement

Vladimir V. Romanov (DSC: writing – review & editing, writing – original draft, investigation; Nikolai I. Rul' (DSC): investigation, writing – review & editing; Vitaliy E. Gasumyants (DSC): writing – review & editing; Ivan D. Venevtsev (DSC): data curation; Konstantin B. Taranets (DSC): data curation; Aleksandr V. Korolev (DSC): investigation; Sergey A. Kukushkin (DSC): conceptualization; Andrey V. Osipov (DSC): conceptualization; Nikolay T. Bagraev (DSC): conceptualization.

Conflict of interest

The authors declare that they have no conflict of interest.

References

- 1. Li F, Roccaforte F, Greco G, Fiorenza P, La Via F, Pérez-Tomas A, Evans JE, Fisher CA, Monaghan FA, Mawby PA, Jennings M. Status and prospects of cubic silicon carbide power electronics device technology. *Materials*. 2021;14(19): 5831.
- 2. Li H, Zhao S, Wang X, Ding L, Mantooth HA. Parallel Connection of Silicon Carbide MOSFETs—Challenges, Mechanism, and Solutions. *IEEE Transactions on Power Electronics*. 2023;38(8): 9731–9749.
- 3. Langpoklakpam C, Liu A-C, Chu K-H, Hsu L-H, Lee W-C, Chen S-C, Sun C-W, Shih M-H, Lee K-Y, Kuo H-C. Review of silicon carbide processing for power MOSFET. *Crystals*. 2022;12(2): 245.
- 4. Baliga BJ. Silicon carbide power devices: Progress and future outlook. *IEEE Journal of Emerging and Selected Topics in Power Electronics*. 2023;11(3): 2400–2411.
- 5. Di Paolo Emilio M. Silicon Carbide Devices. In: *GaN and SiC Power Devices. Synthesis Lectures on Engineering, Science, and Technology.* Cham: Springer; 2024. p.143–163.
- 6. La Via F, Zimbone M, Bongiorno C, La Magna A, Fisicaro G, Deretzis I, Scuderi V, Calabretta C, Giannazzo F, Zielinski M, Anzalone R, Mauceri M, Crippa D, Scalise E, Marzegalli A, Sarikov A, Miglio L, Jokubavicius V, Syväjärvi M, Yakimova R, Schuh Ph, Schöler M, Kollmuss M, Wellmann P. New approaches and understandings in the growth of cubic silicon carbide. *Materials*. 2021;14(18): 5348.
- 7. Xu M, Girish YR, Rakesh KP, Wu P, Manukumar HM, Byrappa SM, Udayabhanu, Byrappa K. Recent advances and challenges in silicon carbide (SiC) ceramic nanoarchitectures and their applications. *Materials Today Communications*. 2021;28: 102533.
- 8. Kimoto T. Bulk and epitaxial growth of silicon carbide. *Progress in Crystal Growth and Characterization of Materials*. 2016;62(2): 329-351.
- 9. Harris GL. Properties of silicon carbide. United Kingdom: IEE; 1995.

- 10. Tarasenko SA, Poshakinskiy AV, Simin D, Soltamov VA, Mokhov EN, Baranov PG, Dyakonov V, Astakhov GV. Spin and optical properties of silicon vacancies in silicon carbide–A review. *Status Solidi (b)*. 2018;255(1): 1700258.
- 11. Abderrazak H., Hmida EBH. Silicon carbide: synthesis and properties. In: *Properties and applications of Silicon Carbide*. 2011. p.361–388.
- 12. Soltys LM, Mironyuk IF, Mykytyn IM, Hnylytsia ID, Turovska LV. Synthesis and Properties of Silicon Carbide. *Physics and Chemistry of Solid State*. 2023;24(1): 5-16.
- 13. Masri P. Silicon carbide and silicon carbide-based structures: The physics of epitaxy. *Surface science reports*. 2002;48(1-4): 1–51.
- 14. Chaussende D, Ohtani N. 5–Silicon carbide. In: Fornari R. (eds.) *Single Crystals of Electronic Materials*. Cambridge: Woodhead Publishing; 2019. p.129–179.
- 15. Pal M, Maity NP, Maity R. Silicon carbide membranes for micro-electro-mechanical-systems based CMUT with influence factors. *Materials Physics and Mechanics*. 2022;49(1): 85–96.
- 16. Kukushkin SA, Osipov AV. Topical review. Theory and practice of SiC growth on Si and its applications to wide-gap semiconductor films. *Journal of Physics D: Applied Physics*. 2014;47: 313001.
- 17. Kukushkin SA, Osipov AV. Epitaxial silicon carbide on silicon. Method of coordinated substitution of atoms (A Review). *Russian Journal of General Chemistry*. 2022;92: 584–610.
- 18. Nishino S, Powell JA, Will HA. Production of large-area single-crystal wafers of cubic SiC for semiconductor devices. *Applied Physics Letters*. 1983;42(5): 460–462.
- 19. Severino A, Locke C, Anzalone R, Camarda M, Piluso N, La Magna A, Saddow S, Abbondanza G, D'Arrigo G, La Via F. 3C-SiC film growth on Si substrates. *ECS Transactions*. 2011;35(6): 99–116.
- 20. Grashchenko AS, Kukushkin SA, Osipov AV, Redkov AV. Vacancy growth of monocrystalline SiC from Si by the method of self-consistent substitution of atoms. *Catalysis Today*. 2021;397–399: 375–378.
- 21. Kukushkin SA, Osipov AV. Interaction of silicon vacancies in silicon carbide. *Technical Physics Letters*. 2024;50(21): 19–23. (In-Russian)
- 22. Kleiner R, Koelle D, Ludwig F, Clarke J. Superconducting quantum interference devices: State of the art and applications. *Proceedings of the IEEE*. 2004;92(10): 1534–1548.
- 23. Clarke J. SQUIDs. Scientific American. 1994;271(2): 46-53.
- 24. White RM. *Quantum theory of magnetism*. Moscow: Mir; 1985. (In-Russian)
- 25. Kukushkin SA, Osipov AV. Anomalous properties of the dislocation-free interface between Si (111) substrate and 3C-SiC (111) epitaxial layer. *Materials*. 2021;14(1): 78.
- 26. Kukushkin SA, Osipov AV. Dielectric Function and Magnetic Moment of Silicon Carbide Containing Silicon Vacancies. *Materials*. 2022;(15): 4653.
- 27. Bagraev NT, Kukushkin SA, Osipov AV, Klyachkin LE, Malyarenko AM, Khromov VS. Registration of terahertz irradiation with silicon carbide nanostructures. *Semiconductors*. 2022;56(14): 2157–2163.
- 28. Rul NI, Romanov VV, Korolev AV, Kukushkin SA, Gasumyants VE. Field dependences of the magnetization of the hybrid SiC/Si structure grown by the vacancy method of coordinated substitution of atoms. *Materials Physics and Mechanics*. 2024;52(6): 1–7.
- 29. De Haas WJ, Van Alphen PM. The dependence of the susceptibility of diamagnetic metals upon the field. *Proceeding of the Royal Netherlands Academy of Arts and Science*. 1930;33: 1106.
- 30. Shoenberg D. Magnetic oscillations in metals. Cambridge: Cambridge University Press; 1984.
- 31. Vonsovskiy SV. Magnetizm. Moscow: Nauka; 1971. (In-Russian)
- 32. Romanov VV, Kozhevnikov VA, Mashkov VA, Bagraev NT. Description of the magnetization of a silicon nanostructures in weak fields at room temperature. The Lifshitz-Kosevich formula with variable effective carrier mass. *Semiconductors*. 2020;54: 1593–1597.
- 33. Aharonov Y, Bohm D. Significance of electromagnetic potentials in the quantum theory. *The Physical Review.* 1959;115(3): 485.
- 34. Bagraev NT, Kukushkin SA, Osipov AV, Romanov VV, Klyachkin LE, Malyarenko AM, Rul' NI. Room-temperature quantum oscillations of static magnetic susceptibility of silicon-carbide epitaxial layers grown on a silicon substrate by the method of the coordinated substitution of atoms. *Materials Physics and Mechanics*. 2022;50(1): 66–73.

MATERIALS PHYSICS AND MECHANICS

53 (1) 2025

УЧРЕДИТЕЛИ

Санкт-Петербургский политехнический университет Петра Великого **Адрес:** 195251, Санкт-Петербург, Политехническая ул., д. 29 Институт проблем Машиноведения Российской академии наук **Адрес:** 199178, Санкт-Петербург, Большой пр-кт В.О., д. 61

ИЗДАТЕЛЬ

Санкт-Петербургский политехнический университет Петра Великого **Адрес:** 195251, Санкт-Петербург, Политехническая ул., д. 29

Журнал зарегистрирован в Федеральной службе по надзору в сфере связи, информационных технологий и массовых коммуникаций (РОСКОМНАДЗОР), свидетельство ПИ №ФС77-69287 от 6 апреля 2017 года.

РЕДАКЦИЯ ЖУРНАЛА

Профессор, д.т.н., академик РАН, **А.И. Рудской** – главный редактор
Профессор, д.ф.-м.н., член-корр. РАН, **А.К. Беляев** – главный научный редактор
Профессор, д.ф.-м.н. **И.А. Овидько** (1961 - 2017) – основатель и почетный редактор
Профессор, д.ф.-м.н. **А.Л. Колесникова** – ответственный редактор
Профессор, д.ф.-м.н. **А.С. Семенов** – ответственный редактор
К.ф.-м.н. **Л.И. Гузилова** – выпускающий редактор
К.ф.-м.н. **Д.А. Китаева** – редактор, корректор

АДРЕС И ТЕЛЕФОН РЕДАКЦИИ

199178, Санкт-Петербург, Большой пр-кт В.О., д. 61

Тел. редакции: +7(812)552 77 78, доб. 224

E-mail редакции: mpmjournal@spbstu.ru Компьютерная верстка Л.И. Гузилова

Подписано в печать 23.05.2025 г. Выход в издания в свет: 09.06.2025 г. Формат 60х84/8. Печать цифровая Усл. печ. л. 10.0. Тираж 100. Заказ____. Цена: Бесплатно

Отпечатано в Издательско-полиграфическом центре Политехнического университета Петра Великого

Адрес: 195251, Санкт-Петербург, Политехническая ул., 29 Тел.: +7(812)552 77 17

Fractional strain analysis on reflection of plane waves at an impedance boundary of swelling porous thermoelastic medium S. Sharma, D. Batra, R. Kumar	non-local 1–21
Study of different theories of thermoelasticity under the Rayleigh wave propagation an isothermal boundary V. Gupta, M. Kumar, Sh. Goel	along 22–37
Multifractal properties of breaking bonds coordinates in heterogeneous materials re by the discrete element method V.L. Hilarov, E.E. Damaskinskaya	evealed 38–47
Influence of free surface on melting and crystallization in nickel and copper: molecular dynamics simulation G.M. Poletaev, Y.V. Bebikhov, A.S. Semenov, R.Y. Rakitin, D.V. Novoselova	48-56
Thermal cycling stability of the martensitic transformation in Ti _{40.7} Hf _{9.5} Ni _{49.8-x} Cu _x (x = 1, 5 or 10 at. %) cast alloys N.N. Resnina, S.P. Belyaev, A.I. Bazlov, A.V. Sibirev, I.V. Ponikarova, M.E. Trofimova, A.M. I	57–67 Ivanov, R.M. Bikbaev
Creation of aluminum matrix composites reinforced with micro- and nanoparticles o carbide with nickel coating and description of their hardening mechanisms E.G. Zemtsova, B.N. Semenov, N.F. Morozov, Yu.V. Sidorov, V.K. Kudymov, V.M. Smirnov	f titanium 68–77
EBSD on bainitic steel to assess parent austenite state after multi-pass hot rolling: Textural analysis versus reconstruction of prior grains A.A. Zisman, N.Yu. Zolotorevsky, D.A. Petrov, S.N. Petrov	78-88
Structural changes in a commercial Al-Cu alloy during hot equal channel angular pre	essing 89–108
Effect of high pressure torsion and annealing on the microstructure and microhardness of Inconel 718 produced by selective laser melting K.S. Mukhtarova, R.V. Shakhov, Sh.Kh. Mukhtarov	ess 109-116
Mechanical and durability properties of sustainable composites derived from recycle polyethylene terephthalate and enhanced with natural fibers: a comprehensive review A. Kumar, R. Bedi	
Stydy of the influence of brombutyl and divinylstyrene caoutchoucs, sevilen on the properties of seawater-resistant rubber E.N. Egorov, N.I. Kol'tsov	143-149
Preparation and characterization of geopolymer/activated carbon composite materials used as a bone substitute material A. Moonphukhiao, B. Samran, S. Chaiwichian	150-158
Magnetism of the hybrid SiC/Si structure grown on silicon surface V.V. Romanov, N.I. Rul', V.E. Gasumyants, I.D. Venevtsev, K.B. Taranets, A.V. Korolev, S.A. A.V. Osipov, N.T. Bagraev	159–164 Kukushkin,

